Search for Quantum Spin Liquid in Triangular Antiferromagnets

Dissertation

zur Erlangung des akademischen Grades

Dr. rer. nat.

eingereicht an der

Mathematisch-Naturwissenschaftlich-Technischen Fakultät

der Universität Augsburg

von

Franziska Grußler

Augsburg, Mai 2024

Erstprüfer: Prof. Alexander Tsirlin
Zweitprüfer: Priv.-Doz. Dr. Hans-Albrecht Krug von Nidda
Tag der mündlichen Prüfung: 18.07.2024

Contents

1 Introduction

P. W. Anderson coined the term quantum spin liquid (QSL) in 1973 when he introduced his idea of a resonating valence bond solid on the triangular lattice [1]. Today, the analogy to an ordinary liquid is still popularly employed to convey an illustrative understanding of the complex nature of a QSL. Thus, QSLs are described as systems of highly correlated spins which evade conventional magnetic order even at zero temperature. Naturally, this description does not fully capture the nature of the QSLs, where the spins also need to be quantum-mechanically entangled and facilitate quantum fluctuations.
Initially, the driving force behind the interest in QSLs is its connection to high-temperature superconductivity. Until today, the perception of the quantum spin liquid has changed and adapted multiple times from its introduction in 1973, resulting in a plethora of proposed theoretical models describing this novel state of matter. Therefore, the QSL is now well established as an interesting and many-faceted research field of its own, which entails among others fractional excitations and topological properties. [2–4]

Despite the large interest in QSLs, also in light of potential application in quantum technology, the search for real-life materials proves to be challenging and is an ongoing process. Sample preparation and crystal growth are the starting point in the endeavor of synthesizing spin-liquid materials and has been practiced and improved for centuries.

The first records of crystal preparation date back to 77–79 AD as part of the *Historia Naturalis*, an encyclopedia consisting of 37 books aiming to summarize the knowledge of natural science of the time. Author of this impressive and unique work, that also offers invaluable insights into the culture of ancient Roman times, is the roman scholar and natural scientist Gaius Plinius Secundus, known as Pliny the Elder. While at the time of Pliny the Elder crystals are retrieved with comparatively simple methods, like the extraction of vitriol by evaporating mine or spring waters, many different technically advanced and more complicated methods of growing crystals are employed today. However, they are still based on the same mechanisms, e.g. melt, solution and vapor growth, that have already been known for many centuries. [5, 6]

Until the 17th century the rock-crystals were widely believed to be an organic material that is formed by bacteria in the soil. This opinion was first challenged by the Danish scientist Nicolaus Steno, also known as Niels Stensen, who argued that crystals grow in an inorganic process at high temperatures, where tiny particles are formed in an aqueous solution and assemble into crystals. Niels Stensen is also regarded as one of the founders of crystallography, with his observation of constant interfacial angles independent of the shapes of investigated quartz crystals. [5, 7]

Although Niels Stensen assertion on the formation of crystals fundamentally reshaped the perspective on crystal growth, aspirations to answer the question why crystals form and what mechanisms underlie the process only arose much later. Today, a manifold of techniques of growing single crystals can be employed, which can be tailored to meet required properties like size, purity and control of the defect structure. The crystal growth techniques can be roughly divided in three categories, depending on the nature of their nutrient phase, which can be either liquid (melt or solution), vaporous (condensation, sublimation or reaction) or a strained solid. [5]
The growth of a crystal from a nutrient phase takes place in three stages. First a driving force needs to be present, which leads to a departure of the system from its equilibrium condition by forming a supersaturated or supercooled state. In the nucleation stage, clusters of particles spontaneously form and dissociate in the nutrient phase. When the clusters by chance become larger than the critical size, the growth stage is entered, where the particles grow into crystals. [7]

Many advances in crystal growth were made in the 20th century and the invention of different methods enabled the growth of single crystals of more and more complicated compounds. In the category of melt growth, zone melting was first implemented in 1928 by P. Kapitza to grow a Bi single crystal. The growth of high-quality single crystals of Bi was a hot topic at the time and crystal growth methods and research was advanced, among others, by L. Shubnikov who observed the Shubnikov-de Haas effect in such Bi single crystals in 1930 together with W. J. de Haas [8]. The basic mechanism behind zone melting, is creating a molten zone in a bar of material via a movable heater and creating two opposing interfaces. One of the interfaces serves as a feeding rod, where material is dissolved, while the second interface is used as a seeding rod, where the material recrystallizes and the single crystal is formed. In recent times, the promising quantum spin-liquid candidate $YbMgGaO_4$ was synthesized in single crystalline form with the zone melting method. [5, 9]

$YbMgGaO_4$ fitted right into the model proposed for triangular lattice antiferromagnets by P. W. Anderson. Therefore, $YbMgGaO_4$ was introduced as a prospect QSL in 2015, not least because it fulfilled the most comprehensible and essential requirement of evading long-range magnetic order to lowest temperatures. However a structural peculiarity of the material finally disputed the initial interpretation as a spin liquid candidate. The complexity of real-life materials is a common difficulty faced in the search for QSL materials. [2, 10]

Nevertheless, the triangular lattice remains a viable host for potential QSLs and the investigation of $YbMgGaO_4$ turned the interest to the related compound family of $A\mathrm{Yb}X_2$ (A: alkaline metal, X: chalcogen). The synthesis, characterization and investigation of multiple members of this family is the focal point of this thesis.
In contrast to $YbMgGaO_4$ the synthesis of $A\mathrm{Yb}X_2$ single crystals is based on a solution growth method. The premise of solution growth is to solve the material in a liquid medium, with a subsequent recrystallization under controlled conditions that allow the formation of single crystals [5]. For $A\mathrm{Yb}X_2$ generally a high-temperature self-flux method is applied that simultaneously uses ACl as flux and for providing the respective

alkaline metal ion. In contrast to the floating zone method used for $YbMgGaO_4$, substantially smaller crystals are produced in this way for $AYbX_2$. Therefore, the one of the goals of this thesis is to produce crystals large enough for specific measurements. While for many measurements performed in this work the achieved sample size is sufficient, samples are also provided for low-temperature dilution fridge measurements as well as potential future INS measurements and need to fulfill the specifications of those measurements, which are in general dependent on larger crystal size.

The structure of the thesis is as follows. In Chapter 2 the fundamentals of magnetism are reviewed and an introduction to the QSL physics is presented, both tailored to the specific case of the family of Yb-based triangular antiferromagnets $AYbX_2$. Additionally, the concept of heat capacity and its connection to magnetic entropy is discussed.

In the subsequent Chapter 3 the measurement techniques employed in the preparation of this work are covered, which includes methods for sample characterization like X-ray diffraction (XRD) and energy dispersive X-ray spectroscopy (EDX) as well as measurements addressing the magnetic properties.

The up-to-date research on $YbMgGaO_4$ is summarized in Chapter 4, illuminating the extensive investigation necessary to identify or disprove a QSL.

The following Chapters 5-9 address the synthesis, characterization and low-temperature ($T > 0.4\,\mathrm{K}$) investigation of the spin-liquid candidates $NaYbO_2$, $KYbO_2$, $KYbS_2$ and $NaYbSe_2$ as well as the doping series $KYb(S_xSe_{1-x})_2$. For all compounds a short summary of the current state of research is presented in the beginning of the respective chapter. The characterization of the crystal structure is done by performing Rietveld refinements on powder XRD measurements. For investigation of the magnetic and physical properties low-temperature and high-field magnetization, susceptibility, electron spin resonance (ESR) and specific heat measurements are performed on most compounds and summarized in a preliminary phase diagram. For the previously studied $NaYbO_2$ (Chapter 5) results of the aforementioned measurements are available from literature and my master thesis [11]. In this work a pressure study entailing synchrotron XRD, susceptibility and μSR measurements of $NaYbO_2$ is presented. In Chapter 6 the results for the so far less investigated $KYbO_2$ are compared to $NaYbO_2$ to understand the influence of exchanging the alkaline metal of $AYbO_2$. The results obtained on $KYbO_2$ in this thesis are published in Ref. [12]. For $KYbS_2$ only basic measurements are reported in literature up to now, which are complemented and extended to lower temperatures in Chapter 7. $NaYbSe_2$, on the other hand, is also well studied in literature and revisited in Chapter 8 mainly for the purpose of synthesis and characterization of samples for complementary, low-temperature dilution fridge measurements, which are not part of this work. Chapter 9 comprises the synthesis and investigation of the doping series $KYb(S_xSe_{1-x})_2$, with the goal to research the influence of introducing structural randomness on the $AYbX_2$ compounds.

A comparison and summary of all investigated compounds are presented in Chapter 10 and Chapter 11.

2 Background

2.1 Magnetism of Free Ions

The magnetism in solids is mainly mediated via electrons, while the contribution of the nucleus is neglectable in most cases at least for temperatures above 1 K [13]. The orbital angular momentum $\mathbf{l}$ and the spin angular momentum $\mathbf{s}$ are two intrinsic properties of electrons. In classical approaches the orbital angular momentum is derived from the orbital motion of an electron around the nucleus, while a precession of the electron around its own axis was presumed to be the origin of the spin angular momentum. However, the classical view of magnetism is rather limited, as it prohibits magnetic moments in systems in thermal equilibrium, contradicting experimental observations. The classical approach is therefore not applicable to magnetism, an inherently quantum mechanical phenomenon. Although the initial, classical interpretation of the orbital and spin angular momentum is incorrect, it was shown that they can be translated into the quantum picture. The electronic state which is occupied by the electron then defines the angular momentum $\hat{\mathbf{l}}$, with the eigenvalues of $\hat{l}^2 = l(l+1)$ and $\hat{l}_z = m_l$. The latter is the z component of $\hat{\mathbf{l}}$. Additionally, electrons have an intrinsic magnetic moment which is related to the intrinsic angular momentum, namely the spin of the electron $\hat{\mathbf{s}}$. Analogous to $\hat{\mathbf{l}}$, the eigenvalue of $\hat{s}^2$ and the z component are $s(s+1)$ and m_s, respectively. The quantum number s of an electron is $\frac{1}{2}$ and $m_s = \pm\frac{1}{2}$. [14, 15]

To determine the magnetic moment of an atom the contribution of all electrons need to be considered. Since the filled shells have no net angular momentum, the decisive contribution is given by the partially filled shells of the atom. For these not completely filled shells the individual electrons contribute to the total orbital angular momentum $\hat{\mathbf{L}} = \sum \hat{\mathbf{l}}$ and the total spin angular momentum $\hat{\mathbf{S}} = \sum \hat{\mathbf{s}}$. In addition to that, one needs to consider a coupling between the orbital angular and spin momentum. If this spin-orbit interaction is weak one can define the total angular momentum $\hat{\mathbf{J}} = \hat{\mathbf{S}} + \hat{\mathbf{L}}$, where the eigenvalues of $\hat{J}^2$ is $j(j+1)$ and of $\hat{J}_z$ is m_j. The energy eigentstates of the atom without considering the spin-orbit interactions are determined by the values of S and L, leading to $(2L+1)(2S+1)$-fold degeneracy of the energy levels. Taking the spin-orbit interaction into account, the degeneracy is lifted into the so called fine structure determined by the value of J, with a $(2J+1)$-fold degeneracy of energy levels. [14, 15]

The total orbital angular momentum L and the total spin angular momentum S take values that minimize the energy of the atom. A guideline for minimizing the energy of an atom and determining its ground state is defined by the three Hund's

rules.
According to Hund's rules, the first quantum number to be determined is the total spin quantum number S. For electrons the Pauli exclusion principle needs to be considered to achieve a minimization of the Coulomb energy. Therefore the first Hund's rule requires a maximization of S.
Next, the total orbital angular momentum quantum number L also needs to be maximized. This rule is again based on the need to minimize the Coulomb repulsion. The third rule thrives to minimize the spin-orbit energy. The value of J therefore depends on the filling degree of the shell. For a less than half filled shell J is determined by $J = |L - S|$, while for a more than half filled shell J is given by $J = |L + S|$.
The application of Hund's rules is not universal, however. While they give a very good estimation for rare earth ions, other systems like the transition metal ions show deviations from the third rule. In the case of the transition metal ions the crystal field dominates the energy scale and leads to the violation of the third Hund's rule. [14]

The rare earth ions, on the other hand, are well described by Hund's rules, since crystal-field splittings are small compared to the spin-orbit coupling. Yb^{3+} serves as a convenient example for their application. A Yb^{3+} ion contains thirteen 4f electrons, hence a total spin angular momentum quantum number of $S = \frac{1}{2}$ is obtained in accordance with Hund's first rule. The orbital angular momentum quantum number is maximized with $L = 3$ for the nearly completely filled 4f shell. Lastly, $J = |3 + \frac{1}{2}| = \frac{7}{2}$ is derived for a more than half filled shell. The $(2L + 1)(2S + 1) = 14$-fold degeneracy of the spin and orbital angular momenta is lifted by the spin-orbit coupling. The resulting $(2J + 1) = 8$-fold degeneracy of the ground state of the isolated ion can be further reduced by smaller terms like the crystal field, as will be discussed in the following chapter. [14]

With the total angular momentum $\hat{\mathbf{J}}$ the magnetic moment of an atom or ion can be calculated

$$\hat{\boldsymbol{\mu}} = -g_J \mu_B \hat{\mathbf{J}}, \tag{2.1}$$

with the Bohr magneton μ_B. The g-factor g_J is determined as

$$g_J = \frac{3}{2} + \frac{S(S+1) - L(L+1)}{2J(J+1)}. \tag{2.2}$$

Since the magnetic moment is dependent on the value of the total angular momentum J only ions and atoms with partially filled electronic shells have a magnetic moment. Fully filled shells lead to $J = 0$. [14, 16]

2.2 Crystal Electric Field

In a solid the magnetic ions cannot be viewed as isolated and one needs to consider the influence of their environment on the magnetic properties. Magnetic ions that are incorporated into a crystal structure are exposed to the electric field of the surrounding anions, which is called the crystal electric field (CEF). The crystal field theory is a

convenient approach to explaining the effect of the crystal field on the magnetic ions by modeling the orbitals of the neighboring ions as point charges. A more accurate view on the influence of the environment on the magnetic ions can be obtained through the ligand field theory, based on the molecular orbital theory. For the scope of this work the crystal field theory is sufficient since the f-orbitals of the Yb^{3+} ions are localized and do not hybridize with the p-orbitals of the ligands. The effect of the crystal field on the magnetic ion is heavily dependent on the symmetry of the crystal and therefore on the arrangement of the anions surrounding the magnetic ion. In addition to that, it is also dependent on the magnetic ion itself. Two prominent groups of magnetic ions can be differentiated: the 3d transition metal ions and the 4f rare earth ions. The reason for their different behaviors lies in the nature of their orbitals. In the case of 4f elements the orbitals are closer to the nucleus and are shielded from the crystal field by the 5s and 5p shells. The 3d transition metals, on the other hand, feel the full force of the crystal field to the point that the spin-orbit coupling is diminished and Hund's third rule doesn't apply. This becomes evident when the effective magnetic moments are calculated and compared to the experimentally determined values. For the 4f elements good agreement between experiment and calculation is observed, while the 3d transition metals show a rather large deviation, with the exceptions of the half filled and fully filled shells where $L = 0$. The experimental effective moment of the 3d elements is much better reciprocated if the orbital momentum is disregarded: $\mu_{\text{eff}} = 2\mu_{\text{B}}\sqrt{S(S+1)}$. This quenching of the orbital momentum is a direct consequence of the change in the order of the energy levels, where the spin-orbit coupling is replaced by the crystal field interaction in significance.

The octahedral environment imposed on a 3d transition metal is a prominent example for the effect of the crystal field, as depicted in Fig. 2.1. In this case the magnetic ion is often surrounded by non-magnetic ions, i.e. oxygen. For the free atom

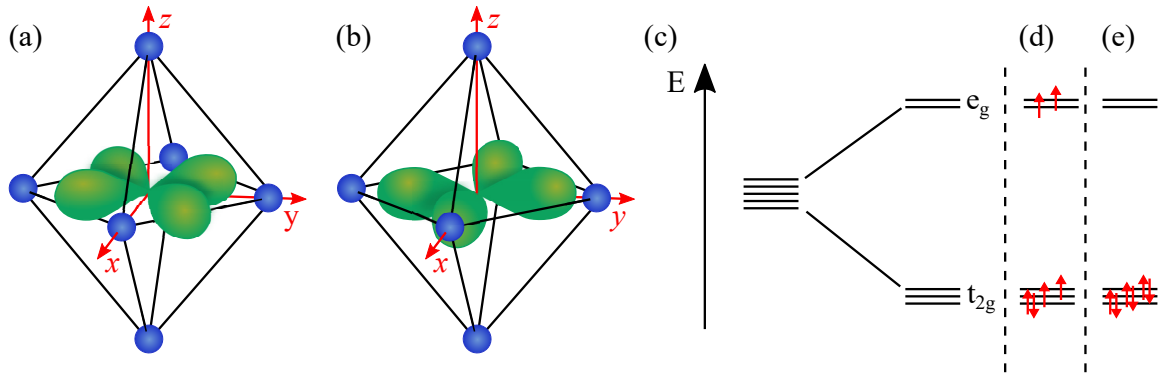

Figure 2.1: *Splitting of the ground state energy levels under the influence of an octahedral crystal field. The $d_{x^2-y^2}$ (a) and the d_{xy} (b) orbital in the octahedral environment are shown exemplarily. (c) The e_g orbitals ($d_{x^2-y^2}$, d_{z^2}) are raised in energy while the t_{2g} orbitals (d_{xy}, d_{xz}, d_{yz}) become energetically favorable. (d),(e) High- and low-spin configuration depending on the crystal field strength compared to the pairing energy. Adapted from Ref. [14].*

the orbitals are $(2L + 1) = 5$-fold degenerate while for a magnetic ion in a crystal this degeneracy can be lifted by the crystal field. In the octahedral crystal field the t_{2g} orbitals, which comprises the d_{xy}, d_{xz} and d_{yz} orbitals, are energetically favorable since the angular distribution of their charge density points between the x-, y- and z-axis and experience less overlap with the neighboring p orbitals [see Fig. 2.1(a)]. In comparison, the e_g orbitals, which contains the d_{z^2} and $d_{x^2-y^2}$ orbitals, are raised in energy since their orientation along the z- axis for the d_{z^2} orbital and the x- and y-axis for the $d_{x^2-y^2}$ orbital shown in Fig. 2.1(b), generates a larger overlap with the p orbitals of the oxygen ions. The lifting of the 5-fold degenerate ground state into the e_g and t_{2g} orbitals is depicted in Fig. 2.1(c). For the transition metal ions with only partially filled 3d shells the electrons can populate the no longer degenerate orbitals in two ways. As stated in the first Hund's rule the electrons strive to singly occupy the orbitals in order to minimizes the Coulomb energy. If the crystal field energy is smaller than the so called pairing energy the first Hund's rule is obeyed resulting in a high spin state, which is known as the weak field case [see Fig. 2.1(d)]. On the other hand, if the crystal field energy is larger than the pairing energy the low spin state (strong-field case) is achieved. The lower energy orbitals are then doubly filled before electrons are elevated to the higher energy orbitals, as shown in Fig. 2.1(e). [14, 16]

Although the crystal field interaction is not strong enough to overcome the spin-orbit coupling for the 4f elements, it still has a significant impact on their energy levels and hence their ground state. The $J(J + 1)$-fold degeneracy of the 4f ions is lifted in the crystal field, resulting in two possible scenarios for the splitting of the energy levels depending on the symmetry of the crystal field and the value of J. The Kramers theorem provides a general rule for the splitting of the energy levels in accordance to the value of J: Systems with an even number of electrons (i.e. an integer value of J) can split into singlets, while a half-integer value of J (i.e. an odd number of electrons) keeps the energy levels at least two-fold degenerate. [14, 17]

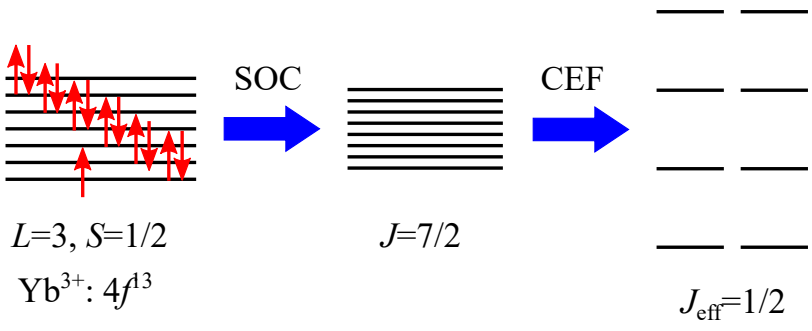

Figure 2.2: *Splitting of the 14-fold spin and orbital degeneracy by the spin-orbit coupling to the 8-fold degenerate ground state of the $J = \frac{7}{2}$ Yb^{3+} ion. In the crystal field of the D_{3d} point group the 8-fold degeneracy is then split into four doublets with an effective $J_{\text{eff}} = \frac{1}{2}$ ground state. Adapted from Ref. [18].*

The ground state of a free Yb^{3+} according to Hund's rules is determined in Chapter 2.1 with $S = \frac{1}{2}$ and $L = 3$. The spin orbit coupling in Yb^{3+} compounds is around 0.36 eV, while the crystal field splitting is typically at least one order of magnitude smaller ($YbMgGaO_4 \approx 0.036\,eV$), confirming that the spin-orbit coupling needs to be considered before the crystal field splitting [9, 19, 20]. It lifts the 14-fold spin and orbital degeneracy to a 8-fold degenerate state with $J = \frac{7}{2}$ (see Fig. 2.2). For Yb^{3+} ions in the crystal field of the D_{3d} point group the 8-fold degeneracy is further split into four doublet states in agreement with the statements of the Kramers theorem. Due to the rather large separation between the Kramers doublets the ground state of $YbMgGaO_4$ and other Yb^{3+} based triangular antiferromagnets is dominated by the lowest Kramers doublet and these systems can be treated as effective spin-$\frac{1}{2}$ systems. [18]

2.3 Dia- and Paramagnetism

In addition to the CEF of neighboring atoms, magnetic moments can also be influenced by externally applied magnetic fields. The magnetic susceptibility χ describes the change of the magnetization $\mathbf{M}$, the magnetic moment per volume, induced by an external magnetic field $\mathbf{H}$: $\chi = \partial\mathbf{M}/\partial\mathbf{H}$. If the correlation between $\mathbf{M}$ and $\mathbf{H}$ is linear this can be simplified to $\chi = \mathbf{M}/\mathbf{H}$. [21]

Magnetic materials can have different responses to the application of a magnetic field.
Diamagnetism is encountered in all materials, although its contribution is generally rather weak. It is characterized by a negative susceptibility. A general understanding of diamagnetism can be obtained from the classical point of view through Lenz's law. An externally applied magnetic field affects the orbital motion of the electrons, which in turn induces a magnetic field that opposes the external field.
Paramagnetism is associated with a positive susceptibility. The Pauli paramagnetism of the conduction electrons in metals and the van Vleck contribution of excited states give temperature independent contributions to the paramagnetism of a material. Van Vleck paramagnetism is also observed in systems with $J = 0$ ground state, where no magnetic response is expected if a magnetic field is applied. The paramagnetism in those systems stems from the excitation to states with $J \neq 0$.
In addition to the rather small temperature independent parts permanent, localized magnetic moments contribute a temperature-dependent paramagnetic response to the susceptibility [see Fig.2.3(a)], described in the Langevin theory of paramagnetism. The randomly oriented magnetic moments are inclined to align in the direction of an externally applied magnetic field, leading to an increase of the magnetization M. The influence of a magnetic field on the magnetization is given by

$$M = M_{\mathrm{sat}} \mathrm{B}_J(y) \tag{2.3}$$

and depicted in Fig. 2.3(b). The saturation magnetization $M_{\mathrm{sat}} = ng_J\mu_{\mathrm{B}}J$ (n: number of spins per unit volume) is reached when all spins are aligned parallel to the magnetic field. The Brillouin function $\mathrm{B}_J(y)$, with $y = g_j\mu_{\mathrm{B}}JB/k_{\mathrm{B}}T$, describes the shape of the magnetization curve:

$$\mathrm{B}_J(y) = \frac{2J+1}{2J}\coth\left(\frac{2J+1}{2J}y\right) - \frac{1}{2J}\coth\left(\frac{y}{2J}\right) \tag{2.4}$$

For small magnetic fields and high temperatures ($y << 1$) the Brillouin function can be simplified using the Taylor expansion and the molar susceptibility can be deduced in the simple form of the Curie law:

$$\chi = \frac{M}{H} = \frac{n\mu_0\mu_{\mathrm{eff}}^2}{3k_{\mathrm{B}}T} = \frac{C}{T}. \tag{2.5}$$

Here μ_0 is the vacuum magnetic permeability and $C = n\mu_0\mu_{\mathrm{eff}}^2/3k_{\mathrm{B}}$ is the Curie constant. The effective magnetic moment μ_{eff} can therefore be determined from measurements of the susceptibility,

$$\mu_{\mathrm{eff}} = \sqrt{\frac{3k_{\mathrm{B}}}{n\mu_0}C}, \tag{2.6}$$

and compared to the effective moment expected from the the value of J which is calculated as

$$\mu_{\mathrm{eff}} = -g_J\mu_{\mathrm{B}}\sqrt{J(J+1)}. \tag{2.7}$$

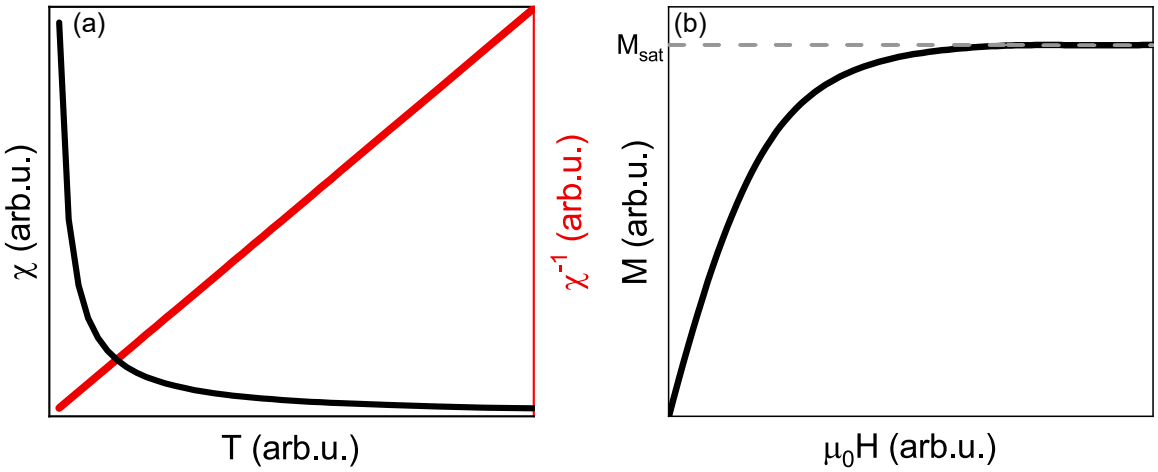

Figure 2.3: *(a) Magnetic susceptibility (black) and inverse magnetic susceptibility (red) of a paramagnet. Plotting the inverse susceptibility allows to linearly fit the data with the Curie law. (b) Brillouin-like magnetization curve of a paramagnetic material. The dashed line indicates the maximum magnetization (M_{sat}) that is reached in the fully polarized regime. Adapted from Ref. [16].*

Conventionally the effective magnetic moment is expressed in terms of μ_B and has no units. An alternative name for the effective moment frequently encountered in literature therefore is the Bohr magneton number. [14, 16]

The Curie law well describes the susceptibility of a paramagnetic material and yields valuable information on the magnetic moments. In practice, commonly the inverse susceptibility is analyzed with the Curie law by applying a linear fit [see Fig. 2.3(a)].

2.4 Exchange Interactions

2.4.1 Origin of Exchange

So far interactions between magnetic moments within solids have not been considered, however, they are essential for explaining the phenomena of long-range magnetic order and spin liquid formation. First the interaction between two magnetic dipoles is considered. The energy that characterizes the interplay of the two dipoles $\boldsymbol{\mu}_1$ and $\boldsymbol{\mu}_2$ with a distance $\boldsymbol{r}$ between them is given by

$$E = \frac{\mu_0}{4\pi r^3}\left[\boldsymbol{\mu}_1 \cdot \boldsymbol{\mu}_2 - \frac{3}{r^2}(\boldsymbol{\mu}_1 \cdot \boldsymbol{r})(\boldsymbol{\mu}_2 \cdot \boldsymbol{r})\right]. \tag{2.8}$$

For two moments with $\mu \approx 1\,\mu_B$ and a distance of 1 Å between them, the magnetic dipolar interaction is estimated to be about 1 K. Therefore, the dipolar interaction is too weak to explain the appearance of magnetic order in most materials and may only become relevant for systems that order in the millikelvin range. [14]

The relevant exchange interactions prompting the formation of long-range order therefore must have a different origin. A simple two-electron model is a convenient starting point to understand the mechanism behind the exchange interactions. The spin part of the electron wave function can either consist of a singlet or a triplet state. The energy difference between the triplet and singlet state $E_S - E_T$ determines which state is favorable. The triplet state is favored in the case of the two electron model, leading to a ferromagnetic exchange between the electrons in agreement with the Pauli exclusion principle. If the electrons are located on different atoms like in the hydrogen molecule, i.e. the distance between the nuclei is small and the orbitals show significant overlap, the situation is reversed. The singlet state becomes energetically favorable due to the energy gain generated by the formation of a chemical bond that exceeds the energy loss due to repulsion between electrons. The triplet state cannot experience this energy gain since the Pauli principle precludes two electrons of the same spin to be in the same place. [14, 15]

For isolators the virtual hopping process provides another point of view on the interaction between magnetic moments. If two electrons are on the same site, they experience a strong Coulomb repulsion, which is called Hubbard U in analogy to the Hubbard model. A system thrives to minimize the on-site Coulomb energy, e.g. in the half filled limit the electrons singly occupy each lattice site and for $U = \infty$ this is

the ground state of the system. If U is large but not infinite, there is a probability t for the electron to hop between two neighboring sites, provided that the spins are oriented antiparallel. The hopping process leads to an energetic saving and makes the singlet state energetically favorable to the triplet state, where the hopping is not possible due to the parallel alignment of spins. [14, 15]

The exchange mechanisms provide the basis for the magnetic interactions in insulating materials. The easiest imaginable process in which the electrons of neighboring magnetic atoms interact is the direct exchange. However, a sufficient direct overlap of the magnetic orbitals is necessary in this case, which is often not realized in real materials. Especially the 4f elements, with their strongly localized electrons which lie close to the nucleus, are not amenable to the direct exchange mechanism. [14]
The magnetic exchange in rare earth and other insulating transition-metal compounds has to be mediated. The Goodenough-Kanamori-Anderson rules describe the magnetic exchange between non-neighboring magnetic ions (M) mediated by a non-magnetic intermediate ion (ligand, L). Two scenarios are possible depending on the interaction geometry. If the magnetic ions and the mediating ion are arranged in a 180° geometry, the d-orbitals of the magnetic ions directly overlap with the same p-orbital of the ligand, as depicted in Fig. 2.4(a) and (b). For simplicity it is assumed that the orbitals of the magnetic ions are occupied by only a single electron each. In the case of an antiferromagnetic arrangement of spins in the magnetic ions, the electrons of the

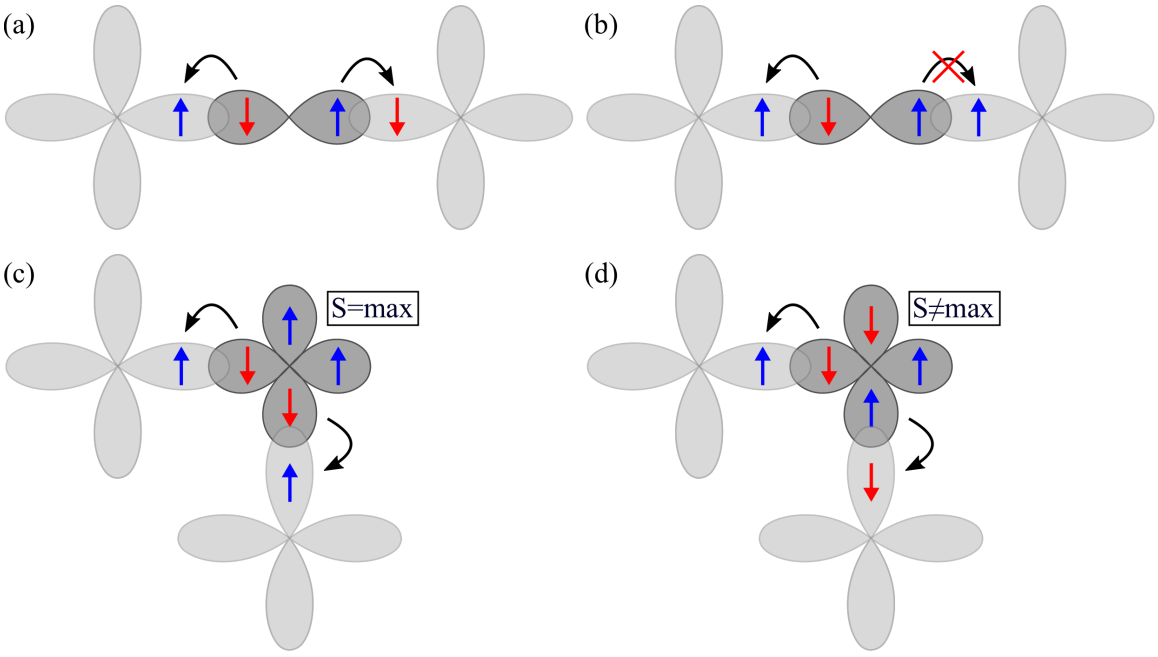

Figure 2.4: *(a),(b) Illustration of the 180° superexchange. Hopping of the ligand electrons is only allowed for antiparallel arrangement of the spins of the magnetic ions. On the other hand, in the case of 90° superexchange hopping is only possible for parallel oriented spins in the magnetic ions (c) and forbidden for antiparallel oriented spins (d).*

ligand are free to hop from the p-orbitals into the d-orbitals and gain energy in the process. On the other hand, the hopping process is forbidden if the spins in the magnetic ions are oriented parallel. The 180° superexchange therefore promotes an anitparallel (antiferromagnetic) coupling between the magnetic ions.
Another way magnetic interaction can be mediated is through the 90° coupling geometry where the d-orbitals overlap with two different p-orbitals [see Fig. 2.4(c) and (d)]. The hopping process in this case is possible for antiparallel and parallel arrangement of the spin of the magnetic ion. If the spins of the magnetic ions are antiparallel, the electrons in the p-orbitals of the ligand have antiparallel spins. Parallel spins in the d-orbitals of the magnetic ion, on the other hand, lead to a parallel arrangement of spins in the p-orbitals of the ligand, which is in accordance with the maximization of S required by the first Hund's rule. The parallel spin arrangement is therefore accompanied by an energy gain and the 90° super exchange favors a parallel (ferromagnetic) spin arrangement. [14, 15]

2.4.2 Heisenberg Model

The interactions between all spins in a system can be described with the Heisenberg spin Hamiltonian

$$H = \sum_{\langle ij \rangle} J_{ij} \hat{\mathbf{S}}_i \hat{\mathbf{S}}_j. \tag{2.9}$$

J_{ij} is the exchange integral or coupling constant describing the interaction between spin i and spin j and should not be confused with the total angular momentum $\mathbf{J}$. $\hat{\mathbf{S}}_i$ and $\hat{\mathbf{S}}_j$ are spin operators. Although their notation indicates that they represent the spin angular momentum they may, in fact, represent any angular momentum operator ($\hat{\mathbf{S}}$, $\hat{\mathbf{L}}$ or $\hat{\mathbf{J}}$).

In general the exchange interactions are not isotropic and the exchange integral is not a scalar but a matrix $\mathbb{J}_{ij}$:

$$H = \sum_{\langle ij \rangle} \hat{\mathbf{S}}_i \mathbb{J}_{ij} \hat{\mathbf{S}}_j. \tag{2.10}$$

Common examples for direction dependent interactions are the Ising case, where interactions are restricted to the z-components,

$$H_{\text{Ising}} = \sum_{\langle ij \rangle} J_{ij} \hat{S}_i^z \hat{S}_j^z \tag{2.11}$$

and the XY spin Hamiltonian

$$\mathcal{H}_{XY} = \sum_{\langle ij \rangle} J_{ij} \left(\hat{S}_i^x \hat{S}_j^x + \hat{S}_i^y \hat{S}_j^y \right), \tag{2.12}$$

for interactions in the x-y plane.

The general Hamiltonian given Eq. 2.10 can also depend on the bond direction. Therefore it can be instructive to split the Hamiltonian into symmetric and antisymmetric parts:

$$\mathcal{H} = \mathcal{H}_{\text{sym}} + \mathrm{H}_{\text{asym}} = \sum_{\langle ij \rangle} \hat{\mathbf{S}}_i \Gamma_{ij} \hat{\mathbf{S}}_j + \sum_{\langle ij \rangle} \mathrm{D}_{ij} \left(\hat{\mathbf{S}}_i \times \hat{\mathbf{S}}_j \right). \tag{2.13}$$

The symmetric part of the Hamiltonian implicates the interactions which do not depend on the bond direction. The asymmetric term is the Dzyaloshinsky-Moriya interaction which induces a sign change upon changing the bond direction. [15]

For the materials discussed in this work the Dzyaloshinsky-Moriya interactions are forbidden due to the inversion centers between the magnetic ions [22].

2.5 Ferro- und Antiferromagetism

Interactions between localized magnetic moments lead to collective magnetism and the formation of long-range order or more exotic ground states. Two prominent cases of magnetic order are ferromagnetism and antiferromagnetism.

In ferromagnets the magnetic moments spontaneously align parallel to each other below the ordering temperature T_{c}. This leads to a non-zero magnetization even when no magnetic field is applied. Ferromagnetism corresponds to a positive coupling constant J_{ij} in the Heisenberg spin Hamiltonian.

Antiferromagnetism is associated with a negative exchange integral J_{ij} and leads to an antiparallel alignment of the magnetic moments. The Néel temperature T_{N} indicates the transition between the paramagnetic high-temperature behavior and the magnetically ordered phase. Antiferromagnetism is often viewed in the sense of two interpenetrating sublattices, where one sublattice only contains spins pointing up and the other spins pointing down. The net magnetization of the antiferromagnet is zero if both sublattices contain the same amount of magnetic moments.

The temperature of the transition to the magnetically ordered phase, T_{c} or T_{N}, depends for both cases of magnetic order on the competition between the exchange interactions and the thermally driven paramagnetic behavior. At high temperatures the thermal energy is larger than the energy gain achieved through the formation of magnetic order. In the paramagnetic regime the susceptibility of ferro- and antiferromagnets therefore follows a Curie-like behavior which can be deduced from the mean-field approach. The mean-field approach introduces a molecular field that is produced by the neighboring spins. The interactions between magnetic moments are then substituted by the interaction between spins and the molecular field. This approach leads to the deduction of the Curie-Weiss law, a modification of the previously introduced Curie law:

$$\chi = \frac{C}{T - \theta_{\text{CW}}}. \tag{2.14}$$

The Curie-Weiss temperature θ_{CW} is positive for ferromagnetic interactions and negative for antiferromagnets. For $\theta_{\text{CW}} = 0$ the Curie law for the pure paramagnet is

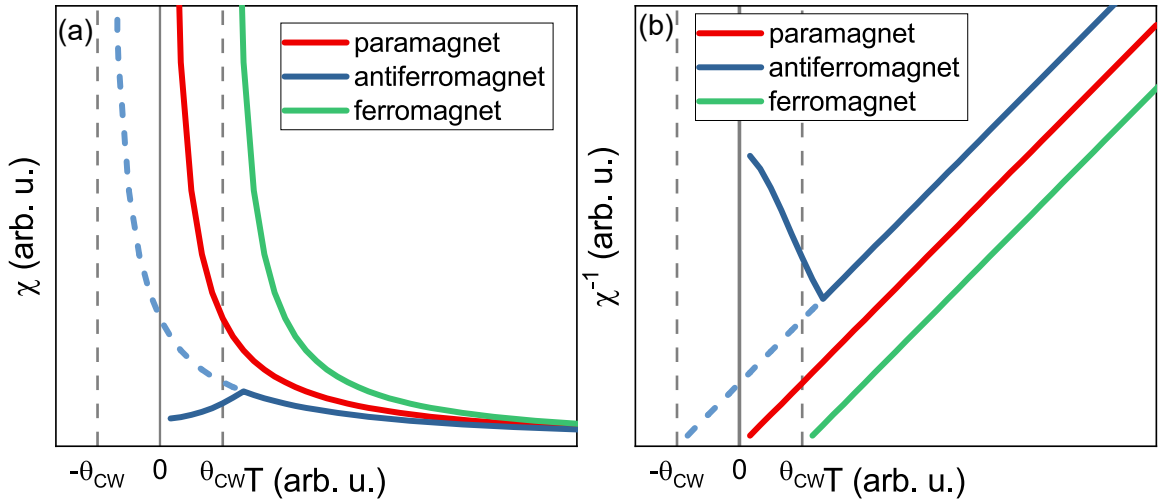

Figure 2.5: *(a) Susceptibility and (b) inverse susceptibility of a para-, antiferro- and ferromagnet. At high temperatures the susceptibility of all three cases of magnetism follows a Curie-like behavior. When approaching the respective ordering temperatures at low temperatures the susceptibilities of the antiferromagnet and the ferromagnet deviate from the Curie-Weiss law. Adapted from Ref. [14].*

retrieved. In Fig. 2.5 typical susceptibility curves for a paramagnet, antiferromagnet and ferromagnet are shown. The Curie-Weiss law is only valid at high temperatures, at low temperatures close to the respective ordering temperatures T_N or T_c deviations from the Curie-Weiss law are expected. While $\theta_\mathrm{CW} = T_\mathrm{c}$ is applicable to some extend, although T_c represents only an estimation in the limits of the mean-field approach, $\theta_\mathrm{CW} = -T_\mathrm{N}$ is incorrect in most cases even in the mean-field approach.

The behavior of an antiferromagnet close to the ordering temperature is best understood in the picture of the two intertwined sublattices mentioned before. The spins in each sublattice are parallel to each other but antiparallel to the spins of the other sublattice. Two scenarios are differentiated based on the direction in which an external field is applied.
If the field is applied perpendicular to the spin directions, the spins of both sublattices are slightly tilted from their (anti-)parallel orientation. This corresponds to a non-zero net magnetization in the direction of the applied magnetic field and therefore results in a constant, non-zero susceptibility $\chi_\perp$ at low temperatures.
On the other hand, if the magnetic field is applied (anti-)parallel to the magnetic moments of the sublattices, the magnetization of one of the sublattices is enhanced compared to the other sublattice. The susceptibility $\chi_\parallel$ is therefore temperature dependent and becomes zero at $T = 0\,\mathrm{K}$. [14]

In literature the Néel temperature is often associated with the kink in the magnetic susceptibility at low temperatures, similar to the observation of a lambda-like anomaly in the specific heat. In Ref. [23] the connection between the specific heat and the susceptibility of antiferromagnets was investigated. It was shown that the magnetic

contribution to the specific heat is proportional to the temperature derivative of the susceptibility:

$$C_{\mathrm{M}}(T) \backsimeq A\frac{\partial}{\partial T}\left[T\chi(T)\right]. \tag{2.15}$$

A is the proportionality constant that is only weakly temperature dependent. An anomaly in the specific heat therefore elicits a similar anomaly in $\partial\chi T/\partial T$, but this anomaly is actually located above T_{N}. According to Eq. 2.15, the lambda-like anomaly at the transition temperature in the specific heat is connected to a positively infinite gradient in the susceptibility. Therefore, the maximum of the temperature derivative of $\chi(T)$ and not the kink in $\chi(T)$ has to be considered to correctly determine the ordering temperature from measurements of the susceptibility.

2.6 Influence of the Crystal Field

The crystal electric field influences the magnetic properties of a material. As mentioned before, Yb^{3+} ions in the crystal field of the D_{3d} point group exhibit four Kramers doublets with a rather large energy gap between the ground state and the first exited doublet, hence the ground state behaves like a spin-$\frac{1}{2}$ state. This analogy facilitates the use of the much simpler spin Hamiltonian of a free ion with spin-$\frac{1}{2}$ to describe the behavior of the Yb^{3+} ions in a magnetic field:

$$H_{\mathrm{eff}} = g\mu_{\mathrm{B}}\mathbf{B}\cdot\mathbf{J}_{\mathrm{eff}}. \tag{2.16}$$

While g would be equal to 2 for a real spin-$\frac{1}{2}$ electron, an effective g-factor has to be assumed to make Eq. 2.16 applicable to the Yb^{3+} pseudospin-$\frac{1}{2}$ systems. Since each of the Kramers doublets is composed of a combination of states with different J_z, the interaction between spin and magnetic field is anisotropic and an effective g-tensor has to be used. [14, 24]

The contribution of the four Kramers doublets to the susceptibility is a statistical average

$$\chi_{\mathrm{vv}} = N_{\mathrm{L}}\mu_0(g_j\mu_{\mathrm{B}})^2\sum_n\sum_{m\neq n}M^0_{nm}\frac{p^0_n - p^0_m}{E^0_m - E^0_n}, \tag{2.17}$$

$$M^0_{nm} = \sum_{\alpha\alpha'}|\langle n^0,\alpha|J_a|m^0,\alpha'\rangle|^2; \quad p^0_n = \frac{\exp[-E^0_n/(k_{\mathrm{B}}T)]}{2\sum_n\exp[-E^0_n/(k_{\mathrm{B}}T)]},$$

with the Landé g-factor $g_j = \frac{8}{7}$. The summation over the CEF doublets with energies E^0_m and E^0_n is expressed through the indices m and n, while the sum over the degenerate states of a doublet is indicated by Greek indices α and α'. p^0_n represents the thermal population of a doublet n. The partition function of the CEF doublets is included in the denominator of p^0_n. J_a is the projection of the total angular momentum operator in the direction of the magnetic field field.

At sufficiently low temperatures ($T << \Delta_{\mathrm{CEF}}$) mostly the lowest Kramers doublet is populated, but thermal excitations to higher-lying doublets give rise to a deviation from the simple Curie behavior. This deviation becomes better visible if the inverse susceptibility χ^{-1} is considered, see Fig. 2.6(a), and is accounted for by a constant, van Vleck-like term χ_{vv}:

$$\chi = \frac{C}{T-\theta} + \chi_{\mathrm{vv}}. \tag{2.18}$$

By fitting the low-temperature part of the data with this formula the ground state properties can be more accurately determined. An example of the application of Eq. 2.18 is shown in Fig. 2.6(a).

At high temperatures all CEF levels contribute to the magnetization and the susceptibility is well described by the Curie-Weiss law, as depicted in Fig. 2.6(a). However, the values for the Curie-Weiss temperature θ_{HT} and Curie constant C determined at high temperatures do not reflect the ground state properties, since the determined Curie constant is related to the $J = \frac{7}{2}$ state. Therefore the effective moment determined at high temperatures is expected to be in agreement with the calculated value for free Yb^{3+} ions $\mu_{\mathrm{eff}} = 4.56\,\mu_{\mathrm{B}}$.

In magnetization measurements the van Vleck contribution becomes apparent in a linear increase of $M(H)$ above the saturation field. In Fig. 2.6(b) a comparison between the standard Brillouin-like magnetization curve of a paramagnet with and without a van Vleck contribution is shown. The van Vleck contribution and the

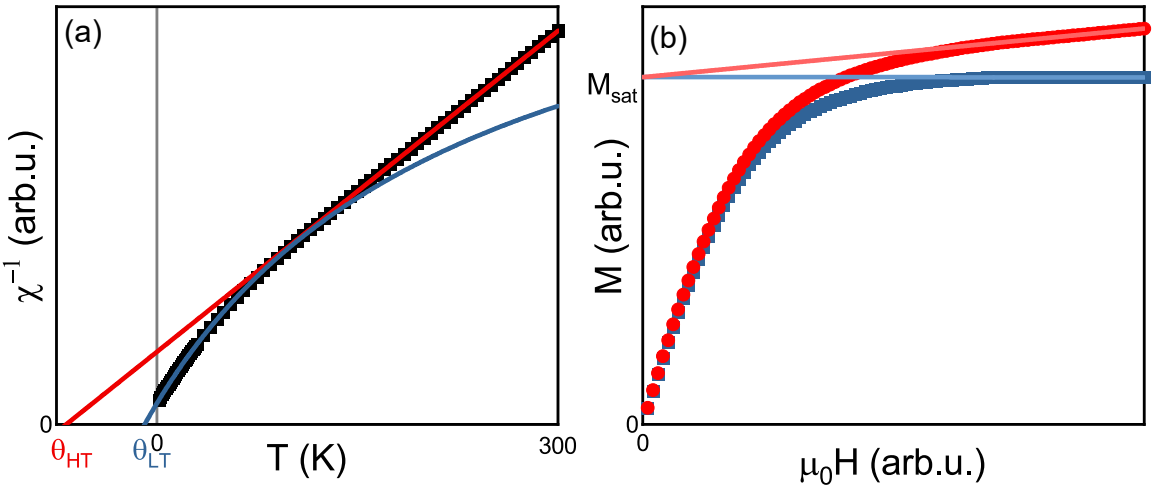

Figure 2.6: *(a) Inverse magnetic susceptibility of a system with a sizable van Vleck contribution. The blue line is a fit to the low-temperature part of the susceptibility using Eq. 2.18. The high-temperature part shows a linear behavior and is fitted with the standard Curie-Weiss law (red line). (b) Field-dependent magnetization with (red) and without (blue) a van Vleck contribution. The blue and red lines represent linear fits to the magnetization in the fully polarized regimes.*

saturation magnetization M_{sat} can be obtained from a linear fit to the magnetization in the fully polarized regime.

2.7 Frustration

Another factor that influences the interactions between magnetic atoms is the geometry of the magnetic lattice. In special cases the interplay of exchange interactions and lattice geometry create a setting, where not all interactions can be satisfied at the same time. Antiferromagnetically coupled Ising spins on the triangular lattice, for example, are unable to fulfill all interactions at the same time. This is illustrated in Fig. 2.7(a) where spin 1 and 2 are antiparallel to each other, fulfilling their antiferromagnetic interactions. Spin 3, on the other hand, can only be antiparallel to spin 1 or spin 2 and is therefore unable to simultaneously satisfy both interactions. This phenomenon is called geometric frustration.

Frustration of a magnetic system can also be caused by competing and random magnetic interactions. In Fig. 2.7(b) this kind of frustration is exemplified for antiferromagnetically coupled spins on the square lattice. If one of the antiferromagnetic bonds is replaced by a ferromagnetic, spin 4 is not able to satisfy both interactions at the same time. This kind of magnetic frustration is often observed in spin glasses.

Magnetic frustration leads to a degeneracy of the ground state, i.e. in the case of the antiferromagnetically coupled Ising spins on the triangular lattice frustration the ground state is sixfold degenerate. The degeneracy can fuel fluctuations, even at temperatures where magnetic interactions would usually overcome thermal fluctuations. This causes a shift of the ordering temperature T_{N} to lower temperatures and motivates the definition of the frustration parameter f,

$$f = \frac{|\theta_{\mathrm{CW}}|}{T_{\mathrm{N}}}, \tag{2.19}$$

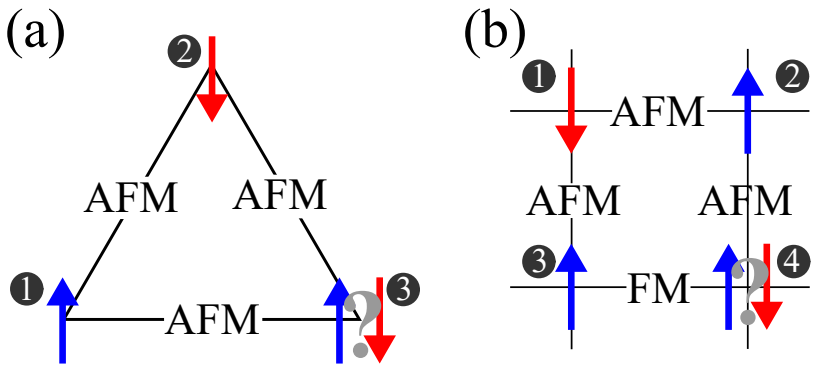

Figure 2.7: *(a) Geometrical frustration on the example of antiferromagnetically coupled Ising spins on the triangular lattice. (b) Exchange frustration on the example of antiferromagnetically coupled Ising spins on the square lattice, where one antiferromagnetic interaction is replaced by a ferromagnetic one. Adapted from Ref. [25].*

that is used to compare the level of frustration of different systems. If a system is not frustrated T_N is usually comparable to the Curie-Weiss temperature θ_{CW} and therefore $f \approx 1$. A frustration parameter larger than one indicates that some degree of frustration is present and for $f > 10$ a system is classified as strongly frustrated. [25,26]

2.8 Spin Liquids

Frustration leads to a degeneracy of the ground state and the degeneracy leads to persisting (quantum) fluctuations even at low temperatures. The fluctuations, however, are not random (like at higher temperatures) but restricted to the ground states of the system. In the case of the Ising spins on the triangular lattice with antiferromagnetic exchange interactions considered previously, six different ground states are available and the spins fluctuate between the different configurations. These kind of systems with highly correlated but still fluctuating spins are called spin liquids in analogy to ordinary liquids. [26]

2.8.1 Fluctuations

Concerning the fluctuations of the spins classical and quantum fluctuations are distinguished. The thermal fluctuations are driven by the thermal energy $k_B T$ of the system. To understand the origin of the quantum fluctuations it is instructive to consider the Heisenberg model for a spin dimer consisting of two arbitrary spins $S_1 = S_2 = S$ with the exchange interaction J: $\mathcal{H} = J\hat{\mathbf{S}}_1\hat{\mathbf{S}}_2$. For ferromagnetic interactions ($J < 0$) a ground state energy of $-|J|S^2$ is obtained independent of whether the spins in Eq. 2.9 are treated in the classical approximation, i.e. as vectors, or quantum mechanically, i.e. as operators. The same does not hold true for antiferromagnetic interactions, where the classical ground state is degenerate; both $|S, -S\rangle$ and $|S, -S\rangle$ are eigenstates with the energy $-JS^2$. In contrast, the quantum treatment yields a non-degenerate ground state with an energy of $-JS(S+1)$, rendering antiferromagnetism an inherently quantum mechanical phenomenon. The eigenstate is a superposition of different $|S_1^z, S_2^z\rangle$ states, for example $\frac{1}{\sqrt{2}}(|\uparrow\downarrow\rangle - |\downarrow\uparrow\rangle)$ in the case of the spin-$\frac{1}{2}$ dimer. In the quantum ground state one cannot differentiate between the $|\uparrow\downarrow\rangle$ and $|\downarrow\uparrow\rangle$ states and the spins can fluctuate between them giving rise to quantum fluctuations that persist down to 0 K. In frustrated magnets the quantum fluctuations are enhanced and can lead to the formation of spin liquids.
To what degree spins can be viewed as classical depends on the size of the spin. The difference between the two scenarios ,$-JS^2$ and $-JS(S+1)$, becomes more insignificant the larger the spins are. Therefore, large spins ($S \geq 2$) allow for a classical treatment, while small spins, especially spin-$\frac{1}{2}$ systems, are of quantum nature. [15, 26, 27]

The nature of the fluctuations divides the realm of spin liquids in those of the classical and the quantum spin liquids.

2.8.2 Classical Spin Liquids

Classical spin liquids are found in the form of spin ice materials like $Dy_2Ti_2O_7$, $Ho_2Sn_2O_7$ and $Ho_2Ti_2O_7$. For these materials the magnetic rare earth ions form a pyrochlore lattice consisting of corner-sharing tetrahedra. The effective ferromagnetic exchange J_{eff} between nearest-neighbors results in frustration due to the Ising nature of the spins. Spin ice compounds follow the so called ice rules, where the ground states are composed of all possible configurations with two spins pointing inward to the center of the tetrahedra and two spins pointing out of the tetrahedra. At low temperatures ($k_{\text{B}}T << J_{\text{eff}}$) the spins fluctuate between the six degenerate ground states. Since the fluctuations are thermally driven for large spins (Dy^{3+}: $S = 3.5$, $L = 0$, $J = 3.5$, Ho^{3+}: $S = 4.5$, $L = 5$, $J = 9.5$), below a certain temperature the energy necessary to traverse between the spin ice configurations is no longer available. The fluctuations slow down and finally freeze. [26]

2.8.3 Quantum Spin Liquids

The quantum spin liquid (QSL) proves to be much more elusive than its classical counterpart. In 1973 P. W. Anderson proposed a QSL ground state for Heisenberg spins on the triangular lattice [1]. The classical ground state for antiferromagnetically coupled spins on the triangular lattice is the long-range ordered 120° state. Anderson introduced so called valence bonds where two spins quantum-mechanically couple to form a spin-0 singlet and gain energy in the process. A valence bond solid occurs when each spin of a system is coupled to one specific other spin and these pairs do not change with time. As a result the valence bonds are static and localized and the system has a non-magnetic ground state. Although the spins are highly entangled with their valence bond partner, a valence bond solid is not a quantum spin liquid since it lacks long-range entanglement and breaks lattice symmetry.
To construct a quantum spin liquid one must go a step further and allow quantum mechanical fluctuations between different valence bonds [see Fig. 2.8(a)]. The ground

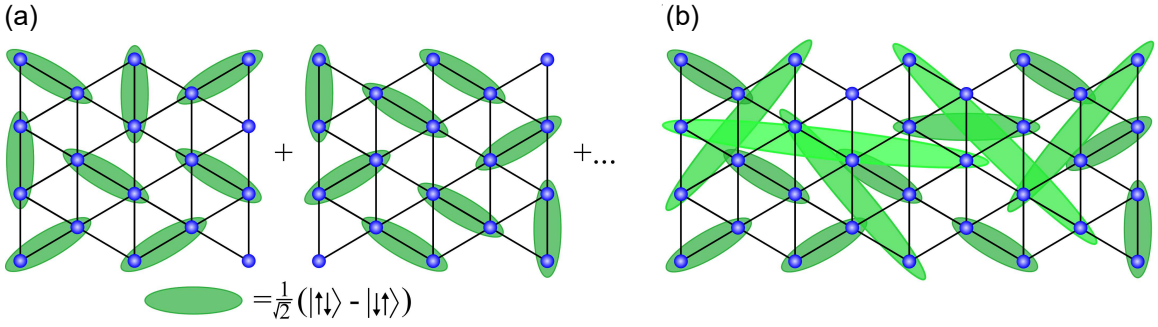

Figure 2.8: *(a) Nearest-neighbor RVB. The valence bonds are not static and the ground state is a superposition of all possible valence bond configurations. (b) RVB state with short- and long-range valence bonds. Adapted from Ref. [26].*

state is a superposition of all possible valence bond configurations. Valence bonds are not restricted to their direct neighbors but can also be formed between second neighbors and so on, as shown in Fig. 2.8(b). Such a system is called a resonating valence bond (RVB) state. [2, 26]

The RVB state facilitates the formation of so called spinons. The spinons origin from the excitations of the valence bonds, where the spin dimer state is excited into a triplet state. As seen before, the triplet state is characterized by a parallel spin arrangement and in the RVB state those two spins can separate. Since the RVB ground state facilitates all possible arrangements of valence bonds the two spins can independently move from one lattice site to the other. The formation of a spinon is illustrated in Fig. 2.9. [2]

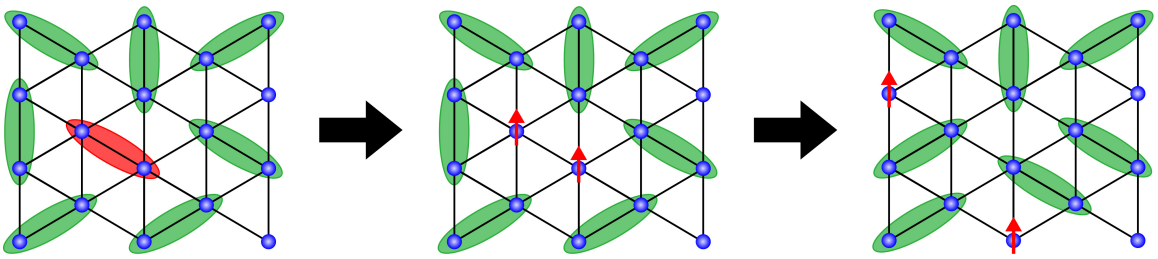

Figure 2.9: *Process of spinon formation. The excitation of a valence bond (red) causes the valence bond to break and creates two unpaired spins. The two spins can move through the lattice independent of each other and therefore represent spin-$\frac{1}{2}$ excitations [2].*

Depending on the range over which the valence bonds are formed two types of spin liquids can be differentiated. The gapped Z_2 spin liquids are characterized by short-ranged valence bonds because a finite amount of energy is required to break one such bond and create an excitation. For the gapless $U(1)$ QSL the valence bond are also formed between distant neighbors. In experiment both types of spin liquids are expected to show a continuum of spinon excitation that is observed in inelastic neutron scattering (INS). They can be differentiated by the behavior of their specific heat. In the case of a gapped spin liquid an exponential behavior is expected in specific heat measurements (as well as in measurements of the magnetic susceptibility). The gapless $U(1)$ spin liquid in a triangular system, on the other hand, is expected to show a sublinear $T^{2/3}$ power-law behavior in measurements of the specific heat. [2]

In general, a quantum spin liquid is often defined by the absence of magnetic order at low temperatures, fueled by the quantum fluctuations of strongly interacting spins. However, the absence of magnetic order is not unique to quantum spin liquids, but can also be attributed to disordered magnets, like cooperative paramagnets. To single out a spin liquid, one needs to find other criteria that are characteristic to the spin-liquid phase. The differentiation between quantum spin liquids and magnets with randomness is a challenging endeavor due to the subtleties in their magnetic behaviors and the need for advanced experimental techniques. A fist step in the uncovering a potential QSL are measurements of the low-temperature specific heat, to reveal the

presence of fractionalized excitations. Different theoretical predictions exist for the low-temperature behavior of the specific heat, depending on the ground state of the spin-liquid, like the aforementioned sublinear $T^{2/3}$ power-law for the gapless $U(1)$ spin liquid in a triangular system. Similarly, thermal transport measurements can be used to probe the mobility of the fractionalized (spinon) excitations in insulating QSL materials. Another important technique to identify a QSL and distinguish it from disordered magnets is inelastic neutron scattering to exclude the presence of static correlations. In QSL candidates a continuous excitation spectrum is expected, indicating dynamic, fluctuating spins. Nuclear magnetic resonance (NMR) measurements are used to investigate the local magnetic envirionments. A sharp, featureless NMR line shape unaffected by cooling to low temperatures indicates that no static magnetism, caused by a static disordered state, is present in the system. Finally, μSR measurements, sensitive to internal magnetic fields, can provide insight in the presence of static or dynamic moments. [2, 28]

2.8.4 Spin Hamiltonian of the Triangular Lattice

Although Anderson originally proposed the QSL ground state for triangular lattice antiferromagnets (TLAFs) for systems with purely nearest-neighbor interactions, it was later shown that the true ground state of these systems indeed is the long-range ordered 120° state [29, 30]. The TLAFs need some additional ingredient to facilitate a QSL ground state. Anisotropic exchange interactions are one way to realize a QSL on the triangular lattice. Another possibility is found in the J_1-J_2 Heisenberg model, where next nearest neighbor exchange interactions are introduced and a spin-liquid phase is expected for $J_2/J_1 \simeq 0.07 - 0.15$.

The model Hamiltonian for QSL candidates in triangular antiferromagnets therefore has to take anisotropic exchange and interactions beyond nearest neighbors into account:

$$\mathcal{H} = \sum_m \left[\mathcal{H}_m^{\mathrm{XXZ}} + \mathcal{H}_m^{\pm\pm} + \mathcal{H}_m^{z\pm}\right]. \tag{2.20}$$

The summation over m describes the nearest neighbor interactions for $m = 1$, next-nearest neighbor interactions for $m = 2$, and so on.

The XXZ Hamiltonian $\mathcal{H}_m^{\mathrm{XXZ}}$ expresses the anisotopy between the xy plane, which is assumed to be isotopic, and the z direction of the triangular lattice, with $J_m^x = J_m^y = J_m$ and $J_m^z = \delta J_m$:

$$\mathcal{H}_m^{\mathrm{XXZ}} = J_m \sum_{\langle ij \rangle} \left(\hat{S}_i^x \hat{S}_j^x + \hat{S}_i^y \hat{S}_j^y + \delta \hat{S}_i^z \hat{S}_j^z\right). \tag{2.21}$$

The second and third term in Eq. 2.20 describe bond-dependent components that are not covered by the XXZ model. $\mathcal{H}_m^{\pm\pm}$ accounts for the anisotropy in the xy plane

$$\mathcal{H}_m^{\pm\pm} = \sum_{\langle ij \rangle} 2J_m^{\pm\pm} \left[\left(\hat{S}_i^x \hat{S}_j^x - \hat{S}_i^y \hat{S}_j^y\right) \cos\phi_\alpha - \left(\hat{S}_i^x \hat{S}_j^y + \hat{S}_i^y \hat{S}_j^x\right) \sin\phi_\alpha\right] \tag{2.22}$$

and $\mathcal{H}_m^{z\pm}$ includes the off-diagonal anisotropy

$$\mathcal{H}_m^{z\pm} = \sum_{\langle ij \rangle} J_m^{z\pm} \left[\left(\hat{S}_i^y \hat{S}_j^z - \hat{S}_i^z \hat{S}_j^y \right) \cos \phi_\alpha - \left(\hat{S}_i^x \hat{S}_j^z + \hat{S}_i^z \hat{S}_j^x \right) \sin \phi_\alpha \right]. \tag{2.23}$$

The pre-factor $\phi_\alpha = 0, \pm 2\pi/3$ accounts for the bond dependency. For $\delta = 1$ and $J_m^{\pm\pm} = J_m^{z\pm} = 0$ in Eq. 2.20 the isotropic Heisenberg Hamiltonian given in Eg. 2.9 is restored. [2]

Based on the Hamiltonian in Eq. 2.20 a phase diagram (see Fig. 2.10) for the triangular lattice is constructed in Ref. [31] using the density-matrix renormalization group (DMRG). The phase diagram shows the anisotropic J_1-only model ($m = 1$ in Eq. 2.20) in the back panel and the isotropic J_1–J_2–$J^{\pm\pm}$ model ($J^{z\pm} = 0$) in the lower panel. The two models show similarly constructed phase diagrams that facilitate a collinear stripe order at higher J_2/J_1 or $J^{z\pm}/J^{\pm\pm}$. A spin-liquid region is also present in both phase diagrams, which appear to be connected, offering even more potential playground for tuning materials toward a quantum spin-liquid phase. [2, 31]

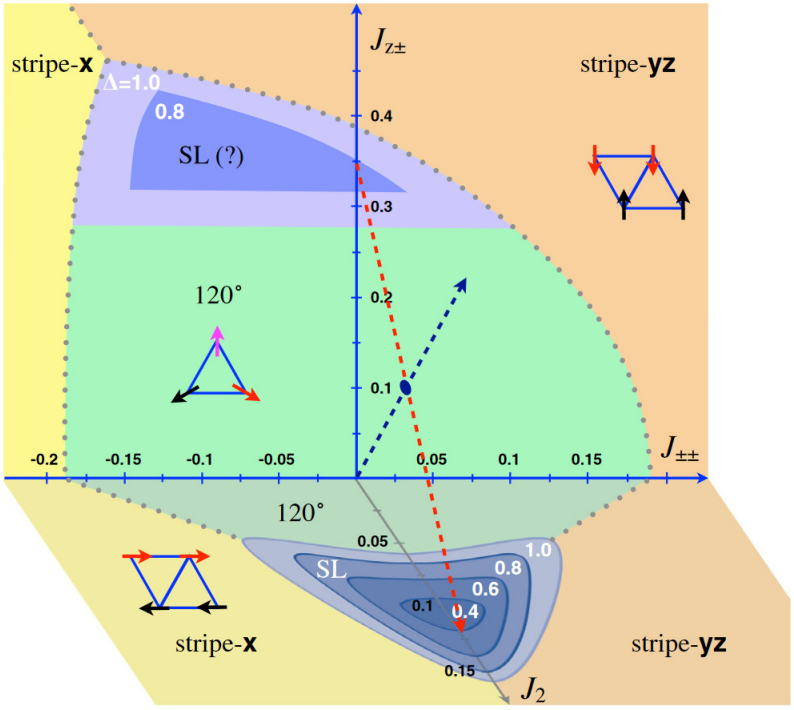

Figure 2.10: *Theoretical phase diagram of triangular lattice antiferromagnets. The back panel is constructed from the anisotropic J_1-only model, while the lower panel is based on the isotropic J_1–J_2 model. Both models exhibit a spin-liquid (SL) phase. [31]*

2.9 Heat Capacity

The heat capacity of a material is a powerful tool to reveal phase transitions and gain insights into low-temperature excitations. It quantifies the amount of heat ∂Q (i.e. energy) needed to raise the temperature ∂T of a system. The heat capacity is therefore intimately connected to the exitations, which contribute to the amount of (thermal) energy the investigated material can absorb in a specific temperature interval. [32]

One differentiates between the heat capacity at constant pressure $C_{\mathrm{p}} = (\partial Q/\partial T)_{\mathrm{p}}$ and at constant volume $C_{\mathrm{V}} = (\partial Q/\partial T)_{\mathrm{V}} = (\partial U/\partial T)_{\mathrm{V}}$, with the internal energy U. While the former is experimentally accessible, the latter is more fundamental and conveniently used in theoretical considerations. They are connected via $(C_p - C_V) = \alpha_V VTB$, with the volume expansion coefficient α_v and the compression coefficient B. In solids the difference between C_p and C_V is small since the thermal expansion coefficient is negligible. [13, 33]

Thermodynamic considerations reveal a direct connection between heat capacity at constant magnetic field and pressure and entropy

$$C_p = T\left(\frac{\partial S}{\partial T}\right)_B. \tag{2.24}$$

The heat capacity consists of different contributions, depending on what kind of excitation are present in a material in a specific temperature range. In crystalline materials exitations of the lattice in form of phonons play an important role. In a classical setting the lattice vibrations are treated as independent, classical harmonic oscillators. From these considerations the Dulong-Petit law is retrieved

$$C_{\mathrm{V,DP}} = 3RN = N \cdot 25\frac{\mathrm{J}}{\mathrm{molK}}, \tag{2.25}$$

with the universal gas constant R and the number of atoms N per formula unit. While the Dulong-Petit law provides an upper limit for the heat capacity of materials, it is temperature-independent and therefore fails to describe the decrease of the heat capacity with decreasing temperature observed in measurements. [13, 32]
Einstein provided a theory to describe the temperature dependence of the specific heat in 1907 by treating the atoms of a solid as free harmonic oscillators, however, their energy is not continuous but quantized. With this model, the decrease of the heat capacity towards low temperatures was successfully described, but at low temperatures the model falls below the measurement values.
In the Debye model the approach of Einstein is improved by taking a coupling between the atoms into account. For a solid with only one atomic species, this is achieved by introducing a linear dispersion relation $\omega = vq$, with the sound velocity v and the wave vector q. Furthermore, Debye assumed a cut-off frequency ω_D, which represents

an upper limit of the phonon frequency without differentiating between longitudinal and transverse phonons. With these assumptions the specific heat is calculated as

$$C_V = \frac{\partial U}{\partial T} = 9Nk_\mathrm{B}\left(\frac{T}{\theta}\right)\int_0^{x_D}\frac{x^4\exp(x)}{(\exp(x)-1)^2}\mathrm{d}x, \tag{2.26}$$

with $x = \hbar\omega/k_\mathrm{B}T$, $x_\mathrm{D} = \hbar\omega_\mathrm{D}/k_\mathrm{B}T$ and the Debye temperature θ, which is defined by $k_\mathrm{B}\theta = \hbar\omega_\mathrm{D}$. For high temperatures ($T \to \infty$, $x \to 0$) the Dulong-Petit law is retrieved (Eq. 2.25). In the low-temperature limit ($T \to 0$, $x \to \infty$) one obtains

$$C_V = \frac{12\pi^4}{5}Nk_\mathrm{B}\left(\frac{T}{\theta}\right)^3. \tag{2.27}$$

This T^3-temperature dependence is in excellent agreement with heat capacity measurements of non-metallic materials at low temperatures. [13, 32, 34]
In metals, an additional contribution from the conduction electrons has to be considered that can be obtained by treating them as a Fermi gas. This yields a linear temperature dependence $C_V = \gamma T$, with the Sommerfeld coefficient γ. The focus of this work is on insulating materials, therefore the electron contribution to the specific heat is not relevant in this context. [13, 32, 34]
Due to its T^3-nature the lattice contribution to the heat capacity becomes insignificant at low temperatures. However, not only phonons contribute to the heat capacity and at sub-Kelvin temperatures, the nuclear and magnetic contributions come into play. The nuclear contribution is based on the specific heat of a two level system

$$C_V = k_\mathrm{B}\left(\frac{\Delta}{k_\mathrm{B}T}\right)^2\frac{\exp(\Delta/k_\mathrm{B}T)}{(\exp(\Delta)/k_\mathrm{B}T+1)^2}, \tag{2.28}$$

with an energy difference of Δ between the two levels. The driving force behind this contribution is the hyperfein splitting of the nuclear spin, which can either origin from an electric field gradient in combination with a nuclear electric quadrupolar moment or from internal and external magnetic fields. The resulting maximum in the specific heat, which is often referred to as the Schottky anomaly, increases exponentially coming from low temperatures, followed by a decrease that follows a T^{-2} dependency. Typically, the Schottky anomaly becomes relevant only at temperatures below $10^{-2}\,\mathrm{K}$ due to the small nuclear magnetic moment. In most measurements only the high-temperature part is observed and accounted for by a T^2 behavior. [13, 32, 34]
For insulating materials, like the $A\mathrm{Yb}X_2$ compounds, the specific heat is composed of the following contributions:

$$C_p = C_\mathrm{lattice} + C_\mathrm{nuc} + C_\mathrm{mag}. \tag{2.29}$$

If the behavior of C_lattice and C_nuc is known, the magnetic contribution of the heat capacity can be extracted from measurements and analyzed.

In ordered magnets excitations in form of spin waves contribute to the specific heat. Depending on the type of magnetic order the heat capacity shows a different temperature dependence. For magnon excitations in 3D ferromagnets a $T^{3/2}$ behavior is expected well below the ordering temperature. In 3D antiferromagnets a T^3 dependence is predicted. In both cases, internal magnetic fields can lead to the formation of a gap in the energy spectrum at very low temperatures, which causes an exponential temperature dependence of the heat capacity. [34]

In the context of spin liquids the heat capacity can give insights on the nature of the spin-liquid ground state as well. Different temperature dependencies are theoretically predicted. An exponential behavior points towards a gapped state, while various power-law behaviors $C_\mathrm{m} \propto T^\alpha$ are possible for gapless systems. Prominent examples are the linear-in-temperature dependence of the spinon Fermi surface QSL [35], that can be reduced to a sublinear $T^{2/3}$ behavior in triangular antiferromagnets in combination with ring exchange. [3, 28, 36]

The experimentally determined heat capacity is often normalized to make it independent of sample specific properties and is therefore referred to as the specific heat capacity [37]. In this work the heat capacity is normalized in relation to the molar number n

$$C_{p,mol} = \frac{C_p}{n} = \frac{C_p M}{m}, \tag{2.30}$$

with the sample mass m and the molar mass M.

Via equation 2.24 the entropy is directly accessible through measurements of the specific heat

$$S = \int_0^T \frac{C_V}{T'} \mathrm{d}T'. \tag{2.31}$$

By isolating the magnetic specific heat and retrieving the magnetic entropy via Eq. 2.31 information on the ground state of a system can be obtained by comparing it to the entropy derived from the free energy F

$$S = -\left(\frac{\partial F}{\partial F}\right)_V. \tag{2.32}$$

For a system with z energy levels this approach leads to an entropy of $R \ln z$ in the high-temperature limit. [34]
Therefore, an experimentally determined entropy that approaches $R \ln 2$ indicates a two-level system. The $A\mathrm{Yb}X_2$ compounds behave like such two-level systems at low temperatures due to the lifting of the 8-fold degeneracy of the Yb^{3+} ions ($J = \frac{7}{2}$) by the crystal field and the resulting gap between the $J_\mathrm{eff} = \frac{1}{2}$ ground state doublet and the first excited doublet.

3 Measurement Techniques

3.1 Powder X-Ray Diffraction

X-ray diffraction (XRD) measurements are used for initial characterization and detection of impurity phases, especially for the polycrystalline samples. A Rigaku Mini Flex 600 (40 kV, 15 mA) diffractometer and an Empyrean diffractometer (40 kV, 40 mA) by Panalytical are utilized for the sample characterization in this work. Both diffractometers are equipped with a Cu X-ray tube yielding the wave length of the $\lambda(K_{\alpha_1})/\lambda(K_{\alpha_2})$ doublet ($\lambda(K_{\alpha_1}) = 1.5406\,\text{Å}$; $\lambda(K_{\alpha_2}) = 1.5444\,\text{Å}$).

The laboratory XRD measurements are performed employing the standard Bragg-Brentano geometry. Information about the crystal structure, the existence of potential impurity phases, sample quality, site disorder, etc. can be obtained from XRD measurements. The basic concept behind those measurements is described by the Bragg equation:

$$2d \sin\theta = n\lambda. \tag{3.1}$$

The equation is derived under the assumption that a crystal consists of parallel planes separated by the distance d, see Fig. 3.1(a). Depending on the wavelength λ of the X-rays and the distance d constructive interference occurs between the diffracted X-ray beams for certain angles θ. A maximum of the intensity is detected for those angles that fulfill the Bragg equation.

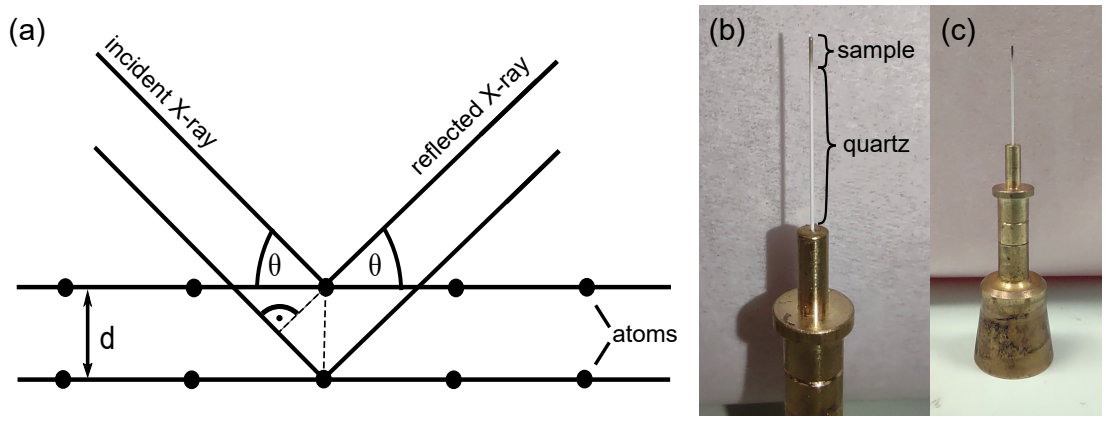

Figure 3.1: *(a) Schematic picture of X-ray diffraction from two lattice planes (adapted from Ref. [38]). (b), (c) Sample holder for the SXRD measurements of* $KYb(S_xSe_{1-x})_2$ *at the ESRF in Grenoble. The powdered sample is fixed in the top part of the capillary by filling the rest of the capillary with crushed quartz glass.*

Most samples were also investigated with high-intensity, monochromatic synchrotron XRD (SXRD) at the European Synchrotron Radiation Facilities (ESRF) in Grenoble and at the synchrotron facility ALBA in Spain. $KYbS_2$ and $KYb(S_xSe_{1-x})_2$ crushed single crystals were measured at the ID22 beamline at the ESRF ($\lambda = 0.35432\,\text{Å}$). All compounds were measured at approximately 290 K. The $KYbS_2$ sample was additionally measured at 5 K, however, due to a broken cryostat window the measurement is contaminated with ice. The polycrystalline $KYbO_2$ was measured at the MSPD beamline at ALBA ($\lambda = 0.32525\,\text{Å}$) at 10 K.

The synchrotron radiation is created by deflecting electrons via a magnetic field. The electrons are generated in an electron gun and accelerated in the linear accelerator to a speed close to the speed of light. After the initial acceleration the electrons access the booster synchrotron. They travel around this large ring, e.g. a circumference of 300 m at the ESRF, to gain even more speed before they proceed to the storage ring. In the storage ring (circumference 844 m, ESRF) the electrons travel at the speed of light under ultra-high vacuum conditions. Different kinds of magnets are used to keep the electrons on their path (bending magnets), keep the electron beam focused and as narrow as possible (focusing magnets) and produce high intensity synchrotron radiation (undulators). Although it is not the main purpose of the bending magnets, they also produce synchrotron radiation due to the energy loss of the electrons when they change direction. This radiation is emitted tangentially to the path of the electrons and is used for the for X-ray scattering and spectroscopy experiments. [39]

The synchrotron X-ray diffraction measurements are performed using an experimental setup especially designed for high resolution powder diffraction. The samples are finely ground and placed into thin-walled glass capillaries [see Fig. 3.1(b),(c)]. To ensure the powder is fixated at the tip of the capillary it is topped of with crushed quartz glass and the open end of the capillary is sealed with vacuum grease. During the measurements the capillary is spun to reduce preferred-orientation effects.

3.2 Energy Dispersive X-Ray Spectroscopy

Energy dispersive X-ray spectroscopy (EDX) is based on the characteristic X-ray emission spectra of the elements. In a compound EDX provides information on the exact composition of elements in a sample, especially useful in the case of doped substances. To generate the characteristic X-rays an electron beam is used to eject an electron in the inner shell, i.e. the K shell [see Fig. 3.2(a)]. The occurring vacancy is subsequently filled by an electron from an outer shell. Only electrons that fulfill the selection rule $\Delta l = \pm 1$ and $\Delta j = 0, \pm 1$ are able to transition into the hole. Depending on the shell the electron originates from, X-rays of characteristic energy are released, corresponding to the energy difference between the two electron shells [see Fig. 3.2(b)].

The characteristic X-rays are termed for the shell the corresponding electron transitions to (K, L, M, ...) and a subscript (α, β, ...). The Greek subscript indicates from which shell above the vacancy the replacing electron originates, i.e. the radiation

emitted if an electron transitions from the L shell to the K shell is termed K_α radiation. The influence of the fine structure of the electron shell is indicated by a subscript number, $K_{\alpha 1}$. [40–42]

EDX measurements are performed to analyze the composition of the $KYb(S_xSe_{1-x})_2$ single crystals and verify the homogeneity of the substitution throughout the individual crystals. The single crystals are fixed on the sample holder using silver epoxy, as shown in Fig. 3.2(c), where an EDX sample holder with an array of crystals prepared for the EDX measurement is depicted. To check the homogeneity different areas of the crystal are investigated separately, the obtained energy spectra are analyzed using the AZtec software. An electron picture of a crystal is shown in Fig. 3.2(e) where the different investigated areas are displayed as well. Fig. 3.2(d) shows a typical energy spectrum determined for $KYb(S_xSe_{1-x})_2$ single crystals.

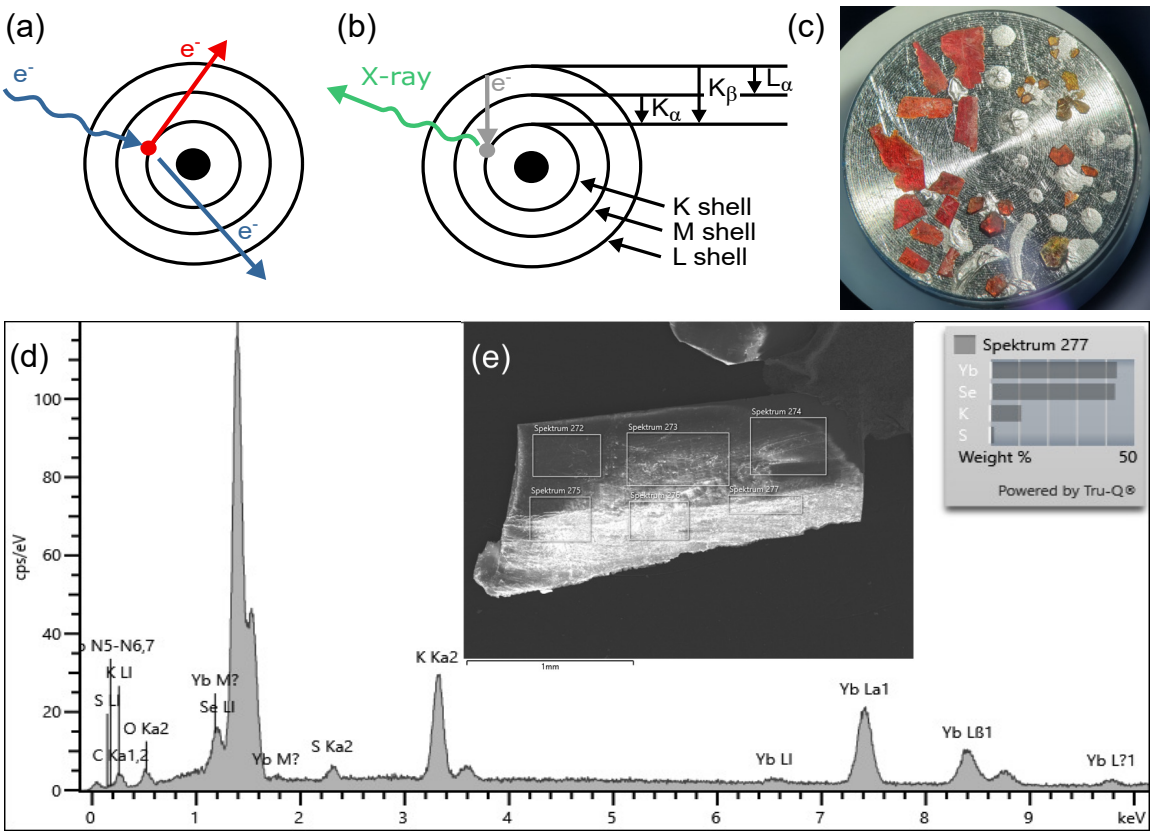

Figure 3.2: *(a) An electron beam (blue) generates a vacancy by ejecting an electron from the inner shell (red) (adapted from Ref. [40]). (b) An outer shell electron (grey) fills the vacancy and emits characteristic X-ray radiation (green) (adapted from Ref. [40]). (c) $KYb(S_xSe_{1-x})_2$ single crystals fixed with silver epoxy on a sample holder. (d) Typical EDX energy spectra of a $KYb(S_xSe_{1-x})_2$ crystal, the inset (e) shows the electron picture of the measured crystal with the different investigated areas.*

3.3 Electron Spin Resonance Spectroscopy

Electron spin resonance (ESR) measurements are used to investigate the local magnetism of magnetic ions in solids. Fig. 3.3(a) shows the schematic setup for an ESR measurement. The sample is placed in a cavity, microwave radiation can be introduced via a wave guide and a static magnetic field transverse to the microwave radiation is supplied by the magnet. While the frequency of the microwave radiation is fixed to a specific value ($h\nu$) the static magnetic field applied to the sample is swept during the measurement.

The magnetic field lifts the $(2J + 1)$-degeneracy of the investigated atom [see Fig. 3.3(b)]. According to the Zeeman effect, the splitting of the energy levels depends on the applied magnetic field:

$$E = g\mu_{\mathrm{B}} m_J B. \tag{3.2}$$

ESR measurements are based on dipole transitions ($\Delta m_J = \pm 1$) between the different Zeeman levels of an atom. Transitions are induced via the microwave field when the energy difference between two adjacent Zeeman levels is $\Delta E = g\mu_{\mathrm{B}} B = h\nu$. The absorption from the transverse magnetic microwave field is measured as a function of magnetic field, see Fig. 3.3(c).

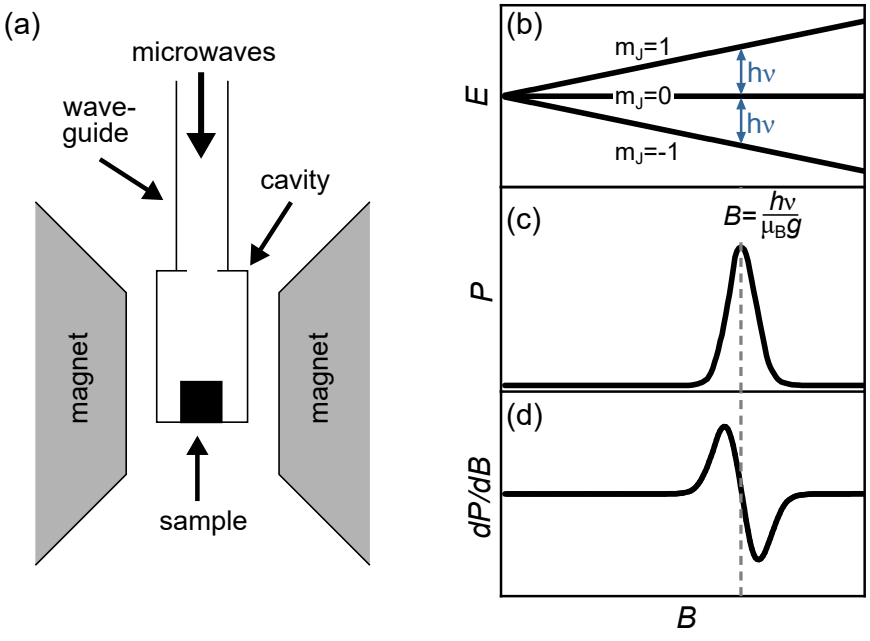

Figure 3.3: *(a) Illustration of the experimental setup of the ESR measurement. (b) Splitting of the degenerate energy levels in a magnetic field on the example of an ion with J=1. (c), (d) Absorption spectrum and first derivative of the absorption spectrum. Adapted from Ref. [14]*

To improve the signal-to-noise ratio a lock-in technique is used that adds a small oscillating magnetic field in the sample space and records the derivative dP/dH of the absorbed power P [see Fig. 3.3(d)].

3.4 Magnetic Property Measurement System

A standard SQUID magnetometer from Quantum Design (MPMS) is used to perform susceptibility $\chi(T)$ and field-dependent magnetization $M(H)$ measurements. Susceptibility is measured under an applied magnetic field of 1 T from 2 K to 300 K and magnetization measurements are performed at 2 K between 0 an 7 T. Additionally, a ^{3}He refrigerator is used to extend the temperature range of the MPMS measurements down to 0.4 K.

For performing the measurements solid, polycrystalline samples are fixated in a plastic capillary using cotton filament. To measure ground polycrystalline samples the powder is filled in a specifically designed capillary. The capillary is attached to a brass sample holder or fixed inside a plastic straw.
Fig. 3.4 shows the different preparation methods for the individual single crystal measurements. Single crystals are glued to a glass sample holder using varnish for standard ^{4}He measurements and either fixed inside a plastic straw with a small piece

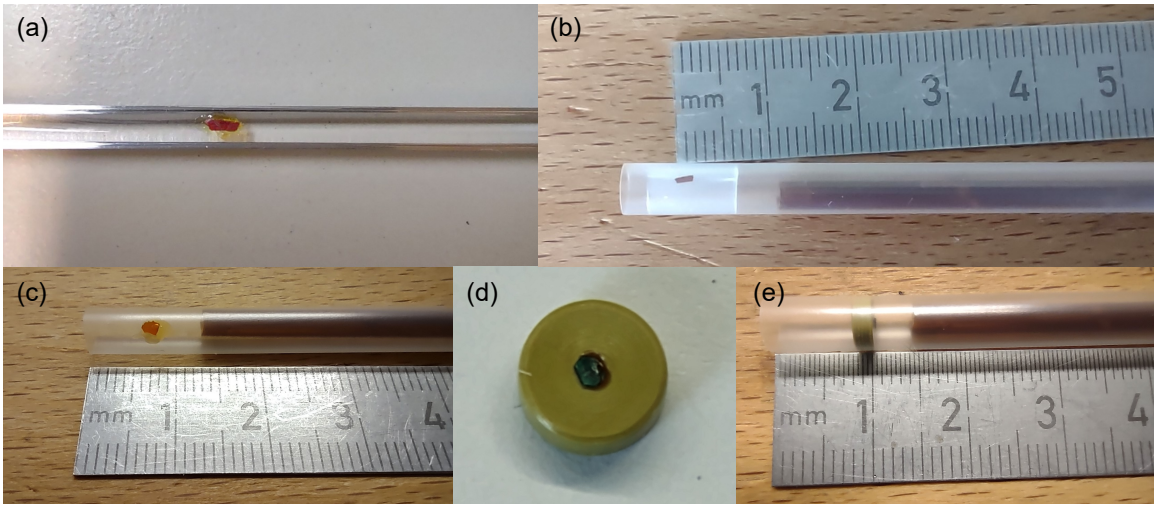

Figure 3.4: *Sample holders used for the $M(T)$ and $M(H)$ measurements with the MPMS. (a) Single crystal of $KYb(S_xSe_{1-x})_2$ fixed to a quartz glass sample holder using varnish for $H \perp c$ measurements between 2 and 300 K. $KYb(S_xSe_{1-x})_2$ sample fixed in a plastic straw with a piece of a plastic straw (b) or glued to the plastic straw using varnish (c) for ^{3}He measurements with $H \perp c$. (d) $KYbS_2$ single crystal attached to a Torlon disk using varnish. (e) Torlon disk with attached $KYbS_2$ single crystal pushed into a plastic straw for $H \parallel c$ measurements with ^{3}He. The samples for the 2-300 K MPMS measurements with $H \parallel c$ were prepared in a similar manner.*

of plastic straw or glued to the plastic straw using varnish for the ^{3}He measurement. For measurements with $H \perp c$ the single crystals are glued onto a Torlon disk with varnish and fixed inside a plastic straw. The background signal caused by the magnetic response of the Torlon disk is measured and subtracted from the measured signal.

In a SQUID (Superconducting Quantum Interference Device) magnetometer the magnetic response of a material to an applied magnetic field is measured by moving the sample through superconducting detection coils. As schematically shown in Fig. 3.5(a), the detection coils consist of two outward coils with counter-clockwise winding and the two inner coils are winding clockwise. This second-order gradiometer setup ensures that the applied magnetic field is not influencing the measurement of the sample signal, since the coils are only sensitive to changes of the magnetic field. By moving the sample through the detection coils the change of the magnetic flux induces a current in the pick-up coils. The current is transformed into a voltage curve by the SQUID and depicted as a function of the sample position. By fitting with an expected response function the magnetic moment of the sample is determined.

The SQUID consists of a superconducting ring with two Josephson junctions [see Fig. 3.5(b)]. A Josephson junction consists of two superconductors separated by a thin insulating barrier. The change of magnetic field detected by the detection coils of the MPMS is conveyed as a flux through the superconducting ring via a flux transformer. The magnetic flux through a superconducting ring is quantized by the flux quantum $\Phi_0 = h/2e = 2.07 \cdot 10^{-15}\,\mathrm{Wb}$ (h: Planck's constant, e: electronic charge), therefore only integer multiples of the flux quantum can be enclosed by the superconducting loop. By applying a bias current to the superconducting ring Cooper pairs tunnel through the Josephson junctions. A change of flux through the superconducting ring changes the phase difference at the two junctions that alters the flow of Cooper pairs and therefore the current of the SQUID. If a gradual change of flux is applied

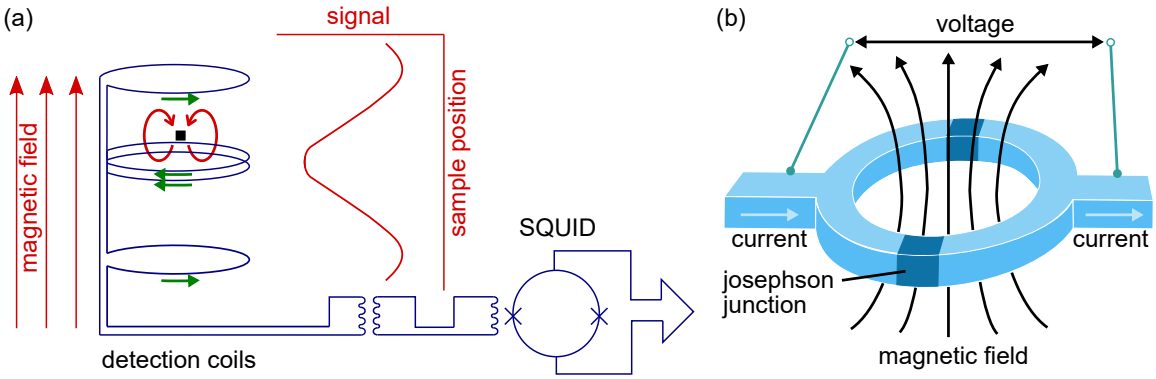

Figure 3.5: *(a) Schematic picture of the MPMS measurement setup. The detection coils pick up on the signal created by moving the sample up and down. The green arrows indicate the winding direction of the coils. The current signal is transformed into a voltage signal by the SQUID (adapted from Ref. [43]). (b) Schematic picture of a SQUID (adapted from Ref. [44]).*

to the SQUID an oscillation of the current is observed, showing a maximum if the flux through the superconducting ring is an integer value of the flux quantum and a minimum if the flux is equal to a half integer value of Φ_0. For the analysis of the sample signal in the MPMS not the change of current in the SQUID is observed, but the influence the changing magnetic field has on the voltage across the SQUID. [44]

Since the SQUID is a very sensitive device it is located outside of the sample chamber and screened by a superconducting shield to ensure that the magnetic field in the sample chamber and any influences of the environment are negligible.

To investigate the influence of pressure on the magnetic properties susceptibility measurements using a miniature ceramic-anvil high-pressure cell [45–48], which is compatible with the standard MPMS setup, are performed. Fig. 3.6(a) shows a schematic picture of the pressure cell. Pressures of up to 7.9 GPa can be achieved with this opposed anvil high-pressure cell, depending on the sample space and culet

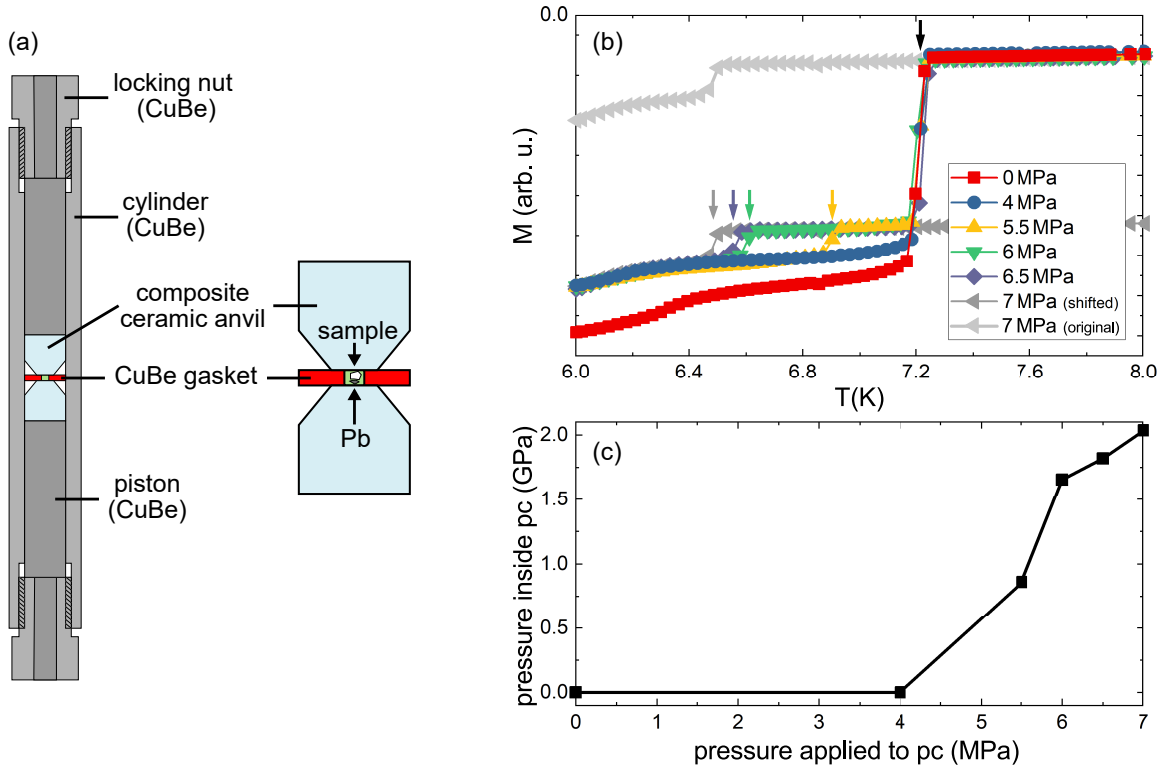

Figure 3.6: *(a) Schematic picture of the miniature ceramic-anvil high-pressure cell used for the susceptibility measurements on $NaYbO_2$ under pressure (adapted from Ref. [45]). (b) Measurements of the superconducting transition of the Pb pieces outside of and inside the pressure cell. The transition temperature of the Pb piece outside of the pressure cell remains at 7.2 K, while the transition temperature of the Pb inside the pressure cell is shifted to lower temperatures with increasing pressure. (c) Comparison of the pressure applied to the pressure cell and the pressure inside the pressure cell determined from the transition temperature of Pb.*

diameter of the anvil. Naturally, a smaller sample space correlates to higher maximum pressure but places strong limitations on the sample size and has to be attuned with the magnetic response of the investigated material. The background magnetization of the cell is small in comparison to similar pressure cells made from different materials.

The sample is placed in the small cut out in the CuBe gasket together with a small piece of Pb and the sample space is filled with Daphne oil as the pressure-transmitting medium. The Pb piece is used to determine the pressure within the sample space by tracking the superconducting transition of Pb that is shifted from about $T_{\mathrm{SC}} = 7.2\,\mathrm{K}$ at ambient pressure to lower temperatures with increasing pressure. For better comparability an additional Pb piece is glued to the outside of the pressure cell using varnish. Fig. 3.6(b) shows an exemplary measurement of the superconducting transition temperature of the Pb. The first transition at about 7.2 K corresponds to the reference Pb piece outside the pressure cell. The Pb piece was detached before the measurement at 7 MPa, therefore only the transition at about 6.5 K is observed. The data of the 7 MPa measurement was shifted for better comparison with the other measurements. The pressure is determined from the temperature difference of the superconducting transition via [49]

$$p = \frac{T_{\mathrm{SC}}(0) - T_{\mathrm{SC}}(p)}{0.365 \pm 0.003}. \tag{3.3}$$

Fig. 3.6(c) shows a comparison between the pressure applied to the pressure cell and the pressure within the sample space. Interestingly, the pressure within the cell seems unaffected by applying an external pressure of 4 MPa to the cell. A sharp increase of the internal pressure is only observed at an external pressure of 5.5 MPa, where a large shift between the superconducting transition of the Pb piece outside and inside the mCAC can be observed in Fig. 3.6(b).
Pressure in the sample space of the gasket is induced by placing the assembled pressure cell with unscrewed locking nut in a press, applying pressure and tightening the locking nut at the top. To determine the background magnetization caused by the magnetic response of the pressure cell and the Pb piece, measurements without a sample are performed beforehand at ambient pressure. The background measurements are performed using the same measurement specifications as for the sample measurements. The extraction of the sample data is done with the MPMS Analyzer program developed by M. Seidler, via point-by-point subtraction of the background signal [50].

In the measurements performed in this work the largest available culet $d = 0.9\,\mathrm{mm}$ diameter is chosen to allow the use of a maximum size $NaYbO_2$ sample to generate the highest possible measurement signal. Despite these preconditions, the sample used in the measurement has a mass of only 0.79 mg.

In addition to MPMS measurements magnetization up to 50 T was measured in the High Magnetic Field Laboratory Dresden (HLD). The measurements on $KYbO_2$ and $KYbS_2$ were performed at about 0.5 K in a triply compensated extraction magnetometer within a 50 T mid-length-pulse magnet. The polycrystalline $KYbO_2$ was ground in a glovebox and fixed between two wooden pieces in a small capton tube [see

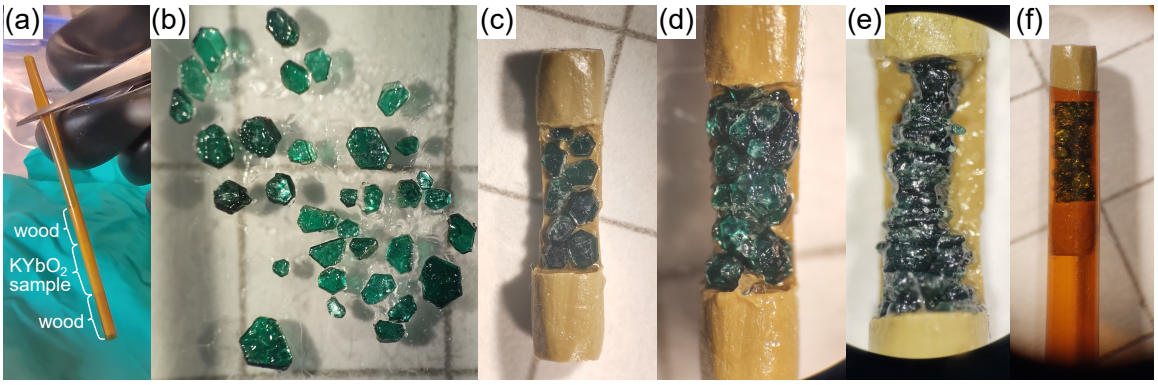

Figure 3.7: *Sample preparation for the high-field magnetization measurements. (a) Ground polycrystalline $KYbO_2$ sample fixed in a capton tube using two pieces of wood. (b) All the $KYbS_2$ crystals used for the measurements. (c)Stacking of crystals into the groove of the sample holder for the $H \perp c$ measurement for a single layer of crystals and (d) for all crystals stacked in the sample holder for the measurement. (e) $KYbS_2$ single crystals stacked for the $H \parallel c$ measurement. (f) Sample holder with the arranged single crystals partially inserted into the capton tube for the measurement.*

Fig. 3.7(a)]. The $KYbS_2$ single crystals were stacked in a small sample holder using vacuum grease to keep them in place. The sample holder was then pushed inside a capton tube, see Fig. 3.7(b)-(f).

3.5 Physical Property Measurement System

Heat capacity and VSM magnetization measurements are performed utilizing a standard PPMS (Physical Property Measurement System) from Quantum Design.

The measurements of the specific heat are performed at 0 T between 0.5 and 10 K with the ^{3}He refrigerator and up to 300 K with the regular PPMS set-up. The polycrystalline $KYbO_2$ is measured in various applied fields between 0.5 and 10 K. For $KYbS_2$ only 0 T measurements are performed since the sample platform is oriented perpendicular to the applied magnetic field. Due to the platelet-like shape of the crystals and the resulting limited thickness ($<<$ 1 mm) attaching the crystals perpendicular to the field is not possible. No field-induced magnetic order is observed for $H \parallel c$ in the field range of the PPMS ($0 - 14$ T).

The samples were attached to the platform using N-grease to ensure a good thermal contact [see Fig. 3.8(b)]. For each sample measurement an individual addenda was created by measuring the heat capacity puck with N-grease applied to the platform without the sample using the same temperature set-points as for the subsequent sample measurements. This enables an exact background subtraction.

Fig. 3.8 shows a schematic picture of the heat capacity puck. Platinum wires connect the otherwise freely suspended sample platform to the puck frame and function as the connection to the heater, thermometer and thermal contact. The measurements are

performed under vacuum conditions and a cap on top of the puck prevents further environmental influences on the measurement.

The specific heat is determined by applying a heat pulse to the sample platform, which transmits a known amount of heat with constant power to the sample. After a fixed amount of time the heat pulse is interrupted and the sample is allowed to cool down for the same duration as the heat pulse. By measuring the temperature of the heating and cooling cycle and fitting with a theoretical model the heat capacity at constant pressure is determined:

$$C_p = \left(\frac{dQ}{dT}\right)_p . \tag{3.4}$$

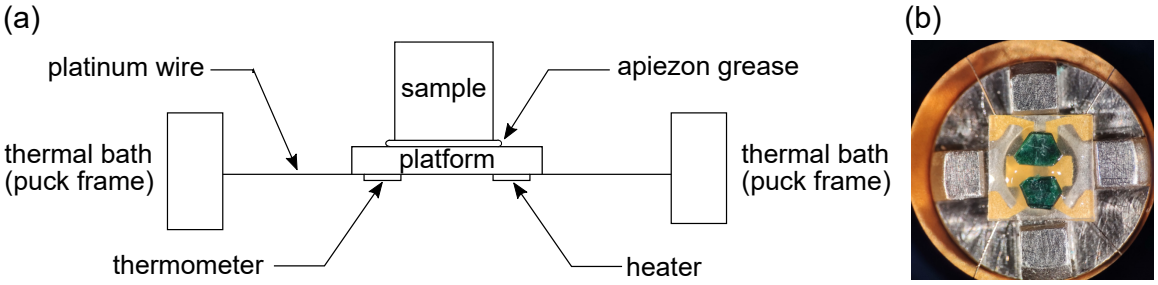

Figure 3.8: *(a) Schematic picture of the heat capacity puck [51]. (b) Two $KYbS_2$ single crystals fixed to the sample platform of the ^3He heat capacity puck using a small amount of N-grease. Two crystals were used in an attempt to compensate the low sample mass, however, due to the low thermal conductivity of the insulating material this approach did not yield better results as the measurements of only one single crystal.*

4 Yb-Based Triangular Antiferromagnets

Anderson's proposal of RVB physics for spin-$\frac{1}{2}$ Heisenberg triangular lattice antiferromagnets in 1973 and their connection to high-temperature superconductivity recognized in 1987 led to an increased interest in the search for real life materials.

One promising material is $YbMgGaO_4$, which was first investigated by Li *et al.* [10] in 2015 with a detailed study on polycrystalline samples. The results of the study suggest $YbMgGaO_4$ to be a QSL candidate which fits right into the model introduced by Anderson. Shortly after large single crystals were available, making $YbMgGaO_4$ an even more interesting candidate to investigate the spin-liquid physics [9].
In the $R\bar{3}m$ symmetry the Yb^{3+} ions are located on a perfect triangular lattice in the *ab* plane, separated by double layers of nonmagnetic Mg/Ga triangular bipyramids. The large distance between the magnetic layers prohibits intralayer magnetic couplings and therefore constricts the magnetism to two dimensions. Site-mixing is inhibited by the large size difference between the magnetic Yb^{3+} and the nonmagnetic Mg^{+2}/Ga^{+3} ions. Additionally, the antisymmetric Dzyaloshinskii-Moriya interactions are forbidden due to inversion symmetry. The interplay of strong spin-orbit coupling and CEF splitting leads to an effective spin-$\frac{1}{2}$ ground state in $YbMgGaO_4$. [9, 10, 52]

The standard thermodynamic measurements performed on $YbMgGaO_4$ are reported in several publications, the key results of the measurements relevant for this work are given in Tab. 4.1. A summary of the experimental findings, highlighting the peculiarities of $YbMgGaO_4$, is given in the following, including brief overviews on measurements like inelastic neutron scattering (INS), μSR and thermal conductivity $\kappa(T)$ which help to shed light on the true ground state of $YbMgGaO_4$.

The field-dependent magnetization $M(H)$ exhibits a rather broad saturation feature and shows a linear increase above the saturation magnetization for both field directions, $H \parallel c$ and $H \perp c$, which was ascribed to the influence of van Vleck paramagnetism [9, 10]. At low temperatures the magnetization shows an untypical deviation from linearity at 2 T, which corresponds to a plateau feature in its field derivative $\chi(H) = \mathrm{d}M/\mathrm{d}H$. A possible explanation for this feature is a suppressed $\frac{1}{3}$ magnetization plateau, indicating an up-up-down (*uud*) magnetically ordered phase, of the nearest-neighbor triangular Heisenberg antiferromagnet [53] that is destroyed due to the strong easy-plane anisotropy [10]. Similarly, an up-up-up-down (*uuud*) phase characterized by a $\frac{1}{2}$ plateau was considered as the origin of the non linearity [54, 55].

Heat capacity measurements in zero magnetic field display no signs of magnetic order down to 60 mK, however, a broad hump is observed at 2.4 K which is shifted

to higher temperatures with increasing magnetic field, which is possibly linked to a crossover into a QSL state. The low-temperature part of the magnetic specific heat in zero field follows a power law (αT^{γ}) with $\gamma = 0.7$, which is close to the theoretically predicted $T^{2/3}$ behavior of an $U(1)$ QSL. The exponent increases with increasing magnetic field and reaches a value of 2.7 at 9 T. [10]
The thermal expansion $\alpha(T)$ mirrors the temperature dependence of $C(T)$, as stated by the Grüneisen relation $\alpha(T) = \Gamma C(T)$, with the Grüneisen constant Γ, and shows a similar power law behavior at low temperatures ($\alpha(T) \propto T^{0.8}$) [54].

μSR studies on single crystals confirmed the absence of spin freezing down to at least 22 mK and showed clear deviation from typical spin glass behavior [56, 57].

Despite its many advantages as a potential spin-liquid material, $YbMgGaO_4$ has one big imperfection: a disorder of Mg^{2+} and Ga^{3+} ions in the nonmagnetic layers, that was already briefly mentioned in the very first publication in 2015. The importance of this disorder was only revealed much later through investigations of the CEF excitations that display an unusual broadness [58, 59]. The broadening of the CEF excitations was traced back to the disorder in the non-magnetic layer, which leads to a distribution of g-values by causing the position of the Yb to vary from the ideal position [59]. Subsequent INS measurements under high magnetic fields (7.8 T and 8 T) revealed a broad excitation continuum. In this field regime $YbMgGaO_4$ is in the fully polarized sate and, contrary to the experimental observation, narrow spin wave excitations are expected [58, 59]. The random distribution of Mg^{2+} and Ga^{3+} ions therefore has influence on the effective spin-$\frac{1}{2}$ g-factors as well as the magnetic couplings [59]. However, the broad continuum was also interpreted as signatures of a spinon-Fermi-surface $U(1)$ QSL, based on the observation of a V-shaped splitting of the excitation continuum at the Γ point. This interpretation is further supported by the good agreement of the measured and theoretically predicted behavior of the V-shaped splitting under the influence of a weak magnetic field [60, 61]. Another approach to explain the (gapped) high energy excitations is based on nearest-neighbor RVB-type correlations. In this case, the high energy excitations are ascribed to the breaking of nearest-neighbor valence bonds, while at low energies gapless excitations are caused by the rearrangement of valence bonds and the concurrent propagation of unpaired spins [62].

The dispute on the ground state of $YbMgGaO_4$ is further fueled by measurements of the thermal conductivity $\kappa(T)$, where the existence of a magnetic contribution, and therefore the presence of magnetic excitations (i.e. gapless spinons), is debated [63, 64]. The absence of a magnetic contribution to the thermal conductivity would imply that no gapless spinons are present in $YbMgGaO_4$, although the large magnetic specific heat suggest the presence of magnetic excitations. An alternative interpretation is that the spinons do not contribute to the thermal transport for some reason [63]. X. Rao *et al.* [64], on the other hand, observed a magnetic contribution to the thermal conductivity, even though it is very small, indicating that magnetic excitations are indeed present in $YbMgGaO_4$. Furthermore, applying a magnetic field leads to an increase of the thermal conductivity at low temperatures caused by phonons scattering

at magnetic exitations. The small magnetic contribution to the thermal conductivity therefore might be due to the fact that the spinons do not carry heat, instead the phononic heat transport might be hindered by the magnetic exitations present in $YbMgGaO_4$.

A frequency dependent peak at 0.099(6) K observed in measurements of the ac-susceptibility, which represents a clear signature of a spin glass, furthers the doubts on the QSL interpretation of $YbMgGaO_4$. Free impurities or the freezing of only a small fraction of spins, with most spins remaining dynamic, are considered as the origin of the spin glass signature in the ac-susceptibility. [62, 64, 65]

Applying hydrostatic pressure to $YbMgGaO_4$ results in an uniform compression of the structure. Both the Yb-O distances and the Yb-O-Yb bridging angles shrink as a result, while the structural randomness is not impacted. An increase of J_1 is assumed from the structural changes, while J_2 should not be affected. The μSR measurements at 2.6 GPa do not show any significant changes compared to the measurements at ambient pressure in zero field. In an applied longitudinal field a change of the scaling behavior is observed, indicating an evolution towards a frozen state in line with the ac-susceptibility measurements. However, bulk spin freezing at ambient pressure is excluded by dc-susceptibility and μSR measurements. Overall, the spin dynamics of $YbMgGaO_4$ appear collective and are not affected by pressure. [66]

The nature of the ground state of $YbMgGaO_4$ is the center of an ongoing debate. Several experimental findings, like the absence of magnetic order [10, 54, 58], the $C_p \propto T^{0.7}$ behavior of the low-temperature specific heat [10, 58], and the excitation continuum observed in INS measurement [58, 67, 68] initially pointed towards an intrinsic gapless QSL ground state. In this line of thought the spinon Fermi surface QSL [67], a RVB-like state [68], or a J_1-J_2 driven QSL state [58, 69–72] were proposed. The question of the presence or absence of a magnetic contribution to the thermal conductivity [63], the broad transition to saturation at low temperatures in $M(H)$ measurement [54], the frequency dependent peak in the ac-susceptibility [65], etc., however, emphasize the importance of the Mg^{+2}/Ga^{+2} disorder. In this pathway the possibility of the mimicry of a QSL was proposed, where the signatures pointing towards a QSL are ascribed to the structural disorder and the resulting randomness of exchange couplings [31, 73, 74].

The investigation of $YbMgGaO_4$ as a potential QSL and the complications due to the disorder in the non-magnetic layer roused the interest in a compound family that is closely related to $YbMgGaO_4$. The $AYbX_2$ compounds consist of an alkaline metal in the A position and a chalcogen in the X position. Most members of the $AYbX_2$ compound family have the same $R\bar{3}m$ space group as $YbMgGaO_4$, although there are some exceptions, like $CsYbSe_2$ [75], $CsYbO_2$ [76] and $TlYbS_2$ [77] which crystallize in the hexagonal $P6_3/mmc$ space group.

In the $R\bar{3}m$ space group the magnetic ions are arranged on a triangular lattice. The individual magnetic layers are separated by a single layer, which consists of only one nonmagnetic element: the alkaline metal A. Therefore, disorder is evaded in these materials. The polycrystalline $NaYbO_2$ was the first member of the $AYbX_2$ family

which was extensively studied, but was quickly followed by multiple sister compounds, like $NaYbSe_2$, which are also available in single crystalline from. Not all of these compounds proved to be spin-liquid candidates. $KYbSe_2$ for example exhibits magnetic order at low temperatures [78, 79]. Nevertheless, the $A\mathrm{Yb}X_2$ compound family is providing a diverse playground for the investigation of triangular antiferromagnets which show a wide range of phenomena and phases. In the following, some rather well studied compounds ($NaYbO_2$, $NaYbSe_2$) will be revisited, adding some complementary or reviewed information. Additionally, more in-depth investigations of less investigated members of the $A\mathrm{Yb}X_2$ family, like $KYbO_2$ and $KYbS_2$, are provided. The influence of disorder on the potential QSL candidate $KYbS_2$ is studied by doping with Se towards the magnetically ordered $KYbSe_2$.

Table 4.1: *Overview of the characteristic properties of $YbMgGaO_4$. The measurements in Ref. [10] are performed on polycrystals, therefore, only averaged values are determined. The low-temperature (LT) susceptibility in Ref. [10] and Ref. [67] was fitted with the standard Curie-Weiss law. In Ref. [9] the van Vleck contribution χ_{vv} determined from the magnetization measurements was subtracted before fitting with the Curie-Weiss law.*

	XRD		**Susceptiblity (LT)**		**Magnetization**	
	lattice parameter (Å)		$\boldsymbol{\theta_{\mathrm{CW}}}$ **(K)**		$\boldsymbol{\chi_{\mathrm{vv}}}$ $\left(\frac{\mathbf{emu}}{\mathbf{mol}}\right)$	
	$\boldsymbol{a}$ **(Å)**	$\boldsymbol{c}$ **(Å)**	$\boldsymbol{H} \parallel \boldsymbol{c}$	$\boldsymbol{H} \perp \boldsymbol{c}$	$\boldsymbol{H} \parallel \boldsymbol{c}$	$\boldsymbol{H} \perp \boldsymbol{c}$
[10]	3.40212(8)	25.1191(6)	−4.11(2) (av.)		0.00681(6) (av.)	
[9]	3.4061(22)	25.130(16)	−1.47	−2.7	0.0150(2)	0.00382(8)
[67]	–	–	−3.2	−4.78	0.00899(6)	0.000469(2)

	Magnetization					
	$\boldsymbol{M_{\mathrm{sat}}}$ $\boldsymbol{(\mu_{\mathrm{B}})}$		$\boldsymbol{H_{\mathrm{sat}}}$ **(T)**		$\boldsymbol{g}$	
	$\boldsymbol{H} \parallel \boldsymbol{c}$	$\boldsymbol{H} \perp \boldsymbol{c}$	$\boldsymbol{H} \parallel \boldsymbol{c}$	$\boldsymbol{H} \perp \boldsymbol{c}$	$\boldsymbol{H} \parallel \boldsymbol{c}$	$\boldsymbol{H} \perp \boldsymbol{c}$
[10]	1.600(2) (av.)		–	–	3.2 (av.)	
[9]	1.860(3)	1.530(2)	–	–	3.721(6)	3.06(4)
[67]	–	–	–		3.819(2)	3.004(1)
[54]	1.860(3)	1.530(2)	5	7	–	–
[64]	1.8	1.45	5	7	–	–

5 $NaYbO_2$

$NaYbO_2$ was one of the first members of the $AYbX_2$ family that was extensively studied. Hence, numerous publications containing standard analysis methods as well as more specialized techniques are available [11, 80–85]. Prior to the start of my PhD work I contributed in the compilation of Ref. [80] and the investigation of $NaYbO_2$ was the focus point of my Master thesis [11]. In this chapter, the already available information on $NaYbO_2$ is summarized and extended by low-temperature susceptibility data as well as a detailed investigation of the influence of hydro-static pressure on the structural and magnetic properties of $NaYbO_2$ via susceptibility, SXRD and μSR measurements.

5.1 Literature Results

The synthesis of $NaYbO_2$ is a straight forward solid state reaction that is either based on stoichiometric mixtures of Na_2O and Yb_2O_3 [83–85] or Na_2CO_3 and Yb_2O_3 [11, 80–82]. The starting materials are filled into aluminum oxide crucibles heated at 700-1000 °C for 8 h to 4 days depending on the synthesis, including a regrinding and subsequent reheating step.

Neutron powder diffraction [81] and SXRD [80] measurements revealed the absence of impurities in $NaYbO_2$ while the $R\bar{3}m$ symmetry is retained. Additionally, the absence of disorder in the nonmagnetic layer in $NaYbO_2$ compared to $YbMgGaO_4$ makes $NaYbO_2$ an ideal candidate to study QSL physics on the triangular lattice. A comparison of the lattice parameters from different studies on $NaYbO_2$ is given in Tab. 5.1 together with other characteristic values determined from standard measurements.

Field-dependent magnetization measurements showed saturation above 12 T, with a linear increase above the saturation field due to the van Vleck magnetism. At low temperatures a plateau was observed between 4 and 5 T, however the exact value of the plateau is debated, with both $M_{\mathrm{sat}}/3$ and $M_{\mathrm{sat}}/2$ as likely candidates [80, 84, 85]. Both kinds of plateaus are expected in triangular antiferromagnets, corresponding to a *uud* [86] or a *uuud* [55] ordered phase, respectively.

Measurements of the magnetic susceptibility showed no bifurcation between ZFC and FC as would be expected for a spin glass system [80, 85]. No sign of magnetic order was observed down to 0.5 K at fields below 2 T. In magnetic fields larger than 2 T magnetic order appears, indicated by a kink at low temperatures [84]. The inverse susceptibility follows a linear behavior at high temperatures, with a change of slope below 100 K due to the CEF splitting and the increasing population of the ground

state doublet. A depiction of the inverse susceptibility can be found in Ref. [82]. Both, high and low-temperature regimes ($H < 2\,T$), were investigated with the Curie-Weiss law. The negative values for the Curie-Weiss temperature confirms antiferromagnetic interactions [11, 80, 81, 84, 85].

The ESR measurements on polycrystalline samples revealed a rather strong g-factor anisotropy in $NaYbO_2$, indicated by an additional shoulder in the ESR spectra, which made it possible to determine $g_\perp$ and $g_\parallel$ separately. The effective moment and Curie-Weiss temperature obtained from ESR measurements are in good agreement with the results of the susceptibility measurements. The ESR linewidth gives an estimate of the energy gap between ground state and first excited crystal field level, $\Delta = 320\,\mathrm{K}$, that is similar to the one determined from INS measurements of the CEF levels ($\Delta = 400\,\mathrm{K}$ [80]) and supports the assumed pseudospin-$\frac{1}{2}$ scenario. [81, 84]

The three CEF excitations observed in the INS measurement are sharp and resolution limited with no indication of structural disorder [80, 82]. Low energy neutron diffraction measurements confirmed the presence of gapless excitation in $NaYbO_2$ and the absence of magnetic order in zero field, while in an applied field of 5 T *uud* order was observed [80, 81].

μSR and ac-susceptibility measurements showed no signs of spin freezing down to 50 mK and further supported the absence of magnetic order [80].

The absence of magnetic order in zero field was further confirmed by heat capacity measurements down to 70 mK. Similar to $YbMgGaO_4$, a broad maximum was observed in the specific heat. It is located at 1 K in zero field and shifts to higher temperatures if a magnetic field is applied. The appearance of magnetic order was observed at magnetic fields larger than 2 T in the form of a λ-shaped peak, that is initially shifted to higher temperatures with increasing the field up to 4 T. Above 4 T the magnetic ordering temperatures slowly decreases with further increasing magnetic field up to 9 T. At 6 T an additional feature was observed, that can be interpreted as a second ordering peak [84]. The analysis of the low-temperature behavior of the specific heat revealed a power law behavior suggesting gapless excitations with an exponent of $\gamma \approx 2$ for weak applied magnetic fields [80]. In zero field a more complex behavior was observed. While in Ref. [81] the T^2 behavior was postulated for zero field as well, a linear T-dependence of the low-temperature specific heat was determined in Ref. [84]. The analysis in Ref. [80] covers the largest-temperature regime, containing data points down to 70 mK, but found both linear and quadratic temperature dependence fail to describe the low-temperature behavior. Instead an unusual two power-law approach was employed to achieve a satisfactory match: $aT^p + bT^q$, with $p = 2.9$ and $q = 0.5$. The first exponent might be related to the T^3 behavior observed for magnons in long-range ordered antiferromagnets, while the sublinear power-law behavior is reminiscent of the behavior of the low-temperature specific heat in $YbMgGaO_4$.

The magnetic entropy was calculated from the specific heat and reaches a value close to $R \ln 2$ at 40 K, another feature of the pseudospin-$\frac{1}{2}$ ground state [84].

Although $NaYbO_2$ is already well studied, the thermodynamic measurements are revisited in this work to gather reference data for the comparison with the newly studied

Table 5.1: *Characteristic properties of $NaYbO_2$ compiled from the literature. The susceptibility at high temperatures (HT) was fitted with the Curie-Weiss law in Ref. [11] and with the modified Curie-Weiss law in the case of Ref. [84] and Ref. [85]. To describe the low-temperature (LT) behavior the modified Curie-Weiss law was applied in Ref. [11], Ref. [85] and Ref. [81]. In Ref. [80] the low-temperature susceptibility was fitted linearly after the van Vleck contribution from the high-field magnetization was subtracted. In the case of Ref. [84] the susceptibility was also corrected for χ_{vv} and fitted linearly but it is unclear from which measurement χ_{vv} is obtained.*

	XRD		**Susceptibility (HT)**		
	lattice parameter (Å)		$\boldsymbol{\theta_{\mathrm{CW}}}$ **(K)**	$\boldsymbol{\chi_{\mathrm{vv}}}$ $\left(\frac{\mathbf{emu}}{\mathbf{mol}}\right)$	$\boldsymbol{\mu_{\mathrm{eff}}}$ $\boldsymbol{(\mu_{\mathrm{B}})}$
[84]	$a = 3.35$	$c = 16.63$	-100	$1.6 \cdot 10^{-5}$	4.5
[85]	$a = 3.348$	$c = 16.6527$	-120	0.00366	4.5
[80]	$a = 3.34799(5)$	$c = 16.4812(4)$	–	–	–
[81]	$a = 3.34556(3)$	$c = 16.4559(3)$	–	–	–
[11]	$a = 3.344768(9)$	$c = 16.45823(8)$	-110	–	4.66

	Susceptibility (LT)			**Magnetization**		
	$\boldsymbol{\theta_{\mathrm{CW}}}$ **(K)**	$\boldsymbol{\chi_{\mathrm{vv}}}$ $\left(\frac{\mathbf{emu}}{\mathbf{mol}}\right)$	$\boldsymbol{\mu_{\mathrm{eff}}}$ $\boldsymbol{(\mu_{\mathrm{B}})}$	$\boldsymbol{\mu_0 H_{\mathrm{sat}}}$ **(T)**	$\boldsymbol{\chi_{\mathrm{vv}}}$ $\left(\frac{\mathbf{emu}}{\mathbf{mol}}\right)$	$\boldsymbol{M_{\mathrm{s}}}$ $\boldsymbol{(\mu_{\mathrm{B}})}$
[84]	-6	0.000517	2.6	12	0.00559	1.36
[85]	-10	0.00446	2.4	–	0.0117(4)	1.24
[80]	$-5.64(1)$	–	2.84(2)	16	0.00564	1.75
[81]	$-10.3(8)$	0.0053(3)	2.63(8)	–	–	–
[11]	-9.3	0.00576	2.65	–	–	–

	ESR					
	$\boldsymbol{g_{\perp}}$	$\boldsymbol{g_{\parallel}}$	$\boldsymbol{g_{av}}$	$\boldsymbol{\mu_{\mathrm{ESR}}}$ $\boldsymbol{(\mu_{\mathrm{B}})}$	$\boldsymbol{\theta_{\mathrm{ESR}}}$ **(K)**	$\boldsymbol{\Delta}$ **(K)**
[84]	3.28(8)	1.75(3)	2.86	2.4	-9	320
[81]	3.294(8)	1.726(9)	–	–	–	–

$KYbO_2$. In addition to that, $NaYbO_2$ is investigated under pressure to gain insights on the influence of pressure on the exchange couplings. The modification of the exchange coupling by applying pressure might ultimately induce long-range order in $NaYbO_2$, simliar to the spin-liquid candidates $Yb_2Ti_2O_7$ [87] and herbertsmithite [88] where pressure induced magnetic order is observed at 0.1 GPa and 2.5 GPa, respectively.

5.2 Low-Temperature Magnetization

In the magnetization measurements at low temperatures the formation of the aforementioned plateau is observed between 3.5 and 5 T at 0.65 μ_B, see Fig. 5.1(a). The plateau is most pronounced at 0.4 K and smears out with increasing temperature. The temperature evolution is best observed in the second field derivative of $M(H)$, where the beginning and end of the plateau can be traced via the respective minimum and maximum as shown in Fig. 5.1(b). A slight shrinking of the field range of the plateau is observed in the d^2M/dH^2 plot. Also, the flattening of the plateau with increasing temperature is displayed in the shrinking of the minima and maxima in the second derivative.

In other members of the $AYbX_2$ family magnetization plateaus have been observed as well. With a value of about $M_{sat}/3$ it is ascribed to an up-up-down ordered phase [53, 79, 89]. For $NaYbO_2$ a range of saturation magnetizations between 1.24 μ_B [85] to 1.75 μ_B [80] are reported (see Tab. 5.1). Therefore, the plateau can be interpreted as a $M_{sat}/2$ as well as a $M_{sat}/3$ plateau and both interpretations are discussed as likely scenarios in the literature. A $M_{sat}/2$ plateau would indicate the formation of an up-up-up-down (*uuud*) [55] order between 3.5 and 5 T. However, neutron diffraction measurements are available for $NaYbO_2$ where an *uud* order was observed in Ref. [81]. Anisotropy of the Yb^{3+} moments might be the origin of this dissonance [81].

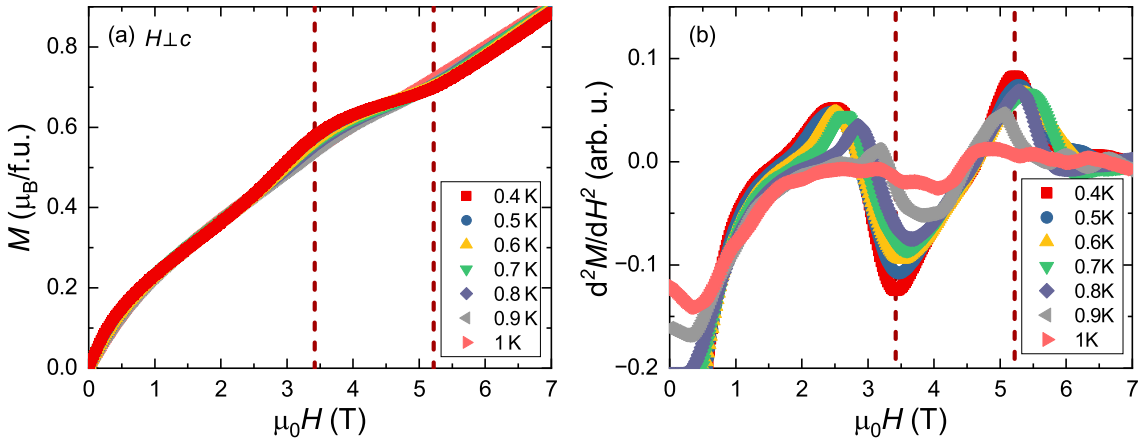

Figure 5.1: *(a) Low-temperature magnetization of $NaYbO_2$ with the plateau feature located between 3.5 and 5 T. (b) Second field derivative of $M(H)$ for determination of the beginning and end of the plateau region via the respective minima and maxima.*

The susceptibility of $NaYbO_2$ was measured down to 0.4 K to observe the transition to the magnetically ordered phase. At low temperatures a kink in the inverse susceptibility is visible [see Fig. 5.2(a)] and the phase transition is located at the inflection point. Therefore, the transition to the magnetically ordered state is best traced by

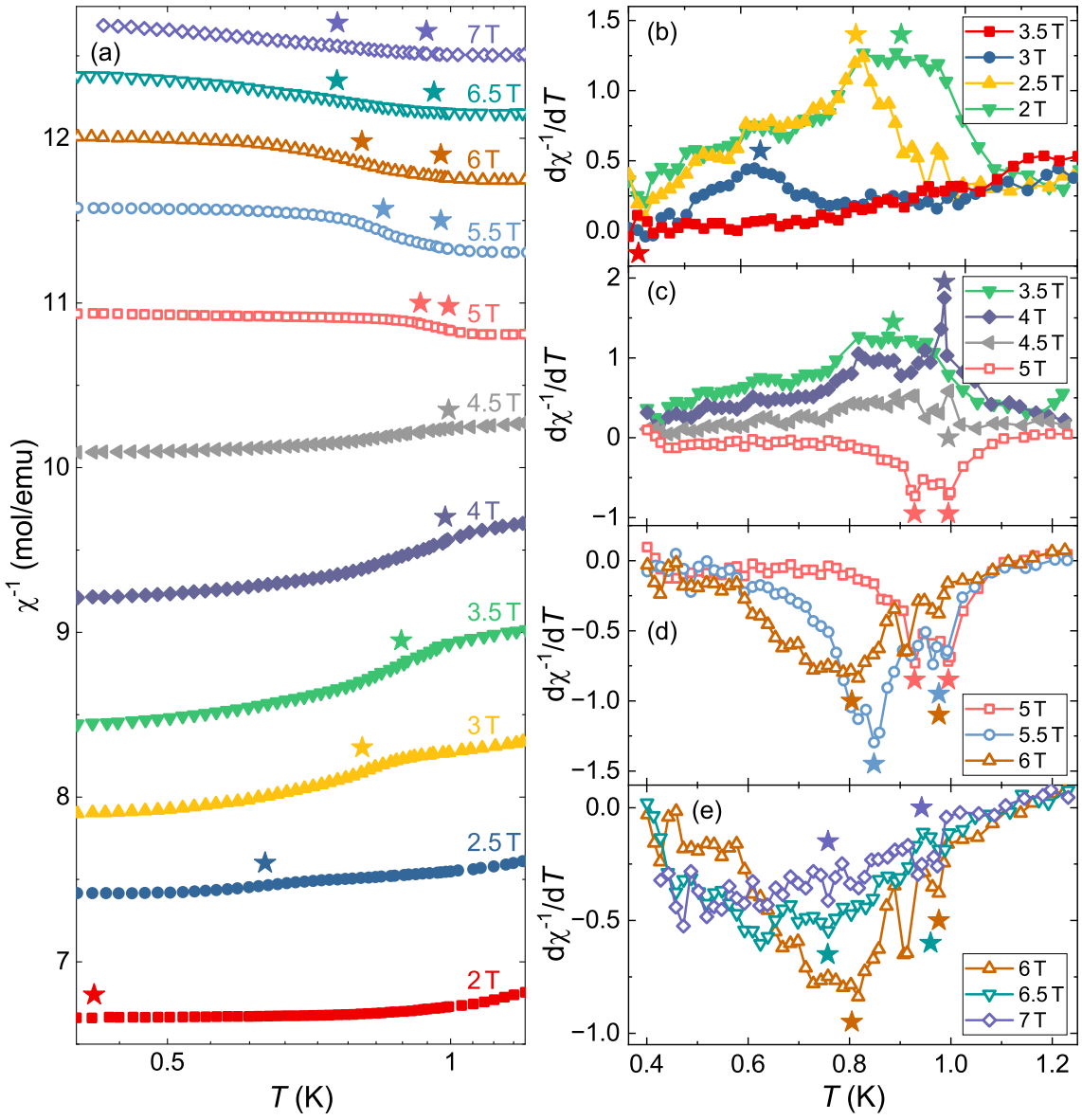

Figure 5.2: *(a) Low-temperature inverse susceptibility of $NaYbO_2$. The transition to the magnetically ordered state is observed as a kink and marked with a star. (b)-(e) First derivative of $\chi^{-1}(T)$ calculated to determine the exact temperature of the transition via the maxima or minima of the derivative. At 5 T two peaks are observed in the derivative for the first time. With increasing field the minima become less distinct and the transition temperatures are harder to determine.*

calculating the first derivative of χ^{-1} and identifying the respective maximum or minimum as shown in Fig. 5.2(b). The phase transition appears for the first time at 2 T and 0.42 K, then shifts up to 1 K at 4.5 T. For higher magnetic fields two transitions are observed in the derivative of χ^{-1}. While the first transition temperature only decreases weakly from 1 K at 5 T to 0.94 K at 7 T, the second phase transition is more temperature dependent and decreases to 0.75 K at 7 T. The temperature evolution of the magnetic phase with increasing field traced by the susceptibility measurements is in good agreement with the observations of magnetic order in the specific heat in Ref. [84]. Ranjith *et al.* [84] also observe two phase transition above 5 T in the specific heat, where an additional, less pronounced peak appears below the original anomaly, and a kink in the susceptibility measurements down to 0.5 K. In Ref. [12] the second transition in the specific heat is also observed, although not as a distinct, additional peak but as a shoulder feature below the lambda-like anomaly of the first phase transition.

The information gained from the low-temperature measurements in this chapter is used to complement the phase diagram presented in Ref. [12] and will be discussed in Chapter 6.8.

5.3 Pressure Study

The influence of hydrostatic pressure on $NaYbO_2$ is investigated in the following via SXRD, susceptibility and μSR measurements. A similar study was performed on $YbMgGaO_4$ as was mentioned in Chapter 4.

5.3.1 Synchrotron XRD

The SXRD measurements at the MSPD beamline (ALBA, Spain) [90] were performed by Alexander Tsirlin and Ece Uykur (HZDR). The data were analyzed by the author. To apply pressure to the sample a diamond-anvil cell loaded with methanol-ethanol mixture was used, which allowed measurements between ambient pressure and 5 GPa. In Fig. 5.3(a) an exemplary SXRD measurement at 4.1 GPa is shown. Applying pressure leads to a shift of the reflection peaks to higher angles, as can be seen on the example of the (003) peak in Fig. 5.3(b).

The $R\bar{3}m$ crystal symmetry remains unchanged up to the highest pressure of the measurement. Same as for $YbMgGaO_4$, two parameters are essential to investigate the influence of pressure on the system: the Yb-O distance and the O-Yb-O angle β. The angle β is equal by symmetry to the Yb-O-Yb angle α, which mediates the nearest neighbor superexchange interaction.

Le Bail refinements were performed to obtain the lattice parameters, which are the starting point for studying the evolution of the local structure under pressure via DFT relaxations. In this way the Yb-O distances and Yb-O-Yb angles were determined by Alexander Tsirlin. Both lattice parameters a and c are found to decrease with

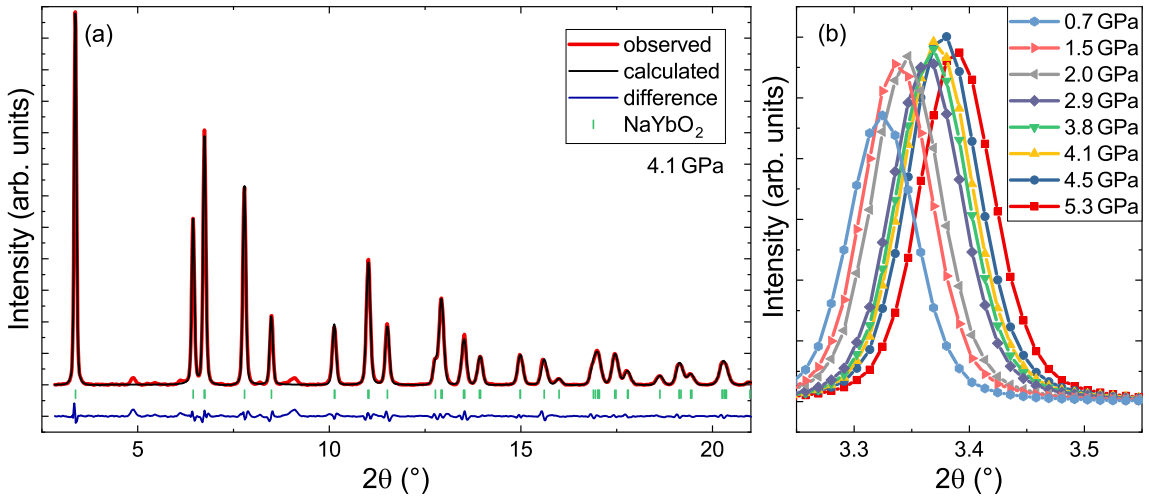

Figure 5.3: *(a) SXRD pattern of $NaYbO_2$ collected in the diamond anvil cell under the pressure of 4.1 GPa. (b) Shift of the (003) peak to higher angles with increasing pressure.*

increasing pressure, however, the decrease is more prominent for c. In comparison, the shrinkage of the lattice parameters for $YbMgGaO_4$ is rather uniform. The pressure evolution of the lattice parameters is shown in Fig. 5.4(a). The pressure evolution of the unit-cell volume as well as the lattice parameters a and c is analyzed by fitting with the second-order Birch-Murnaghan equation of state

$$p(V) = \frac{3B_0}{2}\left[\left(\frac{V_0}{V}\right)^{\frac{7}{3}} - \left(\frac{V_0}{V}\right)^{\frac{5}{3}}\right]. \tag{5.1}$$

This fit was done using the EoSFIT routine [91] determining a bulk modulus of $B_0 = 105(5)$ GPa and unit-cell volume of $V_0 = 160.2(2)$ Å^3 For comparison the same fit as for the unit-cell volume V was applied to a^3 and c^3, yielding $B_{0,a} = 150(8)$ GPa and $B_{0,c} = 70(4)$ GPa for the bulk modulus, respectively. The bulk modulus obtained for $YbMgGaO_4$, $B_0 = 142(2)$ GPa [66], is somewhat larger than that of $NaYbO_2$, rendering $NaYbO_2$ more compressible than $YbMgGaO_4$.

Both, the Yb-O-Yb angle and the Yb-O distances show a decrease with increasing pressure [see Fig. 5.4(b),(c)]. At the maximum pressure of the μSR measurements of 2.4 GPa the Yb-O distances shrinks by 0.2% and by 0.5% at 5.3 GPa. The Yb-O-Yb ($\alpha = \beta$) angle becomes closer to 90° with increasing pressure, a decrease of α by 0.22° up to 2.4 GPa and 0.44° at 5.3 GPa is determined. This observation stands in contrast to the ones made for $YbMgGaO_4$ [66], where applying pressure had a stronger impact on the the Yb-O distances in $YbMgGaO_4$, with a shrinkage of 0.6% at 2.6 GPa. On the other hand, the Yb-O-Yb ($\alpha = \beta$) angle only decreases by 0.07° at 2.6 GPa and 0.2° at 10 GPa for $YbMgGaO_4$, much less than in the case of $NaYbO_2$. This dissimilar behavior can be explained by the anisotropic nature of the compression in the case of $NaYbO_2$, where c decreases much faster than a.

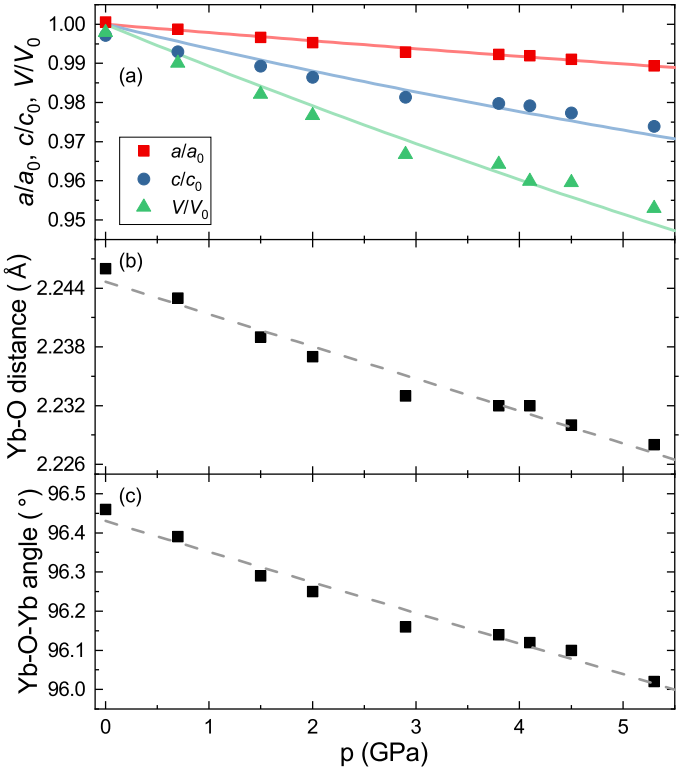

Figure 5.4: *Pressure evolution of the lattice parameters a and c and the unit cell volume V (a), Yb-O distances (b) and Yb-O-Yb angle α (c) determined from Le Bail refinements and DFT relaxation. The solid lines in (a) represent fits with the second-order Birch-Murnaghan equation of state, while the dashed lines in (b) and (c) are guides to the eye.*

5.3.2 Susceptibility

The mCAC allows measurements under applied pressure in the standard MPMS setup. For $NaYbO_2$ a maximum pressure of 2.03 GPa was achieved. The susceptibility measurements are corrected for the background of the pressure cell and are plotted in Fig. 5.5 together with a measurement of $NaYbO_2$ without the pressure cell. The measurements with and without pressure cell show some deviation, as can be seen in Fig. 5.5(a). This can be caused by the restriction to a quite small sample mass (< 1 mg) due to the limited sample space of the mCAC. Although we took great care to determine the exact background of the mCAC for the background subtraction a slight discrepancy between the background measurement of the empty mCAC and the background of the sample measurement is unavoidable. This might be another factor leading to discord between the measurements. Therefore, the low-temperature part of the measurement at ambient pressure with the mCAC was fitted to the one without the mCAC by multiplying χ with a factor of 1.28 and introducing of an offset of 0.0013 $\frac{\text{emu}}{\text{mol}}$. All measurements with the mCAC were adapted in this way [see Fig. 5.5(b)].

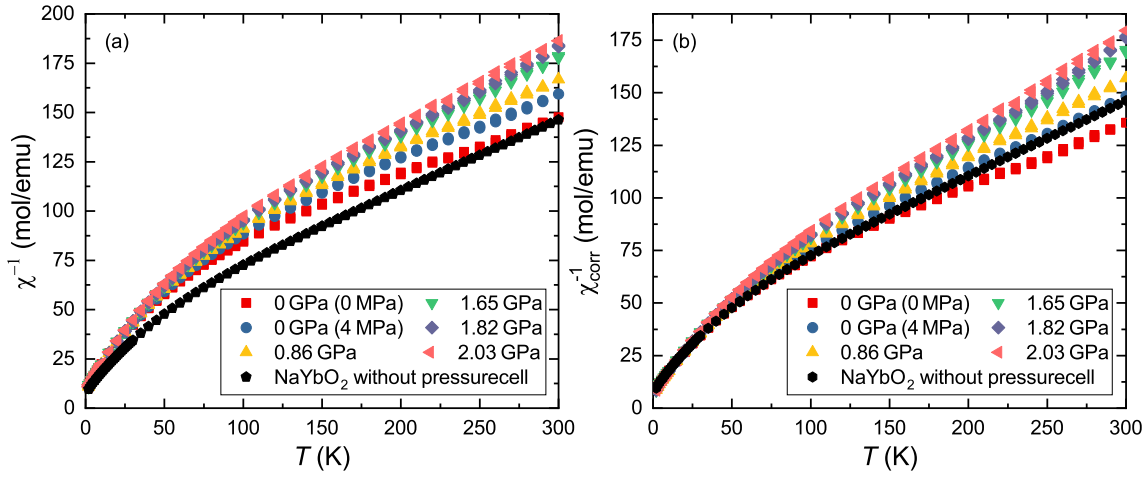

Figure 5.5: *(a) Inverse susceptibility at different applied pressures measured with the mCAC. For comparison a measurement without the pressure cell is shown as well (black hexagons). (b) Susceptibility measurements corrected by fitting the 0 GPa measurement to the measurement without the mCAC.*

After the correction, the susceptibility measurements are fitted with the modified Curie-Weiss law between 10 and 35 K. In Fig. 5.6 the determined van Vleck contribution and Curie-Weiss temperatures are shown as a function of the applied pressure. The van Vleck contribution decreases continuously with increasing pressure from 0.00567 $\frac{\text{emu}}{\text{mol}}$ at 0 GPa to 0.00378 $\frac{\text{emu}}{\text{mol}}$ at 2 GPa. This decrease goes hand in hand with the decrease of the Yb-O distances, which leads to an increase of the crystal field on the Yb^{3+} ions. The consequent enhancement of the CEF splitting leads to the decrease of the van Vleck contribution. The Curie-Weiss temperature starts off at −7.1 K at ambient pressure and increases to around −6.6 K at about 1 GPa and remains rather constant up to the maximum pressure. Since the Curie-Weiss temperature is a measure of the strength of the exchange coupling, a decrease of the absolute value of θ_{CW} indicates a decrease of the exchange couplings. This stands in contrast to the shrinking of the Yb-O distances and Yb-O-Yb angle that indicate an increase of exchange interactions, as was observed in the comparison of $YbMgGaO_4$, $KYbO_2$ and $NaYbO_2$ in Ref. [12]. In this case the shrinking of the Yb-O-Yb angle from 100.36° ($YbMgGaO_4$) to 96.75° ($KYbO_2$) to 95.72° ($NaYbO_2$) was accompanied by a decrease of the absolute value of θ_{CW} ($YbMgGaO_4$: 2.3 K, $KYbO_2$: 5.4 K, $NaYbO_2$: 6.4 K). Using these three values as reference points a change of the Curie-Weiss temperature of about 0.9 K is expected for a 1° change of the Yb-O-Yb angle. For the 0.2° change of the Yb-O-Yb angle inflicted by the applied hydrostatic pressure of 2 GPa an increase of about 0.2 K is expected for the absolute value of θ_{CW} of $NaYbO_2$. When comparing the values obtained in the pressure cell this is not observed, but the change lies within the error bar.

It is noteworthy, that there is a discrepancy between the Curie-Weiss temperature determined without ($\theta_{\text{CW}} = -6.4$ K) and with pressure cell at ambient pressure

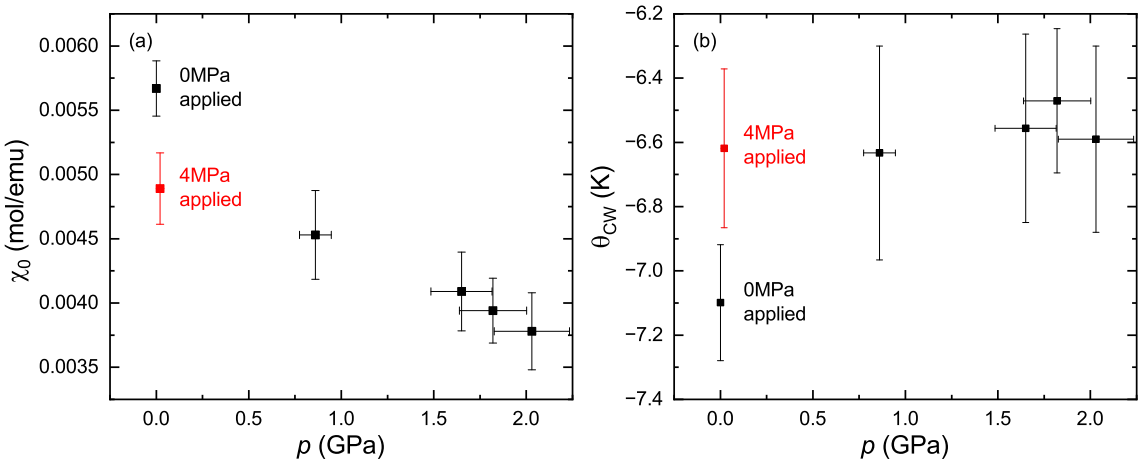

Figure 5.6: *Van Vleck contribution χ_{vv} (a) and Curie-Weiss temperature θ_{CW} (b) determined from the fit with the modified Curie-Weiss law to the susceptibility measurements.*

($\theta_{CW} = -7.1\,K$) as well as between the Yb-O-Yb angle determined from the DFT relaxation based on the experimental lattice parameters of $NaYbO_2$ ($\measuredangle$(Yb-O-Yb) = 95.72°) and the one determined for ambient pressure from the SXRD measurement under pressure ($\measuredangle$(Yb-O-Yb) = 96.46°). The latter is a reflection of a systematic error of the DFT calculations. Additionally, distinctly different values for χ_{vv} and θ_{CW} are obtained for the measurement at ambient pressure, i.e. the measurement where 0 MPa is externally applied to the pressure cell, and the measurement where 4 MPa are applied. In both cases the pressure within the pressure cell was determined to be still at 0 GPa from the Pb superconducting transition, as described in Chapter 3.4. Most likely the background subtraction is the cause of the deviation of the results for 0 GPa compared to the other pressure cell measurements. Since the pressure to the pressure cell is applied manually utilizing a rather rough manometer scale, it is difficult to accomplish exactly the same pressure for the background and the sample measurement. The measurements with an applied pressure at and above 4 MPa might be better comparable to the background measurements than the 0 MPa measurement, considering the conditions in the sample space of the pressure cell. The effective moment is found to be 2.57 μ_B for all applied pressures.

5.3.3 μSR Measurements

The spin dynamics of a system can be revealed via muon spin relaxation (μSR) measurements. μSR measurements on $NaYbO_2$ at ambient pressure were already performed observing persistent spin dynamics down to 100 mK which also survive in an applied longitudinal field [80]. Here the influence of pressure on the spin dynamics is investigated at 0.26 K in zero field (ZF) and in an applied longitudinal field (LF), where the magnetic field is applied parallel to the spin of the implanted muons. Measurements at ambient pressure and at 2.4 GPa are performed and compared to

identify any changes in the spin dynamics. The measurements were performed by Mayukh Majumder at the PSI (Villigen, Switzerland).

The ZF measurements revealed no change of the magnetic ground state in the μSR time spectra under pressure compared to the measurement at ambient pressure and no oscillations are observed. The absence of oscillations indicates that no magnetic order is induced by applying pressure.

To determine the temperature-dependent relaxation rate the ZF μSR time spectra are fitted with

$$A(t) = A_0 \left[f_1 \exp(-\lambda_1 t) + (1 - f_1) \exp(-\lambda_2 t) \right] + B_0. \tag{5.2}$$

A_0 is the initial anisotropy, B_0 the background of the pressure cell. The muon spin relaxation rates λ_1 and λ_2 correspond to the muons implanted at two sites near O^{2-}. The fraction of muons spins at the two sites is denoted as f_1.

In Fig. 5.7(a) the temperature dependence of the relaxation rates are shown. The temperature development of λ_1 is in good agreement with the measurement in Ref. [80]. At high temperatures ($T > 20\,\mathrm{K}$) $NaYbO_2$ is in the paramagnetic regime and the relaxation rate λ_1 is temperature independent. The step-like increase below 10 K indicates the formation of spin-spin correlations. At low temperatures the relaxation rate becomes level again as the correlations are fully developed below 1 K. The measurement performed in the scope of the pressure study apparently reach this state at a slightly lower temperature compared to Ref. [80], where λ_1 becomes constant at about 3 K already. No obvious difference between the measurement under

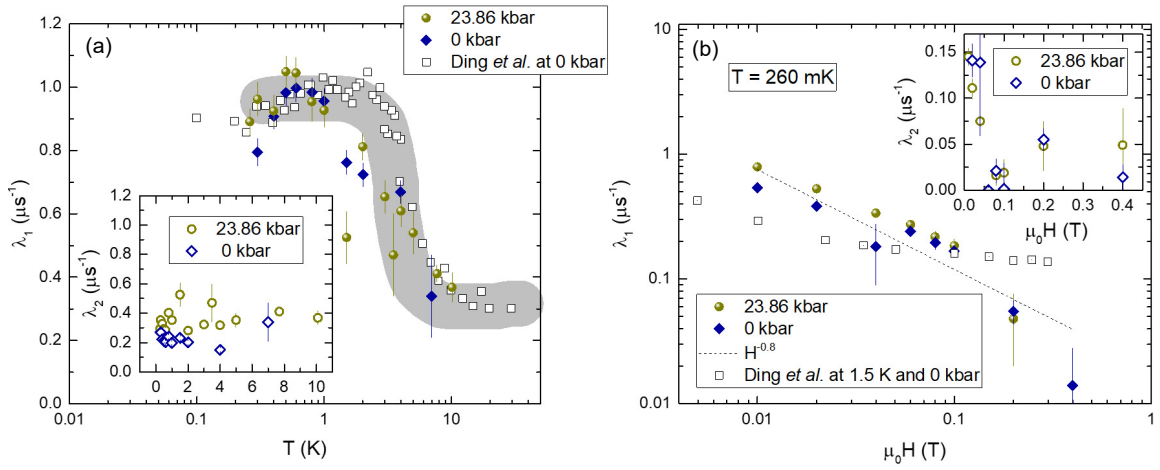

Figure 5.7: *(a) Zero field μSR relaxation rate λ_1 at ambient pressure and 2.4 GPa. For comparison the μSR measurement at ambient pressure without a pressure cell performed in Ref. [80] is shown as well. The inset shows the temperature dependence of λ_2.*
(b) Longitudinal field μSR relaxation rate λ_1 at ambient pressure and at 2.4 GPa is fitted with the same power-law. The measurement at higher temperature in Ref. [80] follows a power-law as well, although with a smaller exponent. The graphs were prepared by Mayukh Majumder.

pressure and at ambient pressure is observed and even similar absolute values are retrieved.
For λ_2, shown in the inset of Fig. 5.7(a), no temperature dependence is observed, however the absolute values are rather similar to the background of the pressure cell and difficult to determine with great accuracy.

The LF measurements are performed to investigate the field dependence of the relaxation rate $\lambda(H)$. To identify the relaxation rate the LF measurements were fitted with a stretched exponential $\exp\left[-(\lambda(H)t)^{\beta}\right]$, taking the time-independent and field-independent background, caused by the sample holder and pressure cell, into account. For the measurement at ambient pressure as well as under 2.4 GPa a power law behavior $\lambda(H) = H^{-\gamma}$ with $\gamma = 0.8$ is determined [see Fig. 5.7(b)]. Such a power-law behavior is a manifestation of the universal scaling that was initially introduced for system with glassy dynamics by Keren *et al.* [92]. For comparison, the field-dependent relaxation rate determined in Ref. [80] at 1.5 K is shown in Fig. 5.7(b), as well, which follows a power law with a smaller exponent. Since the measurements in the pressure study where performed at a much lower temperature of 0.26 K a higher exponent is expected.

For $YbMgGaO_4$ applying pressure led to an increase of γ from 0.3 at ambient pressure to 0.8 at 2.6 GPa. Such an increase of the scaling parameter is usually observed in glass-like system when the spins start to freeze. The possibility of spin freezing in $YbMgGaO_4$ is excluded by dc-susceptibility and μSR measurements at ambient pressure. Instead the increase of γ is ascribed the structural randomness and its role in the persistence of the collective spin dynamics. The constant value for γ with increasing pressure in the disorder-free $NaYbO_2$ supports this interpretation. [66]

6 $KYbO_2$

After many promising results were obtained on the easy to prepare $NaYbO_2$ the focus broadened to closely related compounds of the $AYbX_2$ family. One of them is $KYbO_2$ which was already briefly studied in 2008 by Dong *et al.* [93] before the discovery of $YbMgGaO_4$ as a potential QSL and the subsequent enhanced interest in the family of $AYbX_2$ compounds. In the context of this work, $KYbO_2$ is utilized to investigate the influence of the alkaline metal A on the magnetism of the $AYbO_2$ compounds. Therefore, the results presented in the following chapter are directly compared to $NaYbO_2$ using available, unpublished data [11] as well as data from Ref. [80] and Ref. [12]. In the latter, the results on $KYbO_2$ obtained throughout my PhD work are published.

6.1 Literature Results

Despite the availability of a synthesis report by Dong *et al.* [93] the preparation of $KYbO_2$ proved to be sensitive and challenging. Dong *et al.* [93] prepared polycrystalline samples via a deceivingly simple solid state reaction and carried out powder XRD, susceptibility, and heat capacity measurements.

For the sample preparation in Ref. [93] Yb_2O_3 and KO_2 were used as starting materials, with an 50% excess of KO_2. The reactants were handled in a glove box to prevent a reaction of KO_2 with the air moisture. They were mixed, enclosed in a gold tube and finally sealed in an evacuated quartz tube with a piece of TiO as an oxygen getter. Thereafter, they were heated at 650 °C for 16 h. Powder XRD measurements revealed small amount of extant KO_2 and Yb_2O_3. The $KYbO_2$ samples need to be stored in a glovebox and exposure to the atmosphere should be kept at a minimum due to the extraordinary sensitivity of $KYbO_2$ to moisture, which will lead to a decomposition within minutes.
The synthesis of $KYbO_2$ was part of my Master thesis [11] and the samples prepared there are further investigated in this work. The synthesis was based on the method used by Dong *et al.* [93] but differs in a few points, since the original approach yielded no satisfactory results. The same starting materials were used but the excess of KO_2 was amplified to 75%. Instead of a gold tube a platinum crucible was utilized. Since an ampule based synthesis was not successful the platinum crucible with the reactants inside was placed in a horizontal furnace and the synthesis was carried out at 650 °C for 16 h under an argon flow of 20 sccm. The resulting sample showed a

small Yb_2O_3 impurity, as will be discussed in Chapter 6.1, and needed to be stored in argon atmosphere due to rapid decomposition in contact with air moisture.

The powder XRD measurements in Ref. [93] confirmed the $R\bar{3}m$ space group, the determined lattice parameters are displayed in Tab. 6.1.

Susceptibility was measured between 2 and 300 K. The high-temperature part can be nicely described by the Curie-Weiss law, yielding similar values for the Curie-Weiss temperatures θ_{HT} and the effective moments μ_{eff} in Ref. [93] and Ref. [11] (see Table 6.1). The effective magnetic moment is close to the calculated value of $4.54\,\mu_{\mathrm{B}}$ for free Yb^{3+} in both cases. At lower temperatures the susceptibility deviates from the Curie-Weiss law due to the CEF effect. The analysis of the low-temperature part yielded smaller values for the Curie-Weiss temperature and effective moments (shown in Table 6.1), offering a more realistic description of the low-temperature ground state properties. In Ref. [11] the low-temperature susceptibility was fitted with modified Curie-Weiss law (Eq. 2.18) allowing for an additional χ_{vv} term to account for the van Vleck contribution. All fits, at low and high temperatures, resulted in negative Curie-Weiss temperatures indicating antiferromagnetic exchange interaction but no sign of magnetic order was observed down to at least 2 K.

The absence of magnetic order was confirmed by specific heat measurements down to 2 K in Ref. [11] and down to at least 0.5 K in Ref. [93]. Instead of a sharp peak indicating a phase transition a broad maximum was observed, similar to $NaYbO_2$ and $YbMgGaO_4$, signaling the presence of short range correlations.

Table 6.1: *Characteristic properties of $KYbO_2$ from Ref. [93] and Ref. [11]. Both, the high-temperature (HT) and low-temperature (LT) susceptibilities, were fitted with the standard Curie-Weiss law in Ref. [93]. In Ref. [11] the high-temperature behavior of the susceptibility was fitted with the standard Curie-Weiss law, while at low temperatures the modified Curie-Weiss law was applied.*

	XRD		**Susceptibility HT**	
	lattice parameter		$\boldsymbol{\theta_{\mathrm{CW}}}$ **(K)**	$\boldsymbol{\mu_{\mathrm{eff}}}$ **(μ_{B})**
[93]	$a = 3.4001(2)$ Å	$c = 18.497(1)$ Å	$-77(3)$	4.31(5)
[11]	–	–	-90	4.32

	Susceptibility LT			
	$\boldsymbol{\theta_{\mathrm{CW}}}$ **(K)**	$\boldsymbol{\chi_{\mathrm{vv}}}$ $\left(\frac{\mathbf{emu}}{\mathbf{mol}}\right)$	$\boldsymbol{\mu_{\mathrm{eff}}}$ **(μ_{B})**	$\boldsymbol{g}$
[93]	$-8.5(5)$	–	–	–
[11]	-5.02	0.00456	2.64	3.05

The frustration parameters $f = 17$ and $f = 10$ are calculated using the lowest measured temperature of the heat capacity measurement 0.5 K and the respective Curie-Weiss temperatures determined in Ref. [93] and Ref. [11], respectively.

6.2 Synchrotron XRD

The high-energy synchrotron X-ray diffraction measurements yield information on the sample quality and allow to identify the space group of the material. As aforementioned, SXRD measurements for $KYbO_2$ at 10 K were carried out at the MSPD beamline [94] (ALBA, Spain) by Alexander Tsirlin and Aleksandr Zubtsovskii utilizing a multianalyzer setup, suitable for powder diffraction measurements, with a wavelength of $\lambda = 0.32525$ Å.

According to the SXRD measurements $KYbO_2$ possesses the same $R\bar{3}m$ space group as $NaYbO_2$ and $YbMgGaO_4$, as was already reported in Ref. [93]. The narrow peaks indicate high crystallinity of the sample [see Fig. 6.1(a)]. In the SXRD spectrum two minor impurity phases are observed which are identified as Yb_2O_3 and $KOH \cdot H_2O$ [see Fig. 6.2(b)]. Since $KYbO_2$ is prone to decompose if handled outside of an inert gas atmosphere, these impurities are inevitable and need to be considered in the interpretation of any measurements performed on $KYbO_2$. As a consequence, the contact of $KYbO_2$ to air moisture needs to be kept at a minimum and diligent sample handling is required when performing measurements to keep the influence of the impurities as small as possible.

Rietveld refinement of the SXRD data returns low atomic displacement parameters (ADPs). The high ADP of Yb was the first indication of structural disorder in

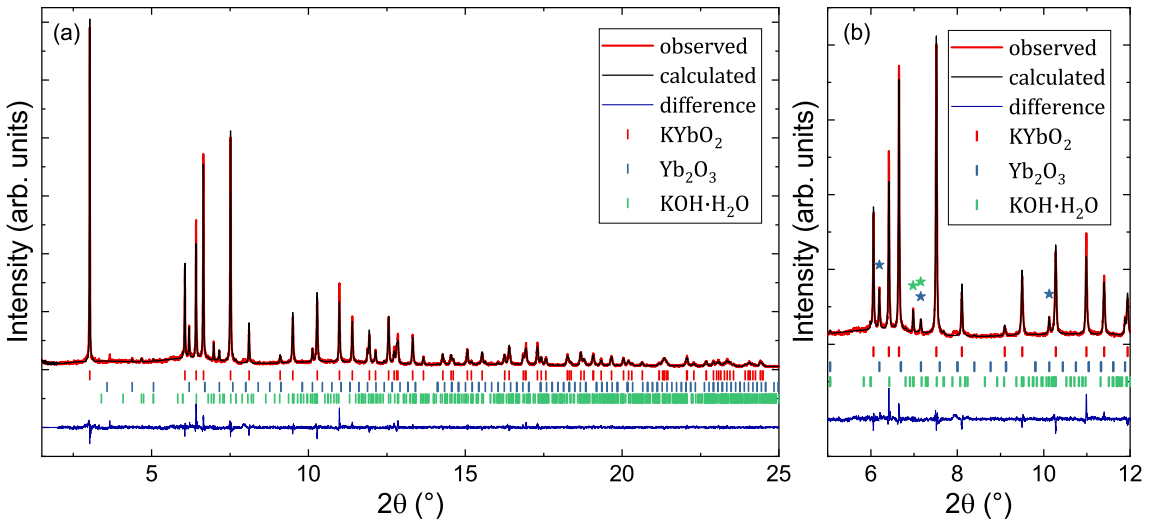

Figure 6.1: *(a) Structure refinement of the synchrotron diffraction data acquired at 10 K. (b) Reflections of the impurity phases marked with stars are better observed in the enlargement of the angular range between 5 and 12°. Adapted from Ref. [12].*

Table 6.2: *(a) Atomic displacement parameters (U_{iso}) and atomic positions of $KYbO_2$ obtained from the Rietveld structure refinement of the SXRD pattern measured at 10 K [12]. (b) For comparison the ADPs and atomic positions of $NaYbO_2$ from Ref. [80] are shown as well. Table adapted from Ref. [12].*

(a) $KYbO_2$					**(b) $NaYbO_2$**				
atom	***x/a***	***y/b***	***z/c***	U_{iso} **(Å²)**	**atom**	***x/a***	***y/b***	***z/c***	U_{iso} **(Å²)**
O	0	0	0.2288(3)	0.005(1)	**O**	0	0	0.2375(1)	0.0007(4)
Yb	0	0	0.5	0.0015(2)	**Yb**	0	0	0.5	0.00015(3)
K	0	0	0	0.0046(5)	**Na**	0	0	0	0.0032(3)

$YbMgGaO_4$ ($U_{iso}(Yb) \approx 0.01$ Å^2 at 100 K [9]). The Yb ADPs of $KYbO_2$ and $NaYbO_2$, on the other hand, are well below 0.01 Å^2 at 10 K (see Tab. 6.2), therefore no disorder is expected in these compounds.

The obtained lattice parameters are in good agreement with the previous study [93]. In comparison to $NaYbO_2$ (see Tab. 6.3) the lattice parameters of $KYbO_2$ are a bit larger, due to replacement of the smaller Na^+-ions ($r = 1.02$ Å) by larger K^+ ions ($r = 1.38$ Å) [95]. This change is more prominent for the c direction with an increase of 12.1%. The lattice parameter a, and therefore the Yb-Yb intralayer distance, d(Yb-Yb) = a, changes only slightly by 1.6%. The effect of the increase of a is twofold. First, the [YbO_2] layers expand, as can be discerned by the 0.8% increase of the Yb-O distance. Second, the Yb-O-Yb angle increases as well. Together, the expansion of the [YbO_2] layer and the increase of the Yb-O-Yb angle accounts for the overall 1.6% increase of the Yb-Yb distance. The flattening of the Yb-O-Yb angle (which is equal by symmetry to the O-Yb-O angle) directly influences the local environment of the Yb^{3+}.

The exchange of K by Na leads to a similar effect as the application of hydrostatic pressure on $NaYbO_2$. The larger K atoms have the effect of negative pressure applied to the crystal structure. The anisotopic impact on the crystal structure observed in the pressure study on $NaYbO_2$ is mirrored and enhanced in the comparison of $NaYbO_2$

Table 6.3: *Comparison of the lattice parameters, Yb-O and A-Yb (A =Na, K) distances (given in Å) and Yb-O-Yb bridging angles of $NaYbO_2$ and $KYbO_2$. Table adapted from Ref. [12].*

	a	***c***	**Yb-O dist.**	**∡Yb-O-Yb**	***A*-Yb dist.**
$NaYbO_2$ [80]	3.34481(4)	16.4585(2)	2.25537(3)	95.723(1)°	3.35466(3)
$KYbO_2$ [12]	3.39731(4)	18.453(3)	2.27232(3)	96.756(1)°	3.64786(5)

and $KYbO_2$. While for the lattice parameter a nearly the same relative change as for an applied pressure of 5.3 GPa is observed, the relative change of the lattice parameter c upon substitution with K is tenfold larger than through hydrostatic pressure.

6.3 ESR Measurements

ESR measurements probe the local magnetism of the Yb^{3+} ions. The measurements were performed and analyzed by Hans-Albrecht Krug von Nidda and Mamoun Hemmida. As shown in Fig. 6.2(a), fitting with the field derivative of a single Lorentzian gives a satisfactory description of the Yb-ESR line at all measured temperatures ($5 - 30$ K). An additional field derivative of a Lorentzian accounts for the shoulder at low fields that is most likely due to the Yb_2O_3 impurity observed in SXRD measurements. Also, slight deviations are observed between 2.8 and 3.5 kOe that can be ascribed to insufficient background subtraction due to a slight mismatch of the quality factor between sample and background measurement.

Generally, the ESR measurements of the $AYbX_2$ compounds reveal strong easy-plane anisotropy, especially compounds that are available in the single crystalline

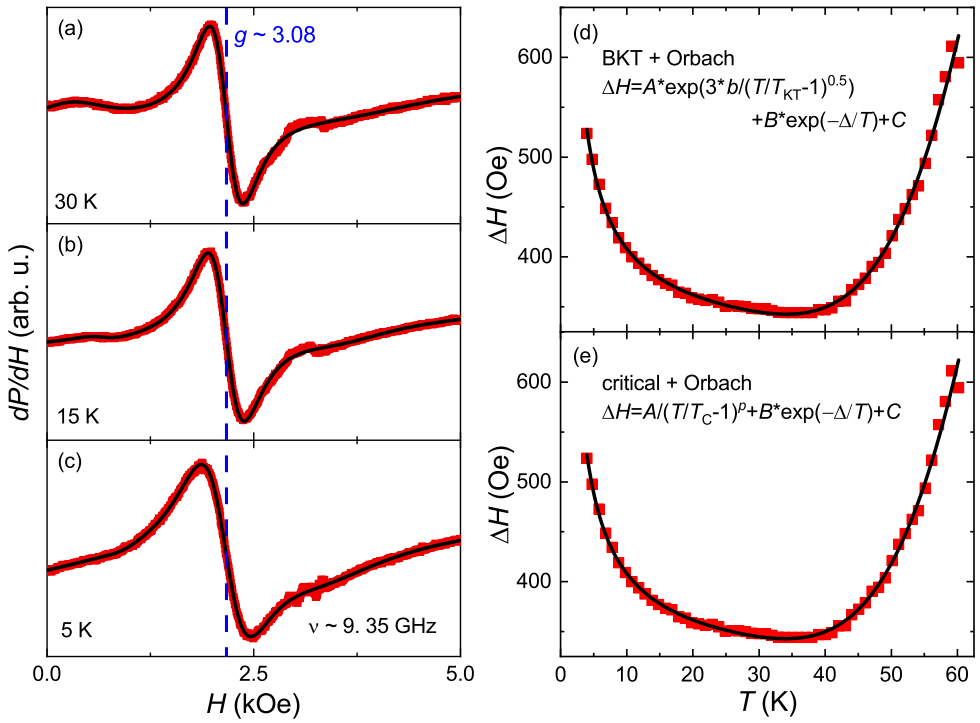

Figure 6.2: *(a)-(c) ESR measurements of $KYbO_2$ taken at the X-band frequency at 30 K, 15 K and 5 K. The spectra are fitted with the field derivative of a symmetric Lorentz line (black solid line). (d,e) ESR linewidth fitted with a combination of Orbach process at high temperatures and two possible models (BKT and critical) at low temperatures. Adapted from Ref. [12].*

form, as for example $KYbS_2$ that will be discussed in the following chapter. But even the polycrystalline $NaYbO_2$, for which direction dependent measurements are not possible, reveals an additional shoulder in the ESR measurement that can be ascribed to a sizable anisotropy of the g-factor [84]. The ESR measurement of $KYbO_2$, on the other hand, appears to be purely isotropic with a g-factor of $g = 3.08(3)$. Considering the structural changes observed in the SXRD measurements, a change of the ground-state Kramers doublet of Yb^{3+} compared to $NaYbO_2$ is to be expected. The anisotropic lattice expansion and the corresponding change in the $[YbO_2]$ layers influence the g-value and anisotropy of the g-tensor.

The ESR linewidth as a function of temperature increases at high temperatures due to an Orbach process that can be described as $\Delta H \propto \exp(-\Delta/T)$. An Orbach process involves the population of the first excited CEF doublet, separated from the ground-state doublet by an energy gap Δ via phonon absorption and subsequent emission of a phonon [96–98]. The energy gap determined from the high-temperature fit is $\Delta \simeq 350\,\mathrm{K}$. Similar values are found for $NaYbO_2$ ($\Delta = 350\,\mathrm{K}$ [96], $\Delta = 320\,\mathrm{K}$ [84]).

The low-temperature part of the ESR linewidth is investigated in two ways. On one hand, a classical critical behavior in the vicinity of a phase transition is employed to describe the increase at low temperatures: $\Delta H \propto (T/T_\mathrm{c} - 1)^{-p}$, with the critical temperature T_c. The fit yields a critical temperature of $T_\mathrm{c} = 0.15\,\mathrm{K}$ and a critical exponent $p = 0.77$, closely related to the $T^{-0.75}$ power-law behavior observed in sibling compounds [96, 99]. On the other hand, the behavior can be ascribed to the proximity to a Berezinskii-Kosterlitz-Thouless (BKT) transition. The low-temperature behavior is then described as $\Delta H \propto \exp[3b/((T/T_\mathrm{KT}) - 1)^{0.5}]$, with the Kosterlitz-Thouless (KT) temperature T_KT and $b = \pi/2$ [100]. The fits are visibly indistinguishable and have nearly identical values for χ^2 and R^2. The critical temperatures obtained from the two different models $T_\mathrm{KT} = 0.14\,\mathrm{K}$ and $T_\mathrm{c} = 0.15\,\mathrm{K}$ are nearly identical. However, the description of the low-temperature ESR linewidth with the BKT scenario is a bit uncertain, since its application to another family of triangular antiferromagnets, $A\mathrm{CrO}_2$ (A = H, Li, Na) [101], was challenged in recent years [102]. Further information would be necessary to justify the application of BKT scenario in this case.

6.4 High-Field Magnetization

High-field magnetization measurements are performed at the HLD to determine the temperature-independent van Vleck contribution. Since Yb^{3+} is a Kramers ion its $J = \frac{7}{2}$ multiplet is split into four doublets by the CEF, creating the effective pseudospin-$\frac{1}{2}$ ground state. At low temperatures the magnetism of $KYbO_2$ is dominated by this pseudospin-$\frac{1}{2}$ ground state, but the influence of higher lying CEF level needs to be considered in the form of the van Vleck contribution. In magnetization measurements the van Vleck contribution becomes visible as a linear increase above the saturation field, see Fig. 6.3(a). Therefore a simple linear fit in the saturated field region can be used to determine the van Vleck contribution. For $KYbO_2$ this fit was applied

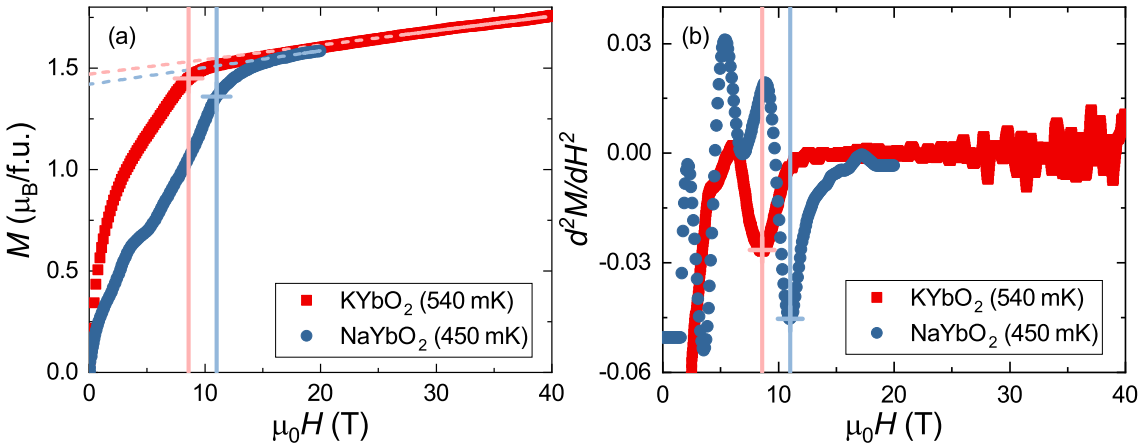

Figure 6.3: *(a) High-field magnetization of $KYbO_2$ and $NaYbO_2$ measured up to 40 T at 0.54 K and up to 20 T at 0.45 K, respectively. The increase above the saturation magnetization is fitted linearly to determine the van Vleck contribution. For $NaYbO_2$ the high-field magnetization data was taken from Ref. [80]. (b) Second derivative of $M(H)$ used to determine the saturation fields.*

between 27 and 40 T yielding $\chi_{\mathrm{vv}} = 0.00715\,\mu_{\mathrm{B}}/\mathrm{T} = 0.00399\,\frac{\mathrm{emu}}{\mathrm{mol}}$. A slightly larger van Vleck contribution is found for $NaYbO_2$ ($\chi_{\mathrm{vv}} \approx 0.0056\,\frac{\mathrm{emu}}{\mathrm{mol}}$) [80, 84]. By correcting the magnetization for the van Vleck contribution a saturation magnetization of $1.47\,\mu_{\mathrm{B}}$/f.u. is obtained, comparable to the saturation magnetization calculated from the ESR g-value: $M_{\mathrm{sat,ESR}} = g\,S = 1.54\,\mu_{\mathrm{B}}$/f.u., $S = \frac{1}{2}$.

In Fig. 6.3 the magnetization of $KYbO_2$ is directly compared to $NaYbO_2$ using data from Ref. [80]. The high-field magnetization measurement of $NaYbO_2$ was fitted to the low-temperature MPMS magnetization measurement performed as part of this work, in the same way that the high-field magnetization was scaled for $KYbO_2$, resulting in a much lower saturation magnetization $M_{\mathrm{sat}} = 1.36\,\mu_{\mathrm{B}}$ compared to Ref. [80]. This value is in perfect agreement with the ones determined in other studies [84, 85], suggesting the scaling of the high-field data in Ref. [80] might be off.

The saturation field is determined via the respective minimum in the second derivative of $M(H)$ as shown in Fig. 6.3(b). As is already obvious from the $M(H)$ measurement, $KYbO_2$ reaches saturation at about 9 T, slightly before $NaYbO_2$ at about 11 T.

In contrast to $NaYbO_2$, no plateau feature is observed in the high-field measurement of $KYbO_2$.

6.5 Susceptibility

The susceptibility of $KYbO_2$ measured between 2 and 300 K shows the behavior typical for the $AYbX_2$ family, with a linear behavior at high temperatures that evolves into a gradual change of slope below 150 K, as depicted in Fig. 6.4(a). The

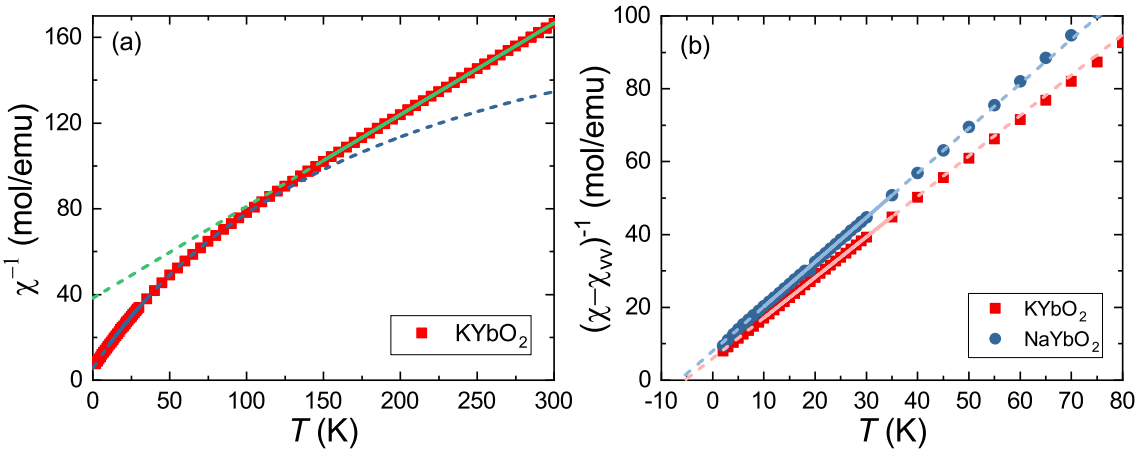

Figure 6.4: *(a) Measurement of the susceptibility and inverse susceptibility of* $KYbO_2$ *between 2 and 300 K at 1 T. Between 150 and 300 K a linear Curie-Weiss fit was applied (green line). At lower temperatures the data is fitted with the modified Curie-Weiss law between 10 and 35 K (b) Inverse susceptibility of* $KYbO_2$ *and* $NaYbO_2$ *after correction for the van Vleck contribution. A linear behavior is observed and fitted with the Curie-Weiss law. Adapted from Ref. [12].*

high-temperature behavior above 150 K was previously reported [11,93], therefore the analysis here focuses on the low temperatures behavior that reflects the magnetism of the pseudospin-$\frac{1}{2}$ ground state.

To investigate the low-temperature behavior one needs to consider the influence of the van Vleck contribution. This can be done in two ways. On one hand the low-temperature part of the susceptibility can be fitted with the modified Curie-Weiss law (Eq. 2.18), as was done in Ref. [11]. On the other hand, the van Vleck contribution determined from the high-field magnetization measurements can be subtracted, yielding a linear behavior between 10 and 50 K [see Fig. 6.4(b)]. In Tab. 6.4 the results of the fits for $KYbO_2$ are given and compared to those of $NaYbO_2$. For $KYbO_2$ rather similar Curie-Weiss temperatures and effective moments are obtained with the two different methods. The van Vleck susceptibility determined from the high-field magnetization measurement is a bit smaller compared to the fit with the modified Curie-Weiss law. The negative value of the Curie-Weiss temperatures corresponds to antiferromagnetic interactions and the effective magnetic moment $\mu_{\text{eff}}^{\text{LT}} = 2.68\,\mu_{\text{B}}$ is in excellent agreement with the one calculated from ESR g-value $g = 3.08$: $\mu_{\text{eff}}^{\text{ESR}} = g\sqrt{S(S+1)} = 2.67\,\mu_B$, with $S = \frac{1}{2}$.

Compared to $NaYbO_2$, the slope of $(\chi - \chi_{\text{vv}})^{-1}$ of $KYbO_2$ is less steep, as can be clearly seen in Fig. 6.4(b). Since the g-value of $KYbO_2$ ($g = 3.08$) is larger than the powder-averaged g-factor of $NaYbO_2$ ($g_{\text{av}} = 2.86$) $KYbO_2$ also has a higher effective moment resulting in a less steep slope.

The Curie-Weiss temperatures are useful to evaluate the strength of the magnetic interactions. The absolute value of the Curie-Weiss temperature is larger for $NaYbO_2$

Table 6.4: *Results of the low-temperature analysis of the susceptibility for $KYbO_2$ and $NaYbO_2$. (a) Susceptibility between 10 and 35 K was fitted with the modified Curie-Weiss law. (b), (c) Van Vleck contribution determined from the high-field magnetization was subtracted from the susceptibility and a linear fit was applied to the corrected measurements. The corresponding van Vleck contributions are the ones determined from the magnetization measurements.*

	(a) $KYbO_2$ [11]	**(b) $KYbO_2$**	**(c) $NaYbO_2$**
χ_{vv} ($\frac{emu}{mol}$)	0.00457(11)	0.00399(1)	0.00564(6) [80]
θ_{LT} (K)	−5.0(1)	−5.4(2)	−6.4(6)
μ_{eff}^{LT} (μ_B)	2.64(3)	2.68(6)	2.56(6)

than for $KYbO_2$ indicating stronger interactions in the former compound. This is further validated by the higher saturation field of $NaYbO_2$ (11 T) compared to $KYbO_2$ (9 T). Since the magnetic interactions are weaker in $KYbO_2$ a smaller magnetic field is sufficient to overcome these interactions and align the magnetic moments. An explanation for the decline of the interaction strength is found in the structural changes observed in the SXRD measurements when substituting Na by K, namely the increase of the Yb-O-Yb angle. Since the magnetic interactions are mediated via this angle, the change has a direct influence on the interaction strength.

6.6 Low-Temperature Magnetization

At temperatures below 0.7 K a plateau feature is observed in the magnetization measurements of $KYbO_2$, see Fig. 6.5. To determine the field range of the plateau the second field derivative of $M(H)$ is calculated where the beginning and end of the plateau are indicated by a minimum and maximum, respectively. As mentioned before no magnetization plateau is observed in the high-field magnetization measurement, although the data is obtained at 0.54 K. In the MPMS data the plateau feature is already clearly observed at this temperature. Reasons for the absence of the plateau feature in the high-field measurements might be a slight sample heating caused by the very short magnetic pulse or the extended exposure to air moisture that was unavoidable during the sample mounting. In contrast to sibling compounds like $AYbSe_2$ (A = Na, K, Rb, Cs) in which such a magnetization plateau was observed on single crystals for magnetic fields applied in the *ab*-plane, the plateau in $KYbO_2$ is not centered at $\frac{1}{3}$ of the saturation magnetization [103, 104]. The plateau in $KYbO_2$ is formed at about 0.7 μ_B/f.u. which is close to $\frac{1}{2}$ of the saturation value (M_{sat} = 1.47 μ_B/f.u.). While the $\frac{1}{3}$ plateau is confirmed via neutron scattering experiments in applied magnetic fields to correspond to an up-up-down (*uud*) ordered phase [79, 89], the $\frac{1}{2}$ plateau would indicate the formation of a up-up-up-down (*uuud*)

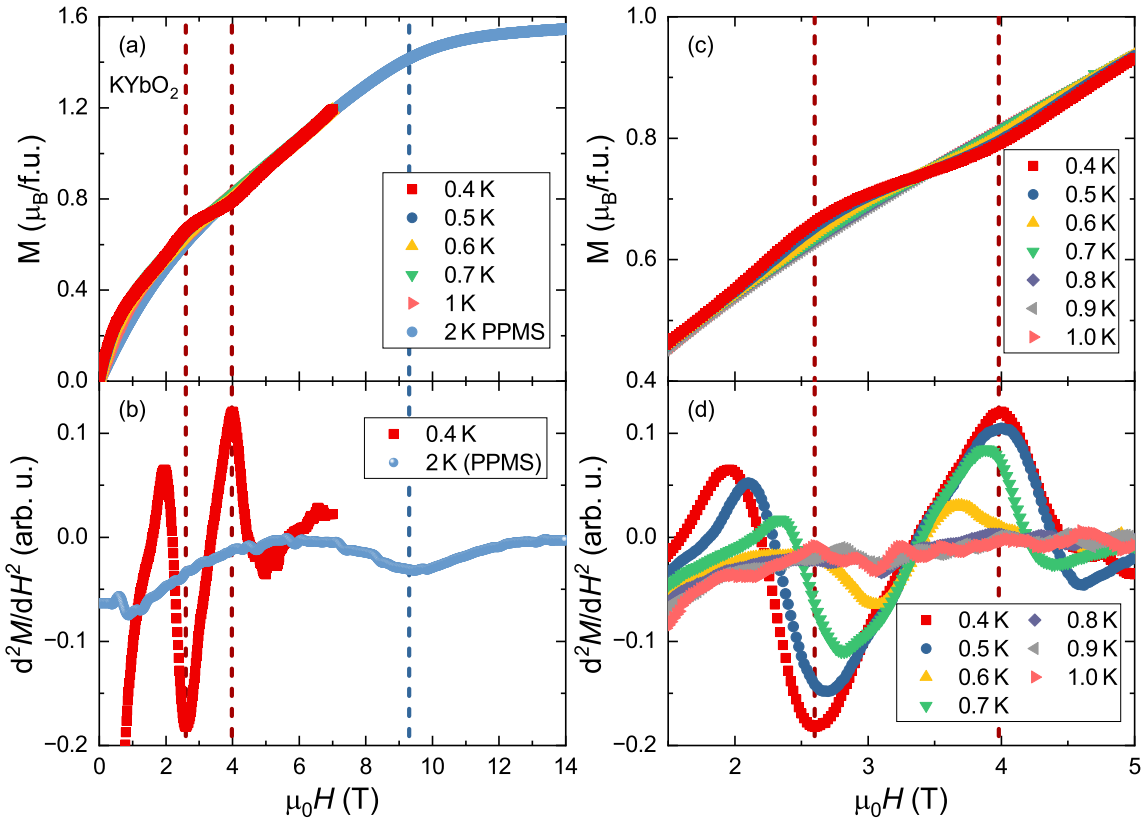

Figure 6.5: *(a) Comparison of the magnetization measured up to 7 T with the MPMS (at 0.4 to 1 K) and up to 14 T with PPMS VSM option (at 2 K). A plateau at about half the saturation magnetization is observed for low temperatures (≤ 0.7 K). (b) Second derivative of $M(H)$ at 0.4 K (MPMS) and 2 K (PPMS). Beginning and end of the plateau region as well as the onset of saturation can be determined from the respective minima and maxima. (c) Magnetization plateau for multiple temperatures. With increasing temperature the plateau becomes less distinct. (d) Second derivative of $M(H)$ in the plateau region. The fading of the plateau is reflected in the less pronounced minma and maxima with increasing temperature. Adapted from Ref. [12].*

ordered phase, which is supported by the isotropic nature of the Yb^{3+} moments. The plateau feature weakens with increasing temperature. The smearing out of the plateau can also be well observed in the second field derivative of $M(H)$, where the maxima and minma indicating the beginning and end of the plateau become less pronounced with increasing temperature. A narrowing of the field range of the plateau becomes apparent from $\mathrm{d}^2M/\mathrm{d}H^2$, as well. Above 0.7 K no clear extrema are discernible anymore suggesting the breaking down of the *uuud* ordered state.

Low-temperature susceptibility measured in various applied magnetic fields reveals further evidence of field-induced magnetic order in $KYbO_2$. A kink in the susceptibility is observed at the transition to the magnetically ordered phase as shown in Fig. 6.6(a). The kink changes curvature between 3.25 and 3.5 T. At lower fields the susceptibility

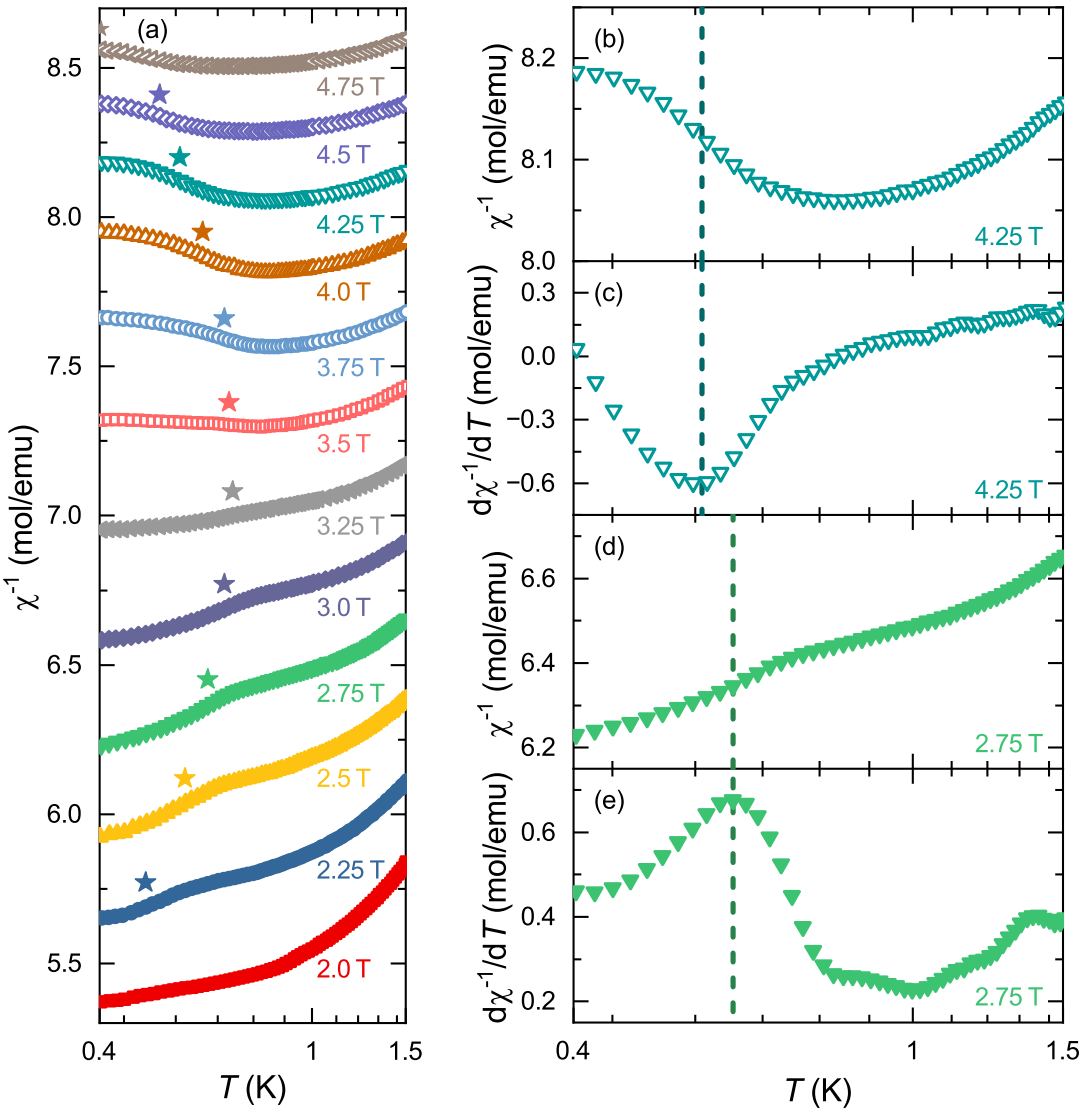

Figure 6.6: *(a) Inverse susceptibility of $KYbO_2$ measured between 0.4 and 1.8 K under various applied magnetic fields. The temperatures of the magnetic phase transitions are marked with stars. (b)-(e) Examples for the determination of the transition temperature from the minimum or maximum of the first derivative of $\chi^{-1}(T)$ at 4.25 T and 2.75 T. Adapted from Ref. [12].*

follows a downward curvature and above 3.5 T an upward curvature is observed. As described in Chapter 5.2, the transition to the magnetically ordered phase is located at the inflection point, that coincides with a maximum or minimum in the first derivative of $\chi^{-1}(T)$. Therefore the temperature derivative of $\chi^{-1}(T)$ is used to determine the exact position of the transition temperature. The correlation between the inflection point in $\chi^{-1}(T)$ and the extrema in $\mathrm{d}\chi^{-1}/\mathrm{d}T$ can be nicely observed in Fig. 6.6(b). In contrast to $NaYbO_2$, the maxima and minima are more unambiguously identified and no additional features are observed up to 5 T. The first transition is observed at 0.49 K in an applied field of 2.25 T and subsequently shifted to higher temperatures with increasing magnetic field until it reaches 0.71 K at 3.25 T. For higher applied magnetic fields the transition temperatures decreases. Above 4.75 K the kink is shifted below 0.4 K the minimum temperature available for the measurement.

6.7 Specific Heat Measurements

The magnetic order observed in the low-temperature, field-dependent magnetization and susceptibility measurements can be further investigated by measurements of the specific heat. Those measurements were performed with the ^{3}He refrigerator insert of the PPMS to achieve temperatures below 0.8 K necessary to observe the magnetic order. In zero applied magnetic field no magnetic order intrinsic to $KYbO_2$ is observed down to the lowest measured temperature of 0.5 K [see Fig. 6.7(a)]. However, a small anomaly at 2.3 K is present in the measurement. The temperature of this small peak is too high to be connected to the *uuud* order indicated by the $M(H)$ measurements, however, it is in good agreement with the magnetic ordering transition temperature of the Yb_2O_3 impurity phase [105]. The peak is only observed in 0 T and suppressed in applied magnetic fields. The broad maximum observed in heat capacity measurements of all members of the $A\mathrm{Yb}X_2$ compound family at low temperatures is also present in $KYbO_2$ and indicates the development of short-range interactions. By applying magnetic fields a shift of the broad maximum to higher temperatures is observed. Magnetic order is first observed for 2.5 T at slightly above 0.5 K. The λ-shaped peak is shifted to higher temperatures with increasing magnetic field up to 3 T [see Fig. 6.7(b),(c)]. Above 3 T the ordering peak is shifted to lower temperatures again and disappears below the measurement range in an applied field of 5 T. These observations are in good agreement with the low-temperature susceptibility measurements.

The specific heat of $NaYbO_2$ reveals a similar behavior to $KYbO_2$ with no magnetic order observed in zero field and a first indication of field-induced magnetic order appearing at 2 T. The ordering peak becomes more pronounced with increasing magnetic field and shifts to higher temperatures up to 5 T, then is shifted to lower temperatures again with further increasing magnetic field. In contrast to $KYbO_2$ an additional shoulder is observed for $NaYbO_2$ at high magnetic fields (6-8 T) that might indicate another magnetic transition as was suggested in Ref. [84] where the anomaly is observed in the form of a second, smaller peak.

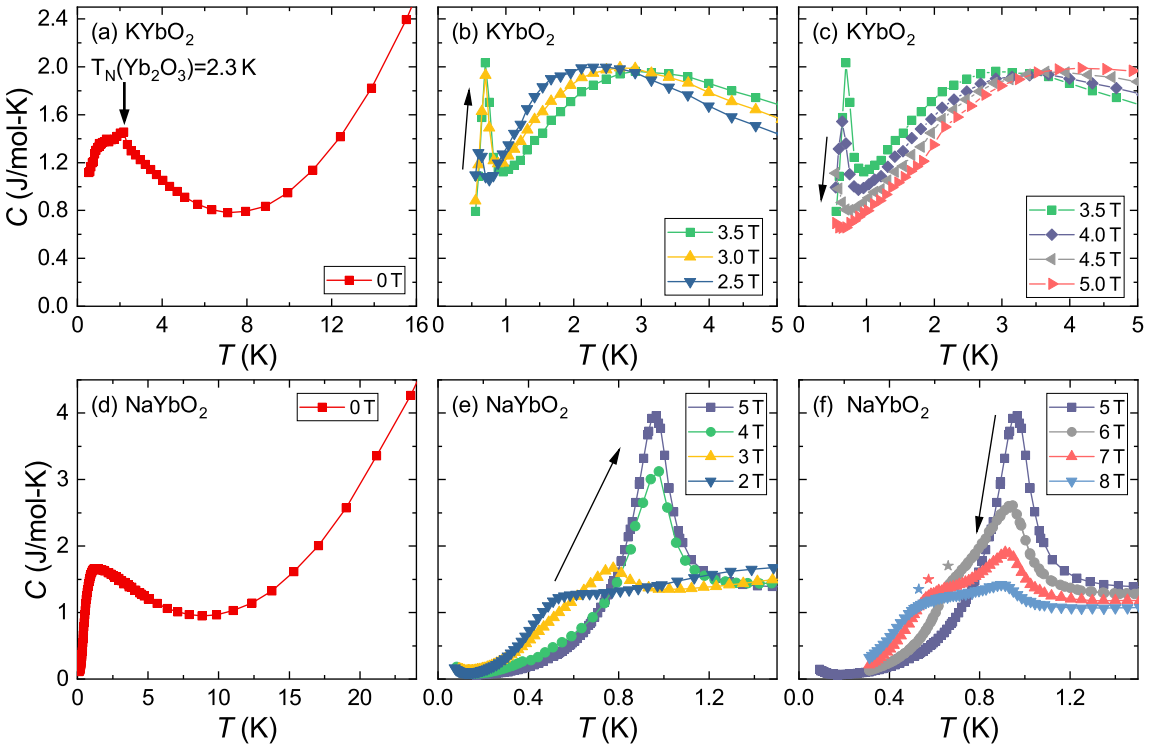

Figure 6.7: *Specific heat of $KYbO_2$ (a)-(c) and $NaYbO_2$ (d)-(f) in zero field and applied magnetic fields [12].*

6.8 Phase Diagram

The field-temperature phase diagram of $KYbO_2$ is composed by taking into account all anomalies and phase transitions observed in magnetization, susceptibility and specific heat measurements described previously. In the same way the phase diagram of $NaYbO_2$ is deduced for comparison. A side-by-side depiction is shown in Fig. 6.8 highlighting the changes introduced by the substitution of K by Na.

In general, the layout of the phase diagrams of $NaYbO_2$ and $KYbO_2$ are very similar. Both compounds show a field-induced magnetically ordered phase, that is divided into different parts. Starting from low fields a small region of an ordered phase preceding the plateau phase is indicated by the peaks in specific heat and low-temperature susceptibility measurements. In the single crystalline sister compounds this phase was ascribed to a 120° ordered phase [103]. At slightly higher magnetic fields, the plateau phase is identified from the field-dependent magnetization measurements. Above the plateau phase magnetic order is still observed in susceptibility and heat capacity measurements. For $NaYbO_2$ this phase can be traced up to 9 T, while for $KYbO_2$ it is only hinted at before the anomalies disappear below the respective measurement range. This phase is most likely a noncollinear V-type phase. Although no direct evidence of this V-type phase has been provided in $AYbX_2$ compounds, a similar phase has been observed and identified in Co-based triangular antiferromagnets [106].

Additionally, the V-type phase is predicted by theory [107, 108]. In this part of the magnetically ordered phase the only significant difference between the phase diagrams is located. In the low-temperature susceptibility as well as the specific heat a second ordering peak is observed for $NaYbO_2$. This leads to the additional area in the V-type phase of $NaYbO_2$. The high-field magnetization measurements provide the saturation field that restricts the magnetically ordered phase and marks the beginning of the fully polarized region. At low temperatures and low magnetic fields no magnetic order is observed, therefore this region potentially hosts a quantum spin-liquid phase.

Aside from the additional phase observed in $NaYbO_2$ the differences between the two phase diagrams are more subtle. Overall, a shift of all phases to lower fields is observed when substituting Na by K. While magnetic order is first observed around 2 T for both compounds, the onset of the *uuud* phase is located at lower fields for $KYbO_2$. In addition, the field range of the plateau phase is more narrow compared to $NaYbO_2$ ($\Delta H = 0.5\,\mathrm{K}$). As mentioned before, a rather large margin of the saturation magnetization is determined for $NaYbO_2$, allowing for a $M_{\mathrm{sat}}/2$ as well as $M_{\mathrm{sat}}/3$ plateau interpretation, expected for the *uud* state. In contrast, the plateau in $KYbO_2$ is rather unambiguously located at $M_{\mathrm{sat}}/2$ indicating the formation of a *uuud* phase. The assumed V-type phase has a similar field range for both compounds. Finally, $KYbO_2$ enters the fully polarized phase at a lower magnetic field than $NaYbO_2$. The differences between $NaYbO_2$ and $KYbO_2$ are in line with the observation of weakening magnetic interactions observed in $KYbO_2$, indicated by the smaller absolute value of $\theta_{\mathrm{CW}}^{\mathrm{LT}}$ compared to $NaYbO_2$.

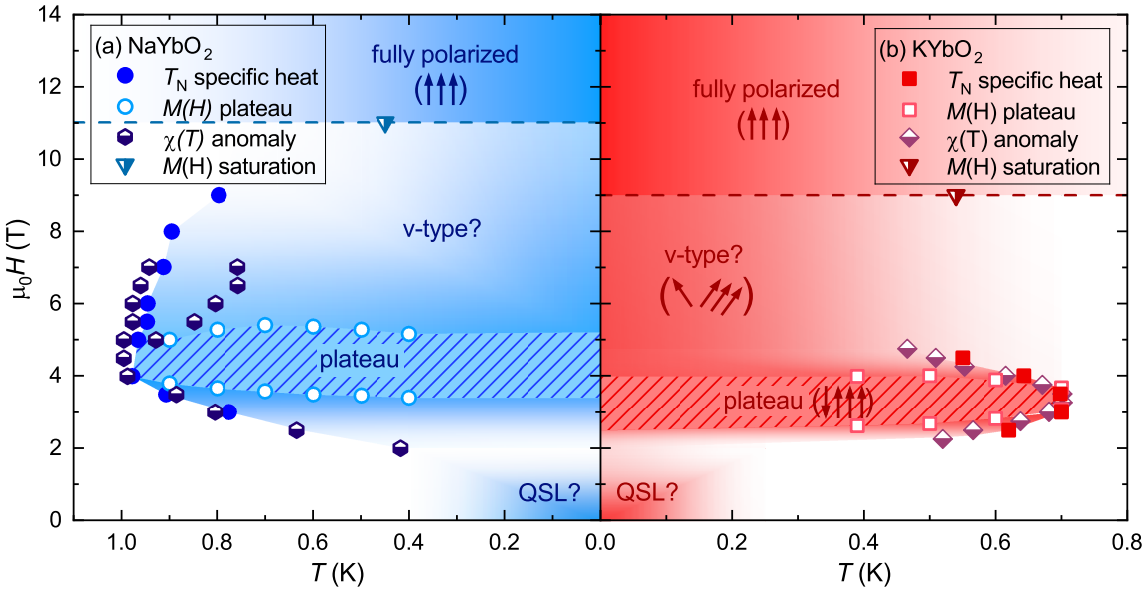

Figure 6.8: *Direct comparison of the phase diagrams of $NaYbO_2$ (a) and $KYbO_2$ (b). Both compounds show field induced magnetic order but no signs of magnetic order are observed for small applied magnetic fields. Adapted from Ref. [12].*

7 $KYbS_2$

Although the investigation of $NaYbO_2$ and $KYbO_2$ offers many insights into the physics of the $AYbX_2$ family, the polycrystalline nature of those compounds presents a limitation. Fortunately, with exception of the oxides, several members of the $AYbX_2$ compounds are available in single crystalline form. Most of these materials have been extensively studied by other groups as my PhD work developed. $KYbS_2$ received less attention so far, although small single crystals were synthesized for the first time in 2020 and the performed standard measurements indicate that $KYbS_2$ is a promising candidate for further investigation [109]. In this chapter, detailed insights into the improvement of the crystal growth are provided. The crystals are investigated using SXRD, ESR, magnetization and susceptibility measurements to determine a detailed phase diagram. The absence of magnetic order in zero field is confirmed by specific heat measurements down to 0.4 K.

7.1 Literature Results

Synthesis and standard measurements of $KYbS_2$ were first published by Iizuka *et al.* [109] in 2020. They succeeded in growing small single crystals (approximately $0.5 \times 0.5 \times 0.01\,\mathrm{mm}^3$) using a self-flux method. The $KYbS_2$ crystals were investigated using single-crystal XRD, magnetization and heat capacity measurements. All relevant results and characteristic properties are summarized in Tab. 7.1.

Single crystal XRD confirmed that $KYbS_2$ crystallizes in the $R\bar{3}m$ space group.

Susceptibility was measured in an applied field of 0.1 T for both field directions, $H \perp c$ and $H \parallel c$, between 1.9 and 300 K and displays no signs of magnetic order. For $H \perp c$ the susceptibility behaves similarly to the polycrystalline compounds $NaYbO_2$ and $KYbO_2$ discussed before. A linear behavior was observed at high temperatures and a Curie-Weiss temperature of $\theta_{\mathrm{HT},\perp} = -91.8\,\mathrm{K}$ and an effective magnetic moment of $\mu_{\mathrm{eff}} = 4.54\,\mu_{\mathrm{B}}$ by a linear fit. An analogue analysis at high temperatures for $H \parallel c$ was not possible due to the non-linear behavior which was ascribed to the influence of the CEF. The low-temperature behavior of the susceptibility for both field directions was fitted with the modified Curie-Weiss law (Eq. 2.18) which takes the van Vleck contribution into account and yielded a more realistic estimate for the Curie-Weiss temperature and the effective moment at low temperatures (see Tab. 7.1). The negative Curie-Weiss temperatures indicate predominantly antiferromagnetic interactions and the difference between $H \perp c$ and $H \parallel c$ hints at the anisotropic nature of the exchange interactions.

Table 7.1: *Characteristic properties of $KYbS_2$ from Ref. [109]. The high-temperature (HT) susceptibility is fitted with the standard Curie-Weiss law and the susceptibility at low temperatures (LT) with the modified Curie-Weiss law.*

XRD			**Susceptibility (HT)**		
lattice parameter				$\boldsymbol{\theta_{\mathrm{CW}}}$ **(K)**	$\boldsymbol{\mu_{\mathrm{eff}}}$ **(μ_{B})**
$a = 3.9415(3)$ Å	$c = 21.748(2)$ Å		$\boldsymbol{H \perp c}$	-91.9	4.54

Susceptibility (LT)						
	$\boldsymbol{\theta_{\mathrm{CW}}}$ **(K)**	$\boldsymbol{\chi_{\mathrm{vv}}}$ $\left(\frac{\mathbf{emu}}{\mathbf{mol}}\right)$	$\boldsymbol{\mu_{\mathrm{eff}}}$ **(μ_{B})**	$\boldsymbol{g}$	$\boldsymbol{g_{av}}$	$\boldsymbol{M_{\mathrm{s}}}$ **(μ_{B})**
$\boldsymbol{H \perp c}$	-12	0.0044	3.16	3.6	3.2	1.83
$\boldsymbol{H \parallel c}$	-5	0.019	1.79	2.07		1.0

Anisotropy is also evidenced in the field-dependent magnetization measurements for $H \perp c$ and $H \parallel c$. Saturation is not reached in the measurements up to 7 T performed in Ref. [109] for both field directions. In fact, after the magnetization was corrected by the van Vleck contribution from the low-temperature fit to the susceptibility, the magnetization only reached half of $M_{\mathrm{s}} = gS$ at 7 T for the respective field directions.

The heat capacity was measured down to 0.4 K and did not display any signs of magnetic order. The characteristic broad maximum featured in all members of the $A\mathrm{Yb}X_2$ is also present in $KYbS_2$, but appears to consist of two peaks rather than a single peak. In Ref. [109] this double peak structure was linked to the 2D spin-$\frac{1}{2}$ Ising-like anisotropic Heisenberg model and a formation of a semi-classical liquid state. To calculate the magnetic specific heat the phonon contribution was fitted with a combination of Debye and Einstein model. With the magnetic specific heat the magnetic entropy can be determined, which was found to exhibit a plateau at $R \ln 2$ around 30 K.

The absence of magnetic order down to at least 0.4 K evidenced by the specific heat measurement allowed the calculation of a minimal frustration parameter $f = |\theta|/T_{\mathrm{N}}$ for both field directions. Since no magnetic order was observed the lowest measured temperature is used for T_{N}: $f_{\perp} \geq 30$ and $f_{\parallel} \geq 12$.

7.2 Synthesis

The synthesis of $KYbS_2$ single crystals is done analogous to Ref. [109]. The reagents are weighed in the ratio KCl : Yb : S = 80 : 2 : 3. The S pieces are ground and mixed with the KCl powder; the Yb metal is cut into small pieces, placed at the bottom of a quartz glass and covered with the KCl-S mixture [see Fig. 7.1(a)]. The ampules are alternately evacuated and filled with argon gas three times, then filled

with approximately 200 mbar argon to ensure an inert gas atmosphere for the reaction. In a box furnace the ampules are heated to 850 °C over four hours, held at that temperature for two weeks and subsequently cooled down to room temperature over 160 h. After the reaction the solidified flux has a green shimmer if the synthesis was successful [left sample in Fig. 7.1(b)] and dark green crystals on the inside of the ampule wall are discernible [see Fig. 7.1(c)]. If the synthesis was not successful the flux inside the ampule has a yellowish color [middle and right sample in Fig. 7.1(b)]. The ampules are broken and the shards are placed in water to dissolve the flux. The crystals are attached to the wall of the ampule and can be easily plucked of after dissolving the flux. In general a vast number of rather small crystals grow in the synthesis with a few larger ones in between [see Fig. 7.1(d)-(g)]. In the first attempts following this procedure a maximum crystal size of 0.6 mm × 0.7 mm was obtained.

To improve the crystal size the synthesis was altered in two directions.
On one hand, the temperature at which the synthesis is performed was varied. Since the synthesis temperature is already quite close to the melting point of Yb (819 °C) decreasing the temperature significantly was not considered. Increasing the temperature to 875 °C and 900 °C still yields a successful synthesis, however compared to the synthesis at 850 °C significantly less crystals grow and they are smaller in size. To verify if the temperature within the furnace matches the set temperature of 850 °C, a thermocouple was inserted to determine the exact temperature where the samples are located in the furnace. This yielded a temperature of 860 °C, therefore the temperature of the synthesis was corrected to 840 °C.
On the other hand, the influence of the holding time at the synthesis temperature on the crystal size was investigated. Shortening the holding time to one week yielded no crystals. Increasing the holding time, however, leads to an overall increase of the crystal size, i.e. more crystals of mediocre size with the occasional crystal larger than $1 \times 1\,\mathrm{mm}^2$, see Fig. 7.1(h). The best results were obtained for extended holding times of up to two months.

When considering these improvements of the crystal growth one needs to keep in mind that, despite ensuring the correct synthesis conditions, many synthesis attempts did not work. This might have various possible reasons, like the change from the originally used Yb-metal to another batch of Yb-metal (most consistent and success results seemed to be achieved by using 99.99% Yb from the MPC of Ames University) or simply switching from one box furnace to another. However, this does not explain why out of two samples, which were prepared the exact same way (same ratio, similar absolute weight of reactants, same batch of starting materials), placed together in the same furnace for the same amount of time, only one sample would contain multiple and large crystals while the other would not contain any crystals. With this in mind, an influence of the size of the quartz glass or changes in the gas atmosphere within the ampule are also considered as potential reasons for the inconsistent synthesis results. Out of 49 synthesis attempts fulfilling the standard requirements of a minimum two week holding time at 840 °C/850 °C only 19 attempts were successful in growing crystals (not considering crystal size). Ten out of the 19 successful attempts contained

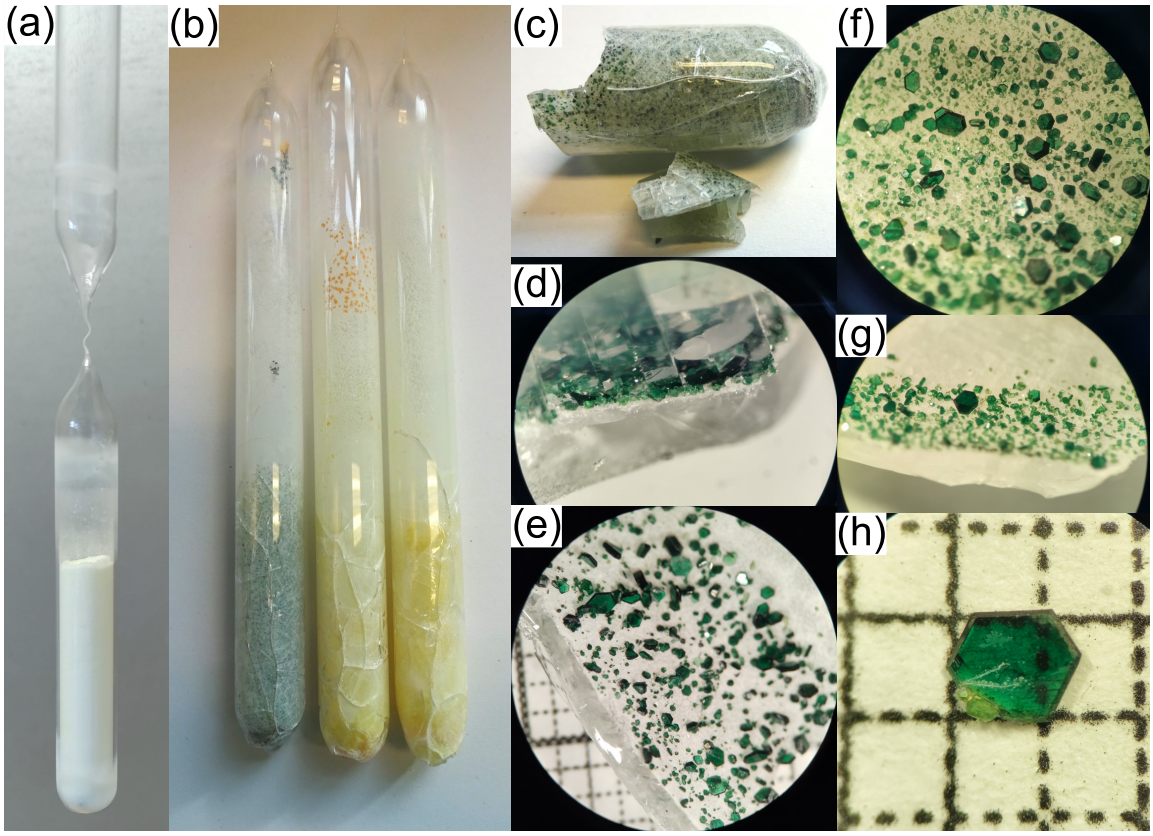

Figure 7.1: *(a) Starting materials for the single crystal synthesis in the quartz glass during evacuation of the ampule. At the top of the ampule a thin neck was fashioned through which the atmosphere is pumped out. After evacuation approximately 200 mbar Argon gas is filled into the ampule. (b) Three samples from the same synthesis attempt (left to right: 19, 23, 20). All samples were prepared in the same way, with the same batch of starting material and were annealed in the same furnace for 50 days. Only for sample 19 the synthesis was successful, as is already externally discernible by the green color of the ampule compared to the yellow colored ampules of samples 23 and 20. (c) Bottom part of sample 19. Small green points on the inside of the ampule are already visible from the outside before removing the flux. (d) Crystals on the wall of the quartz glass under the solidified flux. (e)-(g) Crystals on quartz glass shards after dissolving the flux in water. (h) $KYbS_2$ single crystal on mm-paper as an example for the maximum achieved crystal size. This crystal is from sample 74 that was kept at 840 °C for two month.*

larger crystals, all but one of those ten synthesis attempts had a holding time of at least three weeks. Overall successful synthesis are most likely achieved through consistently using the same furnace, the same temperature profile and, if possible, the same starting materials.

For μSR measurements polycrystalline $KYbS_2$ was synthesized by following the first step of the $KErSe_2$ single crystal synthesis described in Ref. [110]. Single crystals of $KErSe_2$ were prepared in a two-step method where first the polycrystalline material were synthesized and then combined with KCl flux to produce single crystals.
As starting materials K, Yb and S are used with the ratio K : Yb : S = 1.1 : 1 : 2. Due to the high reactivity of K with water, all synthesis preparations have to take place under argon atmosphere. The starting materials are weighed in a glove box and filled into an aluminum crucible or glassy carbon crucible (no difference in the synthesis result was observed when switching the crucible material), see Fig. 7.2(a) and (b). The crucible is placed in a quartz glass ampule. To seal the ampule it has to be taken out of the glove box, therefore a disposable glove is fixed on top of the quartz glass with a cable tie to keep the argon atmosphere in the ampule intact. An oxyhydrogen blowpipe is used for closing the ampule. Since the synthesis is supposed to take place under vacuum one first needs to shape the top of the quartz glass into a thin neck. Then the glove is removed and the ampule is connected to a pump for evacuation. The transition to the pump has to happen fast and precise otherwise the K will react with the air moisture, which, in the worst case, leads to an explosion of the crucible. After evacuation the quartz glass is closed by melting the thin neck. The ampules

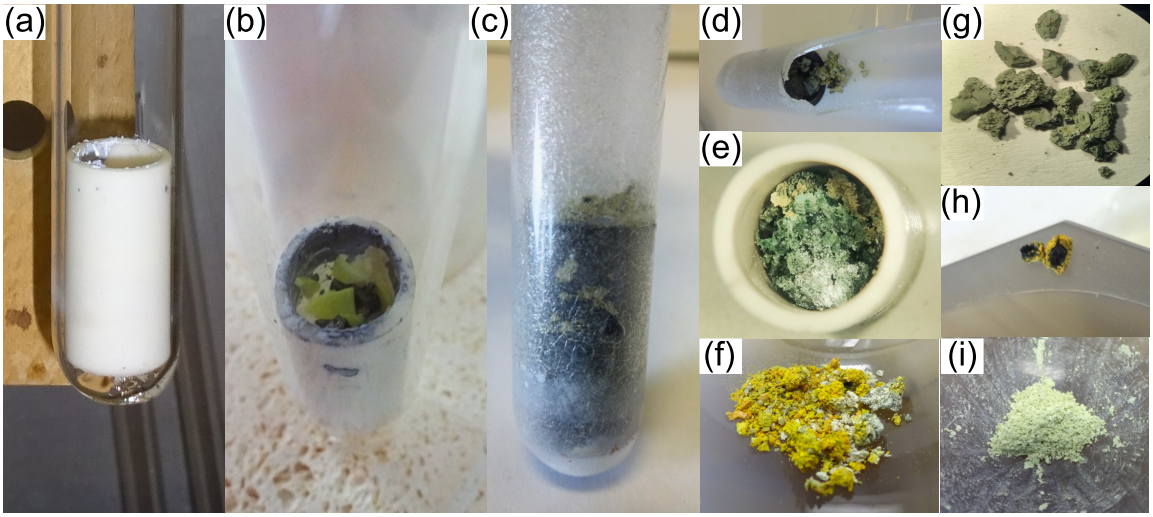

Figure 7.2: *(a),(b) Starting materials for the synthesis of polycrystalline $KYbS_2$ in an aluminum crucible sealed in a quartz glass before the synthesis. (c),(d) After the reaction the inside of the quartz glass is opaque, the (glassy carbon) crucible contains a mixture of different colored granules. (e)-(g) Examples for the results of different syntheses. (h) Larger granules are often black on the inside and are discarded. (g) Light green $KYbS_2$ powder after sorting, grinding and checking via XRD.*

are placed in a box furnace and slowly (10 K/h) heated to 220 °C and kept at this temperature of 24 h to achieve equilibrium. Subsequently, the temperature is raised to 900 °C (10 K/h) and held for three days before cooling down to room temperature over 24 h. After the synthesis the inner wall of the quartz glass is opaque due to a reaction with K. The resulting material is an inhomogeneous mix of green, yellow/orange and white chunks [see Fig. 7.2(e)-(g)]. The material is sorted by color and ground in small batches for XRD measurements. The obtained polycrystalline $KYbS_2$ is of light green color as shown in Fig. 7.2(i). Before the μSR measurement the polycrystalline powder is additional susceptibility measurements are performed to confirm its quality and exclude the presence of foreign phases.

7.3 Synchrotron XRD

For investigation of the structural properties of $KYbS_2$, synchrotron XRD measurements were performed by Alexander Tsirlin on powdered single crystals at the ID22 beamline at the ESRF in Grenoble with a wavelength of $\lambda = 0.35432$ Å. Measurements were carried out at 250 K and 5 K to exclude the possibility of structural changes at low temperatures. Indeed, no signs of a structural transition are observed when cooling down. The low-temperature measurement was contaminated with ice, due to technical difficulties during the measurement. Therefore only the higher temperature measurement was analyzed via Rietveld refinement. The result of the refinement and the measured spectrum is shown in Fig. 7.3.

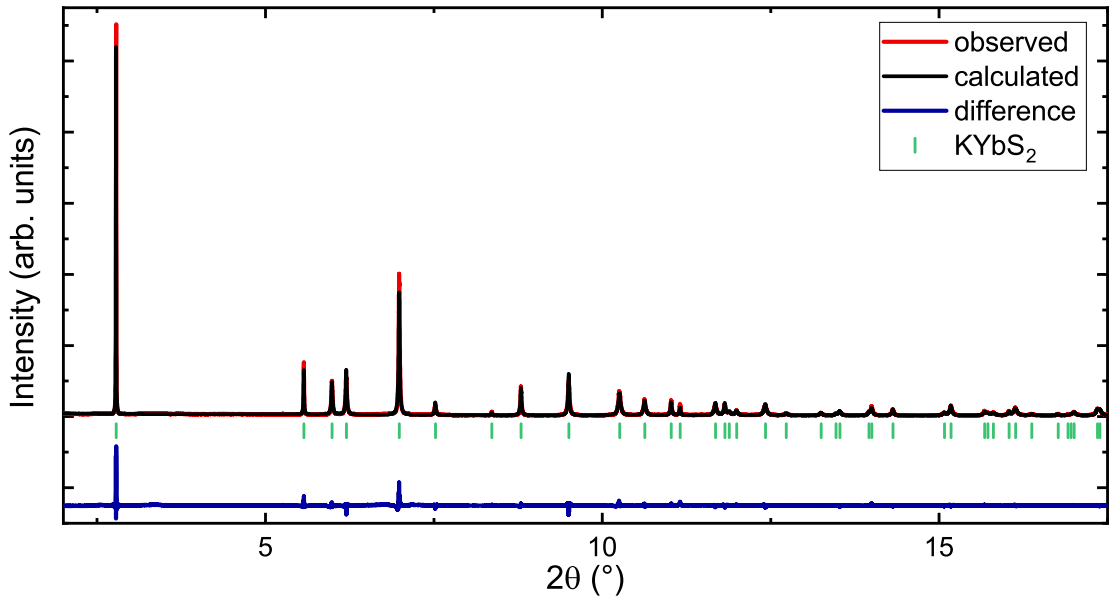

Figure 7.3: *SXRD measurement of $KYbS_2$ (red line). The measured spectrum is fitted with a Rietveld refinement (black line). The blue line shows the difference between calculated an measured data and the green strokes mark the position of the reflexes of $KYbS_2$.*

Table 7.2: *Atomic displacement parameters (U_{iso}) and positions as well as lattice parameters, characteristic distances and Yb-S-Yb angle of $KYbS_2$ determined from the Rietveld structure refinement of the SXRD measurement at 250 K.*

atom	***x/a***	***y/b***	***z/c***	**U_{iso} (Å²)**
S	0	0	0.23255(8)	0.008(5)
Yb	0	0	0.5	0.007(2)
K	0	0	0	0.0151(7)

a	***c***	**Yb–S dist.**	**K–Yb dist.**	**∡ Yb–S–Yb**
3.96369(3)	21.8711(2)	2.7043(9)	4.30398(6)	94.2499(6)°

The $R\bar{3}m$ space group is confirmed for $KYbS_2$. Narrow peaks indicate high crystallinity of the sample and no impurity phases are observed in the spectrum. Although the crystals were ground thoroughly with ethanol for the experiment the overestimation of the $(00l)$ intensities could not be prevented, a feature commonly observed in XRD measurements of the $AYbX_2$ compound family. The Rietveld analysis returned satisfactorily low ADPs (U_{iso}) excluding the presence of the off-center displacements in $KYbS_2$. Results of the structure refinement, including ADPs, are given in Tab. 7.2.

7.4 ESR Measurements

ESR measurements on $KYbS_2$ single crystals were performed to investigate the local magnetism of the Yb^{3+} ions. The measurements were carried out and analyzed by Hans-Albrecht Krug von Nidda and Mamoun Hemmida. ESR g-values are obtained by fitting the angular dependence of the g-value with $g(\theta) = g_{\parallel}^2 \cos^2(\theta) + g_{\perp}^2 \sin^2(\theta)$, as shown in Fig. 7.4(a). The g-values reflect the large anisotropy already obvious when looking at the measurement of the angular dependence, with a much larger $g_{\perp} = 3.24(1)$ compared to the parallel component $g_{\parallel} = 0.80(2)$. The field derivative of a single Lorentzian is sufficient to describe the field derivative of the Yb ESR lines for both field directions ($H \perp c$ and $H \parallel c$), see insets in Fig. 7.4(a).
The ESR g-values can be used to calculate the saturation magnetization via $M_{sat} = gS$, with $S = \frac{1}{2}$, and the effective magnetic moment via $\mu_{eff} = g\sqrt{S(S+1)}$. This results in a saturation magnetization of $M_{sat}^{\perp} = 1.62\,\mu_B$ for $H \perp c$ and $M_{sat}^{\parallel} = 0.35\,\mu_B$ for $H \parallel c$. The effective magnetic moments for $H \perp c$ are determined as $\mu_{eff}^{\perp} = 2.81\,\mu_B$ and for $H \parallel c$ as $\mu_{eff}^{\parallel} = 0.69\,\mu_B$. $KYbS_2$ therefore exhibits a much stronger anisotropy compared to $NaYbO_2$, suggesting a distinctly different macroscopic regime.

By analyzing the intensity of the ESR line, which is directly proportional to the the magnetic susceptibility, further magnetic properties of $KYbS_2$ can be deduced,

see Fig. 7.4(b). The inverse susceptibility for $H \perp c$, shown in the inset of Fig. 7.4(b), is fitted linearly at low temperatures and gives a Curie-Weiss temperature of $\theta_{\mathrm{LT}}^{\mathrm{ESR}} = -12\,\mathrm{K}$.

By fitting the high-temperature part of the ESR linewidth with an Orbach process the energy gap between the ground state Kramers doublet and the first excited doublet can be determined. To analyze the temperature dependence of the ESR linewidth over the whole measured temperature spectrum, the Orbach fit is combined with two different models describing the low-temperature part, as was done for $KYbO_2$. In Fig. 7.4(c) the BKT model is applied to fit the low-temperature ESR linewidth, while in Fig. 7.4(d) the classical critical behavior in the vicinity of a phase transition is assumed to describe the ESR linewidth at lower temperatures.

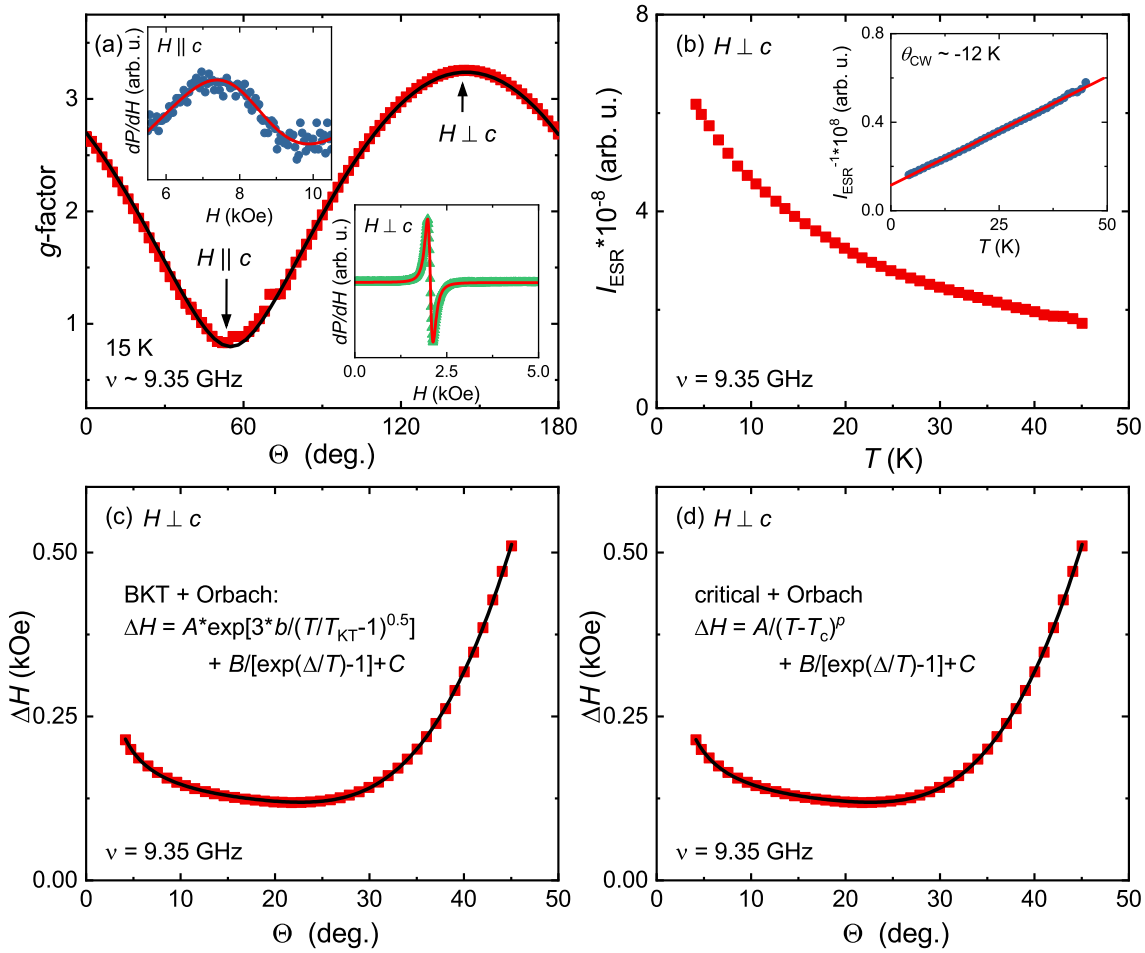

Figure 7.4: *(a) Angular dependence of the g-value. The insets show the field derivative of the ESR lines for $H \perp c$ and $H \parallel c$ fitted with the field derivative of a single Lorentzian line. (b) ESR intensity of $KYbS_2$ proportional to the magnetic susceptibility; the inverse intensity is shown in the inset. (c),(d) Temperature dependence of the ESR linewidth fitted with two different models (see text for details).*

For both fitting models the same value for the energy gap of 232 K is retrieved, which is a smaller compared to $KYbO_2$ and $NaYbO_2$ ($\Delta = 350\,\mathrm{K}$). Since S^{2-} is less electronegative than O^{2-} a smaller CEF is expected. Nevertheless, the sizable value of Δ supports the effective spin-$\frac{1}{2}$ ground state assumed for the $A\mathrm{Yb}X_2$ compounds. Concerning the low-temperature part, two very similar critical temperatures are obtained, $T_{\mathrm{KT}} = 0.20\,\mathrm{K}$ and $T_{\mathrm{c}} = 0.13\,\mathrm{K}$. Although, visually both fits describe the data equally good, only four fitting parameters are necessary to describe the data in the case of the BKT scenario, while a comparable fit quality for the critical behavior is only achieved when using six fitting parameters. This slight advantage of the BKT scenario is naturally no unambiguous proof for the applicability of the BKT theory to the $A\mathrm{Yb}X_2$ family, as previously discussed for $KYbO_2$. The critical exponent $p = 0.85$ determined from the fit with the critical behavior is a bit larger but still comparable to $KYbO_2$ and similar compounds investigated in Ref. [96, 99].

7.5 High-Field Magnetization

The high-field magnetization of $KYbS_2$ was measured to determine the saturation field and magnetization as well as the van Vleck contribution. The measurements up to 30 T were performed at 0.55 K at the HLD in collaboration with Yurii Skourski (HZDR). For $H \perp c$ two characteristic features are observed in Fig. 7.5(a): a magnetization plateau around 4 T and a kink at about 10 T. The second field derivative of $M(H)$ is calculated to determine the exact field position of the features [see Fig. 7.5(b)]. Compared to the measurement on $KYbO_2$, in which no plateau feature is observed in the high-field measurement, the plateau is clearly visible between 3.1 and 5 T in the single crystal measurement of $KYbS_2$, although it is not as distinct as in the MPMS measurement. Since the magnetization plateau is well in the range of the MPMS measurements it is investigated in detail with the ^{3}He refrigerator option (see Chapter 7.7).

The kink at higher fields indicates the transition to the fully polarized state. From the second field derivative a saturation field of $H_{\mathrm{sat}} = 10.3\,\mathrm{T}$ is determined. Above the saturation field, $M(H)$ increases linearly due to the van Vleck paramagnetism. The van Vleck contribution and the saturation magnetization are obtained by linearly fitting the high-field magnetization between 14.6 and 29 T. This yields a van Vleck contribution of $\chi_{\mathrm{vv}} = 0.0126\,\frac{\mathrm{emu}}{\mathrm{mol}}$. For single crystalline $NaYbSe_2$ the van Vleck contribution was determined in a similar manner but yielded a significantly smaller van Vleck term $\chi_{\mathrm{vv}} = 0.00765\,\frac{\mathrm{emu}}{\mathrm{mol}}$ [103]. For $KYbO_2$ and $NaYbO_2$ much smaller van Vleck contributions are obtained as well. Furthermore, the saturation magnetization determined from high-field $M(H)$ measurements after subtracting the van Vleck term $M_{\mathrm{sat}}^{\perp} = 1.4\,\mu_{\mathrm{B}}$ is smaller than the one calculated from the ESR g-value ($1.6\,\mu_{\mathrm{B}}$).

In the case of $H \parallel c$, also shown in Fig. 7.5, the magnetization is much lower compared to $H \perp c$ and increases gradually up to at least 30 T without showing signs of saturation or other unusual features. According to ESR measurements a saturation

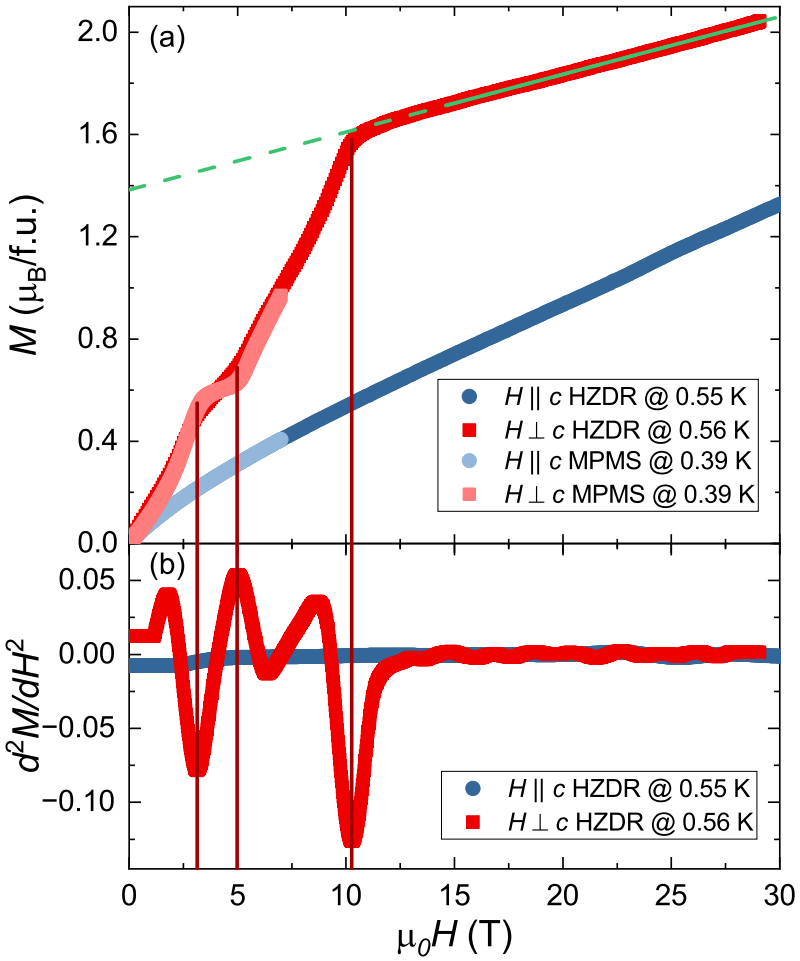

Figure 7.5: *(a) High-field magnetization measurement of $KYbS_2$ for $H \perp c$ (red) and $H \parallel c$ (blue). A linear fit (green line) is applied to the high-field part for $H \perp c$ to determine the van Vleck contribution. (b) Second field derivative of $M(H)$ to determine the confines of the magnetization plateau and the position of the saturation field.*

magnetization of $M_{\mathrm{sat}}^{\parallel} = 0.35\,\mu_{\mathrm{B}}$ is expected for $H \parallel c$, however, this value is exceeded without development of the characteristic change of slope observed for $H \perp c$.

Overall, the high-field measurement is in excellent agreement with the low-temperature measurements performed with the MPMS for both field directions. They confirm the substantial g-tensor anisotropy inferred from the ESR analysis. This anisotropy is so strong that the $H \parallel c$ signal is dominated by the linear term and does not show any clear signatures of saturation. In Ref. [103] a similar behavior of the high-field magnetization was observed for $NaYbSe_2$ and the linearity of the $H \parallel c$ curve is connected to a gradual tilting of the spins out of the ab plane leading to a three-sublattice umbrella-like state.

7.6 Susceptibility

Magnetic susceptibility was measured between 2 and 300 K at a magnetic field of 1 T for both field directions. A markedly different behavior is observed depending on the direction in which the magnetic field is applied, see Fig. 7.6. The inverse susceptibility for $H \parallel c$ shows a distinct change of slope at about 25 K. For $H \perp c$ the inverse susceptibility behaves linearly at high temperatures in accordance with the Curie-Weiss law and deviates from the Curie-Weiss law at lower temperatures. The high-temperature part is therefore fitted with the Curie-Weiss law returning a Curie-Weiss temperature of $\theta_{\mathrm{HT}} = -67(7)\,\mathrm{K}$ and an effective moment of $\mu_{\mathrm{eff}} = 4.72(20)\,\mu_{\mathrm{B}}$. The effective moment is in good agreement with the free electron value for Yb^{3+}, $\mu_{\mathrm{eff}} = 4.54\,\mu_{\mathrm{B}}$. In Ref. [109] a slightly higher Curie-Weiss temperature of $-92\,\mathrm{K}$ was determined from the linear high-temperature behavior.

The Curie-Weiss law, however, yields overestimated values for θ_{CW} in this temperature region and does not accurately reflect the size of the magnetic interactions of the ground state of $KYbS_2$. The reason for this discrepancy is the crystal field splitting, which changes the nature of the electronic state with decreasing temperature and subsequently leads to the change of slope in the susceptibility at low temperatures.
To accurately determine the magnetic properties, the low-temperature susceptibility needs to be investigated. This can be done in two ways: by fitting the low-temperature part with the modified Curie-Weiss law (Eq. 2.18), which takes the van Vleck contribution into account, or by subtracting the van Vleck contribution determined from the high-field magnetization measurement and fitting the corrected susceptibility linearly. It proved to be difficult to apply the latter method to $KYbS_2$, since subtracting the van Vleck contribution yields a linear behavior only over a small temperature region ($T < 17\,\mathrm{K}$), see Fig.7.6(b). At higher temperatures the corrected susceptibility deviates from the linear behavior, indicating that the effect of the excited CEF levels cannot be described by the T-independent term. Nevertheless, the corrected susceptibility was fitted linearly between 2 and 17 K resulting in an effective magnetic moment of $2.83(10)\,\mu_{\mathrm{B}}$, in excellent agreement with the one determined from the ESR measurement ($\mu_{\mathrm{eff}}^{\mathrm{ESR}} = 2.81\,\mu_{\mathrm{B}}$), and a Curie-Weiss temperature of $-7.3(9)\,\mathrm{K}$. The absolute Curie-Weiss temperature is therefore smaller than the one determined from the ESR intensity ($\theta_{\mathrm{LT}}^{\mathrm{ESR}} = -12\,\mathrm{K}$). A dissonance between the Curie-Weiss temperatures obtained from ESR and susceptibility measurements for $H \perp c$ is also observed in the case of $NaYbSe_2$ and $NaYbO_2$. For $NaYbSe_2$ and $NaYbS_2$ an even larger difference between the Curie-Weiss temperatures from ESR and susceptibility is found for $H \parallel c$. It is also worth noting, that the Curie-Weiss temperatures determined from ESR measurements do not reflect the pronounced anisotropy observed in the susceptibility measurements.
Additionally, the second analysis method is applied by fitting the low-temperature part of the susceptibility with the modified Curie-Weiss law [see Fig. 7.6(a)]. The effective moment, calculated from the ESR $g_{\perp}$-value, is used to constrain the fit and make it less ambiguous. This yields a Curie-Weiss temperature of $\theta_{\mathrm{LT}}^{\perp} = -5.4(3)\,\mathrm{K}$, which

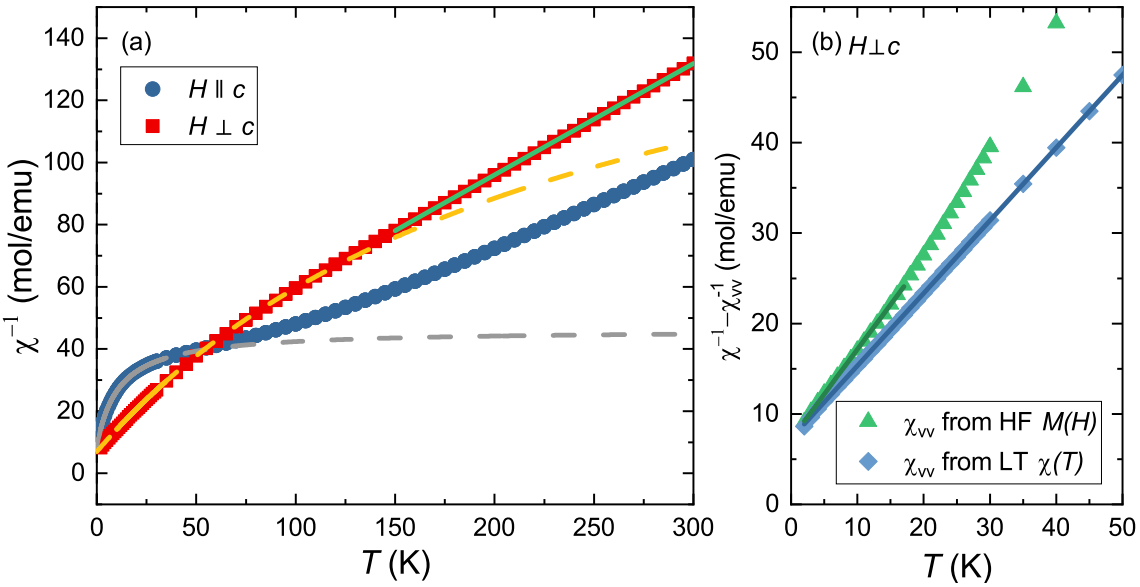

Figure 7.6: *(a) Inverse magnetic susceptibility of $KYbS_2$ for both field directions. At high temperatures the susceptibility for $H \perp c$ is fitted with a linear Curie-Weiss law (green line). The low-temperature part for both field directions is fitted with the modified Curie-Weiss law ($H \perp c$: yellow line; $H \parallel c$: grey line). (b) Inverse susceptibility corrected by the van Vleck contribution determined from the high-field $M(H)$ measurement (green triangles) and from the low-temperature fit to the susceptibility (blue triangles).*

providing an even smaller absolute value of θ_{LT} than determined from the corrected susceptibility. The fit with the modified Curie-Weiss law also returns a smaller van Vleck contribution of $\chi_{\mathrm{vv}} = 0.0095(3)\,\frac{\mathrm{emu}}{\mathrm{mol}}$ compared to the high-field magnetization measurement.
A fit with the modified Curie-Weiss law treating all parameters as free parameters yields a Curie-Weiss temperature of $-8.8(1)\,\mathrm{K}$, in between the ones determined from the ESR measurement and the susceptibility corrected based on the high-field measurement. In this case, a much lower van Vleck contribution of $0.0056(2)\,\frac{\mathrm{emu}}{\mathrm{mol}}$ is obtained, which is not even half of the one determined from the high-field magnetization measurement. For comparison, the susceptibility was corrected with the van Vleck value determined form the fit with the modified Curie-Weiss and all free parameters [see Fig. 7.9(b)]. This yields a linear behavior of $\chi(T)$ over a much larger temperature range and an effective moment of $3.15\,\mu_{\mathrm{B}}$, which is a bit larger compared to the findings of the ESR measurement ($\mu_{\mathrm{eff}}^{\mathrm{ESR}} = 2.81\,\mu_{\mathrm{B}}$) but in excellent agreement with Ref. [109].

The low-temperature susceptibility for $H \parallel c$ was also fitted with the modified Curie-Weiss law, leaving all fit parameters free, see Fig. 7.6(a). A Curie-Weiss temperature of $\theta_{\mathrm{LT}}^{\parallel} = -1.8(1)\,\mathrm{K}$, a van Vleck contribution of $0.02188(5)\,\frac{\mathrm{emu}}{\mathrm{mol}}$ and an effective moment of $\mu_{\mathrm{eff}} = 1.22(1)\,\mu_{\mathrm{B}}$ are determined from this fit. The effective moment is considerably larger compared to the one determined from the ESR g-value of $\mu_{\mathrm{eff}} = 0.69\,\mu_{\mathrm{B}}$.

Antiferromagnetic exchange interactions are implied by the negative Curie-Weiss temperatures for both field directions. The significant difference between the Curie-Weiss temperature for $H \perp c$ and $H \parallel c$ reflects the strong easy-plane anisotropy inferred from the ESR measurements.

7.7 Low-Temperature Magnetization

The high-field magnetization measurements for $KYbS_2$ already gave a good impression of the low-temperature behavior, which will be discussed in more detail in this chapter.

For $H \parallel c$ no unusual features at low temperatures and no changes with increasing temperature are observed in agreement with the measurements to high magnetic fields, see Fig. 7.7(a).

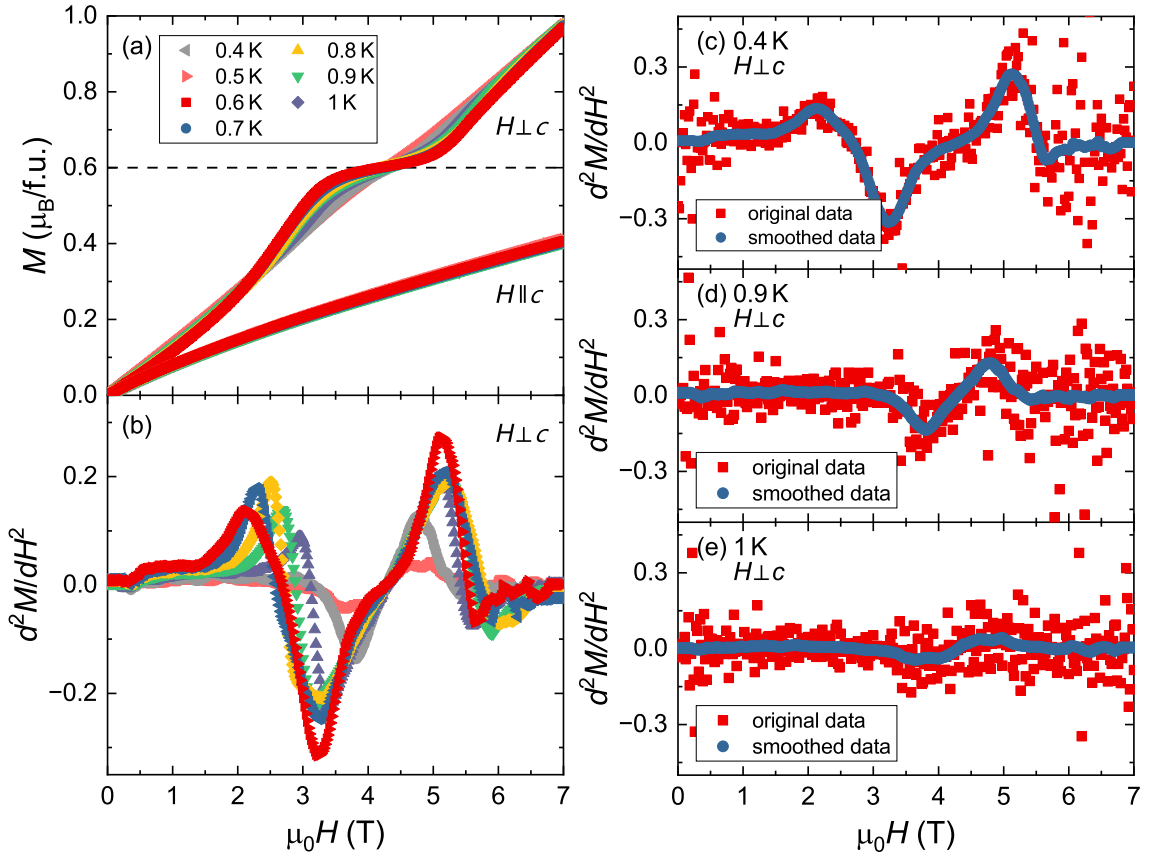

Figure 7.7: *(a) Low-temperature magnetization of $KYbS_2$ for $H \perp c$ and $H \parallel c$. A plateau is observed for $H \perp c$ while the magnetization continuously increases for $H \parallel c$. (b) Second derivative of $M(H)$ to determine the field limits of the magnetization plateau via the respective minimum and maximum. (c)-(e) Second derivative of $M(H)$ before and after smoothing.*

The presence of a magnetization plateau for $H \perp c$ is already observed in the high-field magnetization measurements discussed previously. At 0.4 K this plateau feature is very distinct in the field range between 3.2 and 5.1 T, although it still is slightly tilted. As shown in Fig. 7.8(a), subtracting the χ_{vv} term obtained from the high-field magnetization results in a completely flat plateau feature. The plateau becomes less pronounced and its width decreases with increasing temperature. This development is nicely observable in the second derivative of $M(H)$, see Fig. 7.7(b). Since the derivative of the original data is rather noisy, the derivative is smoothed to determine the position of the minimum and maximum in $\mathrm{d}^2M/\mathrm{d}H^2$, which marks the beginning and end of the plateau feature. In Fig. 7.7(c)-(e) the derivatives for different temperatures provide a comparison between the original and smoothed curves. For 0.4 K and up to 0.9 K the maxima and minima are clearly discernible in the original as well as the smoothed derivative. At 1 K the plateau feature is no longer visually discernible in the magnetization and in the derivative one can hardly discern any extrema, however the smoothed curve still provides two rather wobbly extrema. A similar behavior is observed in the analysis of the magnetization plateau of other compounds in this work. At higher temperatures, weakly pronounced extrema are still observed in the derivative of the magnetization, although the plateau feature in the magnetization not observable by eye anymore.

The plateau feature is located at 0.51 μ_B which is 36% of the saturation magnetization determined from the high-field magnetization measurement and 31% of the M_{sat} determined from ESR measurements. In the comparable compounds $A\mathrm{YbSe}_2$ (A = K, Rb, Na, Cs) the plateau feature is claimed to be a $\frac{1}{3}$ plateau indicative of *uud* order [103, 104]. For NaYbSe_2 the plateau is found above the $\frac{1}{3}$ mark of the

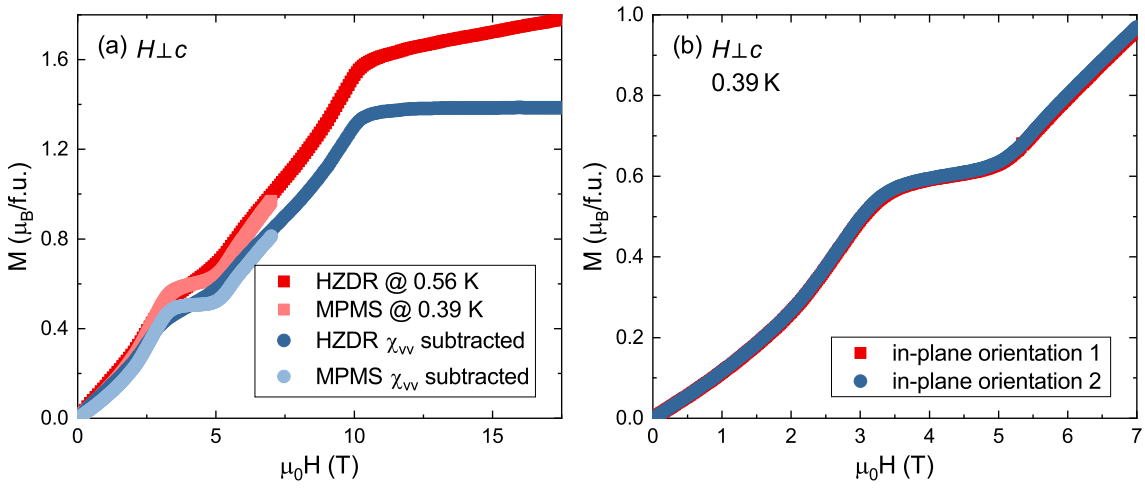

Figure 7.8: *(a) Original high-field and low-temperature measurements and measurements after subtraction of the van Vleck contribution. (b) Comparison of two magnetization measurements of $KYbS_2$ at 0.39 K for two different in-plane orientations. The difference between the two orientations is about 0.6% at the plateau field as well as at 7 T.*

saturation magnetization at 40%, but was still ascribed to the *uud* order in Ref. [103]. For $NaYbSe_2$ and $KYbSe_2$ INS measurements in the field range of the plateau phase provide prove of the *uud* order [111]. In the case of $KYbS_2$ the saturation value is close to $M_{sat}/3$ and therefore a *uud* order is also the most likely interpretation of the plateau feature for $KYbS_2$.

A $KYbS_2$ single crystal was measured in two different in-plane orientations with virtually no difference observed between the measurements, rendering $KYbS_2$ free of in-plane anisotropy [see Fig. 7.8(b)].

The field-induced magnetic order in $KYbS_2$ can also be traced in the low-temperature magnetic susceptibility. At the transition to the magnetically ordered phase the susceptibility shows a kink. In Fig. 7.9(a) the susceptibility for different applied magnetic fields is shown and the transition temperature is marked by a star. Same as observed in $NaYbO_2$ and $KYbO_2$ the inverse susceptibility initially exhibits a

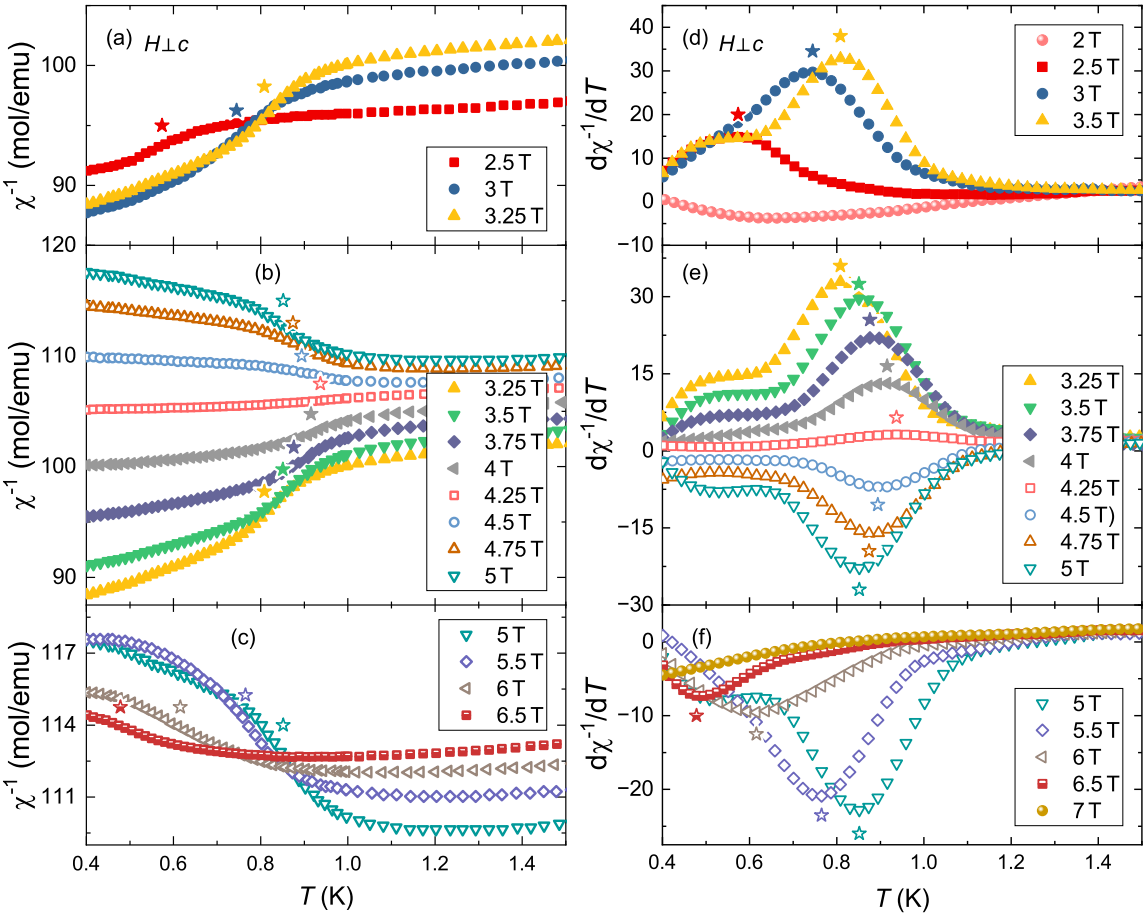

Figure 7.9: *(a)-(c) Inverse magnetic susceptibility at low temperatures measured at different applied magnetic fields. The transition to the magnetically ordered phase is characterized by a kink and marked with a star. (d)-(f) First derivative of χ^{-1} calculated to determine the position of the magnetic transition.*

downward curvature at the transition temperature at low fields, that changes to an upward curvature above 4.25 T. The exact position of the transition is determined by calculating the first derivative and identifying the respective maximum or minimum [see Fig. 7.9(b)]. This yields insights into the development of the field-induced magnetic order beyond the *uud* ordered phase. Magnetic order in the susceptibility measurement is first observed for 2.5 T and can be traced up to 6.5 T, at the maximum field of 7 T the transition is already below the minimum temperature of 0.4 K attainable in the measurement. Starting from 2.5 T at about 0.57 K the magnetic order shifts to higher temperature up to 4.25 T reaching a maximum temperature of 0.94 K. At higher fields the magnetic transition temperature becomes smaller until it is below 0.4 K at 7 T.

The low-temperature susceptibility clearly outlines a magnetic field induced ordered phase in which the *uud* ordered plateau phase is included. Due to the restrictions of the available magnetic field strength and temperature range, the susceptibility only partially reveals the extend of the magnetically ordered phase.

7.8 Specific Heat Measurements

The specific heat was measured down to 0.4 K at zero field in the PPMS. In field measurements with the available setup are only possible for $H \parallel c$ and were performed up to 6 T without any sign of magnetic order. Dilution fridge measurements performed by Sebastian Bachus are available in Ref. [112] and proofed that no magnetic order appears up to at least 13.5 T down to 0.4 K for $H \parallel c$.

In Fig. 7.10 the zero field measurement for $KYbS_2$ is shown. The ^{3}He refrigerator of the PPMS was used to measure the low-temperature specific heat between 0.4 and 10 K while the standard PPMS setup is used to measure the specific heat between 2 and 300 K. The ^{4}He measurement up to 90 K is relatively stable, with the three data points taken at each temperature being rather consistent, but they start to disperse with further increasing temperature. Most likely this development towards higher temperatures is due to the small mass of the single crystals (< 1 mg). Therefore, the data was reviewed rejecting the unreasonable data points. The rejection of data points is based on the value of χ^2 which accounts for the fit quality in the heat capacity measurement and is unusually large for the respective second and third measurement at each temperature. The comparison between the original and reviewed data is shown in Fig. 7.10(a). At 300 K the specific heat reaches a value of 93.4 J/molK close to the classically expected Dulong-Petit value of $C = 3nR = 100.3$ J/molK, with the number of atoms per formula unit $n = 4$ and the molar gas constant R. As can be seen in Fig. 7.10(b) the overlap area between ^{3}He and ^{4}He measurements is not completely identical, with the ^{3}He measurement slightly above the ^{4}He measurement. At low temperatures the ^{3}He option provides more accurate measurements, therefore the ^{3}He data is preferred up to 10 K where both data sets match up.

In zero field, no lambda-like peak indicating magnetic order is observed. A broad maximum centered at about 2 K is present, as was already observed in Ref. [109]

where a double peak structure is reported which is not discernible here. Analogous to Ref. [109] the specific heat was fitted with a combination of Einstein $C_{\mathrm{E}}(T)$ and Debye $C_{\mathrm{D}}(T)$ models to determine the phonon contribution to the specific heat:

$$C_{\mathrm{ph}}(T) = (1-p)C_{\mathrm{D}}(T) + pC_{\mathrm{E}}(T), \tag{7.1}$$

with

$$C_{\mathrm{D}}(T) = 9nR\left(\frac{T}{\theta_{\mathrm{D}}}\right)^3 \int_0^{\frac{\theta_{\mathrm{D}}}{T}} \frac{x^4 e^x}{(e^x-1)^2}\mathrm{d}x \tag{7.2}$$

and

$$C_{\mathrm{E}}(T) = 3nR\left(\frac{\theta_{\mathrm{E}}}{T}\right)^2 \frac{e^{\frac{\theta_{\mathrm{E}}}{T}}}{(e^{\frac{\theta_{\mathrm{E}}}{T}}-1)^2}. \tag{7.3}$$

θ_{E} and θ_{D} are the respective Einstein and Debye temperatures. The parameter p in Eg. 7.1 scales the relative contributions of the Einstein and Debye model.

The fit shows good agreement at low temperatures and up to 160 K, see Fig. 7.10(a). At higher temperatures the data points deviate more from the fit. The Einstein and Debye temperatures are determined as 342 K and 193 K, respectively, in good agreement to the values determined in Ref. [109] ($\theta_{\mathrm{E}} = 391$ K and $\theta_{\mathrm{D}} = 212$ K). The ratio p between the Debye and Einstein models is obtained as 0.57. The phonon contribution determined by the fit can be used to calculate the magnetic specific

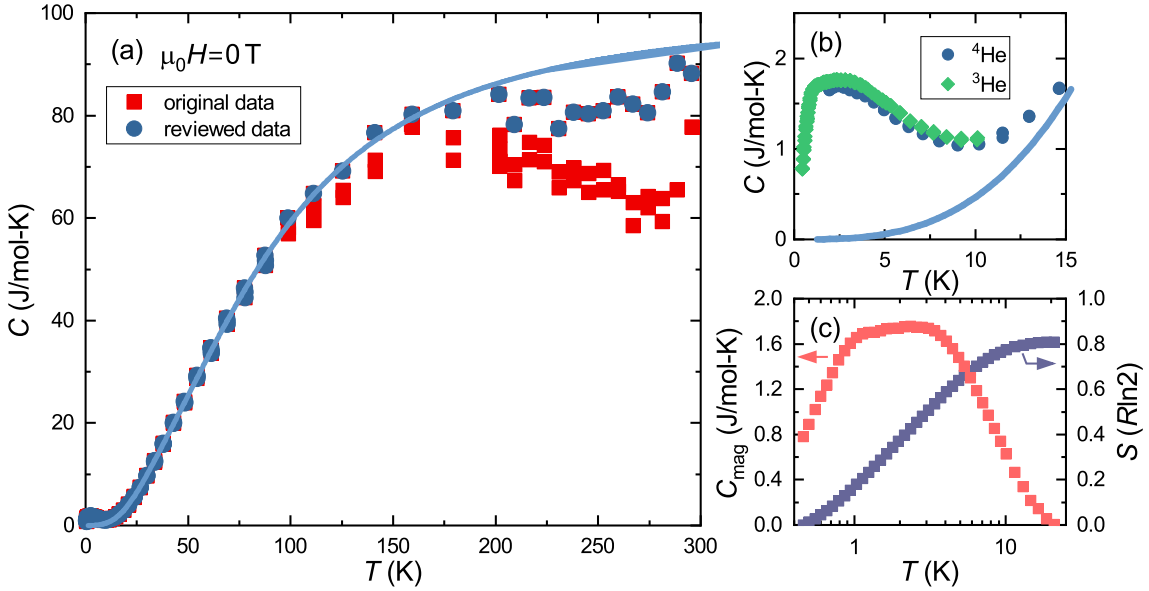

Figure 7.10: *(a) Specific heat of $KYbS_2$ measured between 0.4 and 300 K in zero applied magnetic field. The red data points are the original data, the blue data points is the reviewed data after sorting out the unreasonable measurements. The light blue line is the phonon fit C_{ph} to the specific heat. (b) Comparison between ^{3}He and ^{4}He measurement at low temperatures. (c) Magnetic specific heat and entropy of $KYbS_2$.*

heat of $KYbS_2$. Below 3 K the phononic contribution to the specific heat becomes negligible as can be observed in Fig. 7.10(b).

The magnetic part of the specific heat and the magnetic entropy of $KYbS_2$ are shown in Fig. 7.10(c). C_{mag} is calculated by subtracting the determined phonon contribution from the specific heat data. This way of obtaining the magnetic specific heat is not ideal, since C_{mag} becomes negative above 20 K. An improvement of the fit function used to determine the phonon contribution and better measurements of the specific heat measurement at high temperatures are necessary to remedy this non-physical behavior. Nevertheless, the magnetic entropy is calculated by integrating C_{mag}/T for $T < 20\,\mathrm{K}$. The entropy saturates at about 80% of the value expected for a pseudospin-$\frac{1}{2}$ system, $S = R\ln 2$. A saturation at about 90% $R\ln 2$ is achieved if the measurements presented in this work are extended by available dilution fridge measurements below 0.4 K.

7.9 Phase Diagram

The phase diagram depicted in Fig. 7.11 is constructed from the high-field and low-temperature magnetization measurements as well as the low-temperature susceptibility measurements. Further measurements in a dilution refrigerator were performed on $KYbS_2$. Field- and temperature-dependent specific heat and magnetic Grüneisen parameter measurements were carried out by Sebastian Bachus [112] and thermal expansion and magnetostriction measurements were performed by Noah Oefele. These measurements are not part of this thesis and are therefore not included in the phase diagram, nevertheless, they confirm the phase boundaries of the *uud* phase determined from the magnetization plateau (red striped area in Fig. 7.11) as well as the transition to the fully polarized state above 10.3 T, indicated as the blue colored area. The development of the field-induced magnetic order observed in susceptibility measurements between 2.5 and 6.5 T is also confirmed by the dilution fridge measurements and can even be traced up to the polarized state due to the availability of higher magnetic fields and lower temperatures. An additional phase transition between the potential QSL state and the magnetically ordered phase is observed in magnetostriction measurements. The magnetically ordered phase is therefore clearly enclosed in the red colored area depicted in Fig. 7.11.

The magnetically ordered phase in $KYbS_2$ is subdivided into three areas, out of which only the *uud* phase is identified so far. The phase below the *uud* phase is most likely a kind of 120° order, in $NaYbSe_2$ a similar phase below the *uud* phase is assumed to be of an oblique 120° (Y-coplanar) ordered nature [103]. In accordance to $NaYbSe_2$, $KYbSe_2$ and $RbYbSe_2$, the phase above the *uud* order is probably a V-type (2:1 coplanar) order induced by the the increasing magnetic field [103, 104].

As discussed in Chapter 7.7, the magnetization plateau can be traced even at temperatures above the magnetically ordered phase. A similar observation was made in Ref. [104] for $KYbSe_2$ and $RbYbSe_2$, where this phenomenon was ascribed to

strong spin fluctuations. The constant width of the plateau phase with increasing temperature indicates that thermal fluctuations have no influence on the plateau phase.

At low temperatures and magnetic fields no magnetic order is observed. In zero field the absence of magnetic order is verified by heat capacity measurements down to at least 50 mK. In the additional dilution fridge and μSR measurements also no apparent magnetic order is observed. Therefore, a potential QSL state might be realized in $KYbS_2$ in this area of the phase diagram.

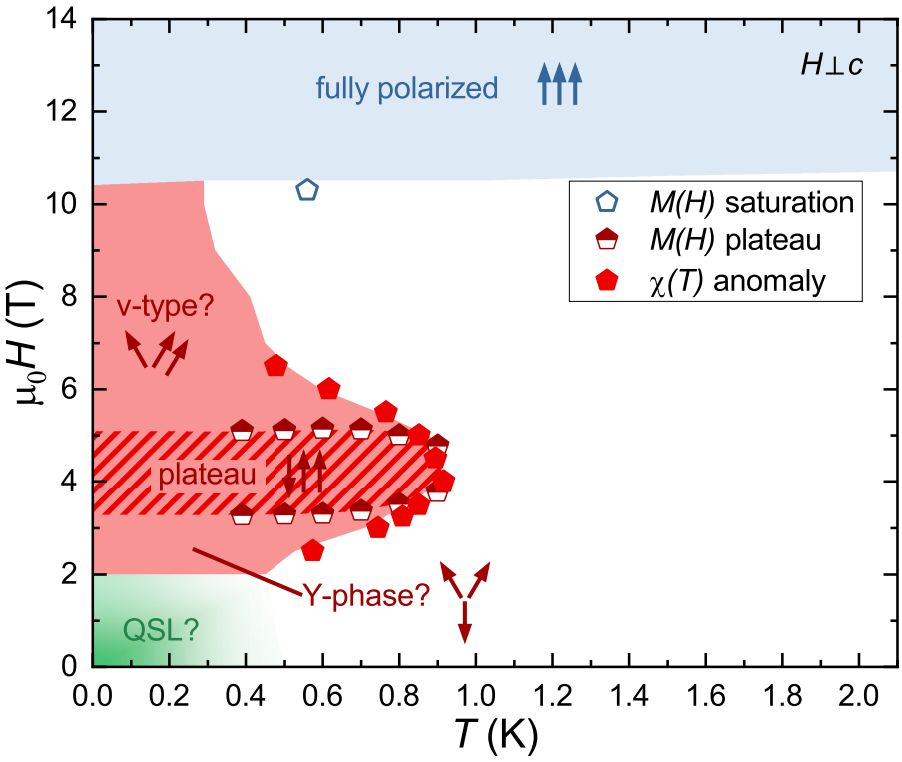

Figure 7.11: *Phase diagram of $KYbS_2$ for $H \perp c$ containing all phase transitions observed in magnetization and susceptibility measurements. The red area marks the magnetically ordered phase determined from the magnetic transition observed in the susceptibility. Within the magnetically ordered phase the uud phase is identified via the magnetization plateau. The areas directly above and below the uud phase are most likely a Y- and V-type phase. Above the magnetically ordered phase the saturation observed in the high-field magnetization reveals the fully polarized phase (blue). At low fields and low temperatures the potential QSL phase is indicated as the green colored area.*

8 $NaYbSe_2$

In contrast to $KYbS_2$, $NaYbSe_2$ is already quite well studied in literature. The primary goal for this compound is not to investigate the general properties but to verify the present results and extend them to lower temperatures and by more exotic investigation methods such as magnetic Grüneisen parameter measurement at millikelvin temperatures, which are not reported in literature so far. The results of these measurements are especially valuable for the comparison to $KYbS_2$ to better understand the influence of the surrounding atoms on the magnetism of the $AYbX_2$ compounds. In this line of thought, dilution fridge measurements are of great interest, but they go beyond the scope of the present work. Instead the focus is on the crystal growth and characterization, as well as preparatory MPMS measurements down to 0.4 K for the dilution fridge measurements, which also serve as an indicator of crystal quality and provide a preliminary layout of the phase diagram of $NaYbSe_2$.

8.1 Literature Results

Like $KYbS_2$, $NaYbSe_2$ is available in single crystalline form. $NaYbSe_2$ grows into crystals of the size of multiple millimeter, although the crystals remain very thin. While for $KYbS_2$ the thickness of crystals is usually larger than 0.1 mm, the thickness of $NaYbSe_2$ is only a fraction of this value.
The synthesis of $NaYbSe_2$ crystals was first described by Gray *et al.* [113] in 2003. There, a molten chalcogenide flux reaction with Yb, Ge, Se and Na_2Se_2 as starting materials was carried out which produced small hexagonal shaped red-orange platelets. As a result of the increased interest in the $AYbX_2$ family following the discovery of $YbMgGaO_4$, the compound was revisited in 2019 using the same self-flux method applied to $KYbS_2$, with NaCl, as flux and Na source, as well as elementary Yb and Se as starting materials [103]. However, instead of placing the starting materials directly into the quartz glass, a quartz glass with an internal glassy carbon crucible was used. In this way mm-sized crystals were synthesized.

A summary of the results of the standard experimental analysis is given in Tab. 8.1.

XRD measurements confirmed the $R\bar{3}m$ space group and the absence of disorder was evidenced by narrow ESR lines. The g-values for both field directions were determined from ESR measurements and the energy gap between ground state and first excited doublet were derived from the ESR linewidth. Additionally, the Curie-Weiss temperatures were determined from the ESR intensity. [96, 103]

Table 8.1: *Characteristic properties of $NaYbSe_2$. The high-temperature (HT) susceptibility in Ref. [103] was fitted with a modified Curie-Weiss law. At low temperatures (LT) the van Vleck contribution χ_{vv} obtained from the high-field magnetization measurements was subtracted and the Curie-Weiss law was applied for both field directions. In Ref. [114] the high- and low-temperature susceptibilities were both analyzed using the modified Curie-Weiss law.*

	XRD		**Susceptibility (HT)**			
	lattice parameter			$\boldsymbol{\theta_{CW}}$ **(K)**	$\boldsymbol{\mu_{eff}}$ **(μ_B)**	$\boldsymbol{\chi_{vv}}$ **($\frac{emu}{mol}$)**
[103]	–	–	$\boldsymbol{H \perp c}$	-66	4.5	$1.6 \cdot 10^{-5}$
[114]	$a = 4.07$ Å	$c = 20.77$ Å	$\boldsymbol{H \perp c}$	-51	–	$2 \cdot 10^{-4}$

	Susceptibility (LT)			**Magnetization**		
		$\boldsymbol{\mu_{eff}}$ **(μ_B)**	$\boldsymbol{\theta}$ **(K)**	$\boldsymbol{H_{sat}}$ **(T)**	$\boldsymbol{\chi_{vv}}$ **($\frac{emu}{mol}$)**	$\boldsymbol{M_s}$ **(μ_B)**
[103]	$\boldsymbol{H \perp c}$	2.43	-7	12	0.00765	1.5
[103]	$\boldsymbol{H \parallel c}$	1.1	-3.5	25	0.0144	0.49
[114]	$\boldsymbol{H \perp c}$	–	-13	–	–	–

	ESR				
	$\boldsymbol{g_\perp}$	$\boldsymbol{g_\parallel}$	**Δ (K)**	$\boldsymbol{\theta_\perp^{ESR}}$ **(K)**	$\boldsymbol{\theta_\parallel^{ESR}}$ **(K)**
[96]	3.13(4)	1.01(1)	160(30)	-14	-14.3

Measurements of the susceptibility showed the distinctly different behavior of $\chi(T)$ when the magnetic field is applied perpendicular or parallel to c. The susceptibilities above 70 K were fitted with the modified Curie-Weiss law, however, considering a temperature independent core diamagnetic contribution as well as the van Vleck susceptibility, $\chi_0 = \chi_{dia} + \chi_{vv}$. For the low-temperature ($T < 70$ K) analysis the van Vleck contribution was determined from the high-field magnetization measurements via a linear fit in the fully saturated field range ($\mu_0 H > 13$ T for $H \perp c$, $\mu_0 H > 22$ T for $H \parallel c$). After subtracting the van Vleck contribution the effective magnetic moment and the Curie-Weiss temperature for both field directions were determined by linearly fitting the corrected susceptibility data.
In small applied fields no signs of long-range magnetic order were observed down to 0.5 K in the susceptibility. When applying a magnetic field larger than 2 T a kink in $\chi(T)$ was observed, indicating a magnetic phase transition. In addition to that, a plateau feature appeared between 3 and 5 T in the field-dependent magnetization measurements at about one third of the saturation magnetization, reminiscent of an *uud* ordered state. No magnetic order was observed in $\chi(T)$ and $M(H)$ for fields

applied along $H \parallel c$, which is explained by the spins being gradually canted out of the ab plane and the consequently unbroken threefold rotational symmetry. [103]

The absence of magnetic order in zero field was further supported by measurements of the specific heat in zero field down to 50 mK. A superposition of two maxima at 1.1 K and 1.2 K was described in Ref. [103] and associated with a high degree of frustration in the triangular lattice. The magnetic specific heat revealed a linear power-law behavior, indicating a gapless QSL ground state. The entropy was calculated from the magnetic specific heat and reaches $R \ln 2$ at 15 K, as expected for a pseudospin-$\frac{1}{2}$ system. In applied magnetic fields ($H \perp c$) the specific heat develops a lambda like anomaly above 2 T which shifts to higher temperatures with increasing the field up to 5 T. Above 5 T the trend is reversed until the magnetic order disappears above 9 T. For $H \parallel c$ magnetic order is established at a much larger field of 9 T and vanishes above 21 T. [103]

CEF levels were determined from INS measurement. Three resolution limited peaks were observed further evidencing the absence of structural disorder. INS measurements also excluded the presence of short and long-range order down to 40 mK. [103, 114]

Ac susceptibility measurements in combination with μSR measurements excluded the possibility of spin ordering or freezing down to 0.1 K [115].

8.2 Synthesis

Jens Maier assisted in the synthesis of the crystals as part of his Bachelor work, however he was not involved in selecting and cleaning of crystals and performing measurements.

The synthesis of $NaYbSe_2$ single crystals was done similar to Ref. [103] by filling the reagents (NaCl : Yb : Se = 20 : 1 : 2.4) into a glassy carbon crucible which was subsequently inserted into a standard quartz tube. Instead of sublimed Se used in Ref. [103] purchased Se granules were used for the synthesis. The Se was ground and mixed with the NaCl; the Yb metal was cut into small pieces and placed at the bottom of the crucible and covered with the NaCl-Se mixture. Then the crucible was inserted into a quartz glass which was subsequently sealed under vacuum conditions and placed into a box furnace. The same heating procedure as in Ref. [103] was used with an initial heating step to 400 °C with 180 K/h and a holding time at this temperature of two hours to ensure equilibrium. After this, the temperature is slowly raised (20 K/h) to 850 °C and held there for one week, then cooled down to room temperature with 40 K/h. The crystals obtained after dissolving the flux in water are very thin and covered with a black residue (see Fig.8.1). Most of the crystals are quite small ($< 1\,\mathrm{mm}^2$) with only a few larger ones with lateral dimensions of up to 2 mm. Finding a crystal suitable for measurements is challenging and those crystals have to be painstakingly cleaned by scratching the dirt of the surface with a scalpel.

Changes of the ratio of the reagents (i.e.: NaCl : Yb : Se = 20 : 1 : 2, NaCl : Yb : Se = 20 : 1 : 1.8, NaCl : Yb : Se = 20 : 1 : 2.2) did not lead to a significant

improvement of crystal size and quality. Similar, no obvious improvements were observed when changing the maximum temperature (900 °C, 950 °C) of the synthesis. The holding time was only varied insignificantly (up to 12 days) therefore no statement on the influence of a longer holding time can be made. For the synthesis of $KYbS_2$ a longer holding time had a positive impact on the crystal size, however a similar trend is not expected for $NaYbSe_2$ based on experiences made during the synthesis of $KYb(S_xSe_{1-x})_2$. For $KYb(S_xSe_{1-x})_2$ an extended holding time does not appear to have a significant impact on the size of crystals with dominant Se content.

Attempting the synthesis according to Ref. [116] yielded similar results. The ratio for the starting materials in this case is NaCl : Yb : Se = 10 : 2 : 3. Again Se granules were used, in accordance with Ref. [116], crushed and mixed with the NaCl. The reagents were directly filled into a quartz glass, sealed with an argon atmosphere of 200 mbar, and heated to 850 °C or 950 °C for one week or up to 11 days.

Another synthesis attempt was made by deploying the method used for $KYbS_2$ and adjusting it to $NaYbSe_2$. The ratio was significantly different in this case with a bigger surplus of NaCl flux: NaCl : Yb : Se = 80 : 2 : 3. The reactants were directly filled into the quartz glass. A synthesis under vacuum as well as 200 mbar argon atmosphere was performed, no difference was observed between the two methods. The furnace program was altered as well, the reagents were directly heated to 840 °C over four hours and held at that temperature for two weeks, then cooled down to room temperature over 160 h. The crystals grow on the walls of the quartz glass and have to be carefully broken to remove them. The crystals are rather large but very thin

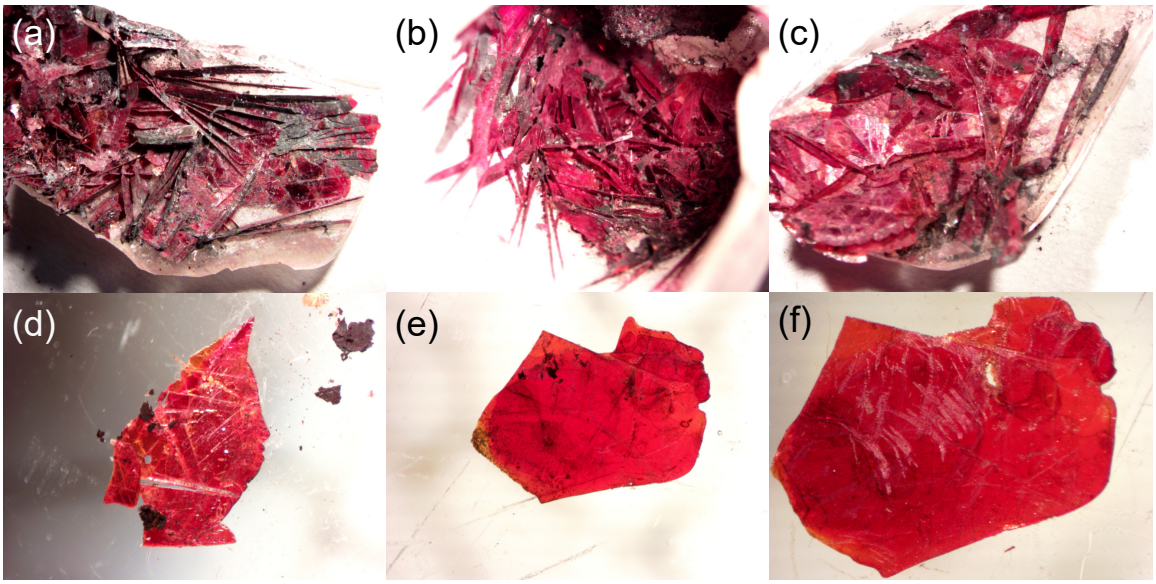

Figure 8.1: *$NaYbSe_2$ crystals synthesized directly in the quartz glass similar to $KYbS_2$. The synthesis using a glassy carbon crucible yielded similar results. (a)-(c) $NaYbSe_2$ crystals grown on the wall of the quartz glass. (d),(e) Crystals extracted from the quartz glass wall, before cleaning. (f) Same crystal as in (e) after cleaning.*

and still quite dirty, see Fig. 8.1. Fig. 8.1(e) and (d) show the same crystals before and after cleaning.

8.3 Characterization

Powder XRD measurements on several small, cleaned single crystals were performed with the Empyrean and did not reveal the presence of any impurity phases. The $(00l)$ reflexes are dominant in the XRD spectrum due to the plate-like structure of the crystals and the observed reflexes are in good agreement with literature.

A Rietveld refinement of the powder XRD data (see Fig. 8.2) yielded reasonable values for the atomic displacement parameters and the obtained lattice parameters are comparable to literature [113]. The characteristic parameters determined from the Rietveld refinement are given in Tab. 8.2.

Since the purity of the single crystals is hard to judge only by visual examination and XRD performed on single crystals, promising candidates were further investigated in the MPMS using the ^{3}He refrigerator. The results of those measurements are shown in Fig. 8.3. For the crystals shown in Fig. 8.3(a) and (b) the low-field part of the $M(H)$ measurements show a clear deviation from the expected behavior, although the plateau feature anticipated in $NaYbSe_2$ is present. These deviations are not necessarily connected to an impurity phase, since the investigated crystals are very thin and light ($m < 0.1\,\mathrm{mg}$) and therefore the signal at low fields might simply be too weak to be correctly detected. No unusual behavior is observed in the only slightly

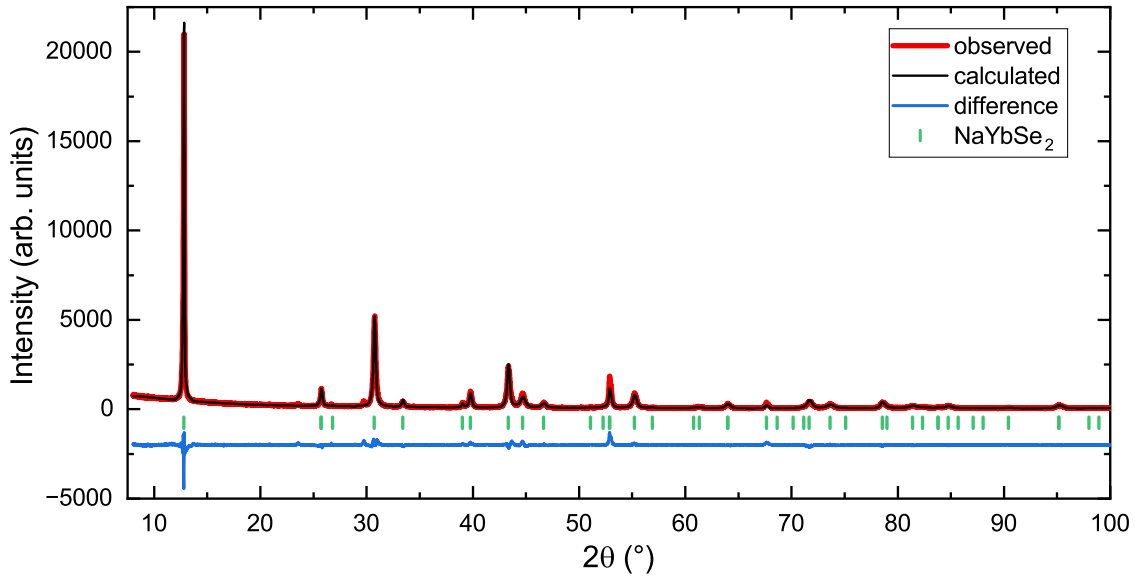

Figure 8.2: *Rietveld refinement of the lab powder XRD measurement on multiple crushed single crystals. Although the crystals were thoroughly ground using ethanol the $(00l)$ reflexes are still significantly overestimated.*

Table 8.2: *Atomic displacement parameters (U_{iso}) and atomic positions as well as lattice parameters, characteristic distances and Yb-Se-Yb angle of $NaYbSe_2$ determined from the Rietveld structure refinement of the lab XRD measurement.*

atom	***x/a***	***y/b***	***z/c***	$\boldsymbol{U_{iso}}$ **(Å²)**
Se	0	0	0.244062(99)	0.0055(13)
Yb	0	0	0.5	0.0099(11)
Na	0	0	0	0.0113(55)

a	***c***	**Yb–Se dist.**	**Na–Yb dist.**	**∡Yb–Se–Yb**
4.0539(3)	20.761(1)	2.8390(1)	4.1774(2)	91.118(5)°

heavier (0.11 mg) crystal shown in Fig. 8.3(c). From the $M(H)$ measurement this crystal would be judged sufficient for further measurements, although it is still rather light and relatively small so its usability is limited. The crystals shown in Fig. 8.3(d) and (e), on the other hand, show a nice plateau feature with no deviation from the expected behavior of the $M(H)$ measurements, they are large enough to be used for more challenging measurements, i.e. measurements of the specific heat using a dilution refrigerator where a thermometer (approximately $0.5 \times 0.7\,\mathrm{mm}^2$) has to be glued directly to the surface of the crystals. Lastly, the crystal in Fig. 8.3(d) is comparatively heavy but does not develop a distinct plateau feature at the lowest measured temperature 0.4 K. Therefore it is not considered for further measurements.

8.4 Susceptibility

For $H \perp c$ the susceptibility shows the same behavior as observed for $KYbS_2$, $KYbO_2$ and $NaYbO_2$. The linear high-temperature behavior is again fitted with the Curie-Weiss law between 150 and 300 K [see Fig. 8.4(a)]. An effective magnetic moment of $\mu_{\mathrm{eff}} = 4.59(9)\,\mu_{\mathrm{B}}$, close to the calculated effective moment of free Yb^{3+} ions $\mu_{\mathrm{eff}} = 4.54\,\mu_{\mathrm{B}}$, and a Curie-Weiss temperature of $\theta_{\mathrm{CW}}^{\mathrm{HT}} = -55(4)\,\mathrm{K}$ are obtained. Both values are in good agreement with previous studies (see Tab. 8.1).

The low-temperature part of the susceptibility is initially fitted with the modified Curie-Weiss law, the results of the fit are summarized in Tab. 8.3. Compared to the values determined in Ref. [103] ($\theta_{\mathrm{LT}} = -7$, $\mu_{\mathrm{eff}}^{\mathrm{ESR}} = 2.43\,\mu_{\mathrm{B}}$) the values of the Curie-Weiss temperature $\theta_{\mathrm{LT}} = -12.9(3)\,K$ and the effective moment $\mu_{\mathrm{eff}} = 3.02(1)\,\mu_{\mathrm{B}}$ are larger here. However, the effective moment derived from the ESR g-value is in between the effective moments determined from the susceptibility measurements ($\mu_{\mathrm{eff}}^{\mathrm{ESR}} = 2.71\,\mu_{\mathrm{B}}$) [96]. Furthermore, the obtained Curie-Weiss temperature is in rather good agreement with the one found in Ref. [114] and the one determined from the ESR intensity $\theta_{\mathrm{CW}}^{\mathrm{ESR}} = -14\,\mathrm{K}$ [103].

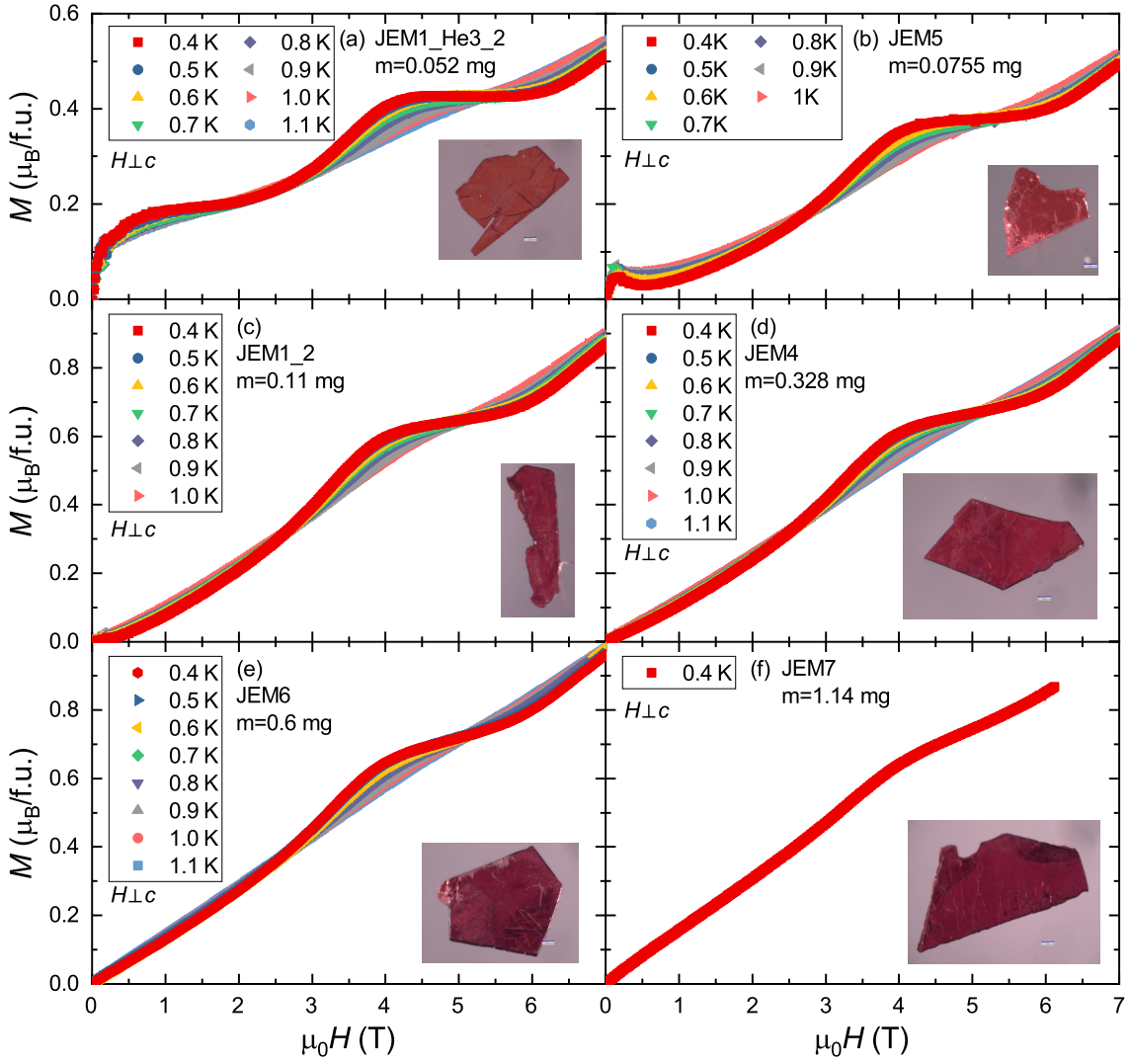

Figure 8.3: *Exemplary $M(H)$ measurements of the $NaYbSe_2$ single crystals to determine the crystal quality and usability for further measurements. (a),(b) Although the crystals appear clean to the eye and develop a distinct plateau the magnetization shows an uncharacteristic behavior at low magnetic fields. (c)-(e) The crystals show a distinct plateau and no irregularities are observed in the measurements. (d) The plateau phase at 0.4 K is noticeably less pronounced in this measurement than for the other crystals.*

Fitting the low-temperature susceptibility with the modified Curie-Weiss with a fixed effective moment calculated from the ESR g-value from literature [96] returns a Curie-Weiss temperature of $-9.6(3)$ K. This value is closer to but still larger than the one in Ref. [103] and a considerably larger van Vleck contribution is obtained, $\chi_{vv} = 0.0103(3)$.

For comparison the low-temperature part susceptibility was also investigated after subtracting the van Vleck contribution χ_{vv}. As shown in Fig. 8.4(b) the susceptibility

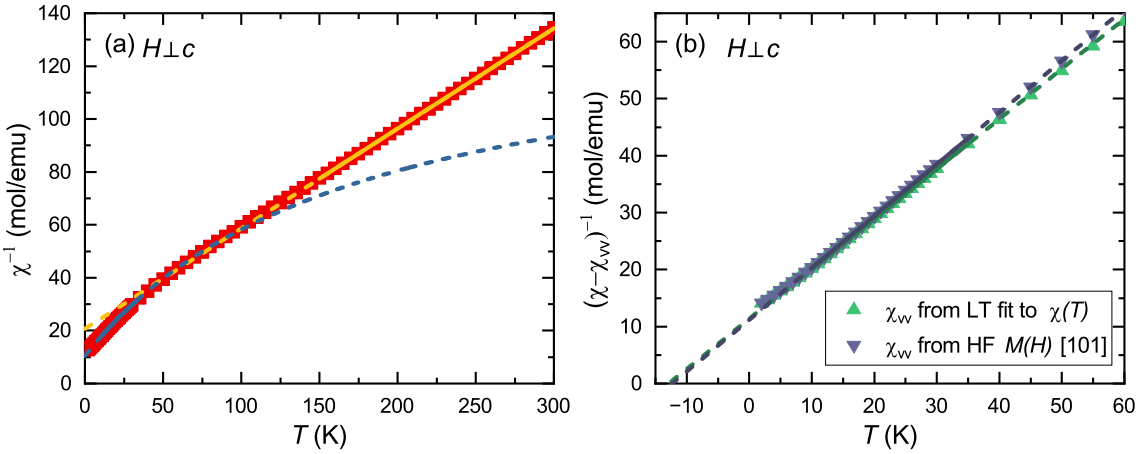

Figure 8.4: *(a) Inverse susceptibility of $NaYbSe_2$ ($H \perp c$) fitted with a Curie-Weiss law at high temperatures (150-300 K) and with a modified Curie-Weiss law at low temperatures. (b) Low-temperature susceptibility after correction with the van Vleck contribution χ_{vv}. The red data points are corrected with χ_{vv} obtained from the low-temperature fit to the susceptibility, the blue curve is corrected with χ_{vv} from the fit to the high-field magnetization in Ref. [103].*

was on one hand corrected using χ_{vv} determined from the high-field magnetization measurement in Ref. [103] and on the other hand using the van Vleck contribution obtained from the modified Curie-Weiss law. In contrast to $KYbS_2$ the van Vleck contribution form the magnetization and the low-temperature fit to the susceptibility are quite simliar, therefore only a marginal difference in slope is observed between the

Table 8.3: *Results of the low-temperature analysis of the susceptibility. (a) Susceptibility between 10 and 35 K ($H \perp c$) or 2 and 35 K ($H \parallel c$) was fitted with the modified Curie-Weiss law. For (b) the effective moment calculated form the ESR g-value was fixed in the fit with the modified Curie-Weiss law for $H \perp c$. Van Vleck contribution determined from the high-field magnetization (c) and from the low-temperature fit (d) was subtracted from the susceptibility and a linear fit was applied to the corrected measurements.*

	$H \perp c$			$H \parallel c$		
	χ_{vv} $(\frac{emu}{mol})$	θ_{LT} (K)	μ_{eff}^{LT} (μ_B)	χ_{vv} $(\frac{emu}{mol})$	θ_{LT} (K)	μ_{eff}^{LT} (μ_B)
(a)	0.0071(4)	−12.9(3)	3.02(1)	0.0178(4)	−8.6(8)	1.52(5)
(b)	0.0103(3)	−9.6(3)	2.72			
(c)	0.00765 [103]	−12.3(5)	2.97(2)	0.0144 [103]	−22(1)	2.12(1)
(d)	0.0071(4)	−12.9(9)	3.02(4)	0.0178(4)	−9.4(4)	1.57(1)

two methods. Linear behavior is observed above 10 K and nearly identical values of θ_{CW} and μ_{eff} are determined, as shown in Tab. 8.3.

The behavior of the susceptibility for $H \parallel c$ is shown in Fig. 8.5(a). For comparison the $H \perp c$ measurement is also included in the graph, revealing a much better agreement between $H \perp c$ and $H \parallel c$ at high temperatures compared to $KYbS_2$. The low-temperature behavior for $H \parallel c$ is analyzed using the modified Curie-Weiss law yielding a Curie-Weiss temperature of -8.6 K, a van Vleck contribution of 0.01782 $\frac{\text{emu}}{\text{mol}}$ and an effective moment of 1.52 μ_B. Fitting with the modified Curie-Weiss law with a fixed effective moment calculated from the ESR g-value does not describe the low-temperature behavior accurately.

Analogue to the $H \perp c$ analysis, the low-temperature susceptibility was corrected for the van Vleck contribution using χ_{vv} determined from the fit with the modified Curie-Weiss law as well as the χ_{vv} from the high-field magnetization measurement in Ref. [103], see Fig. 8.5. In contrast to $H \perp c$, a large difference between the two methods is observed, with the second yielding only a small linear regime and an unrealistic value of $\theta_{CW} = -23.1$ K. This indicates, that the van Vleck contribution from the high-field magnetization is too small and doesn't account for the complete paramagnetic contribution of the susceptibility measurement in this work. In Ref. [103] this is not the case and the corrected susceptibility shows a linear behavior below 30 K. A much smaller Curie-Weiss temperature is obtained there ($\theta_{CW} = -3.5$ K), however the fit range is also rather small. Reasons for the discrepancy between Ref. [103] and this work might be a slight, unavoidable sample dependence. However, the determination of χ_{vv} from the high-field magnetization for $H \parallel c$, where no saturation

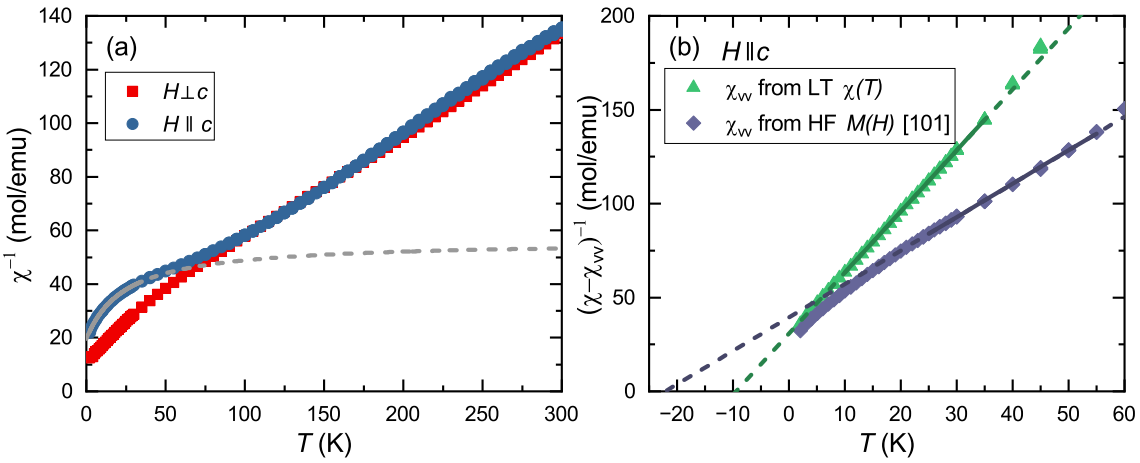

Figure 8.5: *(a) Inverse susceptibility of $NaYbSe_2$ for $H \parallel c$ analyzed with the modified Curie-Weiss law at low temperatures. (b) Low-temperature susceptibility after correction with the van Vleck contribution χ_{vv}. The green data points are corrected with χ_{vv} obtained from the low-temperature fit to the susceptibility, the blue curve is corrected with χ_{vv} from the fit to the high-field magnetization in Ref. [103].*

is observed up to the maximum field of the experiment, makes the linear fit at high fields rather ambiguous and may add to the dissonance, as well.

Overall, the Curie-Weiss temperatures obtained from the low-temperature analysis of the susceptibility for $H \perp c$ and $H \parallel c$ indicate a less pronounced exchange anisotoropy in $NaYbSe_2$ compared to the closely related $NaYbS_2$, with $\theta_{CW} = -13.5\,K$ for $H \perp c$ and $\theta_{\parallel} = -4.5\,K$ for $H \parallel c$, and $KYbSe_2$, with $\theta_{CW} = -12.6\,K$ for $H \perp c$ and $\theta_{\parallel} = -4.7\,K$ for $H \parallel c$ [104, 117]. The van Vleck contribution to the susceptibility for $H \perp c$ is larger in $NaYbSe_2$ ($\chi_{vv} = 0.0071(4)\,\frac{emu}{mol}$l) compared to $NaYbO_2$, in accordance with the reduction of the energy gap Δ between ground state and first excited doublet, determined from the ESR measurements when exchanging O by Se. On the other hand, a difference of 50 K between the energy gaps of $KYbSe_2$ and $NaYbSe_2$ appears to have no notable effect on the van Vleck contribution, resulting in nearly identical values of χ_{vv} ($\chi_{vv}(KYbSe_2) = 0.00112(3)\,\frac{emu}{mol}$). This comparison is made based on the van Vleck contributions determined from fitting the susceptibility measurement with the modified Curie-Weiss law and fixing the effecitve moment calculated from the ESR g-value. Taking the van Vleck contribution determined from the high-field magnetization measurements in Ref. [103] into account a much smaller $\chi_{vv} = 0.00765\,\frac{emu}{mol}$ is retrieved for $NaYbSe_2$. Unfortunately, a comparable measurement is not available for $KYbSe_2$ so far.

8.5 Low-Temperature Magnetization

As already mentioned in Chapter 8.3 the low-temperature magnetization of $NaYbSe_2$ exhibits a plateau, confirming the observation in Ref. [103]. Fig. 8.6(a) shows the plateau located at about $0.65\,\mu_B$ between 4 and 6 T, in excellent agreement with Ref. [103]. In Ref. [103] the plateau is argued to be a $\frac{1}{3}$ plateau that indicates the formation of the *uud* order, as was confirmed by neutron scattering experiments for similar spin-$\frac{1}{2}$ triangular lattice compounds [79, 89]. Although the *uud* order is the most likely origin of the feature in the magnetization, the plateau is located at about 40% of the saturation magnetization, a slightly higher value as expected for the *uud* order. For $KYbS_2$ the plateau was located slightly above $M_{sat}/3$, as well. Neutron diffraction measurements would be desirable to validate the *uud* order of the plateau phase in these compounds as well.

The plateau feature is naturally most prominent at the lowest measured temperature of 0.4 K and becomes less distinct with increasing temperature, but it is still observed up to 1 K. Although, the plateau is well pronounced at 0.4 K, is not completely flat due to the van Vleck contribution, similar to the observations made for $KYbS_2$. In the case of $KYbS_2$ subtracting the linear-in-temperature van Vleck contribution from the low-temperature measurement returned a completely flat plateau feature. To determine the beginning and end of the plateau at each temperature, the second field-derivative of $M(H)$ was calculated as shown in Fig. 8.6(b). The beginning and end of the plateau is characterized by a distinct minimum and maximum in d^2M/dH^2,

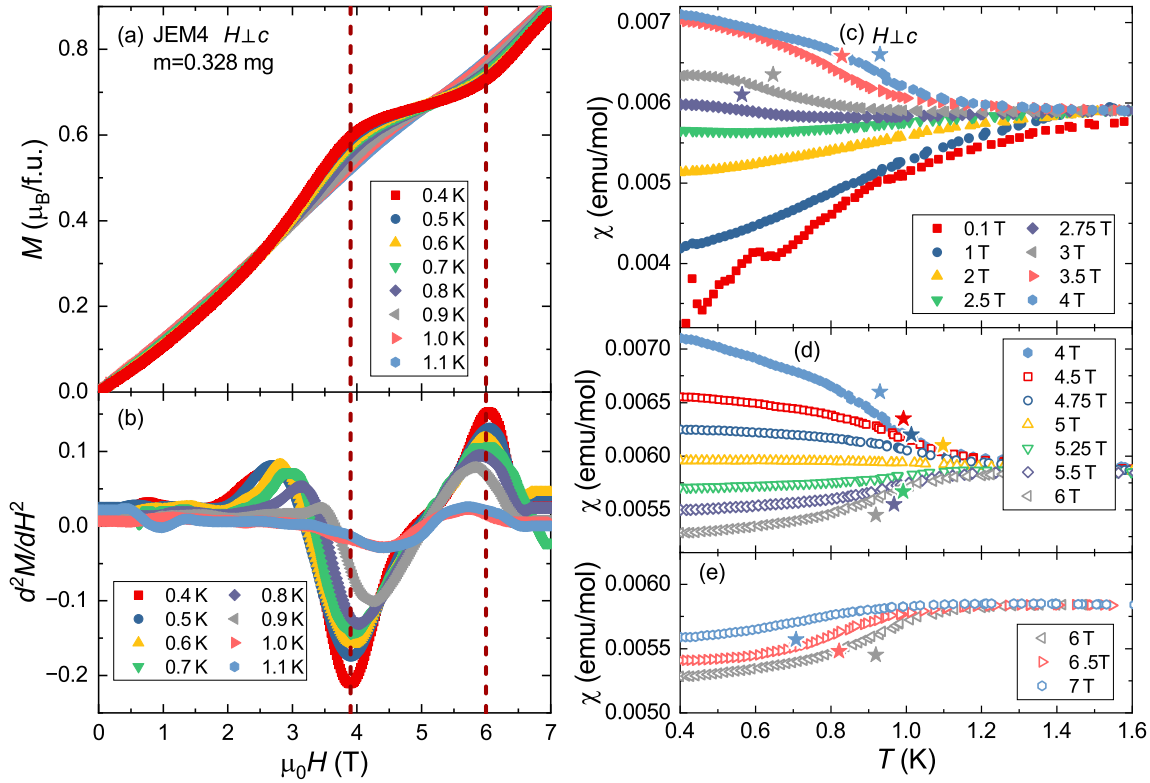

Figure 8.6: *(a) Low-temperature field-dependent magnetization measured between 0.4 and 1.1 K. A very distinct plateau feature is observed at about 0.65 μ_B between 4 and 6 T. (b) Second field derivative of $M(H)$ used to determine the beginning and end of the plateau feature in $M(H)$ by tracing the respective minima and maxima. (c)-(e) Low-temperature susceptibility measurement for tracing the magnetic order up to 7 T. The stars indicate the transition to the magnetically ordered phase.*

respectively. The extrema become less pronounced with increasing temperatures, however, the second derivative of $M(H)$ still shows a weak maximum and minimum at 1.1 K, although no plateau is visually discernible in the magnetization at this temperature anymore. The plateau spans a field range of 4 to 6 T, therefore it is shifted to higher magnetic fields compared to $KYbS_2$, $NaYbO_2$ and $KYbO_2$. This is in agreement with the higher θ_{CW} for $H \perp c$ of $NaYbSe_2$ determined from the susceptibility measurements, indicating stronger exchange interactions in $NaYbSe_2$ compared to the other investigated compounds.

The temperature-dependent magnetization at low temperatures can give additional information about the magnetically ordered phase in $NaYbSe_2$. The magnetic order is best traced via the temperature derivative of $\chi(T)$, as was previously done for $NaYbO_2$, $KYbO_2$ and $KYbS_2$. The stars in Fig. 8.6(c)-(e) mark the transition temperatures which are determined from the derivative. A change of slope is first observed for 2.75 T at about 0.5 K and shifts to higher temperatures with increasing magnetic field up to 1.1 K for 5 T. The magnetic transition can be traced up to the maximum

field of 7 T available for the measurement at about 0.7 K. This magnetically ordered phase well incorporates the *uud* phase indicated by the magnetization plateau. The low-temperature $\chi(T)$ measurements for $NaYbSe_2$ closely resemble those of $KYbS_2$, although the phase transitions are more pronounced in the latter. The transition temperatures, on the other hand, are slightly higher for $NaYbSe_2$, with the highest transition temperature at 1.1 K and 5 T, compared to 0.9 K and 4.25 T for $KYbS_2$.

8.6 Phase Diagram

The low-temperature magnetization measurements are used to assemble a *H*-*T* phase diagram for $NaYbSe_2$ shown in Fig. 8.7. For comparison, the magnetic phase transition observed in specific heat and low-temperature susceptibility measurements in Ref. [103] are included in Fig. 8.7 as well. All data points paint a coherent picture of the low-temperature magnetism in $NaYbSe_2$, which agrees well with the phase diagrams determined for related $AYbX_2$ compounds. Field-induced magnetic order is observed from 2 to 8 T via specific heat and susceptibility measurements. The magnetically ordered phase is segmented into at least three sub-phases. Between 4 and 6 T the *uud* phase is identified from the $\frac{1}{3}$ magnetization plateau in the magnetization measurements. The other two phases are located below and above the *uud* phase. Most likely a Y-type magnetic order is established at lower fields, which transitions to the observed *uud* phase at 4 T. Above the *uud* phase the increasing magnetic field favors the formation of a V-type order that finally transitions to the fully polarized state above 12 T.

In comparison to $KYbS_2$ magnetic order appears at about the same magnetic field of 2 T. The *uud* phase of both compounds span about the same range of magnetic fields, with the plateau phase of $NaYbSe_2$ beginning at slightly higher fields (3.8 T) compared to $KYbS_2$ (3.1 T). For $KYbS_2$ the presumable V-type phase above the *uud* phase can be traced up to the fully polarized state at 10.5 T via dilution fridge measurements. In the case of $NaYbSe_2$ a similar behavior can be expected, however the maximum field of the low-temperature magnetization measurements is limited to 7 T in this work and is only slightly extended to 8 T in Ref. [103]. Saturation is reached at 12 T in $NaYbSe_2$ according to high-field magnetization measurements [103]. The shift of the *uud* and the fully polarized phase to higher magnetic fields in $NaYbSe_2$ compared to $KYbS_2$ is due to the increased exchange interactions present in $NaYbSe_2$. The exchange interactions are directly related to the absolute value of the Curie-Weiss temperatures, which range from 12.9(3) to 9.6(3) K for $NaYbSe_2$ and from 8.8(1) to 5.4(3) K for $KYbS_2$, depending on the method applied to determine the low-temperature behavior of the susceptibility. Comparing the respective methods the Curie-Weiss temperature of $KYbS_2$ is at least 4 K smaller than the one of $NaYbSe_2$.

To further complete the phase diagram measurements in the dilution refrigerator for $NaYbSe_2$ would be desirable to access lower temperatures and higher magnetic fields,

extending the magnetic field range up to the fully polarized phase, and identifying additional phase boundaries.

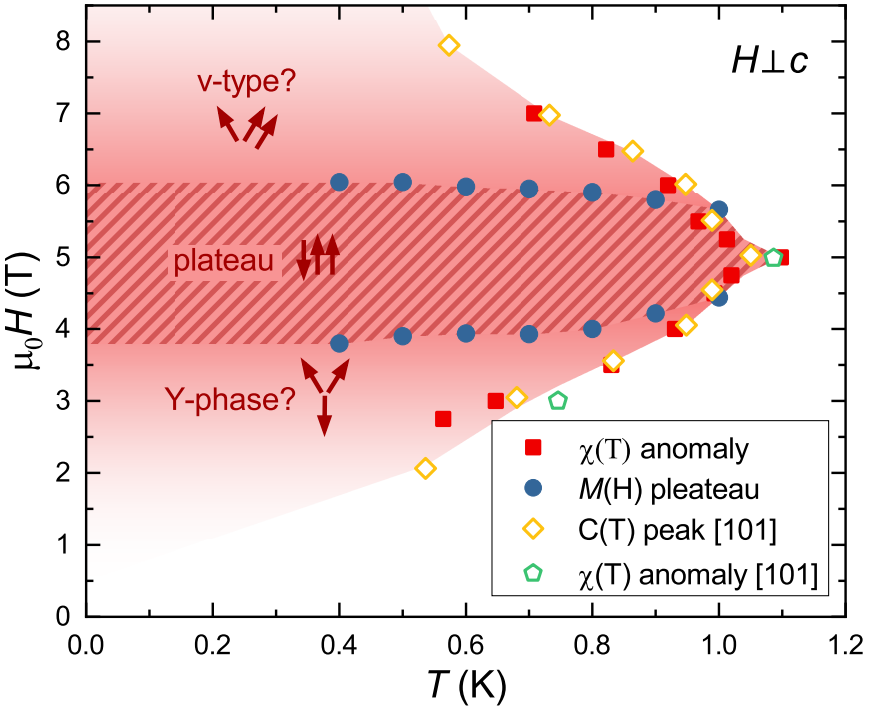

Figure 8.7: *Phase diagram of $NaYbSe_2$ for $H \perp c$ compiled from magnetization and susceptibility measurements at low temperatures. Additionally specific heat and low-temperature susceptibility measurements from Ref. [103] are implemented in the phase diagram for comparison.*

9 $KYb(S_xSe_{1-x})_2$

So far only the influence of exchanging the alkaline metal A of $AYbX_2$ was considered. In this chapter the local environment of the Yb^{3+} ions is altered by substituting the ligand ion X. To this end the sister compounds $KYbS_2$ and $KYbSe_2$ were selected, in the former no signs of magnetic order are observed so far, while the later was found to exhibit magnetic order at 0.29 K in zero field in INS and specific heat measurement [78, 118]. In contrast to the as well attempted substitution of the alkaline metal ($Na_xK_{1-x}YbS_2$), where proofed to be more complicated and hard to control due to the excessive amount of NaCl/KCl flux used in the self-flux synthesis method, it was possible to gradually increase the amount of Se in the compounds and synthesize single crystals for the complete doping series. Since $KYbS_2$ was already thoroughly discussed previously, the first part of this chapter focuses on the already available results for $KYbSe_2$ before highlighting challenges of synthesis and sample characterization of the doped compounds. Synchrotron XRD, ESR, susceptibility and low-temperature magnetization and susceptibility measurements are performed for the different substitution levels to construct preliminary phase diagrams which reveal the effect of Se doping on the magnetism of $KYbS_2$.

9.1 $KYbSe_2$ Literature Results

The synthesis of the $KYbSe_2$ single crystals in Ref. [104] differs from the ones described previously in this work. A two step method was applied, in which polycrystalline $KYbSe_2$ was produced first using K, Yb, and Se as starting materials. Subsequently, the obtained powder was mixed with KCl flux to grow single crystal. With the ratio of $KYbSe_2 : KCl = 1 : 10$ a considerably smaller amount of flux is used in this kind of synthesis compared to the single crystal growth of $KYbS_2$ and $NaYbSe_2$.

XRD measurements confirmed the $R\bar{3}m$ space group. Lattice parameters as well as Yb-Yb distance and the Yb-Se-Yb angle are given in Tab. 9.1.

In measurements of the susceptibility no magnetic order was observed down to 0.4 K in zero field. The typical anisotropy encountered in $AYbX_2$ compounds becomes apparent below 50 K when comparing the measurements for $H \perp c$ and $H \parallel c$. For both field directions a broad maximum was observed at low temperatures indicating short range correlations. Applying a magnetic field ($H \perp c$) larger than 2.5 T induces magnetic order as indicated by a kink in the susceptibility measurements. The formation of *uud* order is evidenced by a $\frac{1}{3}$ plateau in $M(H)$ measurements at 0.42 K. For $H \parallel c$ no magnetic long-range order was observed up to 7 T. The low field

susceptibility was fitted with a linear Curie-Weiss behavior between 200 and 250 K for both field directions. The Curie-Weiss temperatures and the effective moments obtained from the fits are shown in Tab. 9.1. The low-temperature behavior was analyzed using the modified Curie-Weiss law, the Curie-Weiss temperatures determined for both field directions are much smaller compared to the high-temperature fits and give a more realistic representation of the magnetic interactions in the ground state.

Specific heat measurements down to 0.4 K provided no indication of long-range magnetic order as well. Short range correlations are indicated by a broad maximum, as was observed in other members of the $A\mathrm{Yb}X_2$ triangular antiferromagnets. The field induced magnetic order was observed in the specific heat measurements in applied magnetic fields larger than 2 T in accordance with the observations in the low-temperature susceptibility. [104]

The standard measurements down to 0.4 K described so far painted $KYbSe_2$ as a possible QSL candidate, mainly due to the absence of magnetic order. In INS studies however magnetic Bragg peaks were observed below $T_N = 290$ mK, indicating magnetic 120° long-range order, which was subsequently observed in specific heat measurements down to 30 mK in Ref. [118], as well. The J_2/J_1 ratio was also estimated to be within the 120° ordered phase, but close to the QSL phase rendering $KYbSe_2$ an interesting material to explore exotic behaviors. Additionally, the closeness to the QSL phase makes it the perfect candidate to investigate the influence of doping and possibly enter the QSL regime by adjusting the J_2/J_1 ratio.

Table 9.1: *Characteristic properties of $KYbSe_2$ from Ref. [104]. The high-temperature (HT) susceptibility for both field directions is analyzed by fitting with the Curie-Weiss law. At low temperatures (LT) the modified Curie-Weiss law is applied.*

	XRD					
	$\boldsymbol{a}$ **(Å²)**	$\boldsymbol{c}$ **(Å²)**	$\boldsymbol{d}_{\mathbf{inter}}$**(Yb–Yb) (Å²)**		∡ **Yb–Se–Yb**	
[104]	4.1149(5)	22.6911(4)	7.56		93.13(2)°	
	Susceptibility (HT)					
		$\boldsymbol{\mu}_{\mathbf{eff}}$ $(\boldsymbol{\mu}_{\mathbf{B}})$	$\boldsymbol{\theta}_{\mathbf{HT}}$ **(K)**		$\boldsymbol{\mu}_{\mathbf{eff}}$ $(\boldsymbol{\mu}_{\mathbf{B}})$	$\boldsymbol{\theta}_{\mathbf{HT}}$ **(K)**
[104]	$\boldsymbol{H} \perp \boldsymbol{c}$	4.87	−73.5	$\boldsymbol{H} \parallel \boldsymbol{c}$	5.08	−40.3
	Susceptibility (LT)					
		$\boldsymbol{\mu}_{\mathbf{eff}}$ $(\boldsymbol{\mu}_{\mathbf{B}})$	$\boldsymbol{\theta}$ **(K)**		$\boldsymbol{\chi}_{\mathbf{vv}}$ $\left(\frac{\mathbf{emu}}{\mathbf{mol}}\right)$	
[104]	$\boldsymbol{H} \perp \boldsymbol{c}$	3.41	−12.6		0.002	
[104]	$\boldsymbol{H} \parallel \boldsymbol{c}$	0.65	−4.7		0.027	

The INS measurements were analyzed by calculating Quantum Fischer information and revealed multipartite entanglement of the $KYbSe_2$ ground state. [78, 79]

Field- and temperature-dependent specific heat and measurements of the magnetocaloric effect at low-temperature were investigated in Ref. [118] and revealed a detailed phase diagram. Five phases were distinguished in the *H-T* phase diagram. The magnetic order observed in the zero field specific heat measurements below 300 mK invokes a 120° phase in the low-field region. The *uud* phase and the Y-phase typical for the $AYbX_2$ compound family are identified in the low-temperature measurements of $KYbSe_2$, as well. The nature of the additional two phases is not yet evident. They develop below 0.4 K, similar to the 120° ordered phase, and have therefore not been observed in previous measurements.

9.2 Synthesis

$KYb(S_xSe_{1-x})_2$ single crystals were prepared analogous to $KYbS_2$ by altering the ratio of the starting materials stoichiometrically, $KCl : Yb : S : Se = 80 : 2 : 3x : 3(1-x)$. The Se granules and S pieces were ground, mixed with the KCl flux and filled on top of the Yb pieces into the quartz tube in a glove box under argon atmosphere. For the sealing procedure the quartz glass was closed with a disposable glove and a zip tie before removing it from the glove box. This was mainly done to ensure that no potentially toxic substances evaporate while fashioning of the thin neck. For the synthesis the ampules were either sealed with the argon atmosphere preserved from the glove box evacuated and filled with 200 mbar argon atmosphere. The difference between the two methods was neither significant nor systematic. The same heat treatment as for $KYbS_2$ was used and only the impact of altering the holding time on crystal growth and quality was investigated. Longer holding times at 850 °C appeared to only impact the growth of the crystals with larger S content. Here, similar to $KYbS_2$, larger crystals can be connected to longer holding times. The holding time was increased to up to seven weeks. The Se dominant crystals, on the other hand, showed no improvement of size or thickness and even appeared to be negatively impacted concerning the crystal quality by an elongated holding time.

After dissolving the flux, crystals are found on the inner wall of the quartz tube. Similar to $NaYbSe_2$, the crystals are often coated with a black residue which is not soluble in water and has to be mechanically cleaned using a scalpel. Therefore the surface of the crystals often appears rather opaque due to scratch marks and not polished as might be expected from single crystals. An array of crystals over the whole doping series is shown in Fig. 9.1. Starting from the green, hexagonally shaped $KYbS_2$ crystals a change of color is observed already for small amounts of Se content. The crystals with around 90% S have a dark yellow color, but retain the regular form and considerable thickness of the $KYbS_2$ crystals. With increasing Se content the color changes from yellowish to orange. The crystals still have a regular shape and

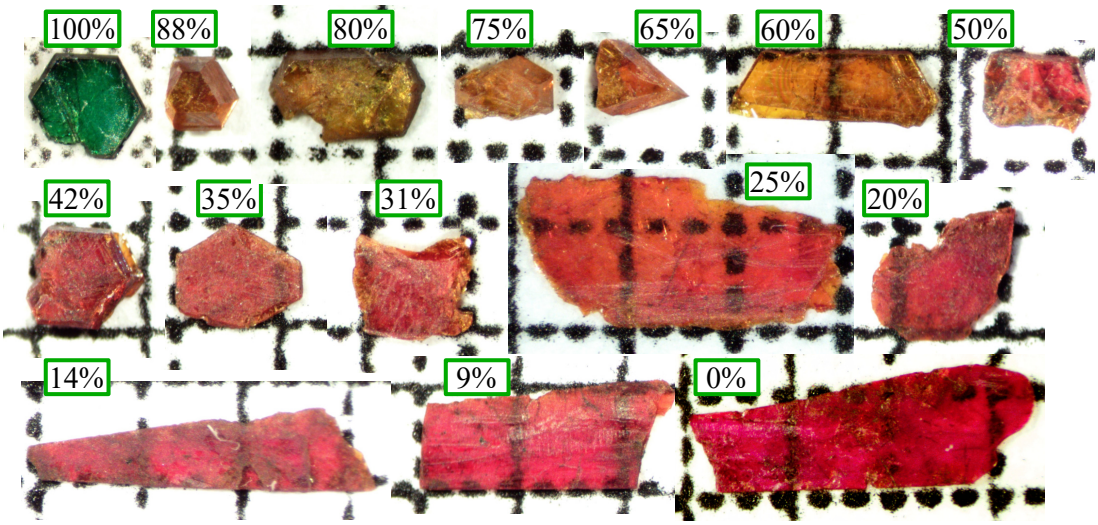

Figure 9.1: *Comparison of different crystals with increasing Se content. The green color of the pure $KYbS_2$ crystal already changes to a yellowish tint for small Se contributions. With increasing Se doping the color changes from orange to a deep red for $KYbSe_2$. While the crystals with dominant S content have a smaller diameter, they are considerably thicker compared to the crystals with higher Se content.*

sizable thickness up to 30% S. For higher Se doping levels they become significantly thinner and adopt the plate-like, irregular form of the $KYbSe_2$ and $NaYbSe_2$ crystals.

9.3 Characterization

After cleaning and identifying visually promising crystals EDX spectroscopy was performed on each individual crystal to determine the Se content. This is an extraordinary effort, since every crystal needs to be manually attached to the sample holder with silver epoxy, investigated, detached, cleaned and labeled according to the respective EDX measurements. This is aggravated by the huge number of investigated crystals and the large fraction of those crystals which are found to have an inhomogeneous Se distribution and are therefore not usable. Fig. 9.2 gives an overview of the ratio of crystals with homogeneous versus inhomogeneous Se distribution on the example of 640 EDX measurements. Out of those 640 ostensibly untainted crystals 41% have an inhomogeneous Se distribution. The other 59% are interpreted as homogeneous, however the actual Se content often differs from the Se content targeted in the respective synthesis. Crystals found to be homogeneous are in many cases not implicitly usable for measurements. While larger crystals are more prone to inhomogeneity than smaller crystals, smaller crystals are often not usable in the experimental setup because of their size or mass. For example, out of the 30 homogeneous crystals with 90% targeted S content, 13 show an actual S content which deviates less than 5% from

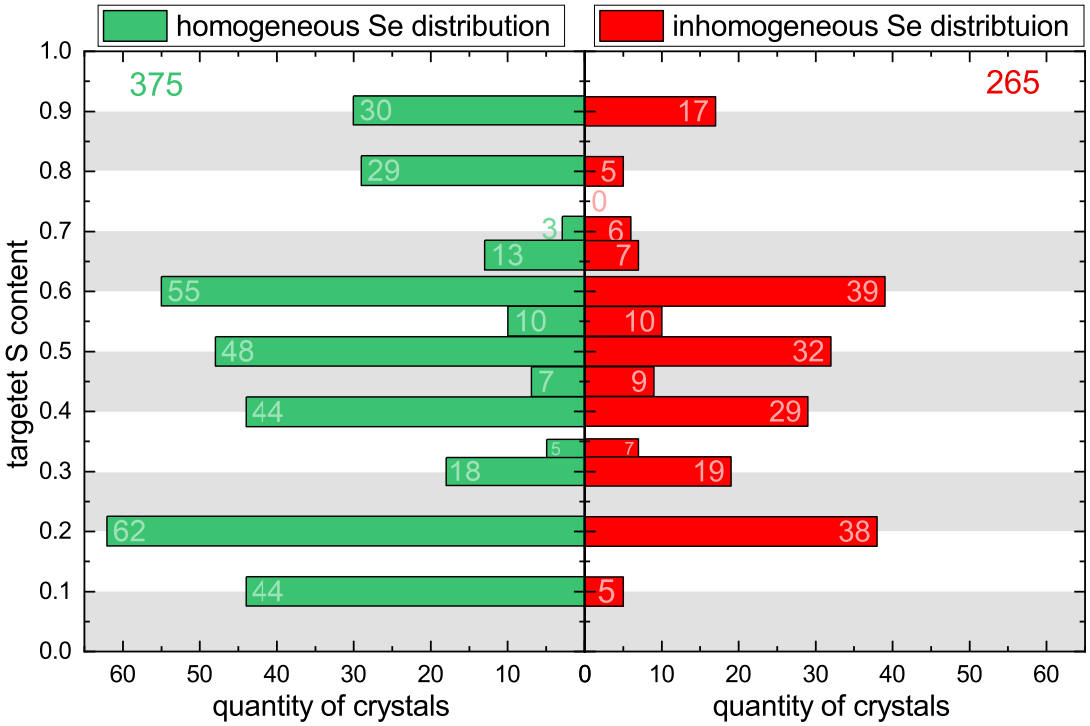

Figure 9.2: *Summary of the EDX measurement results of 640 crystals. The crystals are selected via visual assessment and cleaned of any synthesis residue not dissolvable in water. The individual crystals are investigated via EDX in several small areas on the crystal surface. A deviation of the S content of less than 5% between the different areas is allowed for crystals to be judged as homogeneous.*

the targeted S content and only 5 are large enough to be utilized for single crystal measurements in the MPMS as well as in the dilution fridge.

Generally, a better agreement between the targeted and achieved Se content is observed for the synthesis containing larger amounts of Se. In particular, for those crystals where the S:Se ratio close to 1:1 is intended, a larger deviation occurs, as shown in Fig. 9.3(a). The comparison only includes crystals which were found to be homogeneous in the EDX measurements.
Overall, the grown crystals, irrespective of the S content targeted in the synthesis, cover nearly the complete spectrum of the doping series enabling a detailed investigation.

In Fig. 9.3(b) the quantity of usable crystals according to EDX analysis is depicted in dependence of their diameter (*ab* plane). The statistic only includes crystals which are judged suitable for measurements. Crystals with high Se concentration generally have a larger surface (*ab* plane) but are very thin. Large S content on the other hand yields smaller crystals which are much thicker compared to the Se rich crystals. In terms of mass small, S rich crystals are often comparable to the larger surfaced Se rich crystals. Moreover, the statistic does not include the larger, S rich crystals grown

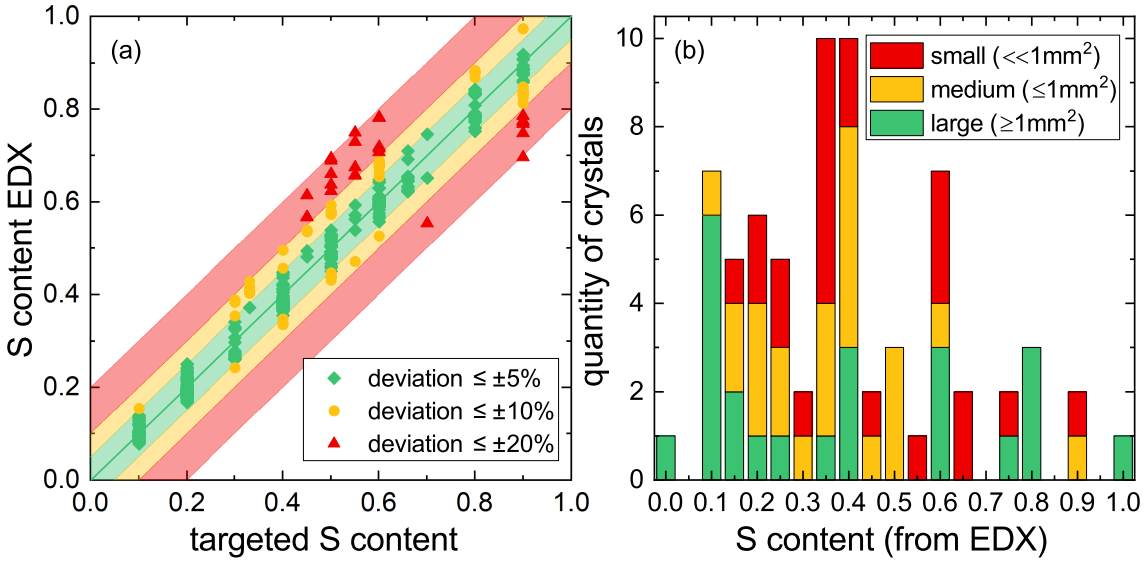

Figure 9.3: *(a) Comparison of the S content targeted in the synthesis and the S content determined from EDX measurements. For this comparison only crystals are considered which show a homogeneous Se distribution. (b) Statistic of crystal size for the different doping levels. Only crystals considered suitable for measurements are considered and thickness of the crystals is not regarded.*

with an elongated holding time at 850 °C, since those syntheses were performed at a later point and are not investigated via EDX at this time.

Remarkably, crystals with an intended S content of 70% are especially elusive. As can be seen in Fig. 9.2, already very little crystals are obtained from this synthesis, and out of the nine crystals only three show a homogeneous Se distribution. Two of them are barely within 5% deviation from the targeted 70% S content [see Fig. 9.3(a)], but none of them are considered suitable for measurements in accordance with Fig.9.3(b). Similarly, growing crystals with a S content between 90% and 100% has not been achieved.

9.4 Synchrotron Measurements

Synchrotron measurements were performed on both end members, $KYbS_2$ and $KYbSe_2$, and six intermediate substitutions at the ID22 beamline at the ESRF in Grenoble. A multianalyzer setup was utilized to investigate the crystals at the wavelength of $\lambda = 0.35432$ Å. Since multiple ground crystals had to be used to fill the capillary for the SXRD measurement, the crystals had to be thoroughly investigated via EDX in advance to determine their exact doping level. Crystals with (nearly) identical composition were selected and finely ground using ethanol for the measurements. In Fig. 9.4(a) an exemplary SXRD measurement for 60% S is shown and fitted with a Rietveld refinement. The doped compounds crystallize with the same $R\bar{3}m$ space

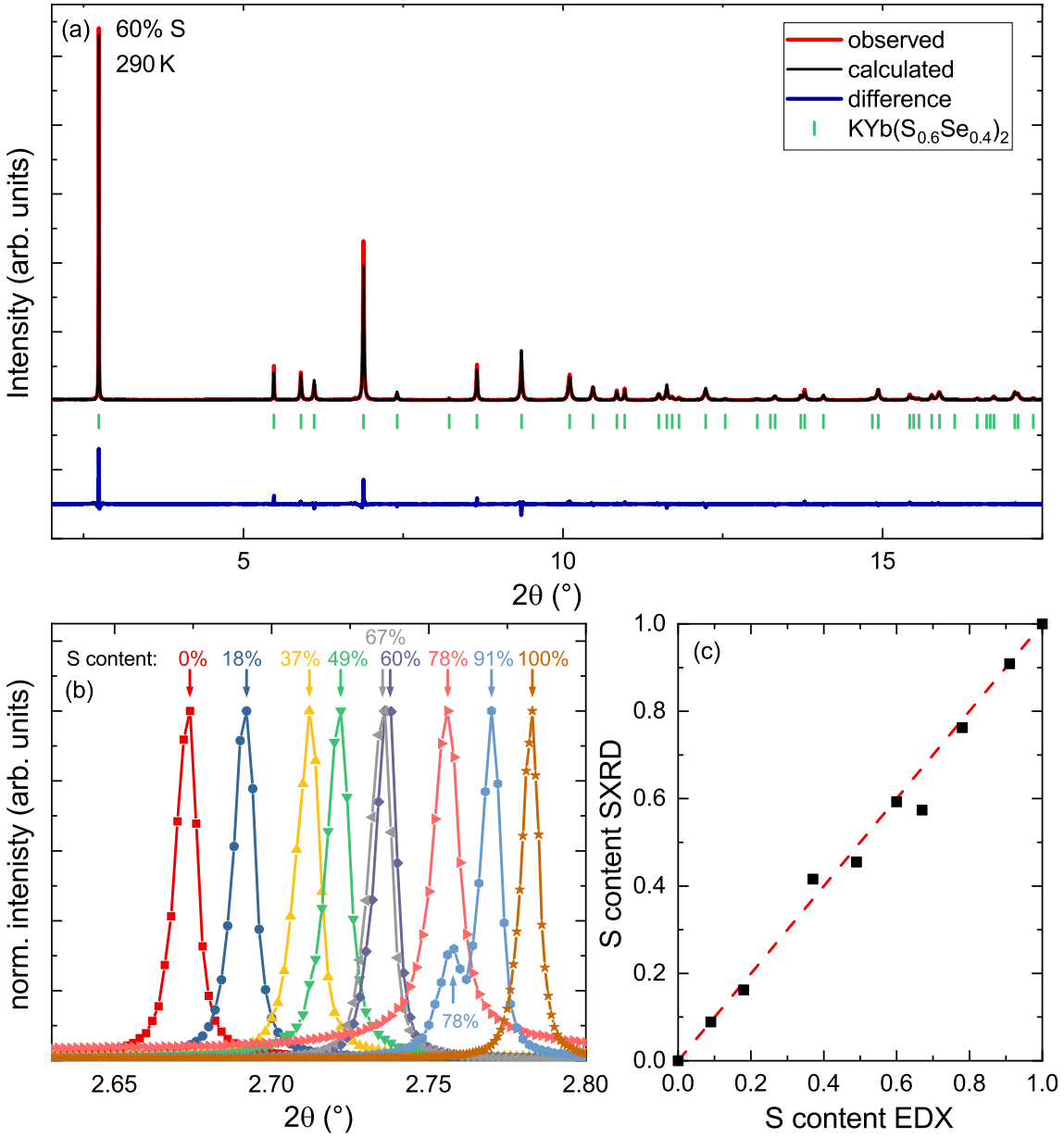

Figure 9.4: *(a) SXRD measurement and Rietveld refinement for crystals with 60% S content. (b) Comparison of the normalized (003) peaks, which is gradually shifted to higher angles with increasing the S content. The S content given in the graph is determined from EDX measurements. For $S = 91\%$ an additional peak is observed which is matched to a second $KYb(S_xSe_{1-x})_2$ phase with $S = 78\%$. (c) S content determined via EDX compared to the one obtained from the Rietveld refinement of the SXRD measurements.*

group as the end members $KYbS_2$ and $KYbSe_2$. No impurity phases are observed for all compounds and high crystallinity of the samples is indicated by narrow peaks in the SXRD measurements. The plate like structure of the crystals leads to an overestimation of the $(00l)$ reflexes which is slightly more prominent in the Se rich compounds, due to their tendency to grow with significantly more lateral expansion. A first, visual impression of the effect of the replacement of S with Se is obtained from the comparison of the (003) peaks of the normalized SXRD measurement in Fig. 9.4(b). Starting from the pure $KYbSe_2$ compound, the (003) peaks are continuously shifted to higher angles with increasing the S content. For the measurement with S= 91% additional peaks in the spectra are observed which are much smaller and located slightly below the distinct reflexes corresponding to the 91% S crystals. In the case of the (003) peak shown in Fig. 9.4(b) the smaller, additional peak of the 91% S measurement is located close to the (003) peak of 78% S sample. Indeed, the additional peaks in the 91% sample are well described by adding a second $KYb(S_xSe_{1-x})_2$ phase with 78% S to the Rietveld refinement. The most likely explanation for the additional peaks therefore is the contamination of the ground 91% S crystals by a 78% S crystal.

From the Rietveld refinement the S content can be determined as well and is compared to the values obtained from EDX measurement in Fig. 9.4(c). Overall, the two methods show good agreement with slight deviations for the S content of 37% (EDX), which was found to be slightly higher in the SXRD measurements (41.5%), and the S content of 67% (EDX), which is found to be much lower (57%). The discrepancy of the EDX and SXRD measurement for the $S_{EDX} = 67\%$ is already apparent in Fig. 9.4(b) where the (003) peak for 67% S is below the peak for 60% S. This is not surprising considering the 70% S crystals are more difficult to synthesize than for other doping levels.

In Fig. 9.5 the development of the lattice parameters, Yb-Yb intralayer distances and Yb-(S/Se)-Yb angles with increasing the S content determined from the SXRD Rietveld analysis are depicted. A decrease of c can be observed from 22.78 Å in $KYbSe_2$ to 21.87 Å in $KYbS_2$. The lattice parameter a decreases as well, although not as significantly, causing a decrease of the cell volume with increasing the S content. This overall shrinkage is well expected when exchanging a larger Se^{2+} ion ($r_{Se} = 1.84$ Å [95]) with a smaller S^{2+} ion ($r_S = 1.70$ Å [95]). The decrease of the lattice parameter c results in a decrease of the Yb interlayer distance by 0.3 Å from $KYbSe_2$ to $KYbS_2$. A nearly linear decrease is also observed for the intralayer distance between the two neighboring Yb ions (Yb–Yb distance) and the distance between the Yb ion and its surrounding S or Se ion (Yb–(S/Se) distance), see Fig. 9.5(b) and (c), respectively.

In contrast to the aforementioned distances, the Yb-(S/Se)-Yb angle initially shows a slight decrease up to 50% followed by an increase towards higher doping levels. The Yb-(S/Se)-Yb angle is influenced by two factors: the Yb–Yb distance and the Yb–(S/Se) distance. Both of those distances decrease, but while the decrease of the Yb-Yb distance results in a shrinkage of the Yb–(S/Se)–Yb angle, a decreasing Yb-(S/Se) distance leads to the opposite effect. Therefore, the decrease of the Yb-

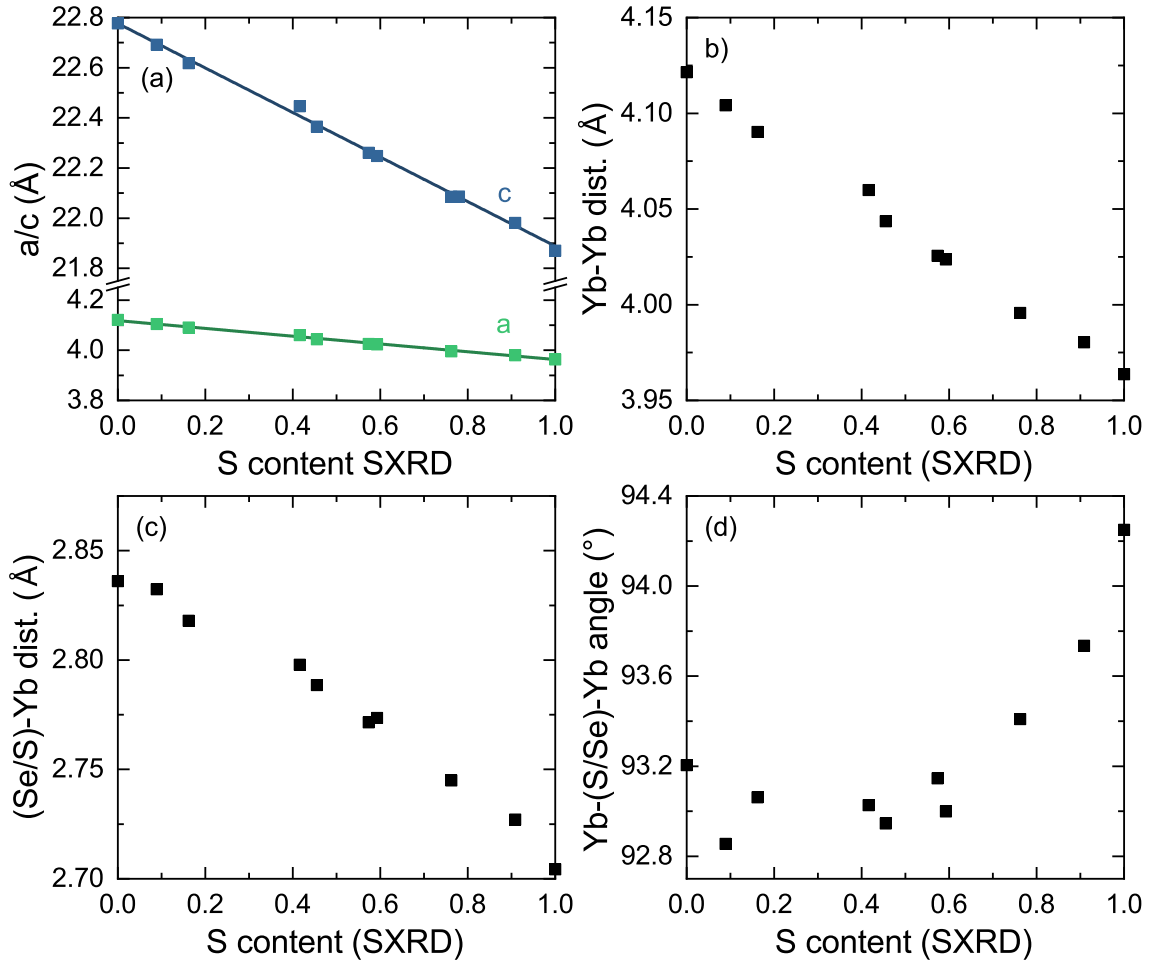

Figure 9.5: *Results of the Rietveld analysis of the SXRD measurements of* $KYb(S_xSe_{1-x})_2$. *The lattice parameters a and c (a) as well as the Yb-Yb distances (b) and the (Se/S)-Yb distances (c) decrease with increasing the S content. (d) The Yb–(S/Se)-Yb angles slightly decrease up to 50% and increase for higher S doping.*

(S/Se)-Yb angle at lower doping levels is compensated by the increase at higher S content and results in an overall increase of the Yb-(S/Se)–Yb angle towards $KYbS_2$.

9.5 ESR Measurements

The ESR measurements give information on the local magnetism of the Yb^{3+} ions. The measurements were performed and analyzed by Hans-Albrecht Krug von Nidda and Mamoun Hemmida. The angular dependence of the g-value was investigated for several members of the doping series, an exemplary measurement for the S content of 53% is shown in Fig. 9.6(a). A large anisotropy is observed in those measurements and the respective g-values for $H \perp c$ and $H \parallel c$ are determined by fitting the angular

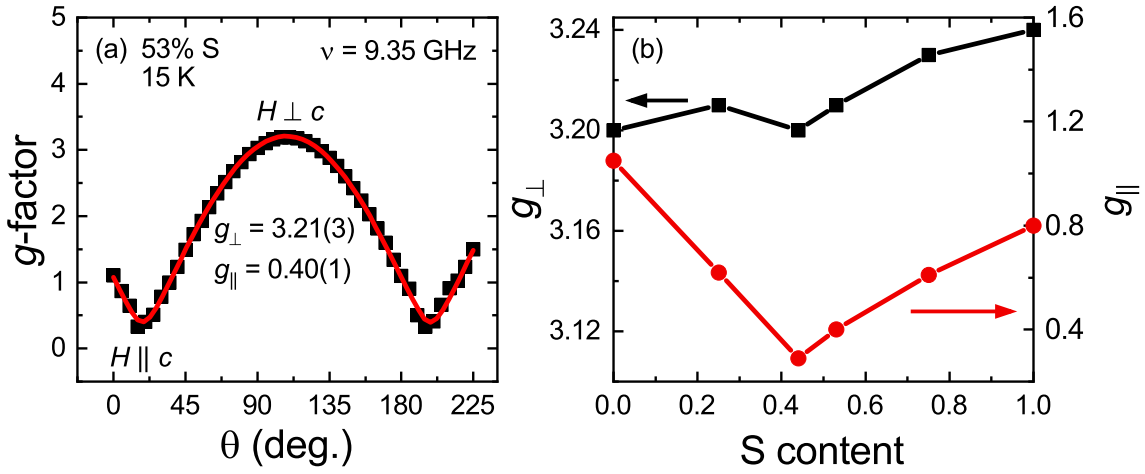

Figure 9.6: *(a) Exemplary measurement of the angle-dependent g-factor for S=53% fitted with* $g(\theta) = g_{\parallel}^2 \cos^2(\theta) + g_{\perp}^2 \sin^2(\theta)$ *(red line) . (b), (c)* $g_{\perp}$ *and* $g_{\parallel}$ *determined from fitting the angle dependent g-value.* $g_{\perp}$ *increases only slightly while the change of* $g_{\parallel}$ *with increasing the S content is more significant.*

dependence with $g(\theta) = g_{\parallel}^2 \cos^2(\theta) + g_{\perp}^2 \sin^2(\theta)$. Fig. 9.6(b) depicts the development of $g_{\perp}$ and $g_{\parallel}$ as a function of the S content in the crystals. $g_{\perp}$ shows a slight increase by 1.2% from $g_{\perp} = 3.20$ for $KYbSe_2$ to $g_{\perp} = 3.24$ for $KYbS_2$. The overall increase of $g_{\perp}$ is interrupted by a minimum at 44% S. A more substantial development is observed for $g_{\parallel}$ where a clear minimum is formed at 44% S. Starting from $g_{\parallel} = 1.05$ for pure $KYbSe_2$ the $g_{\parallel}$ value decreases to $g_{\parallel} = 0.29$ at 44% and then gradually increases to $g_{\parallel} = 0.8$ for $KYbS_2$. The behavior of $g_{\parallel}$ qualitatively follows the development of the Yb-(S/Se)-Yb angle. A similar change of the g-values is observed for $NaYbS_2$ when S is replaced by Se. Only a minor decrease of $g_{\perp}$ from 3.19 for $NaYbS_2$ to 3.13 for $NaYbSe_2$ is determined, while the change of $g_{\parallel}$ from 0.57 for $NaYbS_2$ to 1.01 for $NaYbSe_2$ is more substantial. Interestingly, a much weaker g-tensor anisotropy, $g_{\perp} = 3.0(2)$ and $g_{\parallel} = 1.8(6)$, is obtained for $KYbSe_2$ from INS measurements. [119]

Generally, the doping at the X site of $AYbX_2$ compounds is expected to impact the exchange couplings since the metal-ligand-metal bond angle determines the exchange energy, as was illustrated in Chapter 6 through the comparison of $NaYbO_2$ and $KYbO_2$, whereas g-values of the end members are rather similar to each other. Therefore, not much variance is anticipated in the g-values throughout the doing series, which holds true for $g_{\perp}$ where only a slight increase is observed. However, the change of $g_{\parallel}$ towards the intermediate doping levels is not insignificant.

By measuring the temperature dependence of the ESR linewidth and fitting the high-temperature part with an Orbach process ($\Delta H \propto \exp(-\Delta/T)$) the energy gap Δ between the ground-state Kramers doublet and the first excited CEF level can be obtained. The Orbach process, which describes only the high-temperature part of the linewidth, is again combined with two different models to fit the whole temperature

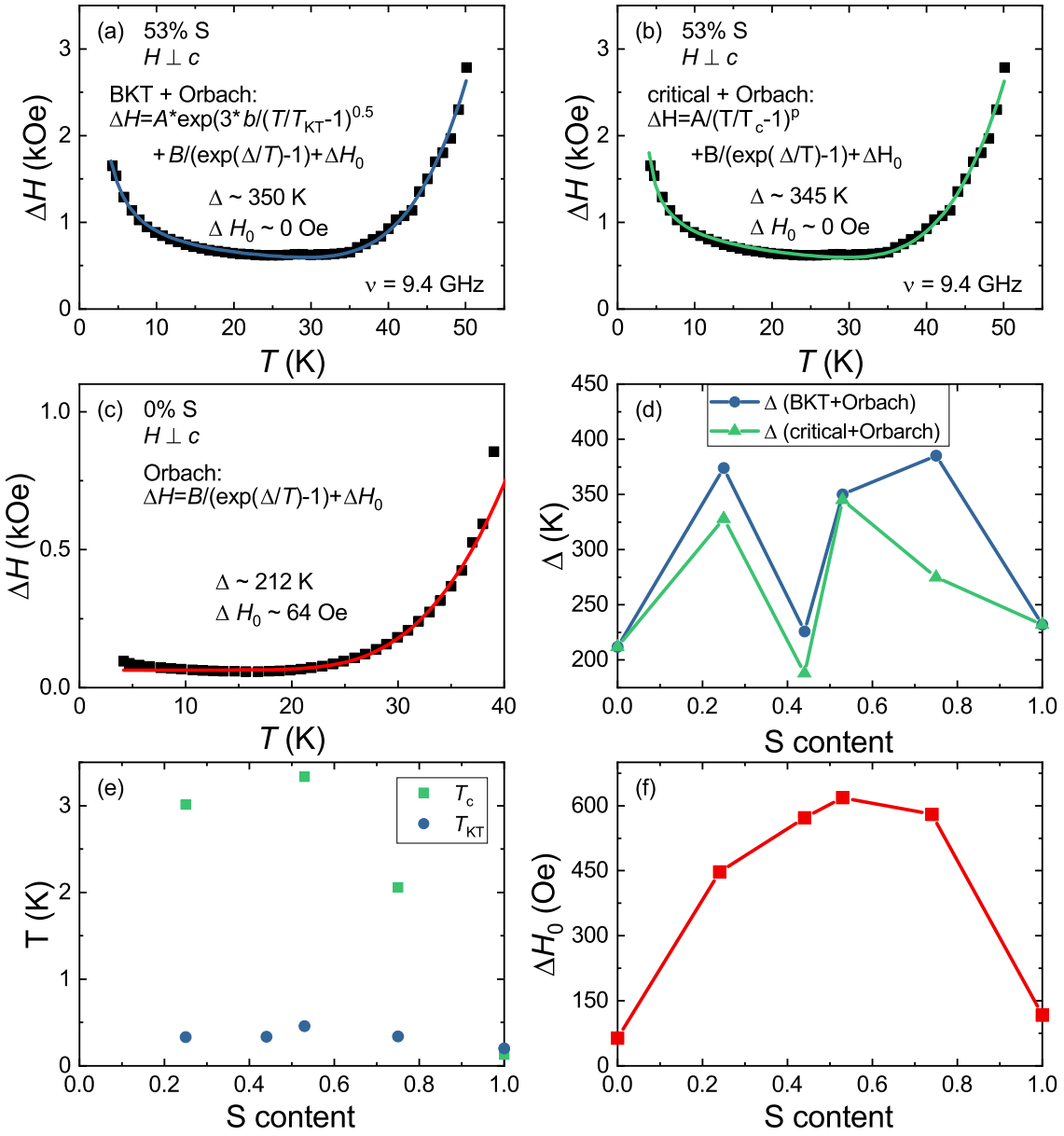

Figure 9.7: *(a), (b) Fit of the ESR linewidth ΔH with two different models (see text for details) on the example of 53% S content for $H \perp c$. (c) Energy gap obtained from the Orbach fit to the high-temperature part of the ESR linewidth, depending on the fit model at low temperatures slightly different values for Δ are obtained. (d) ESR linewidth of pure* $KYbSe_2$ *with an only weakly developed low-temperature part. The high-temperature part is fitted with an Orbach process. (e) Comparison of the critical temperatures determined from fitting with the BKT (T_{KT}) and the classical critical behavior (T_c), showcasing a significant difference between T_{KT} and T_c. (f) Residual linewidth of $KYb(S_xSe_{1-x})_2$ determined by fitting the high-temperature part analogous to the fit of* $KYbSe_2$ *in (c).*

evolution of ΔH. The fit with the first model, assuming the Berezinskii-Kosterlitz-Thouless (BKT) transition at low temperatures, is depicted in Fig. 9.7(a), while in Fig. 9.7(b) the classical critical behavior in the proximity of a phase transition is applied to fit the low-temperature part. Both fit functions describe the data well and visually no difference is observed. Energy gaps between about 200 and 400 K are observed [shown in Fig. 9.7(c)]. The obtained values are slightly influenced by the model used to describe the low-temperature part of the ESR linewidth, with the 75% S sample showing the most significant disagreement. The energy gap of $KYbSe_2$ from the ESR measurement ($\Delta = 212$ K) is in good agreement with the one determined via INS measurements of the CEF excitations in Ref. [119], $\Delta = 200$ K. The critical temperatures T_{KT} and T_{c} determined from the fits are compared in Fig. 9.7(e). In contrast to the results for pure $KYbS_2$, where the critical temperatures are nearly identical, a significant difference between T_{KT} and T_{c} is found for the doped compounds. The critical temperatures T_{c} range between about 0.2 to 3 K and are much larger than T_{KT} which are below 0.5 K. Nevertheless, the critical temperatures show similar qualitative behavior with a maximum at about 50% S [see Fig. 9.7(e)]. In the case of pure $KYbSe_2$ the low-temperature part is only weakly pronounced as can be seen in Fig. 9.7(d). Measurements to lower temperatures would be necessary to make a cogent analysis. Therefore $KYbSe_2$ was only fitted with an Orbach process at high temperatures.
Compared to other $AYbX_2$ compounds, where a $T^{-0.75}$ power-law was observed, the critical exponents of the doped compounds are much smaller (approximately 0.35) [96]. While the Kosterlitz-Thouless temperature and the critical temperature of $KYbO_2$ ($T_{\mathrm{KT}} = 0.14$ K and $T_{\mathrm{C}} = 0.15$ K) and $KYbS_2$ ($T_{\mathrm{KT}} = 0.2$ K and $T_{\mathrm{C}} = 0.13$ K) were rather closely matched, a large diffrence between T_{KT} and T_{C} is determined for the substitution series. The T_{KT} remains somewhat comparable to $KYbS_2$ for the doped crystals, while T_{C} increases by a factor of 10.

The residual linewidth of $KYb(S_xSe_{1-x})_2$ is determined by only fitting the high temperature part of $\Delta H(T)$ with an Orbach process, in analogy to the analysis of $KYbSe_2$. While for the border compounds a rather small residual linewidth is observed, the value obtained for the doped compounds is much higher [see Fig. 9.7(f)]. The broadening of the ESR linewidth compared to the undoped samples is a sign of a distribution of g-values for $H \perp c$. A distribution of g-values, on the other hand, implies that $g_\perp$ is not unaffected by the changing environment of the Yb^{3+} ions, as can be assumed based on the only slight change of angle-dependent measurements of the average $g_\perp$-value discussed previously.

9.6 Susceptibility

To determine the magnetic properties of $KYb(S_xSe_{1-x})_2$ the magnetic susceptibility is investigated. The inverse susceptibility ($H \perp c$) for S = 50% is shown in Fig. 9.8 (a). All members of the doping series show a similar behavior with a linear high-temperature

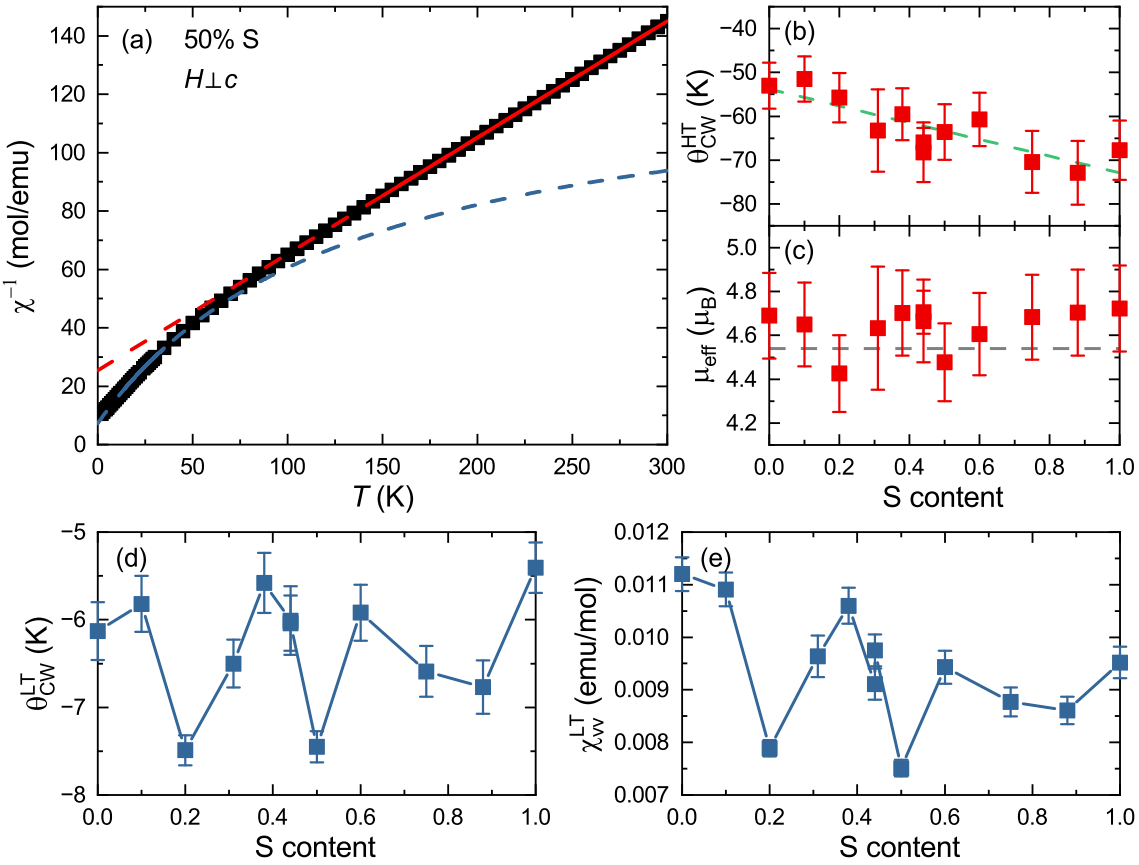

Figure 9.8: *(a) Inverse magnetic susceptibility of $KYb(S_xSe_{1-x})_2$ for $x = 0.5$ showing a linear behavior at high temperatures fitted with a Curie-Weiss law (red line) and a deviation from the Curie-Weiss behavior at low temperatures due to the van Vleck contribution which is fitted with the modified Curie-Weiss law (blue line). (b),(c) θ_{HT} and μ_{eff} determined from the linear fit to the inverse susceptible at high temperatures. (d), (e) θ_{LT} and χ_{vv} determined from the low-temperature fit with the modified Curie-Weiss law with the effective moment fixed from the ESR g-value.*

behavior and the change of slope towards lower temperatures which is typical for the $A\mathrm{Yb}X_2$ compounds. By linearly fitting the high-temperature part the Curie-Weiss temperature θ_{HT} and the effective moment μ_{eff} are obtained. The high-temperature Curie-Weiss temperature shows an overall decrease from $-53(5)\,\mathrm{K}$ for $KYbSe_2$ to $-67(7)\,\mathrm{K}$ for $KYbS_2$, see Fig. 9.8(b). The effective moment is close to the value or free Yb^{3+} ions, $\mu_{\mathrm{eff}} = 4.54\,\mu_{\mathrm{B}}$, throughout the whole doping series, as is depicted in Fig. 9.8(c). At low temperatures the magnetism is dominated by the pseudospin-$\frac{1}{2}$ properties of the ground state Kramers doublet and results in a deviation from the Curie-Weiss law. The measurements are therefore fitted with the modified Curie-Weiss law (Eq. 2.14) between 15 and 35 K taking the influence of the van Vleck contribution χ_{vv} into account. χ_{vv} is treated as a free parameter, while the g-factor is used to fix

the effective magnetic moment. Fig. 9.8(d) and (e) show the values of θ_{LT} and χ_{vv} determined from the low-temperature fit. Compared to Ref. [104], with $\theta_{\mathrm{LT}} = -12.6\,\mathrm{K}$, here a higher Curie-Weiss temperature of $\theta_{\mathrm{LT}} = -6.1(3)\,\mathrm{K}$ is obtained for $KYbSe_2$. The Curie-Weiss temperature determined from the low-temperature behavior of the susceptibility remains rather constant at about $-6\,\mathrm{K}$ for the whole doping series, with two dips at 20% and 50% S content to about $-7.5\,\mathrm{K}$. For $KYbS_2$ the highest Curie-Weiss temperature $\theta_{\mathrm{LT}} = -5.4(3)\,\mathrm{K}$ is found, however the comparison with θ_{LT} determined from the ESR intensity, $\theta_{\mathrm{LT}}^{\mathrm{ESR}} = -12\,\mathrm{K}$, and from the susceptibility corrected by χ_{vv} (from the high-field magnetization measurement),$\theta_{\mathrm{LT}} = -7.3(9)\,\mathrm{K}$, indicates a rather wide window for the Curie-Weiss temperature of $KYbS_2$. No obvious trend is observed and overall a variance of only 2 K is determined for the θ_{LT} of the doping series. Interestingly, the behavior of the Curie-Weiss temperature and the van Vleck contribution displays some similarity. χ_{vv} appears to decrease only slightly from $0.0112(3)\,\frac{\mathrm{emu}}{\mathrm{mol}}$ for $KYbSe_2$ towards $0.0095(3)\,\frac{\mathrm{emu}}{\mathrm{mol}}$ for $KYbS_2$, but two dips are observed at 20% and 50% S, as is the case for θ_{LT}. In the case of $KYbSe_2$ a rather large discrepancy to the van Vleck contribution determined in Ref. [104] is observed. Xing *et al.* [104] obtained a much smaller van Vleck contribution of $0.002\,\frac{\mathrm{emu}}{\mathrm{mol}}$. However, this value appears to be uncharacteristically small compared to the other $AYbX_2$ compounds.

Since the van Vleck contribution is related to excitations to higher CEF levels, it depends on the size of the energy gap Δ between the ground state doublet and the first excited CEF level determined in the ESR measurement. A larger CEF energy gap should lead to a smaller van Vleck contribution and vice versa. As shown in Fig. 9.7

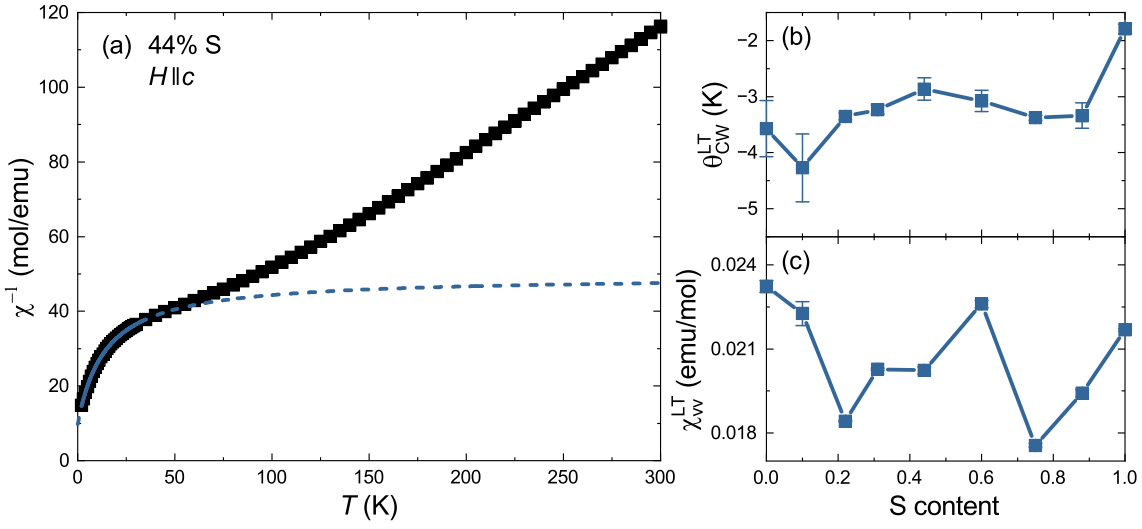

Figure 9.9: *(a) Inverse magnetic susceptibility of $KYb(S_xSe_{1-x})_2$ for $x = 0.44$ and $H \parallel c$. The pronounced downward curve at low temperatures is fitted with the modified Curie-Weiss law (blue line). (b),(c) θ_{HT} and μ_{eff} determined from the low-temperature fit.*

the energy gap possess two maxima at about 25% and 50% S which corresponds nicely with the two minima observe for χ_{vv}.

For $H \parallel c$ only the low-temperature behavior of the susceptibility is investigated by fitting with the modified Curie-Weiss law, see Fig. 9.9. Similar to $H \perp c$, the low-temperature Curie-Weiss temperature stays rather constant at around $-3\,\mathrm{K}$. The van Vleck contribution shows a qualitatively similar behavior compared to the van Vleck contribution for $H \perp c$ with a slight decrease from $KYbSe_2$ to $KYbS_2$, although the second minimum is located higher at about 75% S. The Curie-Weiss temperature obtained for $KYbSe_2$ with $H \parallel c$ is smaller than the one reported in literature, $\theta_{LT} = -4.7\,\mathrm{K}$, but a similar van Vleck contribution is determined $\chi_{vv} = 0.027\,\frac{\mathrm{emu}}{\mathrm{mol}}$ [104].

9.7 Low-Temperature Magnetization

The plateau phase detected in the low-temperature magnetization measurements of $KYbS_2$ and $KYbSe_2$ is also observed throughout the doping series. While the plateau at $0.4\,\mathrm{K}$ is very distinct for the end members, it fades towards the more equally composed samples (see Fig. 9.10). Starting from $KYbSe_2$, the weakening of the plateau feature is rather unobtrusive and a well defined plateau is still observed for up to 14% S content. A clear smearing out of the plateau is noticeable at 22% S which continues up to 31%. For higher S content a change of the plateau feature is hardly discernible from the magnetization measurement and also in the second derivative of $M(H)$ [see Fig. 9.10(b)-(d)] only a weak change is observed for 31-50% S. It is noteworthy that the plateau never disappears completely for the measured degrees of substitution. Further increasing the S content results only in a weak enhancement of the plateau phase up to 88% followed by an abrupt change to the distinct plateau feature observed for $KYbS_2$. Since the crystals with small Se content are more difficult to grow, no crystals with a substitution level between 88% and 100% S were available to observe this change in more detail.

For the individual magnetization measurements a smearing out of the plateau feature with increasing temperature is observed, as was described for the other compounds investigated in this work. The weakening of the plateau feature towards intermediate S/Se content indicates the shift of the plateau phase to lower temperatures, which makes it harder to investigate with the present temperature limitation of $0.4\,\mathrm{K}$. Such a shift of the assumed *uud* ordered phase to lower temperatures could be caused by decreasing exchange interactions. However, the θ_{LT} determined from the low-temperature susceptibility for $H \perp c$ does not suggest such a significant change of the exchange interactions. In $NaYbS_2$ and $NaYbSe_2$ the maximum temperature of the *uud* phase changes only by $0.15\,\mathrm{K}$ for a $1\,\mathrm{K}$ change of the Curie-Weiss temperature. Therefore, the relatively small change of the Curie-Weiss temperature is most likely not the sole origin of the shift of the *uud* phase towards lower temperatures when increasing the disorder at the X site.

As was described in Chapter 7.7, the magnetic order in $KYbS_2$ is nicely traceable through the low-temperature susceptibility measurements. The same holds true for the second end member $KYbSe_2$, see Fig. 9.11. The magnetic order is clearly observed as a distinct kink in χ^{-1}, curving downwards for magnetic fields up to 4 T and upwards for larger magnetic fields. The magnetic order is first observed for a field of 2.25 T slightly below 0.5 K and shifts to higher temperatures with increasing magnetic fields. It reaches a maximum temperature of about 0.9 K at 4 T and is subsequently shifted to lower temperatures again with further increasing field. Above 6 T the magnetic transition disappears below 0.4 T. The stars in Fig. 9.11 mark the transition temperatures which are located at the inflection points. As mentioned

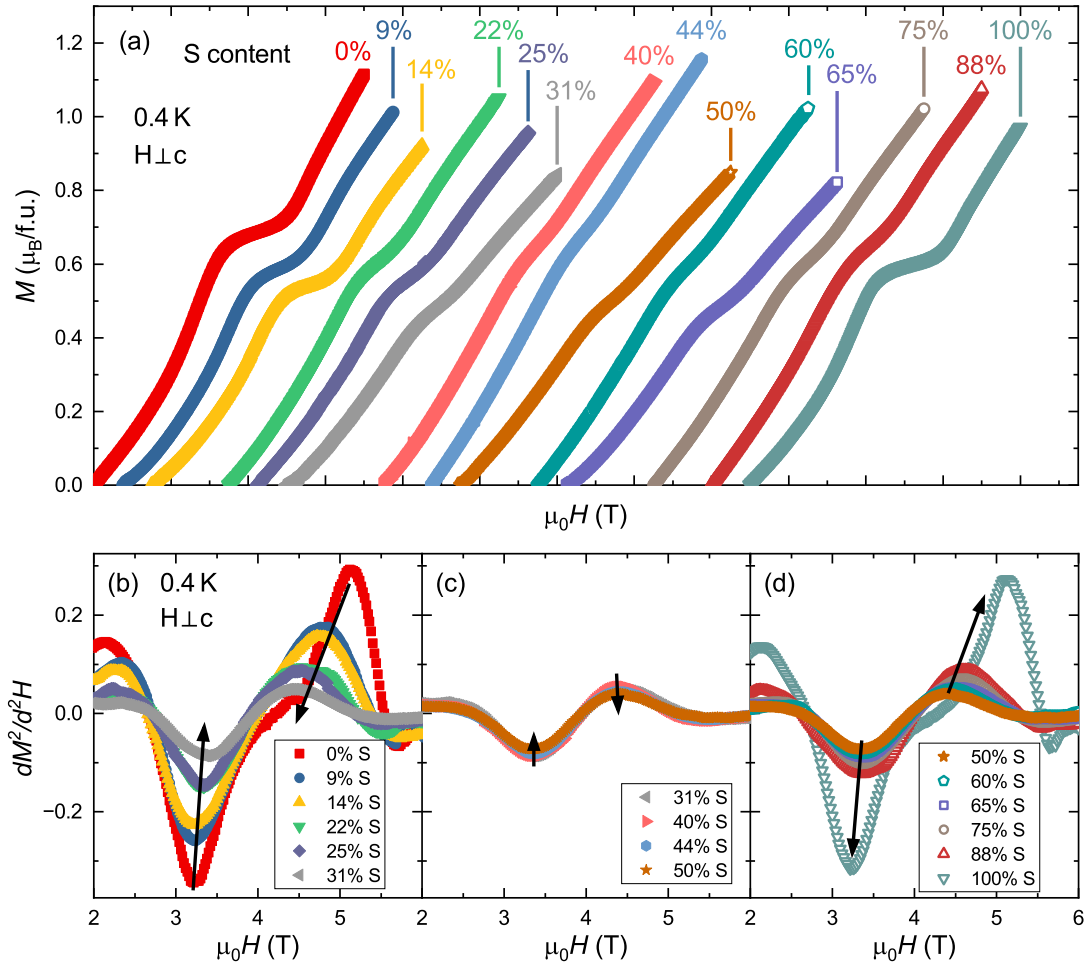

Figure 9.10: *(a) Comparison of the field-dependent magnetization measurements for the $KYb(S_xSe_{1-x})_2$ doping series. All measurements were performed between 0 and 7 T, for better comparability the measurements are shifted relative to each other. The magnetization plateau is clearly observed for the end members $KYbS_2$ and $KYbSe_2$, but fades with increasing S/Se content. (b)-(c) Second derivative of the magnetization for tracing the development of the plateau phase with changing S/Se content.*

before, the inflection point is much easier to trace by the respective maximum or minimum in the first derivative of χ^{-1} as is shown in Fig. 9.11(b).

Tracing the magnetic order in the low-temperature measurements of the susceptibility becomes more challenging for the intermediate compounds.

For 9% S content the magnetic transition is still well observable, but already noticeably less distinct [see Fig. 9.12(a)-(f)]. However, in the calculated first derivative of χ^{-1} the respective maxima and minima are still clearly observed, especially for lower magnetic field. Magnetic order is observed between 2.5 T and 5.25 T. Starting from 2.5 T, the magnetic ordering temperature is shifted up to 0.8 K at 4 T and decreases again for higher magnetic fields.

For 22% S the transition is even less distinct and shifted to a lower temperature regime [see Fig. 9.12(g)-(j)]. Magnetic order is first observed for 2.75 T and disappears below 0.4 K for fields larger than 4.75 T. The maximal transition temperature is reached again around 4 T at 0.6 K. Same as for the 9% sample, the transition temperature in the first derivative of χ^{-1} is better observable for smaller magnetic fields, while at the higher fields the minimum is increasingly hard to discern.

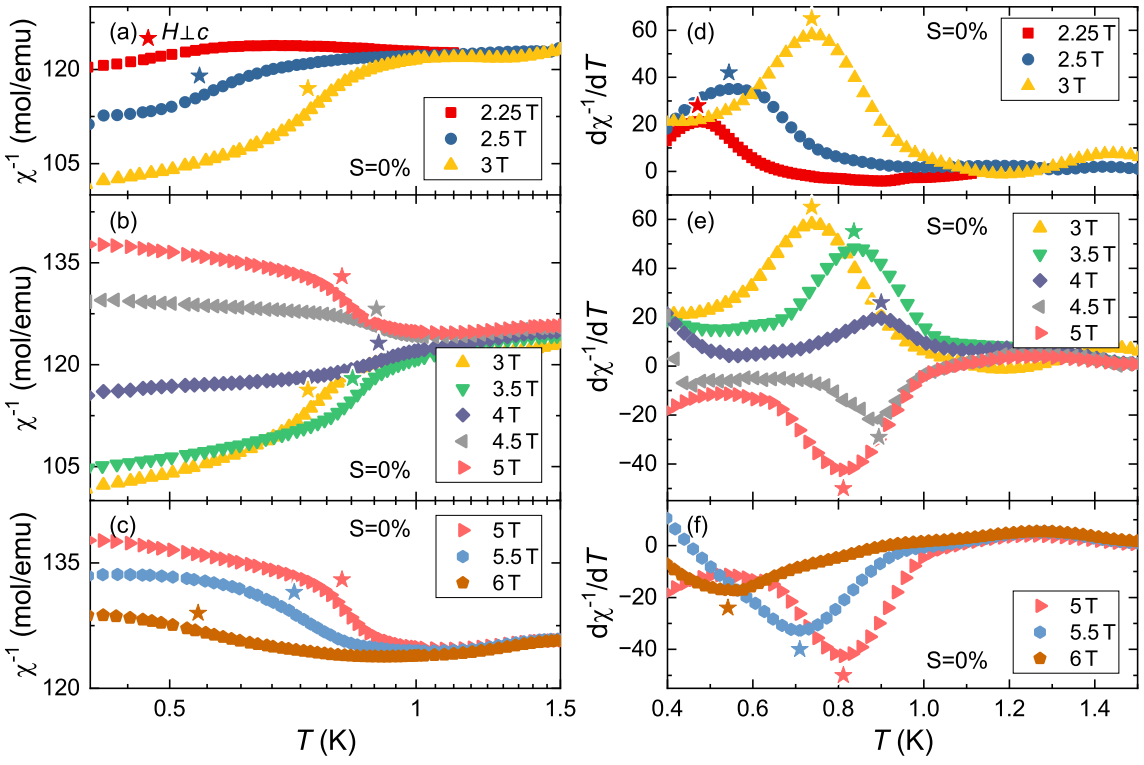

Figure 9.11: *(a)-(c) Inverse magnetic susceptibility of $KYb(S_xSe_{1-x})_2$ in different applied magnetic fields ($H \perp c$). The stars mark the magnetic phase transition at the inflection point. (d)-(f) First derivative of χ^{-1}. The transition temperature to the magnetically ordered phase is determined from the position of the maxima and minima.*

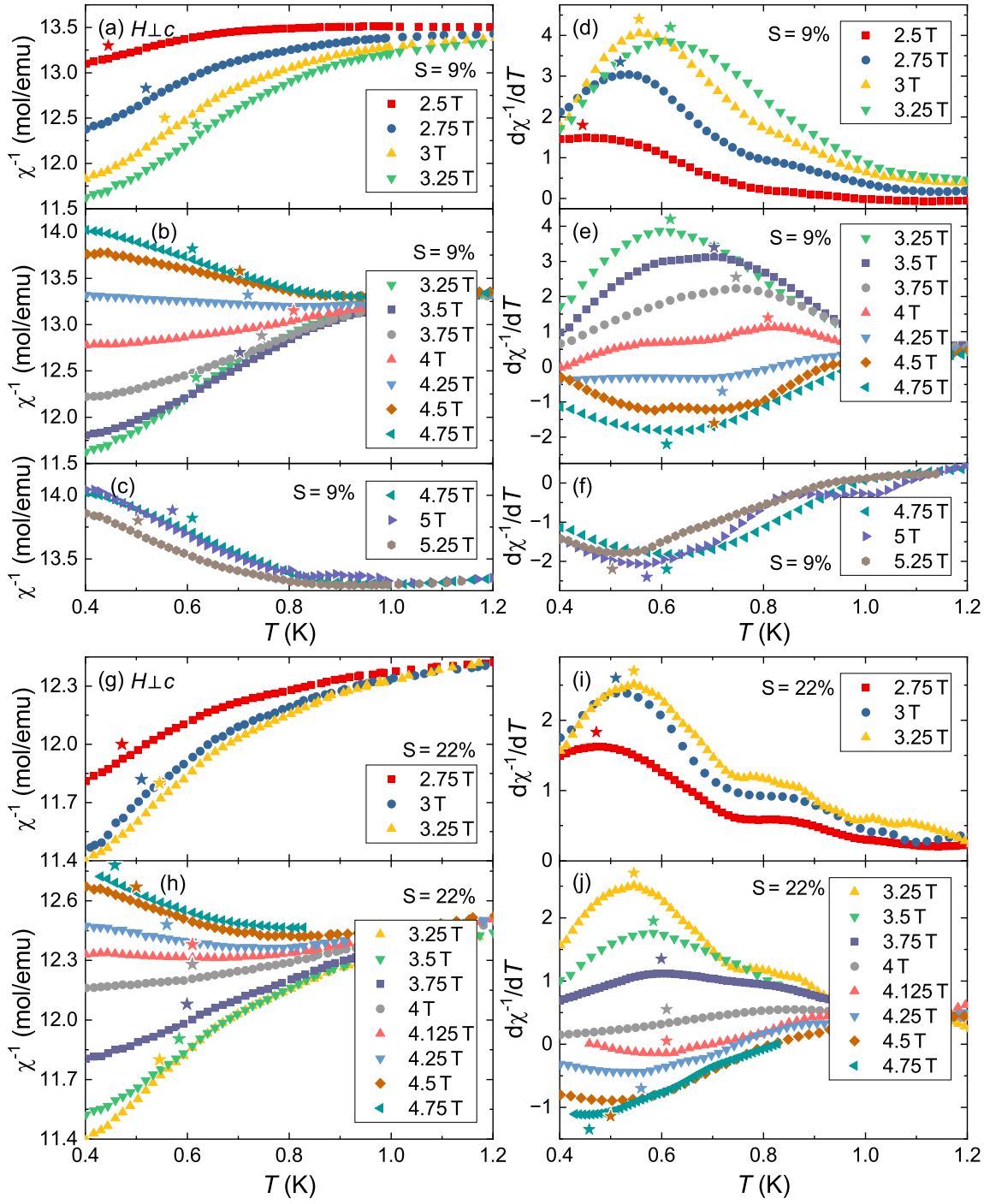

Figure 9.12: *(a)-(c) Low-temperature inverse susceptibility and (d)-(f) derivative of* χ^{-1} *for* $S = 9\%$*. (g),(h) Low-temperature inverse susceptibility and (i),(j) derivative of* χ^{-1} *for* $S = 22\%$*. The stars mark the temperature where the magnetic transition is located.*

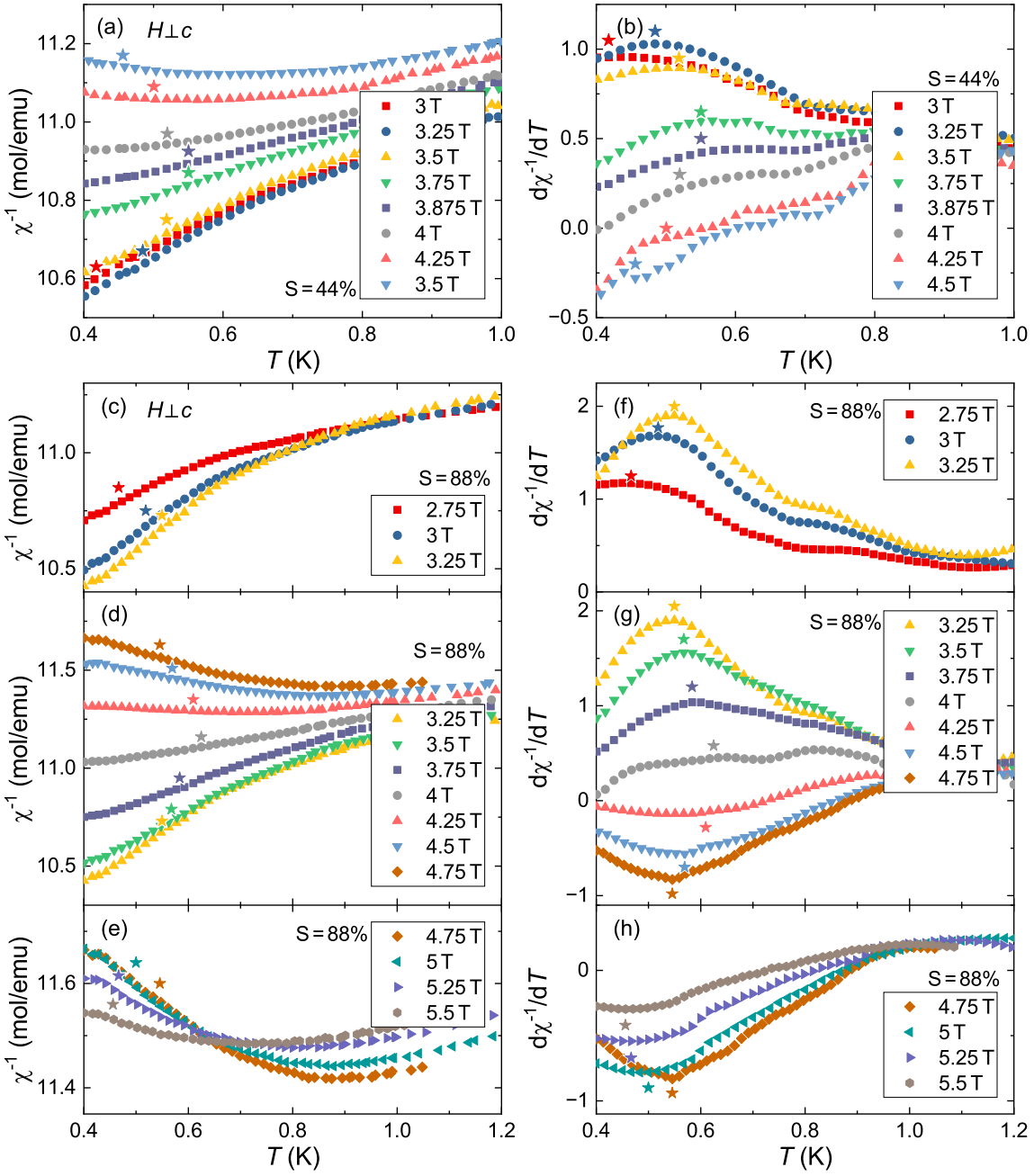

Figure 9.13: *(a) Low-temperature inverse susceptibility and (b) derivative of χ^{-1} for $S = 44\%$. (c)-(e) Low-temperature inverse susceptibility and (f)-(h) derivative of χ^{-1} for $S = 88\%$. The stars mark the temperature where the magnetic transition is located.*

The weakest transition feature is observed for the S content of 44%, shown in Fig. 9.13. The χ^{-1} curves only show a weak downward curvature for fields smaller than 4 T and upward curvature for larger fields. The transition temperatures can only be determined by looking at the first derivative of χ^{-1}, but also there the maxima are only weakly pronounced and the minima are nearly not discernible. Magnetic order is first observed at a magnetic field of 3 T only slightly above 0.4 K. The transition is shifted to higher temperatures up to 3.75 T at about 0.55 K, whereupon the transition temperature decreases again and is observed at 4.5 T and 0.46 K for the last time before the transition disappears below 0.4 K.

For S = 88% the magnetic transition is slightly better observable again (see Fig. 9.13), comparable to the susceptibility measurement with the 22% S content. The respective maxima and minima of the first derivative of χ^{-1} are well pronounced again. The minimum magnetic field for which magnetic order is observed is lowered to 2.75 T again. The transition temperature shifts up to 0.6 K at 4 T, then decreases with further increasing magnetic field. Above 5.5 T the transition temperature is located below 0.4 K and cannot be observed anymore.

Overall, the low-temperature susceptibility reflects the shift of the magnetically ordered phase towards lower temperatures, which was already observed in the magnetization measurements.

The development of the magnetic phase traced by the susceptibility measurements and the *uud* ordered phase, observed in the magnetization, is discussed in the next chapter and illustrated in a *H*-*T* phase diagram.

9.8 Phase Diagram

The phase transitions observed in magnetization and susceptibility measurements are separately depicted in Fig. 9.14 and nicely illustrate the change evoked by the substitution of the X atom in $A\mathrm{Yb}X_2$. In Fig. 9.14(a) and (b) the phase transitions determined from the susceptibility measurement reveal a shift of the magnetically ordered phase to lower temperatures with increasing the S/Se content in the compounds. Additionally, the dome-like shape of the magnetically ordered phase leads to a narrowing of the field range. These effects reaches their apex at about 50% S/Se content.

The decreasing temperature stability of the magnetization plateau observed in $M(H)$ towards intermediate doping levels also reflects the shift of the magnetically ordered phase towards lower temperatures [see Fig. 9.14(c), (d)]. Here, the field range over which the *uud* order expands becomes more narrow towards 50% S/Se content, as well.

The end members show a quite similar behavior in the phase diagram. The *uud* phase extends over nearly exactly the same field region ($3.25 - 5$ T) and the dome-shaped magnetically ordered phase reaches a maximum at about 0.9 K. For $KYbSe_2$ the phase diagram prepared via susceptibility and magnetization measurements down

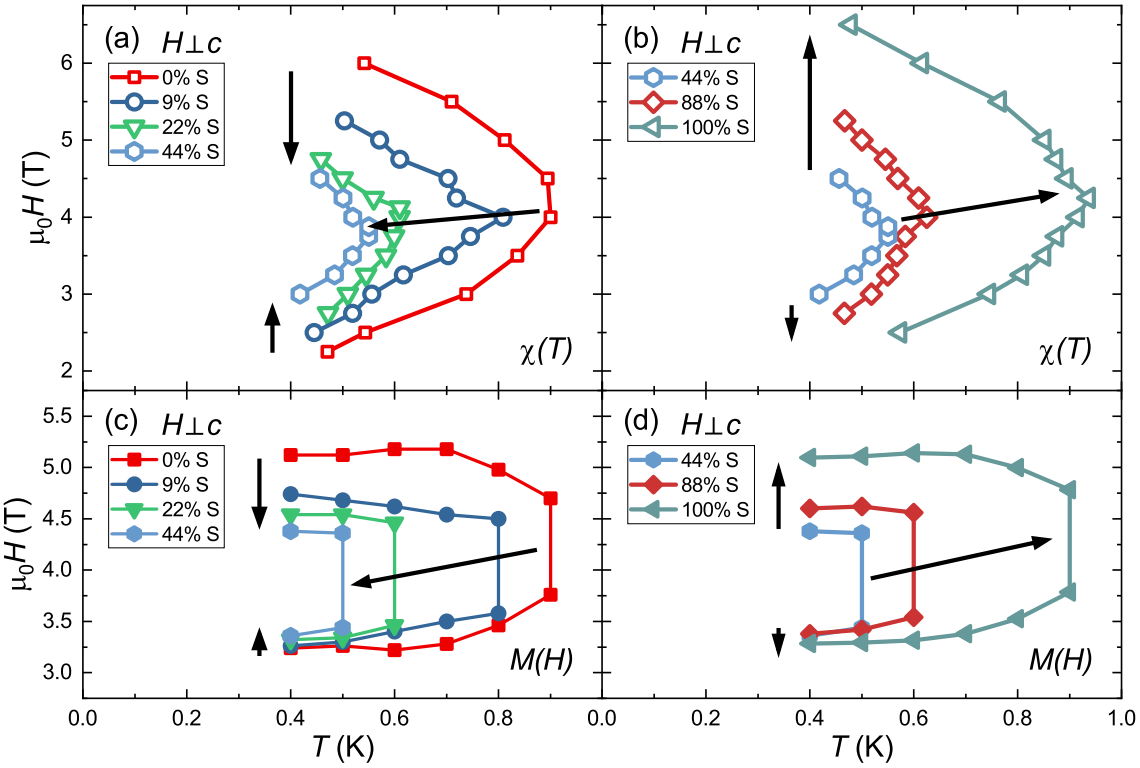

Figure 9.14: *Phase transitions determined from magnetization and susceptibility measurements of $KYb(S_xSe_{1-x})_2$. The magnetically ordered phase observed in the susceptibility is shifted towards lower temperatures with increasing the S content from 0% to 44% (a) then to higher temperatures again up to 100% (b). In the same way, the width of the uud phase determined from the field-dependent magnetization decreases upon approaching 44% (c) and increases towards 100% S (d).*

to 0.4 K in this work is in good agreement with the more detailed phase diagram extracted from low-temperature dilution fridge measurements of the specific heat and the magnetocaloric effect in Ref. [118].

The shift of the magnetically ordered phase towards lower temperatures appears rather gradually from $KYbSe_2$ to 44% S. In contrast, both the change from a quite soft plateau to a very distinct plateau observed in the $M(H)$ measurement and the significant increase of the magnetic transition temperatures from $T_{\mathrm{max}} = 0.6\,\mathrm{K}$ to $T_{\mathrm{max}} = 0.9\,\mathrm{K}$ in the susceptibility are much more abrupt from 88% S to $KYbS_2$.

As aforementioned, a significant reduction of the Curie-Weiss temperatures and therefore the exchange couplings towards intermediate degrees of substitutions is not observed in the analysis of the susceptibility measurements. However, the determined Curie-Weiss temperature is an average parameter and therefore only provides information on the average exchange energy, which remains constant upon doping. Similarly, the average value of $g_\perp$ appears to remain rather unaffected by the Se doping. On the other hand, the shift of the magnetically ordered phase demonstrates the influence of

the structural randomness introduced by doping. A distribution of exchange couplings with the same mean value might be a likely explanation for the observed behaviors. Additionally, a distribution of $g_\perp$ might be present in the compounds.

However, the phase diagram shown in Fig. 9.14 only depicts a small area and leaves many open questions, especially in the low-field, low-temperature region where a potential QSL phase might be located for $KYbS_2$, while magnetic order was found in INS and low-temperature specific heat measurements of $KYbSe_2$ [78, 79, 118]. The KYb(S_xSe_{1-x})$_2$ doping series therefore appears to be an ideal candidate to investigate the influence of doping on a potential QSL towards a magnetically ordered sister compound and to shed light on the question what role the disorder induced by the doping is playing in the QSL formation. In $YbMgGaO_4$ disorder was initially neglected, however, it proofed to play a crucial role in the QSL-like behavior of the compound.

10 Comparison

A large part of this work is the sample preparation and improvement of crystal growth. Two main synthesis approaches can be differentiated, one for polycrystal and one for single crystal preparation. While for the former the synthesis is tailored to the specific compound that is prepared, the single crystal synthesis follows nearly the same procedure for all compounds.

The preparation of polycrystalline samples is based on a solid state reaction which was implemented for the preparation of $NaYbO_2$, $KYbO_2$ and $KYbS_2$. While the synthesis of $NaYbO_2$ is rather straight forward, the preparation of $KYbO_2$ is more challenging. For $NaYbO_2$ the high chemical stability of starting materials and products allow for simple handling of chemicals and heat treatment in a standard box furnace. In contrast, the educts as well as the synthesized $KYbO_2$ itself is prone to react with water. Contact with air moisture influences the reaction and leads to a significant decomposition of $KYbO_2$ in a short amount of time.
The synthesis of polycrystalline $KYbS_2$ is even more challenging than $KYbO_2$, due to the high reactivity of elemental potassium used in the preparation process. Contact with air moisture can cause an active oxidation reaction and has to be prevented. In addition to the extremely sensitive synthesis, the outcome of the synthesis is ambiguous. The products are not homogeneous and have to be carefully sorted to obtain a impurity free $KYbS_2$ sample.

The synthesis of single crystals of the $A\mathrm{Yb}X_2$ compound family was mostly done via the self-flux method described for $KYbS_2$ [109]. Although variations of this method were implemented in literature for $NaYbSe_2$ and $KYbSe_2$, the method applied to $KYbS_2$ proofed to be the most practicable in this work due to omitting an additional crucible which has to be inserted in the quartz glass and the advantage of following an already accustomed process for all synthesis. Additionally, the results of the different synthesis attempts, i.e. with or without a crucible or changes of the heating program, revealed rather similar outcomes considering crystals size and overall quality of the crystals. The biggest impact on crystal size for $KYbS_2$ and $KYb(S_xSe_{1-x})_2$, for the S dominant samples, was found in the holding time at 840 °C/850 °C. For the Se-heavy $KYbSe_2$ and $NaYbSe_2$ no such optimization was observed when varying the synthesis parameters. In contrary, a longer holding time at the maximum temperature seemed to lower the crystal quality.

All compounds investigated in this study possess the $R\bar{3}m$ space group according to (S)XRD measurements. The lattice parameters, characteristic distances and the Yb-X-Yb angles are obtained from Rietveld analysis of powder (S)XRD measurements (see Tab. 10.1). The lattice parameters a are smallest for the $A\mathrm{YbO}_2$ compounds

Table 10.1: *Comparison of characteristic distances and the Yb-X-Yb angle obtained from Rietveld analysis of the (S)XRD measurements. The lattice parameters and distances are given in Å.*

	a	c	Yb-X dist.	A-Yb dist.	∡ Yb-X-Yb
$NaYbO_2$	3.34481(4)	16.4585(2)	2.25537(3)	3.35466(3)	95.723(1)°
$KYbO_2$	3.39731(4)	18.453(3)	2.27232(3)	3.64786(5)	96.756(1)°
$KYbS_2$	3.96369(3)	21.8711(2)	2.7043(9)	4.30398(6)	93.13(2)°
$KYbSe_2$	4.12142(4)	22.7766(4)	2.83609(3)	4.48022(6)	93.2047(9)°
$NaYbSe_2$	4.0539(3)	20.761(1)	2.8390(1)	4.1774(2)	91.118(5)°

and largest for the AYbSe$_2$ compounds. The larger K atom naturally yields a larger lattice parameter a for KYbO$_2$ and KYbSe$_2$ compared to NaYbSe$_2$ and NaYbO$_2$. Similarly, the lattice parameter c is distinctly smaller for AYbO$_2$ compared to KYbS$_2$ and AYbSe$_2$. However, the value of c for KYbS$_2$ is smaller than that of KYbSe$_2$, with $r_S < r_{Se}$, but larger than NaYbSe$_2$, with $r_K > r_{Na}$. The Yb-X distance and the A-Yb distance follow the same qualitative behavior as c. The Yb-X-Yb angle α mediates the super exchange coupling, a smaller angle leads to a stronger exchange coupling. The smallest angle is observed for NaYbSe$_2$ and increases slightly for KYbSe$_2$ and KYbS$_2$. For the oxides α increases further, with the maximum angle for KYbO$_2$.

The results of the ESR measurements are presented in Tab. 10.2. For the single crystalline samples strongly anisotropic g-values are obtained from ESR measurements and also for the polycrystalline NaYbO$_2$ an easy-plane anisotropy is observed. In contrast, KYbO$_2$ revealed a rather isotropic ESR line. While $g_\perp$ is about 3.2 for all compounds, more variation is observed in the value of $g_\parallel$ ranging from 1.8 for NaYbO$_2$ to about 1 for AYbSe$_2$ and 0.8 for KYbS$_2$. Additionally, the energy gap Δ between the ground state doublet and first excited doublet is determined from

Table 10.2: *Comparison of the g-values, energy gap and θ_{CW} determined from measurements of the ESR spectra, linewidth and intensity. The data for $NaYbSe_2$ is taken from Ref. [96].*

	$NaYbO_2$	**$KYbO_2$**	**$KYbS_2$**	**$KYbSe_2$**	**$NaYbSe_2$** [96]
$g_\perp$	3.28(8) [84]	3.08(3)	3.24(1)	3.20(2)	3.13(4)
$g_\parallel$	1.75(3) [84]		0.80(2)	1.05(2)	1.01(1)
Δ (K)	350 [96]	350	232	212	160(30)
θ_{CW} (K)	–	–	−12	–	−14

the ESR linewidth. The large values for Δ of about 220 K for KYbX_2 and 160 K for $NaYbSe_2$ confirm the pseudospin-$\frac{1}{2}$ ground state of the AYbX_2 compounds. For $KYbS_2$ and $KYbSe_2$ the ESR intensity is fitted with a Curie-Weiss law to obtain the Curie-Weiss temperature.

A lot of valuable information can be obtained from the magnetization and susceptibility measurements which are summarized in Tab. 10.3.
High-field magnetization measurements are performed to determine the saturation magnetization and field as well as the van Vleck contribution to the susceptibility. The saturation field is indicated by a noticeable change of slope in the magnetization measurement. In the case of the AYbX_2 compound family the magnetization in the fully polarized phase is not constant but further increases linearly, with a less steep slope, due to the van Vleck contribution. By fitting this increase the saturation magnetization and the van Vleck contribution are determined. Compared to the other compounds, an unusually large van Vleck contribution is determined for $KYbS_2$

Table 10.3: *Comparison of the results obtained from high-field magnetization ($H \perp c$) and low-temperature susceptibility measurements. For $H \perp c$ the susceptibility was, on one hand, analyzed by linearly fitting the susceptibility corrected by the van Vleck contribution from the high-field magnetization, χ_{cor}. On the other hand, the low-temperature part of the susceptibility was directly fitted with the modified Curie-Weiss law with μ_{eff} fixed from the ESR g-value for $H \perp c$ and with all parameters free for $H \parallel c$. The data marked with (a) is taken from Ref. [84], (b) from Ref. [80] and (c) from Ref. [103].*

	high-field $M(H)$ ($H \perp c$)			**low-temp. $\chi_{\mathrm{cor}}(T)$ ($H \perp c$)**	
	M_{sat} (μ_{B})	H_{sat} (T)	χ_{vv} ($\frac{\mathrm{emu}}{\mathrm{mol}}$)	θ_{CW} (K)	μ_{eff} (μ_{B})
$NaYbO_2$	1.36[a]	11	0.00564[b]	−6.4(6)	2.56(6)
$KYbO_2$	1.47	8.6	0.00399	−5.4(2)	2.68(6)
$KYbS_2$	1.4	10.3	0.0126	−7.3(9)	2.83(10)
$NaYbSe_2$	1.5[c]	12[c]	0.00765[c]	−12.3(5)	2.97(2)

	low-temp. $\chi(T)$ ($H \perp c$)		**low-temp. $\chi(T)$ ($H \parallel c$)**		
	θ_{CW} (K)	χ_{vv} ($\frac{\mathrm{emu}}{\mathrm{mol}}$)	θ_{CW} (K)	χ_{vv} ($\frac{\mathrm{emu}}{\mathrm{mol}}$)	μ_{eff} (μ_{B})
$NaYbO_2$	−9.6(3)	0.0026(2)	–	–	–
$KYbO_2$	−5.26(2)	0.00418(2)	–	–	–
$KYbS_2$	−5.4(2)	0.0095(3)	−1.8(1)	0.02188(5)	1.22(1)
$KYbSe_2$	−6.1(3)	0.0071(3)	−3.6(5)	0.0232(2)	1.11(3)
$NaYbSe_2$	−9.6(3)	0.0103(3)	-8.6(8)	0.0178(4)	1.52(5)

from the high-field magnetization. While the kink marking the transition to the fully polarized phase is quite distinct for the single crystalline materials, a more gradual change of slope is observed for the polycrystalline samples, especially $NaYbO_2$. This makes it more difficult to determine the exact saturation field for $KYbO_2$ and $NaYbO_2$. For $NaYbO_2$ the broadening of the transition can be explained by the anisotropic nature of the Yb^{3+} spins which is observed in the ESR spectra. In the magnetization measurement of the polycrystalline material it cannot be differentiated between $H \perp c$ and $H \parallel c$ and therefore both contribute to the resulting magnetization curve. The saturation magnetizations for $H \perp c$ are rather similar for all investigated compounds and range between 1.36 and 1.5 μ_B, in accordance with the similar $g_\perp$ values. The largest saturation field ($H \perp c$) is found for $NaYbSe_2$ at 12 T [103].
The low-temperature part of the susceptibility is analyzed in different manners for $H \perp c$. On one hand, the van Vleck contribution determined from the high-field magnetization is subtracted from the susceptibility measurement and the low-temperature part is fitted linearly according to the Curie-Weiss law. On the other hand, the low-temperature susceptibility is fitted directly with the modified Curie-Weiss law. To constrain the fit with the modified Curie-Weiss law, the effective moment is fixed to the value of $\mu_{\text{eff}}^{\text{ESR}}$ calculated form the ESR g-value. For $KYbO_2$ the different approaches show excellent agreement, while for $NaYbO_2$, $KYbS_2$ and $NaYbO_2$ a discrepancy of at least 2 K is observed for θ_{LT}.

The Curie-Weiss temperature and the saturation field can be used to estimate the strength of the exchange interaction.
Both, the in-plane, $\theta^\perp = -\frac{3}{2}J^{xy}$, as well as the z-component, $\theta^\parallel = -\frac{3}{2}J^z$, of the exchange coupling can be calculated from the Curie-Weiss temperature. For the determination of J^{xy}, both ways of obtaining the Curie-Weiss temperature from the susceptibility are considered. J^z was calculated based on the fit of the low-temperature susceptibility with the modified Curie-Weiss law. The results are given in Tab. 10.4. Additionally, J^{xy} and J^z can be obtained from the saturation field. The saturation field is related to the nearest-neighbor exchange interaction via

$$\mu_0 H_{\text{sat}}^\perp = \frac{9SJ^{xy}k_B}{\mu_B g_\perp} \tag{10.1}$$

and

$$\mu_0 H_{\text{sat}}^\parallel = \frac{3S(2J^z + J^{xy})k_B}{\mu_B g_\parallel}. \tag{10.2}$$

J^{xy} represents the component of the exchange coupling in the ab plane and J^z describes the z-component of the exchange, in accordance with the XXZ model of the triangular lattice introduced in Chapter 2.8.4 [103]. Due to the strong easy-plane anisotropy of the g-tensor only J^{xy} can be obtained from the high field magnetization measurements. The continuous increase of the magnetization for $H \parallel c$ does not allow a simple determination of the saturation field as is the case for $H \perp c$. The exchange couplings are summarized in Tab. 10.4 and illustrated in Fig. 10.1(a).

Table 10.4: *Exchange interactions calculated from the Curie-Weiss temperature and saturation fields. For (a) J^z and J^{xy} are calculated from the susceptibility by fitting with the modified Curie-Weiss law. For (b) the calculation of J^{xy} is based on the susceptibility corrected by the van Vleck contribution from the high-field magnetization. For (c) the saturation field is used to calculate J^{xy}.*

		$NaYbO_2$	$KYbO_2$	$KYbS_2$	$KYbSe_2$	$NaYbSe_2$
(a)	J^z **(K)**	–	–	1.2(1)	2.4(3)	5.7(5)
	J^{xy} **(K)**	6.4(3)	3.54(1)	3.6(1)	4.1(2)	6.4(2)
(b)	J^{xy} **(K)**	4.3(4)	3.6(1)	4.9(6)	–	8.2(3)
(c)	J^{xy} **(K)**	5.4(2)	4.0(1)	5.0(1)	–	5.6(2)

As aforementioned, J^z can only be determined for the single crystalline samples and is generally smaller than the respective J^{xy} value in the $A\mathrm{Yb}X_2$ compound family due to the strong easy-plane anisotropy. Here, a considerable difference between J^z and J^{xy} is observed for $KYbS_2$ and $KYbSe_2$. For $NaYbSe_2$ very similar values for J^z and J^{xy}, calculated from the saturation field, are determined. However, the saturation field used for the calculation of J^{xy} is taken from Ref. [103] and some dissonance between the results in this work and literature has already been addressed in Chapter 8. Therefore, the comparison of J^z and J^{xy} is probably more reliable considering the calculation of J^{xy} from the Curie-Weiss temperatures, where some anisotropy is observed. Still, calculating the exchange couplings from the Curie-Weiss temperatures obtained in Ref. [103] indicates a much stronger exchange anisotropy compared to the findings of this work.
An excellent agreement between J^{xy} calculated from the corrected susceptibility and the saturation field is found for $KYbS_2$, while a slightly lower J^{xy} is obtained for the calculation based on the modified Curie-Weiss law. For $KYbO_2$ the J^{xy} values obtained from the Curie-Weiss temperatures and the saturation field are in rather good agreement, as well. For $NaYbO_2$ and $NaYbSe_2$ the different methods of calculating J^{xy} show a larger variance. Over all, the exchange couplings J^{xy} appear to increase in the order $KYbO_2$, $KYbS_2$, $KYbSe_2$, $NaYbO_2$ and $NaYbSe_2$, see Fig. 10.1(a). Exchanging K by Na leads to an increase of the exchange couplings for $A\mathrm{YbO}_2$ and $A\mathrm{YbSe}_2$ (A =Na, K). Considering $J^{xy} = 9\,\mathrm{K}$ and $J^z = 3\,\mathrm{K}$ calculated from the Curie-Weiss temperatures for $NaYbS_2$ [117] this trend is also true for the $A\mathrm{YbS}_2$ compounds.
In Fig. 10.1(b) the in-plane component of the exchange coupling J^{xy} is compared to the Yb-X-Yb bridging angle, which mediates the super exchange coupling. For J^{xy} the average value was calculated from Tab. 10.4. The correlation between exchange coupling and briding angle is nicely illustrated: a decreasing Yb-X-Yb angle leads to an increase of J^{xy}.

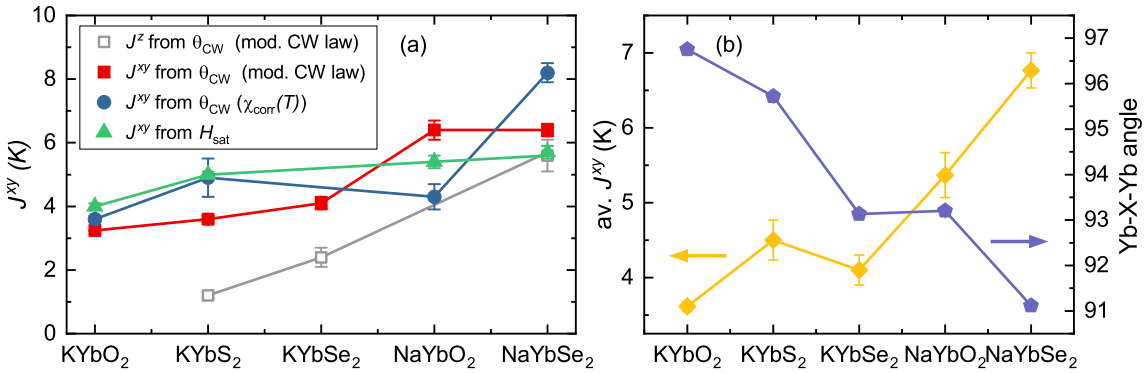

Figure 10.1: *(a) Comparison of the exchange interactions J^z and J^{xy} of the different investigated compounds. J^z (gray) is calculated from the Curie-Weiss temperature obtained from the fit of the susceptibility for $H \parallel c$ with the modified Curie-Weiss law. J^{xy} is, on the one hand, calculated from the Curie-Weiss temperature based on fit with the modified Curie-Weiss law (red) or on the linear fit of the corrected susceptibility (blue) and, on the other hand, calculated from the saturation field (green). (b) Average J^{xy} compared to the Yb-X-Yb angle.*

All investigated compounds possess a plateau feature in the low-temperature magnetization. Signatures of magnetic order are observed in the susceptibility in higher magnetic fields, while no magnetic order is observed in zero field down to 0.4 K.

From the position of the magnetization plateau with respect to the saturation magnetization the nature of the magnetic order can be deduced. A $M_{sat}/3$ plateau indicates the formation of an *uud* magnetic order in the field region of the plateau, while a $M_{sat}/2$ plateau is a sign of *uuud* order. In Tab. 10.5 the calculated M_{plat}/M_{sat} ratio is shown, both M_{plat} and M_{sat} are corrected by the van Vleck contribution. For $KYbO_2$, $KYbS_2$, $NaYbO_2$ and $NaYbSe_2$ the results of the high-field magnetization measurements are used to determine the corrected values of M_{plat} and M_{sat}. In the case of $KYbSe_2$ no high-field magnetization measurements are available so far, therefore the van Vleck contribution determined from the susceptibility measurement is used for the correction of the plateau magnetization value and the saturation magnetization is obtained form the ESR $g_\perp$-value. For all compounds a value larger than $\frac{1}{3}$ is obtained. Indeed, for $KYbO_2$ and $NaYbO_2$ the plateau is close to $\frac{1}{2}$ of the saturation magnetization, although neutron diffraction measurements point toward an *uud* order in $NaYbO_2$ [81]. On the other hand, a *uuud* order appears to be more likely for $KYbO_2$. In the case of the single crystalline samples the ratio of M_{plat}/M_{sat} is closer to $\frac{1}{3}$ than $\frac{1}{2}$. $KYbS_2$, with its rather large χ_{vv} obtained from the high-field magnetization, is closest to the expected value for the *uud* order. The plateaus of $NaYbSe_2$ and $KYbSe_2$ are located closer to $\frac{1}{3}M_{sat}$, as well, indicating the formation of an *uud* order in the respective field range. This field range is nearly identical for $NaYbO_2$, $KYbS_2$ and $KYbSe_2$. For $KYbO_2$ the plateau begins and ends at slightly

Table 10.5: *Comparison of the plateau feature in the magnetization measured at 0.4 K and the maximum temperature of the phase transitions observed in the susceptibility measurements. The value of M_{plat} was determined after subtracting the van Vleck contribution from high-field magnetization measurements for all compounds except* $KYbSe_2$. *For* $KYbSe_2$ *the van Vleck contribution obtained from the susceptility measurement was used and the saturation magnetization was calculated from the ESR g-value.*

	plateau feature (0.4 K)				**phase transition $\chi(T)$**	
	M_{plat}	$M_{\mathrm{plat}}/M_{\mathrm{sat}}$	H_{start}	H_{end}	$T_{\mathrm{N,max}}$	$H(T_{\mathrm{N,max}})$
$NaYbO_2$	$0.61\,\mu_B$	0.45	3.4 T	5.2 T	1.00 K	4.50 T
$KYbO_2$	$0.71\,\mu_B$	0.48	2.6 T	4.0 T	0.71 K	4.50 T
$KYbS_2$	$0.506\,\mu_B$	0.36	3.2 T	5.0 T	0.94 K	4.25 T
$KYbSe_2$	$0.64\,\mu_B$	0.40	3.2 T	5.1 T	0.90 K	4.00 T
$NaYbSe_2$	$0.6\,\mu_B$	0.40	3.9 T	6.0 T	1.10 K	5.00 T

lower magnetic field, while it is placed at slightly higher fields for $NaYbSe_2$ showing a clear correlation with the strength of the nearest-neighbor exchange coupling.

From the susceptibility measurements the magnetically ordered phase can be traced beyond the *uud* or *uuud* phase. For all compounds the magnetic phase remains stable to the highest temperature in the middle of the plateau phase. The magnetically ordered phase of $NaYbSe_2$ reaches the highest temperature of 1.1 K at 5 T, while the magnetic order in $KYbO_2$ is only sustained up to a maximum temperature of 0.71 K at 4.5 T. This again correlates with the strength of the nearest-neighbor exchange coupling.

All magnetic phenomena observed in the investigated compounds can only be traced down to 0.4 K in this work. Measurements to lower temperatures using dilution refrigerators are highly desirable to further investigate the properties of these compounds, as was already done for heat capacity measurements of $NaYbSe_2$ [103] and $NaYbO_2$ [80]. Measurements of the magnetic Grüneisen parameter, thermal expansion, magnetostriction and field-dependent specific heat can further contribute to the compilation of a detailed phase diagram down to millikelvin temperatures, but are beyond the scope of this work.

The phase diagrams presented in this work are mostly deduced from the magnetization and susceptibility measurements. The behavior of the whole $AYbX_2$ compound series is rather similar, resulting in phase diagrams which only differ in subtle details, like the onset of the different phases or the maximum temperature up to which magnetic order persists.
All phase diagrams contain an *uud*/*uuud* ordered phase which is flanked by magnetically ordered phases at higher and lower fields.

The region of the magnetically ordered phase below the plateau phase is expected to be rather narrow, at least in $NaYbO_2$ and $KYbS_2$ where μSR suggests the absence of long-range order in zero field and in $NaYbSe_2$ where heat capacity did not show any indications of the magnetic ordering. Most likely a Y-phase is located in this area.
Above the plateau phase a V-type magnetic order is a probable candidate, which presumably extends up to the fully polarized state. At low magnetic fields no magnetic order is observed, indicating a possible QSL phase at low temperatures in this region. Measurements to lower temperatures might disprove this claim, however, as was the case for $KYbSe_2$ where magnetic order was found at 290 mK.
A variation in the phase diagram is observed for $NaYbO_2$, where an additional phase in the magnetically ordered area above the plateau phase is indicated by susceptibility measurements. The nature and origin of this additional phase is unclear at this time.

11 Summary and conclusion

Overall the behavior of the $A\mathrm{Yb}X_2$ family members investigated here is rather similar. Exchange interactions of several Kelvin are determined for all compounds. A clear dependence of nearest-neighbor exchange on the Yb-X-Yb bond angle is observed, where an decrease of the Yb-X-Yb angle corresponds to an increase of exchange coupling. No magnetic order is observed in this work and in literature for the $A\mathrm{Yb}X_2$ compounds (A =K, Na and X =S, Se, O), with the exception of $KYbSe_2$. The magnetic ordering temperature of $KYbSe_2$ is below the lowest temperature investigated in this work, $T_\mathrm{N} = 0.290\,\mathrm{K}$ [119], therefore, magnetic order can also not be excluded in the investigated $A\mathrm{Yb}X_2$ compounds based on the measurements included here.
Unfortunately, the nature of the $KYbO_2$ samples, namely the severe moisture sensitivity and the porosity of the material, makes measurements towards lower temperatures with a dilution fridge setup complicated. For $NaYbO_2$ and $NaYbSe_2$ low-temperature experiments are available in literature excluding magnetic order down to 50 mK and 40 mK, respectively [80, 103, 114].
Similar, dilution fridge measurements are available for $KYbS_2$ which show no clear signs of magnetic order down to 50 mK, although some so far unclassified features are observed in the specific heat [112] and thermal expansion at low temperatures. The nature of these features is the focus of current investigations, including imminent neutron diffraction measurements on single crystals at low temperatures. $KYbSe_2$ was already investigated by Scheie *et al.* [78] in the temperature range of the magnetically ordered phase via INS and heat capacity measurements. Remarkably, the manifestation of magnetic order is quite subtle in the specific heat, despite the relatively large sample mass of 2.3 mg. Nearly no indication of magnetic order is observed in a lighter sample ($m = 1.2\,\mathrm{mg}$) investigated in the same study. The low-temperature measurements on $KYbS_2$ are performed on a comparatively light sample (m =0.33 mg), which might obscure the traces of the magnetic order in zero field. Therefore, INS measurements are highly desirable to shed light on the low-temperature behavior of $KYbS_2$ and the synthesis of sizable samples ($1 \times 1\,\mathrm{mm}^2$) achieved in this work makes them viable.

The impact of exchanging the alkaline ion in the A position is investigated on the example of $NaYbO_2$ and $KYbO_2$. A prominent difference between $NaYbO_2$ and $KYbO_2$ is the g-factor anisotropy, which is quite distinct in the $A\mathrm{Yb}X_2$ compound family. This holds true for $NaYbO_2$, but the anisotropy vanishes for $KYbO_2$ resulting in a nearly isotropic g-value. Substituting Na by K also leads to an anisotropic expansion of the crystal structure, resulting in a decrease of exchange couplings due to the increase of the Yb-O-Yb angles. The comparison of the phase diagrams visualizes the shift of the different magnetically ordered phases towards lower fields

and temperatures for $KYbO_2$ compared to $NaYbO_2$. The reduction of the magnetic exchange interactions is also observed in the decrease of the saturation field of $KYbO_2$. The investigation of $KYbO_2$ and $NaYbO_2$ therefore presents a pathway to tuning the magnetic interactions by partial substitution of the A position of the $AYbX_2$ compounds. [12]

In a similar line of thought, it was attempted to directly influencing the environment of the Yb^{3+} ions by gradually substituting the ions in the X position. The complete doping series of $KYb(S_xSe_{1-x})_2$ was successfully synthesized for the first time in this work enabling the investigation of the effects of structural randomness in $AYbX_2$ compounds. SXRD measurements showed a gradual and systematic change of the crystal structure. The slight change of the average value of $g_\perp$ in combination with a more drastic change of the average $g_\parallel$-value throughout the doping series leads to an amplified g-factor anisotropy at intermediate S/Se content. No drastic changes of the average low-temperature Curie-Weiss temperature for both field directions are observed. Although, both the average coupling energy as well as the average $g_\perp$-value appear to be unaffected by the introduced randomness, it obviously has impact on the formation of the plateau phase in the magnetization, which is gradually shifted towards lower temperatures when approaching intermediate doping levels. A possible explanation for this incoherent behavior is a distribution of the exchange coupling with the same mean value accompanied by a distribution of the $g_\perp$-value, indicated by the increased residual linewidth for the doped compounds. Measurements towards lower temperatures and INS measurements are desirable to further investigate the suppression of the magnetically ordered phase and to clarify if long-range magnetic order in zero field is present in $KYbS_2$ as well as in $KYbSe_2$.

Bibliography

[1] P.W. Anderson. Resonating valence bonds: A new kind of insulator? *Materials Research Bulletin*, 8(2):153–160, 1973.

[2] Y. Li, P. Gegenwart, and A. A. Tsirlin. Spin liquids in geometrically perfect triangular antiferromagnets. *Journal of Physics: Condensed Matter*, 32(22):224004, 2020.

[3] L. Savary and L. Balents. Quantum spin liquids: a review. *Reports on Progress in Physics*, 80(1):016502, 2016.

[4] L. Clark and A. H. Abdeldaim. Quantum spin liquids from a materials perspective. *Annual Review of Materials Research*, 51:495–519, 2021.

[5] R. S. Feigelson. Crystal growth through the ages: A historical perspective. In *Handbook of Crystal Growth (Second Edition)*. Elsevier, 2015.

[6] T. Paulsen. *Kindler Kokmpakt: Literatur der Antike*. Springer-Verlag, 2017.

[7] I. Sunagawa. *Crystals: Growth, Morphology and Perfection*. Cambridge University Press, 2005.

[8] L. Schubnikow and W. J. De Haas. A new phenomenon in the change of resistance in a magnetic field of single crystals of bismuth. *Nature*, 126:500, 1930.

[9] Y. Li, G. Chen, W. Tong, L. Pi, J. Liu, Z. Yang, X. Wang, and Q. Zhang. Rare-earth triangular lattice spin liquid: A single-crystal study of $YbMgGaO_4$. *Phys. Rev. Lett.*, 115:167203, 2015.

[10] Y. Li, H. Liao, Z. Zhang, Y. Zou, S. Li, F. Jin, L. Ling, L. Zhang, Y. Zou, L. Pi, Z. Yang, J. Wang, Z. Wu, and Q. Zhang. Gapless quantum spin liquid ground state in the two-dimensional spin-$\frac{1}{2}$ triangular antiferromagnet $YbMgGaO_4$. *Scientific Reports*, 5:1–8, 2015.

[11] F. Grußler. *Structural and magnetic characterization of the triangular antiferromagnet $NaYbO_2$*. Master thesis (unpublished), University of Augsburg, 2019.

[12] F. Grußler, M. Hemmida, S. Bachus, Y. Skourski, H.-A. Krug von Nidda, P. Gegenwart, and A. A. Tsirlin. Role of alkaline metal in the rare-earth triangular antiferromagnet $KYbO_2$. *Phys. Rev. B*, 107:224416, 2023.

[13] S. Hunklinger. *Festkörperphysik*. De Gruyter Oldenbourg, 2018.

[14] S. Blundell. *Magnetism in Condensed Matter*. Oxford University Press, 2001.

[15] A. A. Tsirlin. *Lecture notes for "Theory of Magnetism"*. 2018.

[16] C. Kittel. *Einführung in die Festkörperphysik*. Oldenbourg Wissenschaftsverlag, 2002.

[17] J. Jensen and A. Mackintosh. *Rare Earth Magnetism: Structures and Excitations*. 1991.

[18] Y.-D. Li, X. Wang, and G. Chen. Anisotropic spin model of strong spin-orbit-coupled triangular antiferromagnets. *Phys. Rev. B*, 94:035107, 2016.

[19] M. Diviš, J. Hölsä, M. Lastusaari, A.P. Litvinchuk, and V. Nekvasil. Crystal field effect in $YbMnO_3$. *Journal of Alloys and Compounds*, 451(1):662–665, 2008. The 6th International Conference on f-Elements (ICFE-6).

[20] T. Mori, S. Kitayama, Y. Kanai, S. Naimen, H. Fujiwara, A. Higashiya, K. Tamasaku, A. Tanaka, K. Terashima, S. Imada, A. Yasui, Y. Saitoh, K. Yamagami, K. Yano, T. Matsumoto, T. Kiss, M. Yabashi, T. Ishikawa, S. Suga, Y. Onuki, T. Ebihara, and A. Sekiyama. Probing strongly correlated 4f-orbital symmetry of the ground state in Yb compounds by linear dichroism in core-level photoemission. *Journal of the Physical Society of Japan*, 83(12):123702, 2014.

[21] R. Boča. Mean and differential magnetic susceptibilities in metal complexes. *Coordination Chemistry Reviews*, 173(1):167–283, 1998.

[22] T. Moriya. Anisotropic superexchange interaction and weak ferromagnetism. *Phys. Rev.*, 120:91–98, 1960.

[23] M. E. Fisher. Relation between the specific heat and susceptibility of an antiferromagnet. *The Philosophical Magazine: A Journal of Theoretical Experimental and Applied Physics*, 7(82):1731–1743, 1962.

[24] B. Schmidt, J. Sichelschmidt, K. M. Ranjith, T. Doert, and M. Baenitz. Yb delafossites: Unique exchange frustration of $4f$ spin-$\frac{1}{2}$ moments on a perfect triangular lattice. *Phys. Rev. B*, 103:214445, 2021.

[25] A. P. Ramirez. Strongly geometrically frustrated magnets. *Annual Review of Materials Science*, 24(1):453–480, 1994.

[26] L. Balents. Spin liquids in frustrated magnets. *Nature*, 464:199–208, 2010.

[27] A. A. Tsirlin and P. Gegenwart. Frustration mit erstaunlicher Wirkung: Quantenspinflüssigkeiten. *Physik in unserer Zeit*, 50:71–77, 2019.

[28] J. Knolle and R. Moessner. A field guide to spin liquids. *Annual Review of Condensed Matter Physics*, 10(1):451–472, 2019.

[29] D. A. Huse and V. Elser. Simple variational wave functions for two-dimensional Heisenberg spin-$\frac{1}{2}$ antiferromagnets. *Phys. Rev. Lett.*, 60:2531–2534, 1988.

[30] T. Jolicoeur and J. C. Le Guillou. Spin-wave results for the triangular Heisenberg antiferromagnet. *Phys. Rev. B*, 40:2727–2729, 1989.

[31] Z. Zhu, P. A. Maksimov, S. R. White, and A. L. Chernyshev. Topography of spin liquids on a triangular lattice. *Phys. Rev. Lett.*, 120:207203, 2018.

[32] F. Pobell. *Matter and methodes at low temperature*. Springer-Verlag, 2007.

[33] A. P. Cracknell and A. O. Tooke. The specific heats of magnetically-ordered materials. *Contemporary Physics*, 20(1):55–82, 1979.

[34] C. Enss and S. Hunklinger. *Tieftemperaturphysik*. Springer-Verlag, 2000.

[35] Y. Ran, M. Hermele, P. A. Lee, and X.-G. Wen. Projected-wave-function study of the spin-$\frac{1}{2}$ Heisenberg model on the kagomé lattice. *Phys. Rev. Lett.*, 98:117205, 2007.

[36] O. I. Motrunich. Variational study of triangular lattice spin-$\frac{1}{2}$ model with ring exchanges and spin liquid state in $\kappa-(\mathrm{ET})_2\mathrm{Cu}_2(\mathrm{CN})_3$. *Phys. Rev. B*, 72:045105, 2005.

[37] R. Gross and A. Marx. *Festkörperphysik*. De Gruyter, 2018.

[38] L. Spiess, G. Teichert, R. Schwarzer, H. Behnken, and C. Genzel. *Moderne Röntgenbeugung*. Vieweg+Teubner Verlag, 2009.

[39] European Synchrotron Radiation Facility, "How does the ESRF work?". https://www.esrf.fr/home/education/what-is-the-esrf/how-does-the-esrf-work.html. Accessed: 25.05.2023.

[40] L.C. Wagner. *Failure analysis of integrated curcuits*. Kluwer Academic Publishers, 1999.

[41] A.R. West. *Solid State Chemistry and its Applications*. Wiley, 2014.

[42] D. Shindo and T. Oikawa. *Analytical Electron Microscopy for Materials Science*. Springer Japan KK, 2002.

[43] Quantum Design. MPMS Users Manual. 1996.

[44] J. Clarke. SQUIDs. *Scientific American*, 271(2):46–53, 1994.

[45] N. Tateiwa, Y. Haga, Z. Fisk, and Y. Ōnuki. Miniature ceramic-anvil high-pressure cell for magnetic measurements in a commercial superconducting quantum interference device magnetometer. *Review of Scientific Instruments*, 82(5):053906, 2011.

[46] N. Tateiwa, Y. Haga, T. D. Matsuda, and Z. Fisk. Magnetic measurements at pressures above 10 GPa in a miniature ceramic anvil cell for a superconducting quantum interference device magnetometer. *Review of Scientific Instruments*, 83(5):053906, 2012.

[47] N. Tateiwa, Y. Haga, T. D. Matsuda, Z. Fisk, S. Ikeda, and H. Kobayashi. Note: Improved sensitivity of magnetic measurements under high pressure in miniature ceramic anvil cell for a commercial SQUID magnetometer. *Review of Scientific Instruments*, 84(4):046105, 2013.

[48] N. Tateiwa, Y. Haga, T. D. Matsuda, and Z. Fisk. High pressure magnetic measurements on strongly correlated electron systems with a miniature ceramic anvil high pressure cell. *Journal of Physics: Conference Series*, 500(14):142032, 2014.

[49] A. Eiling and J. S. Schilling. Pressure and temperature dependence of electrical resistivity of Pb and Sn from 1-300 K and 0-10 GPa-use as continuous resistive pressure monitor accurate over wide temperature range; superconductivity under pressure in Pb, Sn and In. *Journal of Physics F: Metal Physics*, 11(3):623, 1981.

[50] M. Seidler. MPMS analyzer software. 2021. (https://github.com/miile7/mpms-analyzer).

[51] Quantum Design. PPMS Hardware Manual. 2011.

[52] Y.-D. Li, X. Wang, and G. Chen. Anisotropic spin model of strong spin-orbit-coupled triangular antiferromagnets. *Phys. Rev. B*, 94:035107, 2016.

[53] A. V. Chubukov and D. I. Golosov. Quantum theory of an antiferromagnet on a triangular lattice in a magnetic field. *Journal of Physics: Condensed Matter*, 3(1):69, 1991.

[54] S. Bachus, I. A. Iakovlev, Y. Li, A. Wörl, Y. Tokiwa, L. Ling, Q. Zhang, V. V. Mazurenko, P. Gegenwart, and A. A. Tsirlin. Field evolution of the spin-liquid candidate $YbMgGaO_4$. *Phys. Rev. B*, 102:104433, 2020.

[55] M. Ye and A. V. Chubukov. Half-magnetization plateau in a Heisenberg antiferromagnet on a triangular lattice. *Phys. Rev. B*, 96:140406, 2017.

[56] Y. Li, D. Adroja, P. K. Biswas, P. J. Baker, Q. Zhang, J. Liu, A. A. Tsirlin, P. Gegenwart, and Q. Zhang. Muon spin relaxation evidence for the U(1) quantum spin-liquid ground state in the triangular antiferromagnet $YbMgGaO_4$. *Phys. Rev. Lett.*, 117:097201, 2016.

[57] Z. Ding, Z. Zhu, J. Zhang, C. Tan, Y. Yang, D. E. MacLaughlin, and L. Shu. Persistent spin dynamics and absence of spin freezing in the H-T phase diagram of the two-dimensional triangular antiferromagnet $YbMgGaO_4$. *Phys. Rev. B*, 102:014428, 2020.

[58] J. A. M. Paddison, M. Daum, Z. Dun, G. Ehlers, Y. Liu, M. B. Stone, H. Zhou, and M. Mourigal. Continuous excitations of the triangular-lattice quantum spin liquid $YbMgGaO_4$. *Nature Phys.*, 13:117–122, 2017.

[59] Y. Li, D. Adroja, R. I. Bewley, D. Voneshen, A. A. Tsirlin, P. Gegenwart, and Q. Zhang. Crystalline electric-field randomness in the triangular lattice spin-liquid $YbMgGaO_4$. *Phys. Rev. Lett.*, 118:107202, 2017.

[60] Y. Shen, Y.-D. Li, H. C. Walker, P. Steffens, M. Boehm, X. Zhang, S. Shen, H. Wo, G. Chen, and J. Zhao. Fractionalized excitations in the partially magnetized spin liquid candidate $YbMgGaO_4$. *Nat. Commun.*, 9:4138, 2018.

[61] Y. Shen, Y.-D. Li, H. Wo, Y. Li, S. Shen, B. Pan, O. Wang, H.C. Walker, P. Steffens, M. Boehm, Y. Hao, D.L. Quintero-Castro, M.D. Frontzek, L. Hao, S. Meng, Q. Zhang, G. Chen, and J. Zhao. Evidence for a spinon fermi surface in a triangular-lattice quantum-spin-liquid candidate. *Nature*, 540:559–562, 2016.

[62] Y. Li, S. Bachus, B. Liu, I. Radelytskyi, A. Bertin, A. Schneidewind, Y. Tokiwa, A. A. Tsirlin, and P. Gegenwart. Rearrangement of uncorrelated valence bonds evidenced by low-energy spin excitations in $YbMgGaO_4$. *Phys. Rev. Lett.*, 122:137201, 2019.

[63] Y. Xu, J. Zhang, Y. S. Li, Y. J. Yu, X. C. Hong, Q. M. Zhang, and S. Y. Li. Absence of magnetic thermal conductivity in the quantum spin-liquid candidate $YbMgGaO_4$. *Phys. Rev. Lett.*, 117:267202, 2016.

[64] X. Rao, G. Hussian, W. J. Chu, N. Li, X. Zhao, Z. Dun, E. S. Choi, T. Asaba, L. Chen, L. Li, X. Y. Yue, N. N. Wang, J.-G. Cheng, Y. H. Gao, Y. Shen, J. Zhao, G. Chen, H. D. Zhou, and X. F. Sun. Survival of itinerant excitations and quantum spin state transitions in $YbMgGaO_4$ with chemical disorder. *Nat. Commun.*, 12:4949, 2021.

[65] Z. Ma, J. Wang, Z.-Y. Dong, J. Zhang, S. Li, S.-H. Zheng, Y. Yu, W. Wang, L. Che, K. Ran, S. Bao, Z. Cai, P. Čermák, A. Schneidewind, S. Yano, J. S. Gardner, X. Lu, S.-L. Yu, J.-M. Liu, S. Li, J.-X. Li, and J. Wen. Spin-glass

ground state in a triangular-lattice compound $YbZnGaO_4$. *Phys. Rev. Lett.*, 120:087201, 2018.

[66] M. Majumder, G. Simutis, I. E. Collings, J.-C. Orain, T. Dey, Y. Li, P. Gegenwart, and A. A. Tsirlin. Persistent spin dynamics in the pressurized spin-liquid candidate $YbMgGaO_4$. *Phys. Rev. Res.*, 2:023191, 2020.

[67] Y. Shen, Y.-D. Li, H. Wo, Y. Li, S. Shen, B. Pan, O. Wang, H. C. Walker, P. Steffens, M. Boehm, Y. Hao, D. L. Quintero-Castro, L. W. Harriger, M. D. Frontzek, L. Hao, S. Meng, Q. Zhang, G. Chen, and J. Zhao. Evidence for a spinon fermi surface in a triangular-lattice quantum-spin-liquid candidate. *Nature*, 540:559–562, 2016.

[68] Y. Li, D. Adroja, R. I. Bewley, O. Zhang, A. A. Tsirlin, and P. Gegenwart. Nearest-neighbour resonating valence bonds in $YbMgGaO_4$. *Nat. Commun.*, 8:15814, 2017.

[69] X. Zhang, F. Mahmood, M. Daum, Z. Dun, J. A. M. Paddison, N. J. Laurita, T. Hong, H. Zhou, N. P. Armitage, and M. Mourigal. Hierarchy of exchange interactions in the triangular-lattice spin liquid $YbMgGaO_4$. *Phys. Rev. X*, 8:031001, 2018.

[70] Z. Zhu and S. R. White. Spin liquid phase of the $s = \frac{1}{2}$ $J_1 - J_2$ Heisenberg model on the triangular lattice. *Phys. Rev. B*, 92:041105, 2015.

[71] P. H. Y. Li, R. F. Bishop, and C. E. Campbell. Quasiclassical magnetic order and its loss in a spin-$\frac{1}{2}$ Heisenberg antiferromagnet on a triangular lattice with competing bonds. *Phys. Rev. B*, 91:014426, 2015.

[72] Y. Iqbal, W.-J. Hu, R. Thomale, D. Poilblanc, and F. Becca. Spin liquid nature in the Heisenberg $J_1 - J_2$ triangular antiferromagnet. *Phys. Rev. B*, 93:144411, 2016.

[73] Z. Zhu, P. A. Maksimov, S. R. White, and A. L. Chernyshev. Disorder-induced mimicry of a spin liquid in $YbMgGaO_4$. *Phys. Rev. Lett.*, 119:157201, 2017.

[74] E. Parker and L. Balents. Finite-temperature behavior of a classical spin-orbit-coupled model for $YbMgGaO_4$ with and without bond disorder. *Phys. Rev. B*, 97:184413, 2018.

[75] B. Deng and J. A. Ibers. $CsYbSe_2$. *Acta Crystallographica Section E*, 61(2):i15–i17, 2005.

[76] W. Urland. Magnetische Eigenschaften der Normaltemperaturform von $CsYbO_2$. *Zeitschrift für Naturforschung A*, 35(2):247–251, 1980.

[77] T. Ferreira, J. Xing, L. D. Sanjeewa, and A. S. Sefat. Frustrated magnetism in triangular lattice $TlYbS_2$ crystals grown via molten flux. *Frontiers in Chemistry*, 8, 2020.

[78] A. O. Scheie, E. A. Ghioldi, J. Xing, J. A. M. Paddison, N. E. Sherman, M. Dupont, D. Abernathy, D. M. Pajerowski, Shang-Shun Zhang, L. O. Manuel, A. E. Trumper, C. D. Pemmaraju, A. S. Sefat, D. S. Parker, T. P. Devereaux, J. E. Moore, C. D. Batista, and D. A. Tennant. Witnessing quantum criticality and entanglement in the triangular antiferromagnet $KYbSe_2$. *arXiv preprint*, arXiv:2109.11527 [cond-mat.str-el].

[79] A. O. Scheie, Y. Kamiya, H. Zhang, Sangyun Lee, A. J. Woods, M. G. Gonzalez, B. Bernu, J. Xing, Q. Huang, Q. M. Zhang, J. Ma, E. S. Choi, D. M. Pajerowski, H. Zhou, A. S. Sefat, L. Messio, R. Movshovich, C. D. Batista, and D. A. Tennant. Non-linear magnons and exchange Hamiltonians of delafossite proximate quantum spin liquids. *arXiv preprint*, arXiv:2207.14785 [cond-mat.str-el].

[80] L. Ding, P. Manuel, S. Bachus, F. Grußler, P. Gegenwart, J. Singleton, R. D. Johnson, H. C. Walker, D. T. Adroja, A. D. Hillier, and A. A. Tsirlin. Gapless spin-liquid state in the structurally disorder-free triangular antiferromagnet $NaYbO_2$. *Phys. Rev. B*, 100:144432, 2019.

[81] M. M. Bordelon, E. Kenney, C. Liu, T. Hogan, L. P. Marzieh Kavand, Y. Lyu, M. Sherwin, N. P. Butch, C. Brown, M. J. Graf, L. Balents, and S. D. Wilson. Field-tunable quantum disordered ground state in the triangular-lattice antiferromagnet $NaYbO_2$. *Nature Physics*, 15:1058, 2019.

[82] M. M. Bordelon, C. Liu, L. Posthuma, P. M. Sarte, N. P. Butch, D. M. Pajerowski, A. Banerjee, L. Balents, and St. D. Wilson. Spin excitations in the frustrated triangular lattice antiferromagnet $NaYbO_2$. *Phys. Rev. B*, 101:224427, 2020.

[83] Y. Zhao, Y. Natsume, N. Sawaguchi, and M. Sasaki. Synthesis and optoelectrical properties of ABO_2 (A = Li, Na; B = Y, Yb). *IOP Conference Series: Materials Science and Engineering*, 18(9):092066, 2011.

[84] K. M. Ranjith, D. Dmytriieva, S. Khim, J. Sichelschmidt, S. Luther, D. Ehlers, H. Yasuoka, J. Wosnitza, A. A. Tsirlin, H. Kühne, and M. Baenitz. Field-induced instability of the quantum spin liquid ground state in the $J_{\text{eff}} = \frac{1}{2}$ triangular-lattice compound $NaYbO_2$. *Phys. Rev. B*, 99:180401, 2019.

[85] J. Guo, X. Zhao, S. Ohira-Kawamura, L. Ling, J. Wang, L. He, K. Nakajima, B. Li, and Z. Zhang. Magnetic-field and composition tuned antiferromagnetic instability in the quantum spin-liquid candidate $NaYbO_2$. *Phys. Rev. Mater.*, 4:064410, 2020.

[86] O. A. Starykh. Unusual ordered phases of highly frustrated magnets: a review. *Reports on Progress in Physics*, 78(5):052502, 2015.

[87] E. Kermarrec, J. Gaude, K. Fritsch, R. Khasanov, Z. Guguchia, C. Ritter, K. A. Ross, H. A. Dabkowska, and B. D. Gaulin. Ground state selection under pressure in the quantum pyrochlore magnet $Yb_2Ti_2O_7$. *Nat Commun*, 8:14810, 2017.

[88] D. P. Kozlenko, A. F. Kusmartseva, E. V. Lukin, D. A. Keen, W. G. Marshall, M. A. de Vries, and K. V. Kamenev. From quantum disorder to magnetic order in an $s = \frac{1}{2}$ kagome lattice: A structural and magnetic study of herbertsmithite at high pressure. *Phys. Rev. Lett.*, 108:187207, 2012.

[89] T. Xie, A. A. Eberharter, J. Xing, S. Nishimoto, M. Brando, P. Khanenko, J. Sichelschmidt, A. A. Turrini, D. G. Mazzone, P. G. Naumov, L. D. Sanjeewa, N. Harrison, A. S. Sefat, B. Normand, A. M. Läuchli, A. Podlesnyak, and S. E. Nikitin. Complete field-induced spectral response of the spin-$\frac{1}{2}$ triangular-lattice antiferromagnet $CsYbSe_2$. *npj Quantum Materials*, 8(48), 2023.

[90] F. Fauth, I. Peral, C. Popescu, and M. Knapp. The new Material Science Powder Diffraction beamline at ALBA synchrotron. *Powder Diffraction*, 28:S360, 2013.

[91] R. J. Angel, M. Alvaro, and J. Gonzalez-Platas. EoSFit7c and a fortran module (library) for equation of state calculations. *Zeitschrift für Kristallographie - Crystalline Materials*, 229(5):405–419, 2014.

[92] A. Keren, P. Mendels, I. A. Campbell, and J. Lord. Probing the spin-spin dynamical autocorrelation function in a spin glass above T_g via muon spin relaxation. *Phys. Rev. Lett.*, 77:1386–1389, 1996.

[93] B. Dong, Y. Doi, and Y. Hinatsu. Structure and magnetic properties of ternary potassium lanthanide oxides $KLnO_2$ (Ln=Y, Nd, Sm–Lu). *Journal of Alloys and Compounds*, 453(1):282–287, 2008.

[94] F. Fauth, I. Peral, C. Popescu, and M. Knapp. The new material science powder diffraction beamline at ALBA synchrotron. *Powder Diffraction*, 28(S2):S360–S370, 2013.

[95] R. D. Shannon. Revised effective ionic radii and systematic studies of interatomic distances in halides and chalcogenides. *Acta Crystallographica Section A*, 32(5):751–767, 1976.

[96] J. Sichelschmidt, B. Schmidt, P. Schlender, S. Khim, T. Doert, and M. Baenitz. Effective spin-$\frac{1}{2}$ moments on a Yb^{3+} triangular lattice: An ESR study. *JPS Conf. Proc.*, 30:011096, 2020.

[97] B. Abragam, A. Bleaney. *Electron paramagnetic resonance of transition ions*. Oxford University Press, 1970.

[98] R. Orbach and B. Bleaney. Spin-lattice relaxation in rare-earth salts. *Proceedings of the Royal Society of London. Series A. Mathematical and Physical Sciences*, 264(1319):458–484, 1961.

[99] J. Sichelschmidt, P. Schlender, B. Schmidt, M. Baenitz, and T. Doert. Electron spin resonance on the spin-$\frac{1}{2}$ triangular magnet $NaYbS_2$. *J. Phys.: Condens. Matter*, 31(20):205601, 2019.

[100] M. Heinrich, H.-A. Krug von Nidda, A. Loidl, N. Rogado, and R. J. Cava. Potential signature of a Kosterlitz-Thouless transition in $BaNi_2V_2O_8$. *Phys. Rev. Lett.*, 91:137601, 2003.

[101] M. Hemmida, H.-A. Krug von Nidda, N. Büttgen, A. Loidl, L. K. Alexander, R. Nath, A. V. Mahajan, R. F. Berger, R. J. Cava, Y. Singh, and D. C. Johnston. Vortex dynamics and frustration in two-dimensional triangular chromium lattices. *Phys. Rev. B*, 80:054406, 2009.

[102] K. Somesh, Y. Furukawa, G. Simutis, F. Bert, M. Prinz-Zwick, N. Büttgen, A. Zorko, A. A. Tsirlin, P. Mendels, and R. Nath. Universal fluctuating regime in triangular chromate antiferromagnets. *Phys. Rev. B*, 104:104422, 2021.

[103] K. M. Ranjith, S. Luther, T. Reimann, B. Schmidt, P. Schlender, J. Sichelschmidt, H. Yasuoka, A. M. Strydom, Y. Skourski, J. Wosnitza, H. Kühne, T. Doert, and M. Baenitz. Anisotropic field-induced ordering in the triangular-lattice quantum spin liquid $NaYbSe_2$. *Phys. Rev. B*, 100:224417, 2019.

[104] J. Xing, L. D. Sanjeewa, A. F. May, and A. S. Sefat. Synthesis and anisotropic magnetism in quantum spin liquid candidates AYbSe$_2$ (A = K and Rb). *APL Materials*, 9(11):111104, 2021.

[105] R. M. Moon, H. R. Child, W. C. Koehler, and L. J. Raubenheimer. Magnetic structure of Er_2O_3 and Yb_2O_3. *J. Appl. Phys.*, 38(3):1383–1383, 1967.

[106] X. Z. Liu, O. Prokhnenko, D. Yamamoto, M. Bartkowiak, N. Kurita, and H. Tanaka. Microscopic evidence of a quantum magnetization process in the $S = \frac{1}{2}$ triangular-lattice Heisenberg-like antiferromagnet $Ba_3CoSb_2O_9$. *Phys. Rev. B*, 100:094436, 2019.

[107] M. Ye and A. V. Chubukov. Half-magnetization plateau in a Heisenberg antiferromagnet on a triangular lattice. *Phys. Rev. B*, 96:140406, 2017.

[108] M. Ye and A. V. Chubukov. Quantum phase transitions in the Heisenberg $J_1 - J_2$ triangular antiferromagnet in a magnetic field. *Phys. Rev. B*, 95:014425, 2017.

[109] R. Iizuka, S. Michimura, R. Numakura, Y. Uwatoko, and M. Kosaka. Single crystal growth and physical properties of ytterbium sulfide $KYbS_2$ with triangular lattice. *JPS Conf. Proc.*, 30:011097, 2020.

[110] J. Xing, L. D. Sanjeewa, J. Kim, W. R. Meier, A. F. May, Q. Zheng, R. Custelcean, G. R. Stewart, and A. S. Sefat. Synthesis, magnetization, and heat capacity of triangular lattice materials $NaErSe_2$ and $KErSe_2$. *Phys. Rev. Mater.*, 3:114413, 2019.

[111] A. O. Scheie, Y. Kamiya, Hao Zhang, Sangyun Lee, A. J. Woods, M. O. Ajeesh, M. G. Gonzalez, B. Bernu, J. W. Villanova, J. Xing, Q. Huang, Qingming Zhang, Jie Ma, Eun Sang Choi, D. M. Pajerowski, Haidong Zhou, A. S. Sefat, S. Okamoto, T. Berlijn, L. Messio, R. Movshovich, C. D. Batista, and D. A. Tennant. Nonlinear magnons and exchange Hamiltonians of the delafossite proximate quantum spin liquid candidates $KYbSe_2$ and $NaYbSe_2$. *Phys. Rev. B*, 109:014425, Jan 2024.

[112] S. Bachus. *Thermodynamic measurements on frustrated triangular and honeycomb lattices in the millikelvin range*. Doctoral thesis, University of Augsburg, 2022.

[113] A. K. Gray, B. R. Martin, and P. K. Dorhout. Crystal structure of sodium ytterbium(iii) selenide, $NaYbSe_2$. *Zeitschrift für Kristallographie - New Crystal Structures*, 218(1):19, 2003.

[114] P.-L. Dai, G. Zhang, Y. Xie, C. Duan, Y. Gao, Z. Zhu, E. Feng, Z. Tao, C.-L. Huang, H. Cao, A. Podlesnyak, G. E. Granroth, M. S. Everett, J. C. Neuefeind, D. Voneshen, S. Wang, G. Tan, E. Morosan, X. Wang, H.-Q. Lin, L. Shu, G. Chen, Y. Guo, X. Lu, and P. Dai. Spinon fermi surface spin liquid in a triangular lattice antiferromagnet $NaYbSe_2$. *Phys. Rev. X*, 11:021044, 2021.

[115] Z. Zhang, J. Li, M. Xie, W. Zhuo, D. T. Adroja, P. J. Baker, T. G. Perring, A. Zhang, F. Jin, J. Ji, X. Wang, J. Ma, and Q. Zhang. Low-energy spin dynamics of the quantum spin liquid candidate $NaYbSe_2$. *Phys. Rev. B*, 106:085115, 2022.

[116] Y.-T. Jia, C.-S. Gong, Y.-X. Liu, J.-F. Zhao, C. Dong, G.-Y. Dai, X.-D. Li, H.-C. Lei, R.-Z. Yu, G.-M. Zhang, and C.-Q. Jin. Mott transition and superconductivity in quantum spin liquid candidate $NaYbSe_2$. *Chinese Physics Letters*, 37(9):097404, 2020.

[117] M. Baenitz, P. Schlender, J. Sichelschmidt, Y. A. Onykiienko, Z. Zangeneh, K. M. Ranjith, R. Sarkar, L. Hozoi, H. C. Walker, J.-C. Orain, H. Yasuoka, J. van den Brink, H. H. Klauss, D. S. Inosov, and T. Doert. $NaYbS_2$: A planar spin-$\frac{1}{2}$ triangular-lattice magnet and putative spin liquid. *Phys. Rev. B*, 98:220409, 2018.

[118] S. Lee, A. J. Woods, M. Lee, S. Zhang, E. S. Choi, A. O. Scheie, D. A. Tennant, J. Xing, A. S. Sefat, and R. Movshovich. Magnetic field-temperature phase diagram of spin-1/2 triangular lattice antiferromagnet $KYbSe_2$. *arXiv preprint*, arXiv:2402.06788 [cond-mat.str-el].

[119] A. O. Scheie, E. A. Ghioldi, J. Xing, J. A. M. Paddison, N. E. Sherman, M. Dupont, L. D. Sanjeewa, Sangyun Lee, A. J. Woods, D. Abernathy, D. M. Pajerowski, T. J. Williams, Shang-Shun Zhang, L. O. Manuel, A. E. Trumper, C. D. Pemmaraju, A. S. Sefat, D. S. Parker, T. P. Devereaux, R. Movshovich, J. E. Moore, C. D. Batista, and D. A. Tennant. Proximate spin liquid and fractionalization in the triangular antiferromagnet $KYbSe_2$. *Nature Physics*, 20, 2024.

Acknowledgments

I want to thank Prof. Alexander Tsirlin for being my supervisor and providing the necessary context and guidance to my research. Thank you for always taking time to write detailed answeres to the many mails I sent your way, proof reading papers and submission for conferences and enabling exciting measurements at Grenoble and the HZDR.
Thank you to Priv.-Doz. Dr. Hans-Albrecht Krug von Nidda as the second reviewer of this thesis. I very much enjoyed collaborating with you and Dr. Mamoun Hemmida on the ESR measurements. Thank you to Mamoun for always being joyful and a pleasure to work with.
Philipp Gegenwart I want to thank for providing the environment for the experimental work, the opportunity to present at conferences and visiting research facilities. I highly appreciated your support during my whole PhD time and the input you provided to my research and conference presentations.
I am also thankful to my fellow Ph.D. students for providing a relaxed and helpful work atmosphere, including the obligatory coffee breaks. Thanks also for joining in the after-work bouldering. All of you contributed to keep my motivation up in the lab and in the climbing center. Special thanks to Franziska Breitner, for sacrificing many afternoons doing EDX measurements with me, and Noah Oefele for clearing up confusions and not complaining about my small crystals.
Christine Schäfer I would like to thank for being supportive, understanding and in general interested in me beyond my research. I could always count on your help in administrative issues. Thank you, for always taking time for a short chat when I dropped by your office.
I want to thank Alexander Herrenberger and Klaus Wiedenmann for the many small and large tasks with which they keep the laboratories and measuring devices running. Thank you also for your willingness to help with problems in everyday laboratory work, such as beeping devices and advice on the disposal of toxic substances.
Ein großes Dankeschön an meine Familie, insbesondere meine Eltern, die mich immer unterstützt haben. Danke, dass ihr für mich da gewesen seid, auch wenn ihr nicht verstanden habt warum gerade ein Physikstudium das Richtige für mich war und eine Karriere als Steuerberater nützlicher gewesen wäre. Vielleicht klappt es zumindest mit dem Job in der Schweiz.
Thank you to my friends, Noah, Johanna und Stefan for celebrating the successes, help coping with failures and providing perspective during my PhD work. You always gave me something to look forward to outside of work.
Finally, I would like to thank Max Wolf for his emotional and practical support of my

work. Thank you for believing in me, for pushing me to do things I didn't want to do, for being more enthusiastic about my work than I was at times and for being there every step of the way. It would have been much harder without you.